Adaptive motion compensation in sonar array processing

Adaptive motion compensation in sonar array processing

Proefschrift

ter verkrijging van de graad van doctor
aan de Technische Universiteit Delft,
op gezag van de Rector Magnificus prof.dr.ir. J.T. Fokkema,
voorzitter van het College voor Promoties,
in het openbaar te verdedigen op vrijdag 2 juni 2006 om 10:00 uur,

door

Johannes GROEN

wiskundig ingenieur
geboren te Den Haag

Dit proefschrift is goedgekeurd door de promotoren:
Prof. dr. ir. A. Gisolf
Prof. dr. D.G. Simons

Samenstelling promotiecommissie:

Rector Magnificus, voorzitter

Prof. dr. ir. A. Gisolf,	Technische Universiteit Delft, promotor
Prof. dr. D.G. Simons,	Technische Universiteit Delft, promotor
Prof. ir. P. van Genderen	Technische Universiteit Delft
Prof. dr. M.E. Zakharia	Ecole Navale, Brest, Frankrijk
Prof. dr. A. Stepnowski	Gdansk University of Technology, Polen
Dr. ir. G. Blacquière,	Nederlandse organisatie voor Toegepast Natuurwetenschappelijk Onderzoek
Dr. S.P. Beerens,	Nederlandse organisatie voor Toegepast Natuurwetenschappelijk Onderzoek

Published and distributed by:

Netherlands organization for applied scientific research (TNO)
P.O. Box 96864
2509 JG The Hague
The Netherlands
Telephone: +31 70 374 00 00
Telefax: +31 70 374 06 54
E-mail: info@tno.nl

ISBN-10: 90-5986-187-6
ISBN-13: 978-90-5986-187-6

Copyright 2006 by J. Groen

All rights reserved. No part of the material protected by this copyright notice may be reproduced or utilized in any form or by any means, electronic or mechanical, including photocopying, recording or by any information storage and retrieval system, without written permission from the author: J. Groen, TNO, P.O. Box 96864, 2509 JG, The Hague, The Netherlands.

Printed in The Netherlands

Contents

1. Introduction 9
1.1. Background 10
1.2. Objective 11
1.3. Anti Submarine Warfare 11
1.4. Mine hunting 13
1.5. Requirements analysis 15
1.5.1. Subdivision in four topics 15
1.5.2. Problems and approach 18
1.5.3. Research visualization 18
1.6. Outline 19

2. Simulation of sonar data and images 21
2.1. Introduction 21
2.1.1. Basic physics for the simulator suite 21
2.1.2. Simulator structure 25
2.1.3. Primary assumptions in the model 25
2.1.4. Sonar background knowledge and definitions 25
2.1.5. Outline 29
2.2. Application of the simulator 29
2.2.1. Application to mine hunting sonar 30
2.2.2. Application to Anti-Submarine Warfare (ASW) sonars 31
2.3. Structure of the simulator 33
2.4. Modular methodology with a collection of models 34
2.4.1. Acoustic response of arbitrary targets 34
2.4.2. Reverberation 43
2.4.3. Target shadow 48
2.4.4. Multi-path 49
2.5. Complete simulation for mine hunting 52
2.6. Measured synthetic aperture sonar data 54
2.6.1. Use for signal processing development 55
2.6.2. Potential for classification 59
2.7. Specific features for the Anti-Submarine Warfare towed array sonars 59
2.8. Summary and conclusion 62

3. Adaptive port/starboard beamforming of triplet sonar arrays 63

3.1. Introduction 63
3.2. Triplet beamformers 66
3.2.1. Optimum triplet beamformer 70
3.2.2. Cardioid beamformer 71
3.2.3. Adaptive triplet beamformer 73
3.3. Theoretical performance 76
3.4. Sea trial results in noise 80
3.4.1. Experiment set-up 80
3.4.2. Processing chain 81
3.4.3. Experiment results 82
3.4.4. Discussion 84
3.5. Sea trial results in reverberation 84
3.6. Conclusion 89

4. Doppler corrected array processing 91

4.1. Introduction 91
4.1.1. Background 91
4.1.2. Operational aspects 93
4.1.3. Outline 94
4.2. Theoretical performance in a turn 94
4.2.1. Error sources 95
4.2.2. Shape deviations 95
4.2.3. Doppler shift 98
4.2.4. Doppler spreading 101
4.3. Compensation methods 103
4.3.1. Signal processing chain 103
4.3.2. Method 1: Shape corrected beamforming 105
4.3.3. Method 2: Stabilized beamforming and dynamic matched filtering 106
4.3.4. Method 3: Shape and Doppler corrected beamforming (SDCB) 107
4.4. Required sonar track accuracy 108
4.5. Proof of concept on simulations 110
4.6. North Sea experiments in 2002 111
4.6.1. Experiment description 112
4.6.2. Environmental conditions 112
4.6.3. Signal processing results 113
4.7. Mediterranean experiments in 2003 114
4.7.1. Experiment description 115
4.7.2. Environmental conditions 115
4.7.3. Signal processing results 116
4.8. Conclusion 122

5. Synthetic aperture sonar part I: signal processing with motion compensation.....123
5.1. Introduction.....123
5.1.1. The synthetic aperture sonar signal processing chain.....125
5.1.2. Outline.....126
5.2. Imaging methods.....127
5.2.1. Theory: three approaches to the signal processing kernel.....128
5.2.2. Considerations for imaging performance.....134
5.3. Motion estimation.....138
5.3.1. Results on rail experiments.....143
5.3.2. Results on experimental data with a ship mounted sonar system.....145
5.4. Motion compensation.....151
5.4.1. Validity of motion compensation.....152
5.4.2. Non-directional versus directional motion compensation.....153
5.4.3. Simulated scenarios.....154
5.4.4. Application of motion compensation to simulated scenarios.....156
5.4.5. Application to experimental data from the HUGIN vehicle.....158
5.4.6. Future ultra wide beam system issues.....162
5.5. Conclusion.....164

6. Synthetic aperture sonar part II: wavenumber frequency imaging.....165
6.1. Introduction.....165
6.2. Theory on synthetic aperture processing.....167
6.2.1. Space-time imaging.....168
6.2.2. Space frequency imaging.....169
6.2.3. Convolution imaging.....169
6.2.4. Stolt migration.....170
6.3. Application of Stolt migration.....171
6.3.1. Motion compensation.....171
6.3.2. Migration for a range window.....174
6.3.3. Limited domain processing.....176
6.3.4. Wavenumber frequency interpolation.....176
6.3.5. Tapering in different domains.....179
6.4. Results with simulated data.....180
6.4.1. Influence of integration angle, theory.....180
6.4.2. Influence of integration angle, practice.....182
6.4.3. Influence of platform motion, practice.....184
6.4.4. Parameter sensitivity.....186
6.5. Shadow enhancement for improved target classification.....187
6.5.1. Blurring of the shadow due to large integration angles.....188
6.5.2. Sharper shadows with convolution imaging.....195
6.5.3. Combining convolution imaging with Stolt migration.....201
6.6. Results with experimental data.....202
6.6.1. Application to rail data.....203
6.6.2. Application to data from a UUV.....204
6.6.3. Shadow enhancement.....207
6.6.4. Performance comparison.....209
6.7. Conclusion.....209

7. Conclusions 211
7.1. Anti-Submarine Warfare 212
7.2. Mine Hunting 214
7.3. Recommendations 215

Appendix A. Detection theory 217
A.1. Minimum variance distortionless response beamforming 218

Appendix B. Signal deformation during a maneuver 221

Appendix C. Imaging for a homogeneous medium: 2D case 223
C.1. General expression for 2D imaging 223
C.2. General expression for 2D Stolt migration 224

References 227

List of symbols and abbreviations 235

Summary 241

Samenvatting 243

Acknowledgements 245

Curriculum vitae 247

1. INTRODUCTION

Overhead the albatross hangs motionless upon the air
And deep beneath the rolling waves
In labyrinths of coral caves
The echo of a distant time
Comes willowing across the sand
And everything is green and submarine

D. Gilmour, N. Mason, R. Waters, R. Wright

These lines are taken from a song by the band Pink Floyd, which, at the time back in 1971, was revolutionary in rock music. Both music and lyrics carry the listener to a surreal world in which mysterious echoes affected by water pass by during the over twenty minutes of music. It is an artistic example of the fascination of mankind for underwater sound. This thesis aims at a converse side of this fascination, which is the application of exact sciences to underwater sound. However, in the research on underwater acoustics part of the mystery is kept alive because even at this time not all issues are completely understood. Mathematical and physical models used in this research are often based on assumptions and statistical features. Moreover, measurements used for validation of the methods are limited and, especially at sea, contain intrinsic uncertainties. This sometimes alters underwater acoustics from a science into an art, for which experience is a must.

Transmission of sound through the sea and its applications have been investigated for centuries. However, the main efforts and successes in this field originated from military applications in the 20th century. The history of acoustics is well documented in the book of Hunt (1992). The notes of Leonardo da Vinci already show an application in 1490: "*If you cause your ship to stop and place the head of a long tube in the water and place the outer extremity to your ear, you will hear ships at a great distance from you*". The first quantitative measurement in underwater acoustics was made in 1827 when Daniel Colladon and Charles Sturm measured the speed of sound in Lake Geneva by timing the interval between a flash of light and the sound from the striking of a bell underwater. The "passive" method of listening under water with a single hearing device was used up to World War I. In 1915 Paul Langevin, a French scientist, used the idea to develop a device which is used to this day in boats and submarines to detect objects under the sea. In 1916, under the British Board of Inventions and Research in the United Kingdom a large project started, which led to the Anti Submarine Detection Investigation Committee (ASDIC) in mid 1917. By 1918, both the United States and Britain had built active systems, which were based on transmission and reception. In World War II, the Americans used the term sonar, an acronym for SOund, NAvigation and Ranging, for their system, which eventually fully replaced the name ASDIC.

One of the most famous successes of sonar was not military in nature. The Titanic was found, 73 years after it sank in 1912, first with sonar. However, apart from some civil applications, the majority of progress in the 20th century came from military interest.

1.1. Background

In this research the performance of signal processing techniques in sonar is the central theme. Sonar, the acronym for SOund NAvigation and Ranging, is a well-accepted technique for underwater observation. It uses sound that travels through the water body to extract the information that is of interest. The reason for success of the technique lies in the relatively low energy losses of the traveling acoustic waves.

In recent decades a large component of sonar research has been dedicated to transducers, receivers, acoustic propagation and scattering, and real-time signal processing. The historical line in this research can be found in some of the published books. The first book to mention here is the most referenced book for sonar literature in the last decades and is written by Urick (1975). Other renowned books in the field of sonar signal processing are written by van Trees (1968), Nielsen (1991) and Owsley (1985). Current developments for performance enhancements on sonar systems often are driven by the latest improvements in computational power.

Until now the verification of the actual influence of motion of the sonar sensors on the performance has not been accomplished. Also corresponding motion compensation methods are not available. In this thesis it is shown that such sonar motion is a sensitive parameter for sonar performance. A sonar generally moves during the observations. If this motion is not compensated properly, it will cause sonar performance loss. But the motion can often be compensated and sometimes even utilized for signal enhancement. The sonar signal processing algorithms are always restricted by some kind of real-time aspect. Until now the increase in computational power has in practice merely resulted in an increase of number of hydrophones (underwater microphones) and signal bandwidth. Nevertheless, growing arrays and frequency bands have also increased the sensitivity of the systems. So, lately, both industry and research institutes are looking more seriously into actual improvement in the signal processing based on more advanced physical models. To insert sonar motion into the sonar signal processing chain requires knowledge on the physical effects. Secondly, potential compensation methods need to be designed such that they still suit the computational requirements. Also, a reliable model is necessary for testing and further improving of the methods under different circumstances. These are the fundamental steps that will be investigated in the thesis.

1.2. Objective

The general objective of this research is to study the possibilities to improve the performance of signal processing techniques in sonar. The sonars studied are for military purposes in this case and cover two application areas: Anti Submarine Warfare (ASW) and Mine Hunting (MH). The application areas mainly differ in the acoustic frequency range used. Low frequencies around a kilohertz are necessary for ASW, because the detection ranges of several tens of kilometers are required. The corresponding wavelengths for the sonar systems used are on the order of one meter. For MH the frequencies used are much higher, up to one megahertz, and with a corresponding range of several hundreds of meters. The wavelength is in the order of one centimeter in this case.

1.3. Anti Submarine Warfare

In Anti Submarine Warfare (ASW) detection, localization and classification of targets is usually achieved with long towed array sonar systems. A schematic overview of such a sonar scenario is depicted in Figure 1-1. Large detection ranges imply the use of low frequencies, which in turn imply large arrays for high angular resolution. Towed arrays are fitted in a flexible hose and attached to a vessel with a cable, which brings the advantages of variable sonar depth and compact storage on a winch. The first towed array sonar systems were used for passive applications, which means that no acoustic sources were used. The system only listened to the radiated noise of submarines. Since then submarines have become more and more silent due to the hydrodynamic and propulsion enhancements in the design. For the sonar systems that detect submarines, this meant that passive systems (only listening) were no longer sufficient. This is the reason that development of new systems nowadays mainly lies in the field of active towed array sonars. In the following paragraphs the relevant research topics for the towed array systems will be pointed out.

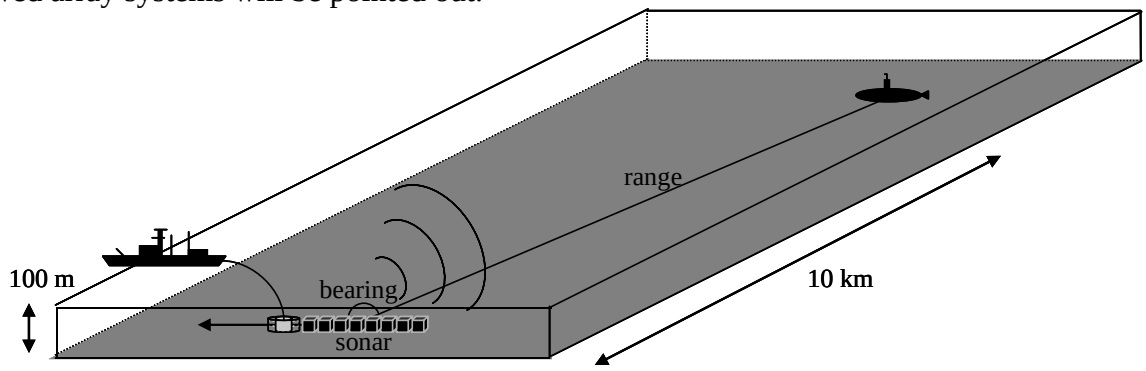


Figure 1-1 *Schematic overview of Anti Submarine Warfare sonar scenario.*

The problem of port/starboard ambiguity of a linear towed sonar array.
The receiving array of a towed low frequency active sonar is a neutrally buoyant tube that contains the hydrophones. This array can normally be regarded as straight within the corre-

sponding signal processing criteria. Therefore, the signal processing output has cylindrical symmetry. In practice this means that it is not possible to determine whether a target is situated on the port or starboard side, i.e. there is no port/starboard discrimination. Solutions to this problem are tow ship maneuvers, multiple arrays, directional sources etc. The most successful technique is the use of multiple arrays. In this thesis, the low frequency active sonar used contains the so-called triplet technology. The technology and the potential with respect to making port/starboard discrimination are explained in detail in Chapter 3. The basic idea is that the conventional linear array is replaced by a linear array of triplets. The triplets consist of three hydrophones that are attached via a small rigid frame. In this way an aperture perpendicular to the linear array is generated. The idea is that this aperture is precisely sufficient to be able to determine whether signals come from the port or the starboard side of the array.

Shallow and coastal areas.
In the last few years the scenario of towed array sonar operations has changed. The operations of ASW used to be in deep water. Nowadays an important task of ASW units is the joint NATO missions, usually taking place in shallow water areas. Reverberation is an important problem that arises due to this shift in operational area. The term reverberation refers to the sum total of the sound that scatters from sea floor, surface or volume to the sonar receiver. Especially from the sea floor the reverberation response is important and can mask targets. Solutions to this problem lie in utilizing Doppler and bandwidth properties of the signal and in beamforming. The use of active sonar in combination with multiple arrays brings in another important feature when sailing along the coast. In this case the reverberation received from the coastal side of the sonar is high. When sailing close enough to the coast the submarine can be expected to sail on the seaward side (the sailing area for the submarine will otherwise get too small and shallow). For this scenario, port/starboard discrimination is very important.

Sensor position deviations during maneuvers
The relative positions of the hydrophones in a towed array have to be known in order to do correct signal processing. Because of hydrodynamic instabilities of the system and ocean currents, the hydrophone positions do not always lie along a perfect straight line. Additionally, the sonar does not always sail along a straight constant velocity track, which obviously will imply increasing relative position errors as time passes. From experience it is known that a straight-line assumption does not degrade performance severely when sailing a straight track. However, when the tow ship maneuvers, e.g. when turning, the array is curved and sails a non-straight track. For optimal detection results these deviations have to be taken into account.

Besides all these problems, one has to bear in mind that the sonar output needs to be presented to the operator just after collecting the data. In other words, there is always a (near) real-time aspect in the signal processing chain. When operating with suitable settings, the processing output of a towed array sonar system shows range, bearing and velocity of a target. Due to the large amount of data it is a problem to carry out all calculations in real time. With smart algorithms it is possible to reduce the required computation power.

1.4. Mine hunting

In general terms, the improvement for Mine Hunting depends on the same performance criteria as ASW. The aim is to use the sonar in such a way that the probability of detection of targets is high and the probability of false alarms is low. What is said for detection can be said about classification as well. At the same time operations should not cost too much time, which brings up the criterion of a high area coverage rate. The overall problem in mine hunting can be summarized as finding all the mines in a reliable and fast way.

The sonars for mine hunting are typically two orders of magnitude higher in frequency than the sonars for ASW. Generally, in a mine hunting scenario a platform with one or more sonar systems is passing an area to search for mines, as depicted in Figure 1-2. In research on mine hunting sonar, a combination of methods is used to achieve detection, 1ocalisation and classification of mines. For all these purposes it is necessary to obtain very high spatial resolutions. One way to achieve this is to develop advanced signal processing methods. Synthetic Aperture Sonar (SAS) is such a method. This has become feasible due to the increased compute power of modern computers. The basic idea behind SAS is the integration of many successive pings from a moving platform, to form a synthetic array that is much longer than the physical array. Possible applications of SAS are the use of sonars mounted on a ship or in small Unmanned Underwater Vehicles (UUVs) for mine-hunting operations. A problem that is not yet solved in mine hunting is the detection of buried mines. Buried mines can still inflict major damage to ships, but are much harder to find. Lower frequencies with better propagation properties are essential, when the sound of the sonar needs to penetrate the sea floor sediment to find these buried mines.

The spatial sonar resolution strongly depends on the frequency used and deteriorates when using a lower frequency. Application of SAS, which typically increases spatial resolution, is a promising technique to enhance the performance for both buried but also non-buried mine scenarios. Unlike its radar equivalent Synthetic Aperture Radar (SAR), the SAS technique is not yet mature. SAS is still in the research and development phase, whereas SAR has been operational for many years. As a consequence, literature on SAR is abundant, but on SAS there is much less. Due to the dimensional differences, methods from radar are often not applicable. For the development of SAS signal processing algorithms, literature from the seismic community showed to be more relevant. In the following paragraphs the topics relevant for this thesis for improved mine hunting sonar processing are pointed out. They are the simulation model, the signal processing techniques, sonar motion compensation, autofocusing and the eventual resolution enhancement.

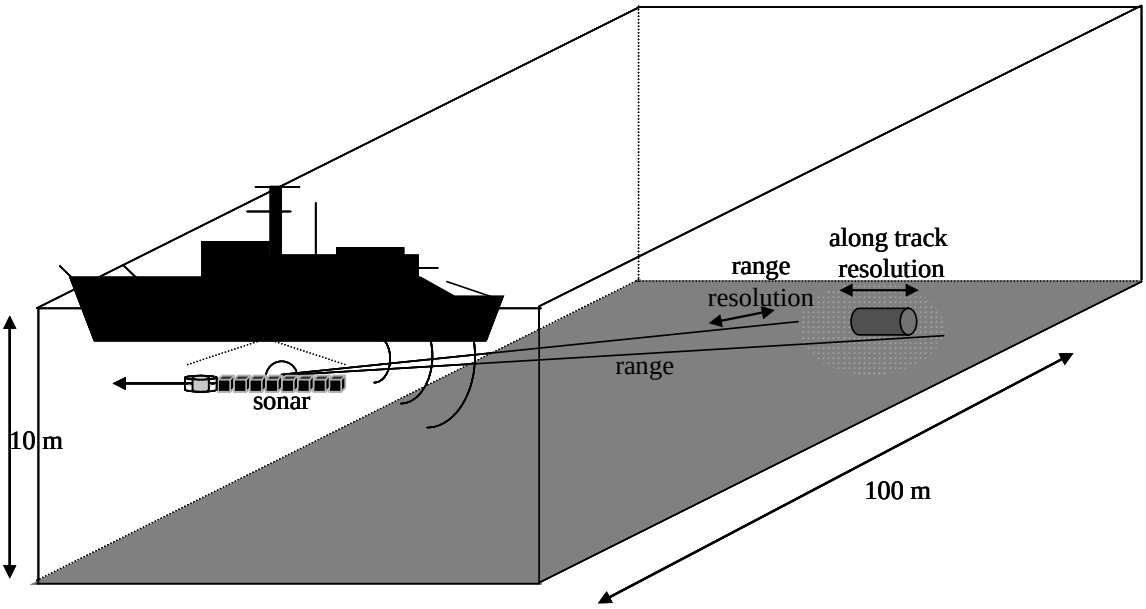


Figure 1-2 *Schematic overview of Mine Hunting sonar scenario.*

Simulation model
Signal processing methods that are to be analyzed are complex and controlled by many parameters, among others: geometric parameters, acoustic parameters and processing parameters. To be able to analyze the effects of various parameter settings, a simulator is needed. Additionally, when such a model takes into account the most relevant physical effects, it can be used in the SAS image formation process. The (synthetic aperture) sonar image of a certain mine in a known environment can be predicted and this prediction can be utilized for better image focusing, object classification and better tuning of the processing parameter.

Processing techniques
In mine hunting sonars the type of processing is an important topic, because it is a large bandwidth real-time system. The actual step of converting the received acoustic data to a sonar image is commonly referred to as SAS processing, beamforming, imaging, focusing or migration. The step is essential since, after data collection, the image usually needs to be constructed in a short time. On the other hand, one does not want to trade this off against performance degradation. Several processing techniques are analyzed, e.g. time domain processing, frequency domain processing, convolution beamforming and Stolt migration.

The basic idea of synthetic aperture processing is to use multiple pings instead of one ping to construct a sonar image. Because for most applications typically the sonar is moving, e.g. with a ship or on an underwater vehicle, the sonar aperture is enlarged. In the following chapters it will become clear that a longer aperture or longer array of hydrophones will result in an improvement in resolution. Thus, a simple definition for synthetic aperture processing is: collecting sonar data series from several pings and combining them coherently afterwards.

Sonar motion compensation
There are many different aspects of sonar motion for SAS. The sonar motion includes the motion of the elements from ping to ping in three dimensions, but also during the ping. The choice of the imaging method also puts restrictions on the way this motion is to be taken into account. Stolt migration turns out to be a suitable method, but it requires that the SAS array be a uniform linear array. Since this is generally not the case, the consequences need to be investigated in SAS research.

Autofocusing
Wavelengths of mine hunting sonars are in the order of a centimeter or even smaller, which implies that for coherent signal processing hydrophone positions have to be known accurately. It is difficult to measure these with non-acoustic sensors, e.g. with an inertial navigation system. A solution to this might be the use of the acoustic data, which is generally referred to as autofocusing. Such autofocusing techniques nonetheless all have their disadvantages like error integration, computational costs and unwanted (unreal) image improvement. The last issue may occur when a certain criterion is optimized and leads to a higher performance than the actual physics would allow. An attractive option is to use a combination of the measurements.

Resolution enhancement
The application of active SAS to high frequency sonar systems has the main goal to enhance spatial resolution. There is obviously a limit to this. The best possible resolution is on the order of the (center) wavelength of the transmitted signal, but it practice the spatial resolution is determined by the (synthetic) array length. The array can not be infinitely long, because then on the far end signals are simply too much attenuated. Additionally, depending on several parameters, this situation even depends on other, more severe effects. The effects that play a role here are sonar position measurement accuracy, acoustic environmental stability, geometry, sonar beamwidths and even the target scattering properties. Fortunately from experience it is known that these effects can generally be dealt with without losing too much resolution.

1.5. Requirements analysis

1.5.1. Subdivision in four topics

Due to improvements in computational power, it is now possible to replace conventional sonar signal processing techniques by more advanced ones. The primary aim of these advanced techniques is compensation for the motion of the sonar. To develop compensation methods and study the corresponding sonar performance is the main objective of this thesis. This section states the problems, the tasks leading to solutions and the research questions that need to be answered on the way. Both the nature and applicability of the compensation methods vary with the field of application. The general goal, analyzing the motion compensation techniques, is verified for different applications. For each method, first a model is used to deter-

mine the candidate methods, with a direct link to physical theory. Then, again for each method, the methods are implemented and tested on simulated and measured data. Due to the variation in applicability, it is wise to make a subdivision at this point.

The four sonar motion compensation problems are defined in the Chapters 3, 4, 5 and 6, consecutively.

Table 1.1 *Subdivision of tasks and research questions for the remainder of the thesis.*

Compensation topic	
Port Starboard beamforming (Chapter 3; ASW)	**Research approach**
	Develop, implement, and validate candidate algorithms that facilitate optimal discrimination between the port and starboard side for a so-called triplet array sonar system. Several measured data sets have been recorded to be able to conclude on the choice of algorithm.
	Research questions
	To detect, localize or classify a submarine normally an active towed array sonar is the best solution. Such a sonar, however, due to the system's symmetry has problems to achieve port/starboard discrimination. A desired solution is to place hydrophone triplets in the sonar array tube instead of single elements. There is an uncertainty in the motion and in particular the roll of such triplets. How can this hydrophone position problem be solved best? The distance between hydrophones in a triplet is relatively small, which makes it difficult to determine port and starboard targets. What is the optimal signal processing for this problem?
Shape and Doppler correction (Chapter 4; ASW)	**Research approach**
	Incorporate the best method to correct for maneuvers of the sonar into the existing signal processing chain of a towed array sonar.
	Research questions
	Each element of a towed array sonar for ASW is subject to motion. This motion results in position differences and Doppler effects. The problem becomes more important when the operations involve higher speed and more maneuvering. How can the sonar tracks be monitored? How can this estimated track be merged into the signal processing chain? What is the performance before and after? How sensitive is it? Which problems need to be solved for proper motion compensation? How is performance defined and measured?
Synthetic aperture sonar (Chapter 5; MH)	**Research approach**
	Integration of multiple pings to form a sonar image gives orders of magnitude higher resolution. Unfortunately, the motion of the sonar has to be known and incorporated down to a few millimeters. The way to solve this is a sequence of algorithms and is investigated and tested on measured data. For each step in the sequence a conclusion on the added value is drawn.
	Research questions
	There is a limit to size and number of receivers for a sonar. However, the more elements and the larger the aperture of the sonar, the better the performance. Can the sonar be enlarged synthetically by moving the sonar and integrating its acoustic snapshots? What is the optimal signal processing for such integration? How is uncertainty in motion treated best? Data driven or adaptive methods are computationally expensive. What is the state-of-the-art potential of such methods for both MH sonar array processing techniques? What are the criteria to choose a certain method? How is performance defined and measured?
Stolt migration (Chapter 6; MH)	**Research approach**
	Stolt migration is a fast method for synthetic aperture sonar signal processing. It is the ideal method, but has its limits with regard to motion. The deviations cannot be too high. It is analyzed in this part when the eventual processing loss can still be recovered. This is verified with theoretical derivations, simulated data and experimental data.
	Research questions
	Even when motion in a sonar is compensated, the resulting sonar image will not be the same as without motion. The expected differences can, nevertheless, be modeled; for the model details see Chapter 2. The modeled result can help to optimize utilization. How is such model implemented best? What is the value of the modeled output?

1.5.2. Problems and approach

Based on the stated problems and requirements, the research can be summarized by a number of questions that clarify the aim of the research project. The main question is a broad question and can be formulated as follows. What is the optimal motion compensation method in terms of sonar performance and what is the final result of applying such method?

Introducing this main question immediately brings up a couple of background issues. During the research the terms sonar performance and desired result of a sonar system will have to be defined. Additionally, for every case, the importance and need for such advanced and complex array processing method will have to pass a critical review. The approach for each of the four problems, as already stated in the previous section, is based on the physical theory, and more specifically on the wave equation. Research questions always lead to new insights and also new questions. In this thesis, for each of the four problems, candidate methods are developed from theory and literature. After the try-out, testing and performance evaluation on simulated and measured data, the methods are qualified as suitable or not suitable. The conclusions, available in Chapter 7 give an assessment for the tested methods and, if required, also a recommendation for further improvement on the performance.

1.5.3. Research visualization

An overview of the relations between the different sonar applications and methods is shown in Figure 1.1. The chart is explained in the remainder of this chapter.

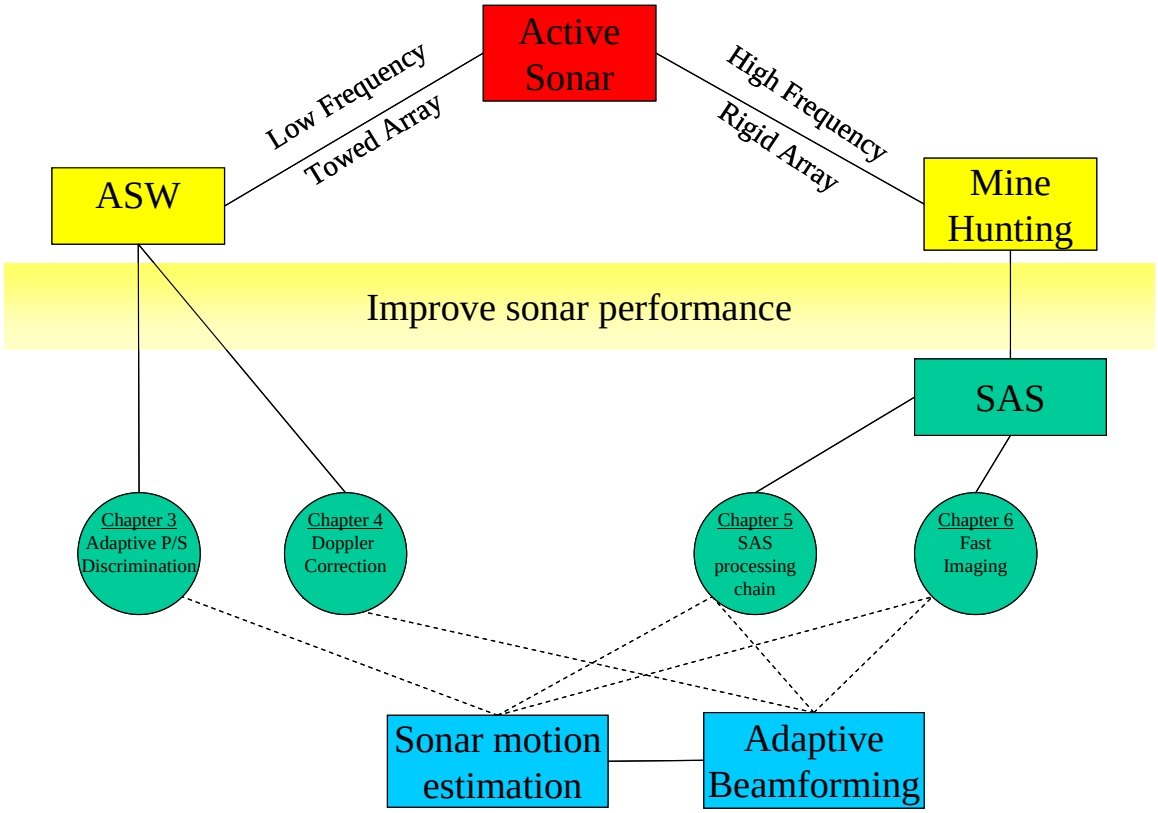


Figure 1-3 *Flow chart of research with applications in yellow, concepts for improvements in green and signal processing algorithms in blue. The four research topics relevant for this thesis are pointed out with the chapter numbers three to six.*

The first application is Anti Submarine Warfare (ASW) and the second is Mine Hunting. In the next sections both are introduced and an outline of the associated research topics is given.

1.6. Outline

The thesis is built up on four main signal processing topics, resulting in seven chapters. The first topic serves as an introductory explanation of the problem (this chapter) and of the simulation model and its application (Chapter 2). This simulation model has been used in the development stage of all four succeeding chapters and Chapter 2 shows the clear link between the actual problems and the theory. The second topic deals with the motion compensation problems in ASW. In Chapter 3 a solution to the port/starboard discrimination problem with triplets in a towed array sonar presented. The subject matter of Chapter 4 is supplementary to Chapter 3 in the sense that the analyzed sonar system is the same, but in this chapter the sonar maneuvering in general is discussed. Topic three, motion compensation in mine hunting, is discussed in the Chapters 5 and 6. First, in Chapter 5, the whole process from acoustic data to sonar image is described, and data driven motion compensation techniques are tested. Following the conclusion of Chapter 5, i.e. the fact that Stolt migration is the best solution for SAS imaging, in Chapter 6 the Stolt migration is analyzed more extensively. The final topic is the

conclusion of the thesis in Chapter 7, in which the optimal methods for each application are summed up and recommendations for future work are given.

The thesis was written based on a collection of articles for conference proceedings and journals. This has induced some overlap in the chapters. An overview of the publications in connection with the chapters in the thesis is given in Table 1.2. Because each chapter has its origin in one or more articles, each of them is readable on its own. A reader who is for instance only interested in mine hunting can simply pass over Chapter 3 and Chapter 4.

Table 1.2 *Publications that shape the following chapters in the thesis.*

Chapter	Publication
2	**Groen, J., B.A.J. Quesson, J.C. Sabel, R.E. Hansen, H.J. Callow & T.O. Sæbø**, 2005, *Simulation of high resolution mine hunting sonar measurements*, Proceedings of the Underwater Acoustic Measurements conference, CD-ROM, June 2005, Heraklion, Greece.
3	**Groen J., S.P. Beerens, R. Been, Y. Doisy & E. Noutary**, 2005, *Adaptive Port-Starboard beamforming of Triplet Sonar Arrays*, IEEE Journal of Oceanic Engineering, Vol. 30, No. 2, July 2005, pp. 348-359.
4	**Groen J., S.P. Beerens &Y. Doisy**, 2004, *Shape and Doppler corrected beamforming for low frequency active sonars*, Proceedings of the UDT Europe, CD-ROM.
4	**Groen J., S.P. Beerens &Y. Doisy**, 2004, *Shape and Doppler correction for a towed sonar array*, IEEE/MTS Oceans proceedings, pp. 613-620.
5	**Groen J. & J.C. Sabel**, 2002, *The choice for the signal-processing kernel in synthetic aperture sonar: considerations and implications*, Acta Acustica, Vol. 88, pp. 658-662, 2002.
5	**Groen J. & J.C. Sabel**, 2002, *Interaction Between Autofocusing and Synthetic Aperture Processing: A Study Based on Simulations and Experimental Rail Data*, Proceedings of the Sixth European Conference on Underwater Acoustics, June 2002, pp. 235-240, Gdansk, Poland.
5	**Groen J., R.E. Hansen & J.C. Sabel**, 2003, *Sonar path correction in synthetic aperture processing*, Proceedings of the Undersea Defence Technology Conference Europe, CD-ROM, June 2003, Malmö, Sweden.
5	**Sabel J.C., J. Groen & B.A.J. Quesson,** 2004, *Experiments with a ship-mounted low frequency SAS for the detection of buried objects*, Proceedings of the Seventh European Conference on Underwater Acoustics, pp. 1133-1138, June 2004.
6	**Sabel J.C., J. Groen & B.A.J. Quesson**, 2005, *Shadow enhancement in synthetic aperture sonar imagery for improved target classification*, Proceedings of the Underwater Acoustic Measurements conference, CD-ROM, June 2005, Heraklion, Greece.
6	**Groen J. & J.C. Sabel**, 2005, *Focusing considerations for wavenumber frequency imaging*, to be submitted to IEE Proc. on radar, sonar and navigation.

2. SIMULATION OF SONAR DATA AND IMAGES

2.1. Introduction

This chapter describes the sonar simulation suite used for the investigation of the signal processing topics in the remainder of the thesis. The name of the software suite is SIMONA, which it received after it was applied to a variety of applications and used by several people. The name refers to the abbreviation SIMulation Of Non-acoustics and Acoustics. The topics in the Chapters 3 to 6 created the need for the simulator. Furthermore, the development of the simulator has also always gone hand in hand with analyses on measured data, which led to high fidelity and a natural modeling process. When certain physical effects showed up in the sonar images and appeared important, the modeling of this effect naturally followed. The aspects of the simulator described in this chapter are fully designed and developed within this PhD research project. When expressions are not novel and derived within the PhD project, corresponding references of literature are always given.

2.1.1. Basic physics for the simulator suite

The wave propagation in the simulator suite is based on the acoustic version of the wave equation in a liquid with constant density ρ. The second order differential equation for the acoustic pressure p in time t and Cartesian coordinates $\mathbf{x} = (x,y,z)$ describes the propagation of acoustic waves in the three dimensional mass of water:

$$\frac{\partial^2 p}{\partial x^2} + \frac{\partial^2 p}{\partial y^2} + \frac{\partial^2 p}{\partial z^2} - \frac{1}{c^2}\frac{\partial^2 p}{\partial t^2} = -\delta(x - x_s, y - y_s, z - z_s)s(t). \tag{2.1}$$

The physical process starts with a normalized acoustic wave signal $s(t)$ transmitted by a source located at (x_s,y_s,z_s). The source is modeled as a point source with a Dirac delta (δ) spatial distribution function. The differential equation describes the propagation of an acoustic wave in the medium and, as will be shown in Section 2.4, is the most important part of the simulator but not the whole.

While propagating, the wave $p(x,y,z;t)$ experiences acoustic energy loss due to spherical spreading described with Eq. (2.1) and additional heat dissipation as will be discussed in Section 2.4. Subsequently, the signal hits the target and is scattered. The reflection process is complicated and a part of the simulator deals with this phenomenon. The reflected signal returns to the receiving part of the sonar, which is generally an array of hydrophones. On the way back the signal again experiences spreading losses. Moreover, during the time the hydro-

phone is receiving, interfering signals from other acoustic sources in the scene are measured as well. The total receiving or listening time is normally referred to as the ping duration. Everything that interferes with the desired target reflection, including ambient noise, noise from point sources (ships, oil platforms) and reverberation, is superimposed on the simulated target signals. These simulated data are used to recognize and quantify the problems with signal distortions (multi-path, Doppler, phase distortions) and sonar motion, and subsequently, develop and test potential compensation techniques. The simulator proved an excellent tool in a wide range of sonar applications such as anti-submarine warfare, torpedo defense, marine mammal localization and mine hunting.

When the propagation of sound is described by Eq. (2.1), the expression for $p(\mathbf{x};t) = p(x,y,z;t)$ in the case of an infinite water mass around the source is given by:

$$p(\mathbf{x};t) = \frac{s\left(t - \frac{r}{c}\right)}{4\pi r}, \quad \text{where} \quad r = \sqrt{(x-x_s)^2 + (y-y_s)^2 + (z-z_s)^2} \quad . \tag{2.2}$$

From this equation it is clear that the acoustic pressure level is reduced according to the reciprocal of the distance to the source. This loss in acoustic pressure and energy per square meter is referred to as spherical spreading loss. The solution of Eq. (2.2) is now utilized twice for the case of sonar: a signal travels from source(s) to target(s) and a signal then travels from target(s) to receiver(s). Thus the received signal is assumed to be a delayed and attenuated version of the transmitted signal. It should be noticed that Eq. (2.2) is obtained with the assumption that the acoustic source is a monopole and has no dimensions. If this is not the case, p becomes frequency dependent. In the simulation model, this frequency dependence is taken into account in a different manner, i.e. by means of a directivity index, which is explained at the end of this section.

Snell's law

Following Lurton (2004), Snell's law is fundamental to ray theory models and describes the refraction of sound rays in a medium where the speed of sound is changing. Figure 2-1 shows the phenomena of reflection and refraction. Although Snell discovered the law of refraction in 1621, he did not publish it and it became known when Huygens (1690) published Snell's result. When the speed of sound varies continuously with depth the medium can be considered as a number of thin layers of constant but different sound speeds. Snell's law is applied to the boundaries of the layers and the sound ray is seen to be curved. In Chapter 3 a ray trace model is used in which the law is applied. In this chapter it is applied for the refraction in the sediment when objects are buried. Snell's law then gives a relation between the grazing angle in water θ and the grazing angle in the sediment θ_s:

$$c_s \cos\theta = c \cos\theta_s, \tag{2.3}$$

where c is the sound speed in water and c_s is the sound speed in the sediment layer.

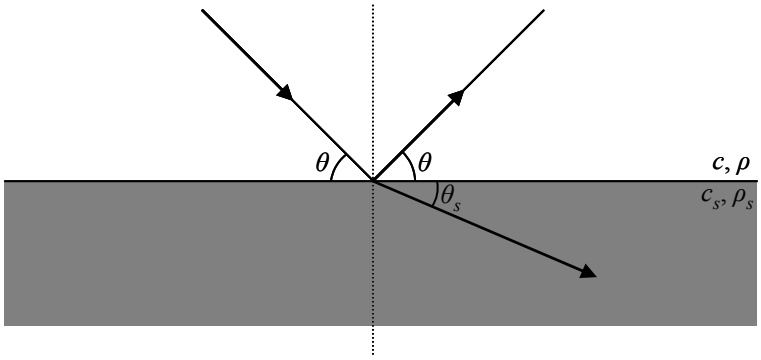


Figure 2-1 *Reflection and refraction of a plane wave, due to the change in sound speed at the interface. The refraction angle is calculated with Snell's law.*

Decibel
Following Lurton (2004), the decibel is a relative unit, not an absolute unit with a physical dimension. The decibel was introduced by the colleagues of Alexander Graham Bell just after his death in 1923. The decibel (abbreviated dB) is simply a numerical scale used to compare the values of like quantities, usually power or intensity. Acousticians introduced the decibel to devise a compressed scale to represent the large dynamic range of sounds experienced by people from day to day, and also to acknowledge that humans perceive loudness increases in a logarithmic, not linear, fashion. Chapman (1998) investigated manifold misuse of the decibel due to careless definitions and the large variety of applications. In the conversions to decibels underwater acousticians often make use of the link between acoustic pressure and intensity, i.e. the acoustic intensity of a plane wave is equal to $p_{\mathrm{RMS}}^2 / \rho c$ calculated with the root mean square pressure. This is valid when the sound speed and density of the medium is constant. For the simulator, the conversion from the linear scale to the decibel scale is defined relative to a comparative level of one micropascal (re 1 μPa):

$$\mathrm{S} = 10 \log_{10}\left(p^2\right), \tag{2.4}$$

where p is acoustic pressure in micropascal and S logarithmic signal level (expressed in dB).

Sonar equation
The approach of propagation with a delayed and attenuated signal shows a direct analogy to the so-called sonar equation for acoustic source, target and acoustic receiver, or in other words, the active sonar equation:

$$\mathrm{S} = \mathrm{SL}\text{-}\mathrm{PL}_1\text{-}\mathrm{PL}_2\text{+}\mathrm{TS}. \tag{2.5}$$

This equation is commonly given in decibels, which is also the case here. It is useful for calculation of the received signal level S for the hydrophones of the sonar. The terms of the sonar equation that determine the value of S are the Source Level SL, the Propagation Loss from source to target PL_1, the Propagation Loss from target to receiver PL_2 and the Target Strength TS and will be discussed separately in this section. This signal level needs to exceed the background. This rise above the background is a stochastic process of which the probability of target detection and the probability of false alarm can be measured. These probabilities deter-

mine the performance of the sonar, which is not a trivial computation. Therefore, usually the signal level and the background level are used to determine the performance of the sonar. The background of a sonar is responsible for the generation of false alarms and may consist of noise with level NL, or reverberation with level RL. Usually one of the two is dominant and then two cases can be considered: the noise-limited case and the reverberation-limited case. For the noise-limited case the signal-to-noise ratio SNR becomes important, which is defined by SNR = S-NL. And for the reverberation-limited case the signal-to-reverberation ratio becomes important, which is defined by SRR = S-RL. Notice the subtraction in these two formulae due to the fact that they are given in dB. To calculate the signal level S the following sonar equation terms have to be defined:

Source Level
The Source Level (SL) of a transmitting transducer or array is a parameter representing its strength as an acoustic source. It is normally expressed in logarithmic terms, since this facilitates its use in calculations of sonar performance. The Source Level is defined as the intensity of the radiated acoustic wave, in decibels relative to the intensity of a plane wave of rms pressure one μPa, referred to a point one meter away from the acoustic centre of the source.

Target Strength
The Target Strength (TS) is defined as the ratio between the incident and back-scattered intensity measured at one meter from the acoustic centre of the target. This term represents the ratio of scattered acoustic energy (back to the hydrophones) to the incoming energy. This definition of Target Strength yields range dependence, because the scatter response of the target is range dependent. However, the term TS is defined as a far field Target Strength and then extrapolated to the range of one meter. In the far field, the target can be considered a point target with a target strength TS. The procedure for non-point targets with large dimensions is described in Section 2.4.1.

Propagation Loss
Propagation Loss is defined as the two-way loss of acoustic energy due to the signal's travel from source to target and back to receiver excluding energy losses occurring at the target. The term includes the aforementioned two-way spherical spreading, and additionally, the absorption loss that accounts for the heat dissipation. The term can be written as $PL = PL_1+PL_2$, where PL_1 is the propagation loss from the source to the target and PL_2 is the propagation loss from the target to the receiver. The total path loss as used in the sonar equation of Horton (1959) is then equal to $TPL = PL_1+PL_2-TS$.

Directivity Index
The Directivity Index (DI) for a source is defined as the ratio of the transmitted acoustic intensity in the direction of the target to the intensity that would have resulted from radiating the same power uniformly in all directions, expressed in decibels. It should be noted that the term DI is not included Eq. (2.5), but it is taken into account in the Source Level, which thus becomes direction dependent. For a receiver, the analogous definition given by Stansfield (1991) is that the Directivity Index is the ratio of the output electrical power generated by an acoustic signal incident along the direction of arrival, to that generated by a uniformly distributed noise field having the same mean acoustic power. In SIMONA the Directivity Index ac-

counts for the directivity of both source and the receiver following these two definitions for source and receiver. It means that the received signal level at the position of the receiver is adjusted for the beampattern characteristics of the hydrophone. It should be noted that the signal level S that includes the directivity index does not represent the acoustic pressure at the position of the receiver. The level S represents the pressure that would be received by a point receiver such that it triggers the same voltage as the actual extended receiver with directivity. Therefore, when the source or receiver is directional, the simulated pressure equals S+DI.

2.1.2. Simulator structure

The simulator is subdivided in underlying modules. Each module corresponds to a physical effect that is modeled based on certain assumptions. These assumptions and their consequences for signal and noise are discussed in this chapter. The philosophy behind the overall model is that it is primarily used for improvement of the signal processing of sonars under investigation. The main aim is to study geometrical behavior of signal processing methods.

2.1.3. Primary assumptions in the model

The most important assumption in the overall model is the constant sound speed in the water. This means that the sound travels to the target and back in a straight line and that there is a direct link between distance and time. Only when buried objects are considered, the sediment is modeled as a layer with a different sound speed and this is described in the last part of Section 2.4.1. The methodology in the simulator for all cases is based upon the fact that all sources, receivers and targets are point-like, or a collection of points. It was found to be a convenient approach that enables simulation of relatively straightforward signal propagation with amplitudes based on Eq. (2.5). This chapter and the following chapters will show that the assumptions yield realistic results.

2.1.4. Sonar background knowledge and definitions

As in every research area, some terms become standard knowledge. The reader of articles or books in that specific research area is required to have some basic knowledge to be able to understand the given explanations. The aim of this thesis is to give the reader a chance to start from a rather basic level, or supply a reference that allows this. Therefore, the explanation of elementary steps in sonar data processing will be given now.

Down-sampling
Down-sampling is useful in sonar signal processing, because usually only a select frequency band is of interest and the rest is merely noise. For active sonar this band is normally chosen based on the transmit frequency band together with the expected Doppler effects. For instance, if the sonar has a sample frequency of 100 kHz and the signal of interest only runs from 9 to 10 kHz, there is an opportunity to compress the data. The way to do this without losing relevant information is called down-sampling. Down-sampling can be performed in the

time domain or in the frequency domain, but it is explained best in the frequency domain. Compressing the data without losing information means that the new down-sampled data needs to obey the Nyquist criterion, which states that the minimum sample frequency is equal to two times the highest frequency in the signal. In the example above, this already brings a data reduction factor of five. Yet, there is more to gain in this example. Transforming the data to the frequency domain and shifting the band of 9 to 10 kHz to a new band of 0 to 1 kHz gives a data reduction factor of 50. This band shift is referred to as demodulation or baseband-ing and can also be applied such that the final frequency band is around zero, i.e. from -500 to +500 Hz in the example. In this case the sample frequency can be reduced to 1 kHz, but then the pressure values in the time series become complex.

Matched filtering

The matched filter is defined as the transfer function that maximizes the SNR at the output. It is assumed here that the signal is known and the noise is uncorrelated, white and Gaussian and in the frequency band of the signal. Only the noise within the signal band needs to be taken into account, because the rest is easily removed by filtering.

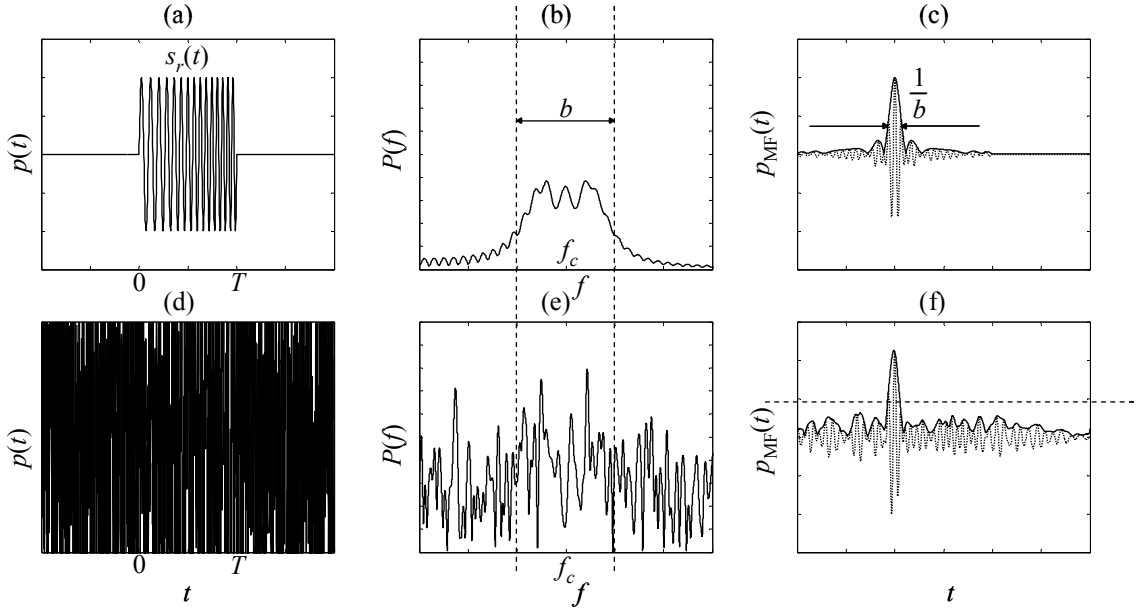


Figure 2-2 *Detection of a chirp signal by means of the matched filter. The top panel shows a noise-free case and the bottom panel shows a noisy case. The left plots show the received data, the middle plots show the received data in the frequency domain and the right plots show the resulting matched filter output both before (...) and after (-) the envelope detector.*

In practice, the matched filter is based on the idea that an expected waveform of the received signal is stored in memory. Usually, the expected signal is the transmit signal of the sonar and is referred to as the replica as shown in Figure 2-2a. This is why the process is sometimes also referred to as replica correlation. When the data are received by the hydrophones a search procedure is applied in order to trace this replica in the data. The matched filter does this by means of convolution of the two. The input is the acoustic data, on the hydrophones or in the beams such as in Figure 2-2d and the output is a time series $p_{MF}(t)$ with peaks when the data correlates with the replica $s_r(t)$ such as in Figure 2-2f.

The mathematical expression for a matched filter operated on a continuous signal of duration T is a cross correlation:

$$p_{\mathrm{MF}}(t) = \int_0^T p(t)\, s_r(t+\tau)\mathrm{d}\tau\,. \tag{2.6}$$

The term matched filtering is sometimes replaced by the name pulse compression, because the pulse content (with all frequencies shown in Figure 2-2b) is compressed to one instant in time. The resulting peak is a compressed version of the pulse as shown in Figure 2-2c, which is a shorter signal containing the same information, i.e. the linear operation enables to go back to the original data. Eq. (2.6) is usually applied in its discrete form, because the sonar data and the replica are digitized. It is also normally applied in the frequency domain for computational benefits. Thus, application of the matched filter results in a better range resolution. It also results in a processing gain, or matched filter gain, which equals $10\log_{10}(bT)$ according to Lurton (2004) in the case of Gaussian noise as background. This is under the assumption that the signal is coherently received with the sonar. For long wideband signals, a significant coherence loss may appear due to medium instationarities, frequency dependence or motion of sonar or target. This coherence will show to be an important criterion in the signal processing schemes described in the Chapters 3, 4, 5 and 6.

Envelope detector
Figure 2-2c and Figure 2-2f show the output of a matched filter. It is, in principle, a set of samples (or pixels) that still represent acoustic pressure. The pressure values fluctuate around the hydrostatic pressure, which is usually already subtracted. Detection is normally achieved by setting a certain threshold plotted by the dashed line in Figure 2-2f, and deciding that a target is found when the sonar output exceeds the threshold. Therefore, two other steps are commonly applied to the sonar output, which are defined as taking the envelope. Qualitatively, the envelope of a signal $p(t)$ is that boundary within which the signal is contained, when viewed in the time domain. First, the fact that the data has these frequency dependent fluctuations within the signal or even within the matched filter output needs to be controlled. This is automatically achieved when the data are properly basebanded around zero and otherwise the Hilbert transform H ensures this. For a real valued time series, adding i times the Hilbert transform makes the negative frequencies zero. Taking the absolute value of the data finalizes the envelope operation, which is formulated by $|p(t)+\mathrm{i}\mathsf{H}[p(t)]|$. Figure 2-2 shows two examples where the matched filter is applied. The top plots shows the procedure on a noiseless signal and the bottom plots show the same results for a signal in noise with a SNR of -10 dB on the input data. The noisy case shows the strong point of the matched filter. Before the matched filter the signal is not visible and after the matched filter a gain lifts the signal above the noise, and moreover, compresses the signal into a sharp peak, which enables accurate travel time estimation.

Resolution cell
For sonar systems temporal resolution of the signal received determines range resolution, which is improved by the matched filter. The explanation of this resolution is now illustrated with an example. In this example, also shown in Figure 2-2, the transmit signal has duration

T, centre frequency f_c, bandwidth b and is defined as $s(t)=\sin\left(2\pi f_c t-\pi b t+\pi b t^2/T\right)$ for $0<t<T$. Such a signal is called a chirp or Linear Frequency Modulated (LFM) signal. Listening to and analyzing such a signal shows that the signal starts at a low frequency f_c-b/2, ends at a high frequency f_c+b/2 and passes through all frequencies in a linear way. The energy of the signal is stretched almost uniformly over the intended frequency band. It has been established, by for example Urick (1975) and Nielsen (1991), that the matched filter output of a signal with energy stretched over a certain band b has a temporal peak width of 1/b after correlation. This is the width where the peak is still higher than three decibels under the maximum. When the signal is defined differently, the temporal resolution is still easily determined by matched filtering the signal with itself and measuring the 3-dB width of the main lobe. Hence, the resolution is now defined by the 3-dB width of the lobe and is given by c/2b. A measure similar to resolution is accuracy, which is defined by the standard deviation for the estimate, i.e. target range or bearing in this case. Accuracy clearly depends on the SNR, which is plotted via a statistical analysis in Figure 2-3b and Figure 2-3c. Woodward (1964) and Edelson (1992), among others, have given analytic formulae for this dependence. The other dimension of the resolution cell in sonar is usually the angular resolution. The following four chapters demonstrate the dependence of the angular resolution on the dimensions of the sonar, i.e. the aperture of the sonar in wavelengths. Lurton (2004) gives a far field formula for the angular resolution of a linear array, which depends on the wavelength λ, the angle of arrival of the signal θ and array length L: $\theta_{3\mathrm{dB}}=50.8\lambda/L\cos\theta$. In this thesis, this formula is often not accurate, but used as first estimate. Resolution is a major subject in the remainder of the thesis. The resolution cell is the box, which has size of the 3-dB width of the main lobe in the two main dimensions of the sonar. These dimensions are usually range and bearing. The resolution cell is sometimes, as for example often occurs in synthetic aperture sonar, computed in x and y coordinates. This does not change formulas with respect to resolution and is only a projection.

Beampattern

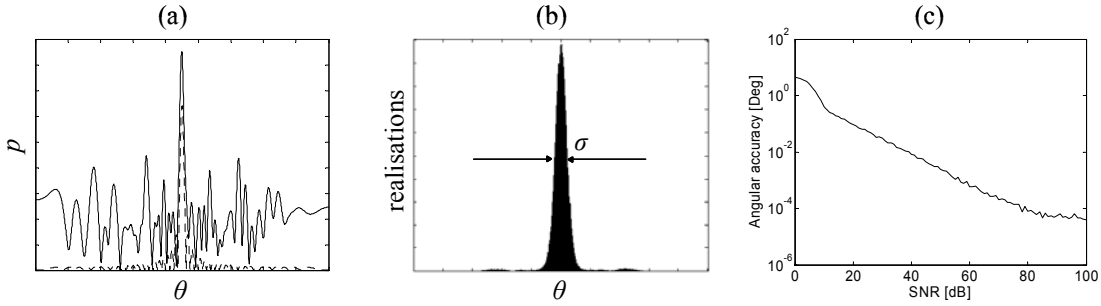


Figure 2-3 *The beamformer output is an acoustic response as a function of angle, which has a peak at the direction of arrival of the signal. The noiseless (--) and noisy (-) case are plotted in panel a. The bearing accuracy (σ) depends on the amount of noise and is plotted in b for a SNR of -10 dB. The dependence on SNR is plotted in panel c.*

The beampattern of a transducer or hydrophone represents the energy response in the far field, for a given frequency, as a function of angle. It is often normalized to the maximum value, but this not mandatory. Instead of one transducer or hydrophone one may also use the definition for an array of transducers or hydrophones. This is shown by the solid line in Figure 2-3a.

A-scan
The name A-scan comes from the field of ultrasonic imaging for medical purposes. The A refers to the first (A) dimension that can be resolved with an acoustic active scanning device, such as sonar. The A-scan is the counterpart of the beampattern and is defined as the energy versus travel time, which is easily translated to range assuming a constant sound speed.

2.1.5. Outline

This chapter describes SIMONA. Section 2.2 deals with this sonar simulator for Mine Warfare and Anti-Submarine Warfare. Section 2.3 supplies a summary on the simulator structure. It consists of modular software that adds each physical effect to the simulated data vector as if obtained from the sonar. Section 2.4 describes the underlying models, with as most important:

- The *acoustic response of the target* that is modeled as point-like or extended.
- *Reverberation*, the echoes from non-targets on the sea floor, which are modeled in two ways: stochastically and by means of point scatterers.
- An *acoustic shadow*, which is modeled by switching off a part of the sea floor scattering behind the target when the target is large compared to the acoustic wavelength.
- *Multi-path,* which is modeled with water surface and sea floor acting as an acoustic mirror.

To illustrate the simulator an example is given in Section 2.5. It includes all the relevant parts of the modular suite. In Section 2.6 the models are verified. It is hard to draw conclusions on the accuracy of the simulator based on one or a few cases, but it seems the only way this can be done. Most efforts went into the modeling of the mine hunting sonar data and a considerable part of this chapter is dedicated to this application. Nevertheless, for completeness, the specific ASW features are presented in Section 2.7. Section 2.8 summarizes and concludes on the results and sets the scene for the following four chapters.

2.2. Application of the simulator

As mentioned in the preceding section, the simulator is used for various applications. The two primary applications are Mine Warfare and Anti-Submarine Warfare (ASW). In this section the role of the simulator and the relevant features for these two applications are discussed.

2.2.1. Application to mine hunting sonar

Mine hunting sonar images have become more complex, because of the variety of situations and the high resolution of current sonar systems. This section gives an overview of the current and emerging technology of mine hunting and states the value of the simulator in this respect.

The simulator as a tool for signal processing development and classification
The design of a synthetic aperture sonar requires a wide range of expertise. The main aspects are the sonar itself (the wet-end), and the set-up of the signal processing chain (the dry-end). The two are clearly linked. The topic of interest for this thesis lies in the dry-end part. The main goal of this chapter is to investigate whether, for given sonar system parameters, the signal processing can be performed in such a way that sonar performance is optimal. As will be clear from the topics in Chapter 5 and 6, the signal processing chain has many degrees of freedom. Currently, as another goal of the simulator, it appears feasible to utilize simulated images for post-processing, i.e. as a classification database generator.

Typical model features for mine hunting
The most important features of SIMONA are an accurate 3D simulation of an arbitrary target response with the corresponding shadow, reverberation, frequency dependent sonar properties and multi-path. The approach for the mine hunting sonar simulations is similar to that of Hunter (2005). The verification and development of SIMONA was realized in parallel with the acquisition of a wide range of data sets in the frequency range of 10 to 200 kHz. State of the art high resolution sonar systems used for mine detection and classification reveal more and more object detail. Therefore, the enormous flow of information enables and calls for automatic post-processing steps, like e.g. computer aided detection/classification or automatic target recognition. In this chapter an example, which was also the last development step for the simulator, is used to explain the simulator. The typical system that is used for this is the so-called SENSOTEK sonar, which is described by Hagen (2001). The idea is to use simulated sonar images to assemble a target data base with dynamic target features. In this chapter a simulated data set is shown in full detail. The setting is an Autonomous Underwater Vehicle (AUV) sailing past a cylindrical target that lies on the sea floor at an across-track distance of 30 m while the sonar insonifies the surrounding patch of sea floor. Sonar images with and without multi-path are compared. Target response, shadow and shadow filling are also analyzed separately in order to demonstrate their significance. Moreover, the possibilities for automatic classification with sonar models are pointed out. On the one hand this depends on the model accuracy and on the other hand on the discriminating ability of the sonar images.

The simulator as a tool to analyze the huge data flow problem for SAS systems on AUVs
The problem with an operational design of such a system is characterized by the following trade-off. The flow of acoustic data depends on the system bandwidth and the number of recorded hydrophones, preferably both of which are large. The signal processing methods (preprocessing, autofocusing, motion compensation and imaging), determine computer memory and computational load requirements. Again, optimal performance of the signal processing chain comes at the expense of a large computational load. For an AUV, the space for data processing and storage is limited, however. Serious on-board processing is not yet an option. Therefore, the AUV is collected after its (mine-hunting) mission and the data are processed on the mother ship. As a consequence, the complete processing of Terabytes of data after collection of the AUV can only take place after the data collection, which is a computational problem. When the AUV has performed a survey of 30 hours, the crew does not want to wait another 30 hours for the result. Complete imaging with the full amount of data from a state-of-the-art mine hunting SAS sonar is not possible at the moment.

The simulator as a tool to design future sonar systems
The simulator is used to investigate the trade-off, signal-processing calculations versus performance and is also used as a tool in the post-processing (in this chapter, Chapter 5 and Chapter 6). However, it also proved to be useful for the design of future systems. For example, if one has to choose between the reduction in beamwidth and bandwidth, it is essential to know which one costs more in terms of performance loss.

2.2.2. Application to Anti-Submarine Warfare (ASW) sonars

Data acquisition is particularly expensive for ASW research as sea trials involve experienced manpower and costly high-tech equipment. Also, at sea, the environment remains unpredictable and many complicating effects are combined. Therefore, the simulator SIMONA was designed to help the development and testing of new algorithms for advanced towed array processing, at low cost, in a controlled environment. The various simulation modules for platform motion, background noise, active and passive target responses and reverberation have been verified with:

- Analytic expressions: target strength of Urick (1975) and reverberation of Lurton (2004).
- Validated models, e.g. the model ALMOST described by Schippers (2004) and the model INSIGHT described by Ainslie (1996). The model ALMOST is based on eigenrays and is in use operationally with the Royal Netherlands Navy. INSIGHT is a ray based sonar performance model, which works by identifying acoustic components, e.g. surface duct, bottom reflection, convergence zone or multi-paths and summing the contributions from each. The input of both ALMOST and INSIGHT consists of the environment in more detail than SIMONA and for instance includes wind speed, bottom roughness, sound speed profiles and subbottom features. The output of both ALMOST and INSIGHT consists of acoustic levels in decibels as an intermediate result and sonar performance in terms of detection ranges or probability of detection as a final result.
- Measurements acquired by TNO or from literature, e.g. the article of Berg (2003).

Due to the practical limitations in variability and flexibility of measurements, the development of the signal processing chain for an ASW sonar requires a realistic simulator. For instance, the noise at sea is difficult to tune and is also difficult to measure at length. The used simulation modules (or underlying models for the different physical phenomena) slightly differ from the mine hunting case. The supplementary models are Doppler, passive targets, tow ship noise, noise correlation for closely placed hydrophones and special waveforms. For ASW the generation of the time series of sonar data, the aim of the simulator, is also performed in a modular way. The extra models needed for such sonars are described in more detail in Section 2.7. It has to be mentioned here that the objective of the simulator for use on sonars for ASW has been primarily research driven. Currently, the primary operational sensors for ASW are the passive towed array and the hull mounted sonar. The so-called towed Low Frequency Active Sonars (LFAS) are expected to perform better for the to-day's mission statement. The difference between an LFAS and a mine hunting sonar is rather substantial. The towed array sonar is operated at a frequency of about 1 kHz where mine hunting sonar frequency ranges from 20 kHz up to 1 MHz. The towed array sonar needs these low frequency sonars due to the longer ranges of interest. Moreover, the towed array sonar is usually omni-directional. The important differences that affect the simulations are given in Table 2.1.

Table 2.1 *Comparison of (simulation) parameters for typical ASW and mine hunting sonars.*

LFAS	Mine hunting sonar
Frequency of about 1 kHz.	Frequency of 20 kHz up to 1 MHz.
System size is on the order of a meter for source and on the order of 100 m for receiving array.	System size is on the order of a decimeter for source and on the order of a meter for receiving array.
Flexible array of receivers towed in a hose.	Rigid array of receivers welded together.
Noise consists of sea noise generated by wind, shipping noise and self (flow) noise.	Noise is dominated by thermal and electronic noise.
Target ranges of interest are on the order of tens of kilometers.	Target ranges of interest are on the order of hundreds of meters.
Ping repetition time is on the order of tens of seconds.	Ping repetition time is only a fraction of a second.
Transmit signals are on the order of seconds, which induces a sensitivity to Doppler effects.	Transmit signals are on the order of milliseconds.
The target velocity may be several meters per second.	The target does not move and may be buried.

After browsing Table 2.1 the conclusion, which will prove to be wrong, may be that there is not a lot of overlap between the two applications and that two simulators would be more appropriate than one. The core computation of the simulator is based on the same principle, i.e. the use of a delayed and attenuated version of the transmit signal Eq. (2.2). For ASW a small step has to be added for the Doppler effect, which becomes significant. Another important overlap is the fact that both sonars usually consist of a source and a line array of receivers. The noise correlation in the so-called hydrophone triplets has been implemented as a special module, which replaces the conventionally modeled noise. This triplet technology is part of the towed array that was extensively used for measurement at TNO and was explained in Chapter 1. The special waveforms are added as modules which may replace the conventional waveforms. However, for the application of the sound travel-times it was necessary to implement interpolation schemes for non-analytic waveforms. A complicated factor in the ASW modeling is the existence of the Doppler effect. Both the active and the passive signals are subject to Doppler shifts. Both the sonar and the target move significantly within the duration of the signal. The corresponding Doppler compression (or the antonym extension if applicable) is calculated analytically for every instant in time, i.e. accounted for in every time sample. This compression causes a certain signal distortion, which is applied in the simulator for both active and passive targets. The Doppler effects will be discussed in detail in Chapter 4.

2.3. Structure of the simulator

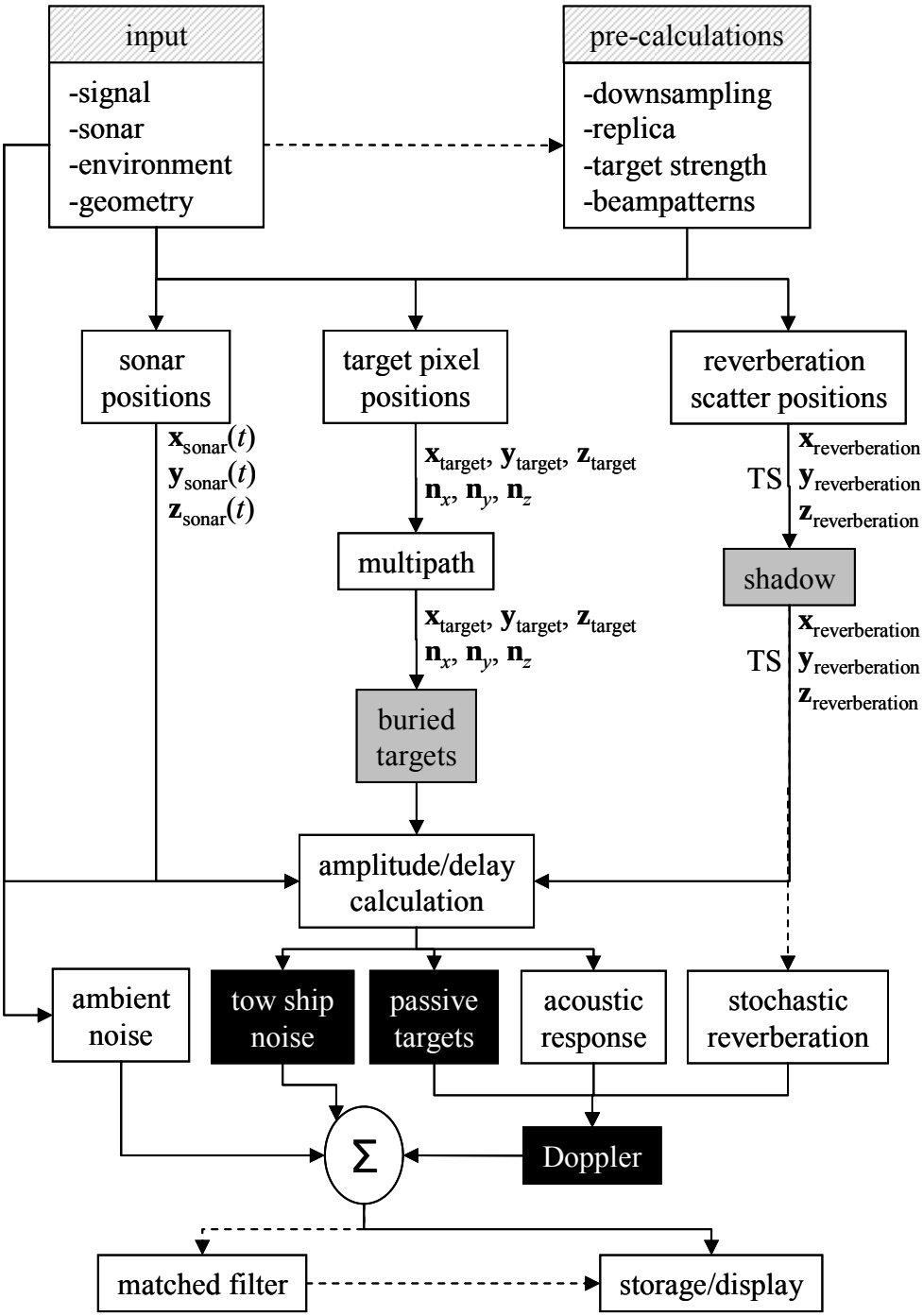


Figure 2-4 *Flow diagram of the sonar simulator SIMONA. The dashed lines are optional. The black modules are used for ASW sonar and the gray modules only for mine hunting sonar. The symbols* **x**, **y**, **z** *refer to position vectors and* **n** *refers to corresponding normal vectors.*

The underlying models of the simulator are discussed separately and in detail in Section 2.4. The rather complex structure of the simulator is explained with a flow diagram in Figure 2-4.

This overview diagram does not give the complete flow, because this would clutter the diagram. However, it does give an overview how the different modules are linked and how the simulated sonar data are generated. First, in the module *input*, the (signal, sonar and environment) parameters are defined, and then the geometry is calculated. In the module pre-calculations some necessary initial calculations are performed that are used in the following core loop. The core loop runs over the point sources, targets and receivers and consists of position calculations, signal generation, application of *delay* and *amplitude* for each combination. Finally, the signals, reverberation and noise are added, to form the hydrophone data in the module $\sum$. In the diagram the black modules are exclusive for ASW applications and the gray modules are exclusive for the mine hunting sonar cases. The construction of the replica, the down-sampling and the matched filtering is performed according to the description of the methods in Section 2.1.4

2.4. Modular methodology with a collection of models

In this chapter the physical process of the signal traveling from the sonar to the target and back as well as the noise are separated into a set of modules. Each separate module adds an effect that can be identified in the sonar images, and is, therefore, important.

2.4.1. Acoustic response of arbitrary targets

The acoustic targets may be point-like or extended. The target can be considered point-like when the signal arrives at the sonar as one peak. This is true when the bandwidth b of the transmit signal is small enough that the whole acoustic target response arrives in one resolution cell, which was $1/b$ in the time direction after replica correlation as explained in Section 2.1.4. Conversion to the range dimension results in a range resolution of $c/(2b)$ for two-way propagation. The point target signal is calculated in the time domain with a travel time τ:

$$\tau = \frac{1}{c}\left(\left|\mathbf{x_s} - \mathbf{x_t}\right| + \left|\mathbf{x_t} - \mathbf{x_r}\right|\right). \tag{2.7}$$

The source position $\mathbf{x_s} = (x_s,y_s,z_s)$, the target position $\mathbf{x_t} = (x_t,y_t,z_t)$ and receiver position $\mathbf{x_r} = (x_r,y_r,z_r)$ are used for the distance between sonar and target. If the sonar moves during the ping the delay time can be adjusted accordingly. The amplitude of the signal is calculated with the terms of the sonar equation: Source Level (SL), two-way Propagation Loss (PL(τ)), Directivity Index (DI) and Target Strength (TS). When the signal can be written as an analytic function of time t, the signal is simply placed at the correct time sample $t_i = \lceil \tau f_s \rceil / f_s$ with corresponding phase shift $2\pi(\tau - t_i) f_{t=0}$ corresponding to start signal frequency $f_{t=0}$. The operation $\lceil . \rceil$ is the ceiling function. The placement of the signal calculation can be realized in the time domain or in the frequency domain. In the frequency domain it becomes a convolution, i.e. multiplication with the transmit signal. It was however found that for a small number of targets,

the time domain often is faster when the transmit signal is known analytically. This is achieved by direct addition to the time series of the analytical formula. Furthermore, the signal has to be given the correct signal strength that is calculated with the sonar equation given by Eq. (2.5). An example of the output of such a point target is shown in Figure 2-5a and Figure 2-7 (the solid line).

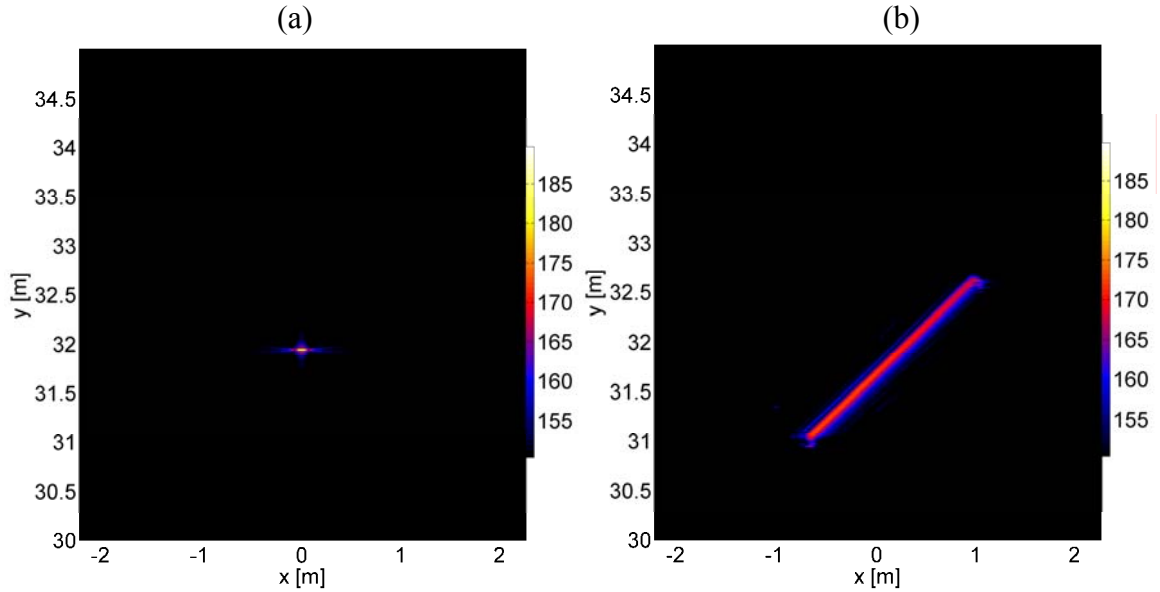


Figure 2-5 *An example of the output of SIMONA after matched filtering and SAS imaging, in which a point-like target simulation is compared with a cylindrical target simulation. Panel (a) shows a SAS image of the point and panel (b) shows a SAS image of the cylinder. In both images x is the along-track coordinate and y the across-track coordinate. The color scale is relative and in decibels.*

Amplitude from the terms of the sonar equation

The Source Level was defined as the energy per square meter per second at one meter from the source position. As explained in Section 2.1.4, the sonar equation is usually given in decibels, i.e. it is a logarithmic expression. The Propagation Loss (PL) is calculated with the formula $20\log_{10}(|\mathbf{x_s}-\mathbf{x_t}|)+ 20\log_{10}(|\mathbf{x_r}-\mathbf{x_t}|)+\mathrm{AL}$, where the Attenuation Loss (AL) is calculated with the law of Thorp (1967) or the more accurate formula of Francois-Garrison derived in the articles by Francois (1982(1) & 1982(2)). The formula of Francois-Garrison is based on a larger set of input variables, and therefore, when part of this set is unknown, Thorp's law may be more reliable. Both in the case of reception and transmission, the beamwidth of the elements depends on the size and shape of the elements. This determines the Directivity Index (DI), which in the simulator gives different values for different target directions. The simulator SIMONA was adapted to be able to take this directivity into account. It depends on the waveform (centre frequency f_c and bandwidth b) and width and height of the elements. From these properties, the theoretical beampattern in both horizontal and vertical direction is calculated and applied. The Target Strength can be defined for a point target, but it can also be calculated for a representative spherical object size that has radius r_s. The formula $20\log_{10}(r_s/2)$ from Urick (1975) is then applicable for acoustically hard objects assuming the geometric scattering regime for rigid objects, which requires the object to be large compared to the acoustic wavelength.

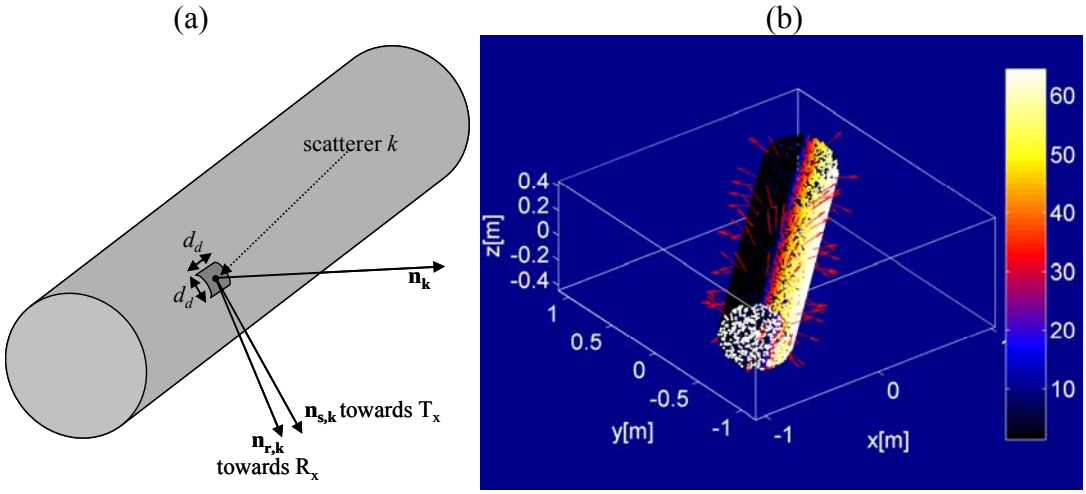


Figure 2-6 *Geometric model of a cylinder with the corresponding scatter behavior for a signal from the y-direction. (a) Scheme for application of the Kirchhoff method applied to one scatterer k (b) Visualization of the model as used in the computer calculations. The color coding is a relative decibel scale and based on the scatter strength for the Kirchhoff method. A selected part of normal vectors is displayed with the red arrows.*

When the target cannot be assumed point-like, the 3D shape can be defined as input, e.g. as in Figure 2-6. The calculation method for the response of such a 3D shape is based on a frequency domain approach in which the Fourier transform of the acoustic pressure is denoted with P. It uses simplifications via the Kirchhoff approximation and the Neumann boundary condition on the outer surface of the 3D shape. T As for instance described by Clay (1977) and Karasalo (2005), the general expression for the acoustic pressure at the receiver $\mathbf{x_r}$ outside of the object surface is derived with Green's theorem:

$$P(\mathbf{x_r};f) = \iint_{\mathbf{x}\in S} \left[G_s(\mathbf{x_r};\mathbf{x};f)\nabla P(\mathbf{x};f) - P(\mathbf{x_r};f)\nabla G_s(\mathbf{x_r};\mathbf{x};f) \right] \cdot \mathbf{n}(\mathbf{x})\,\mathrm{d}S\,. \tag{2.8}$$

This frequency domain expression of the scattered field results in an integral over the surface S with outward normal vectors $\mathbf{n}(\mathbf{x})$, where $P(\mathbf{x};f)$ represents the pressure at the surface points. Following Neubauer (1958), the Green's function in the frequency domain G_s in a homogeneous medium as a function of the wavenumber $k = 2\pi f/c$ is given by:

$$G_s(\mathbf{x_r};\mathbf{x};f) = \frac{e^{ik|\mathbf{x}-\mathbf{x_r}|}}{4\pi|\mathbf{x}-\mathbf{x_r}|}\,. \tag{2.9}$$

Kirchhoff's approximation for the scattered field is obtained by assuming the reflection coefficient R to be known as a function of surface position. The conditions for the validity of the approximation lie in the sufficient smoothness of the object surface and are discussed by Pouliquen (1999). Clay (1977) explains that for this approximation the particle velocity and the pressure of the incident wavefield P_i and scattered wavefield P_s are related. The boundary condition on the object surface S becomes:

$$\begin{aligned} P(\mathbf{x};f) &= \left(1+R_r(\mathbf{x};f)\right)P_i(\mathbf{x};f) \\ \frac{\partial P(\mathbf{x};f)}{\partial n} &= 1-R_r(\mathbf{x};f) \end{aligned} \quad . \tag{2.10}$$

Assuming an acoustically rigid target, i.e. high and constant acoustic impedance target, the scattering of the object can be simplified further with $R_r = 1$, which results in the Neumann boundary condition:

$$\begin{aligned} P(\mathbf{x};f) &= 2P_i(\mathbf{x};f) \\ \frac{\partial P(\mathbf{x};f)}{\partial n} &= 0 \end{aligned} \quad . \tag{2.11}$$

Combining this with the expression of the Green's function of Eq. (2.9) yields:

$$P(\mathbf{x_r};f) = \iint_{\mathbf{x}\in S} -\frac{\mathrm{i}}{\lambda|\mathbf{x}-\mathbf{x_r}|} e^{ik|\mathbf{x}-\mathbf{x_r}|} P_i(\mathbf{x};f) \frac{(\mathbf{x}-\mathbf{x_r})}{|\mathbf{x}-\mathbf{x_r}|} \cdot \mathbf{n}(\mathbf{x})\,\mathrm{d}S \,. \tag{2.12}$$

Due to the derivative of the Green's function, the wavelength $\lambda = c/f$ appears in the denominator of the integrant. Using the Green's function $G_s(\mathbf{x},\mathbf{x_s};f)$ that propagates the wavefield from the source to the incident wavefield leads to the final expression:

$$P(\mathbf{x_r};f) = \iint_{\mathbf{x}\in S} -\frac{\mathrm{i}}{\lambda|\mathbf{x}-\mathbf{x_r}||\mathbf{x_s}-\mathbf{x}|} e^{ik|\mathbf{x}-\mathbf{x_r}|} e^{ik|\mathbf{x_s}-\mathbf{x}|} P(\mathbf{x_s};f) \frac{(\mathbf{x}-\mathbf{x_r})}{|\mathbf{x}-\mathbf{x_r}|} \cdot \mathbf{n}(\mathbf{x})\,\mathrm{d}S \,. \tag{2.13}$$

In a discretized form, this becomes a summation, which results in a (large) number of scatterers that act as secondary targets. For these secondary targets, in accordance with the other targets, the propagation loss is separated from the target model in the simulator. Therefore, for each secondary target k the value of the target strength has to be calculated. The formula in the frequency domain is given by:

$$P(f) = \frac{d_d^2}{\lambda} \sum_k \left(\mathbf{n_k} \cdot \mathbf{n_{r,k}}\right) S(f)\, e^{2\pi \mathrm{i} f \tau_k} \,. \tag{2.14}$$

In this formula, $P(f)$ is the Fourier transform of $p(t) = p(x_r,y_r,z_r;t)$, which is the reflected signal. The Fourier transform of the transmit signal $s(t)$ is denoted with $S(f)$, d_d is the spatial discretization step, which is conveniently chosen constant for all scatterers in Eq. (2.14). The application of the formula for one scatterer is shown in Figure 2-6a. The travel time τ_k is calculated with Eq. (2.7) and inserting the position $\mathbf{x_t} = \mathbf{x_k}$ for each scatterer. The inner product $\mathbf{v_k}\cdot\mathbf{n_{r,k}}$ represents the cosine of the angle between the surface normal unit vector $\mathbf{v_k}$ and the normal unit vector in the direction of the reflected wave $\mathbf{n_{r,k}}$ on scatterer k. It should be noted that this cosine term is only inserted for the ray from scatterer to receiver and not to source. It looks as if the reciprocity criterion is not met here. However, the summation itself naturally accounts for the effect of the ray from source to target point k. Therefore, if desirable, it is

even possible to replace $\mathbf{n}_{r,k}$ by $\mathbf{n}_{s,k}$ in the formula. Gaunaurd (1985) analytically proves this reciprocity for a number of objects. The amplitude of each scatterer depends on the frequency $f = c/\lambda$. Fortunately, since the calculation of all contributions for the summation is performed in the frequency domain, this frequency dependence can be automatically accounted for.

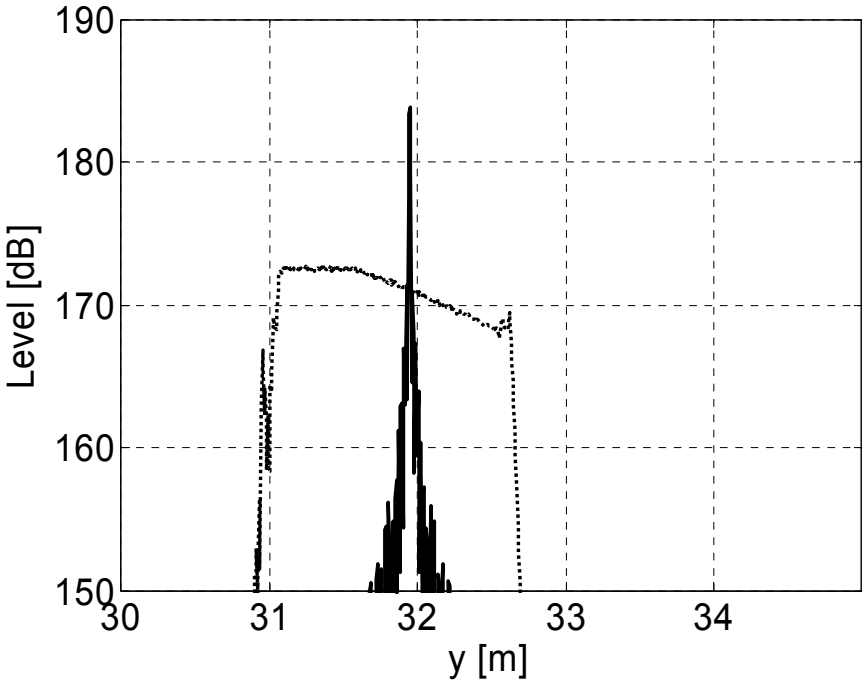


Figure 2-7 *The echo structure (vs. across-track distance y) after matched filtering for the point (-) and the cylinder (···). The level in decibel is after signal processing and a relative measure that is not directly linked to absolute acoustic pressure.*

The acoustic response of a cylinder in a high resolution SAS image is compared with a point-like target in Figure 2-5. The point target in Figure 2-5a becomes visible as a high sharp peak. Careful inspection of the sidelobes provides information on the behavior of the sonar itself, because every scatterer will appear in the image as such impulse response. It can be regarded as the acoustic signature of the sonar, which is analogous to the point spread function in optics. Figure 2-5 shows the response of the cylinder with a SAS image. The extended scattering and even the size of the cylinder can be easily obtained and an idea of the surface roughness of the cylinder can be recognized. Figure 2-7 shows the response of both the point-like target and the cylindrical target versus range (taken equal to y in this case) at the target position, which is the A-scan explained in Section 2.1.4. The point target shows the expected sinc-like function, which is expected from the matched filter output of a wideband signal. The extended cylinder, although still a basic shape, shows an extended response and even a varying output level as a function of y. This can be explained by the interference of the two insonified sides, which form the cylinder (the flat front and the long bended side). In this case, it is easy to define features such that detection can be made, but also a distinction between a point-like and a cylindrical target.

To increase computational efficiency to calculate $P(f)$ from $S(f)$ three extra steps are taken.

1. The scatterers that are not visible are in the shadow zone and can be disregarded in the calculation. This first step takes care of this removal of part of the scatterers. Depending on the target shape, determining the target shadow zone (viz. the back of the object) can be complicated. However, standard computation packages are available for these tasks, for instance in the field of computer games, rendering in image processing and 3D architecture. For now, in this chapter, the assumption is made that the object is convex. The inner products in Eq. (2.14) then determine whether the scatterer is visible or not. This occurs when $\mathbf{n_k}^T\mathbf{n_{r,k}} < 0$, for the source and the receiver. Thus, based on this information, scatterers are removed, which speeds up the computation.
2. The scatterers that correspond to equal travel times are merged before any signal generation, which means all scatterers with smaller travel time differences than $\lambda/(10c)$. A densely sampled time vector is filled with the samples, in which the scatter strength of all coinciding scatterers is summed instantaneously. The temporal separation requirement is set to $\lambda_{max}/(10c)$ in order to solve the wave equation accurately. Here, λ_{max} is the maximum wavelength present in the signal. In this way, scatterer groups with equal travel time are created that can be merged directly and reduce the number of scatterers.
3. The term $e^{2\pi i f\tau}$ in Eq. (2.14) is computationally expensive. However, when the signal properties are known, a reduction can be achieved. For this reduction the centre frequency f_c and the bandwidth b are needed. The formula in Eq. (2.14) is calculated for every discretized frequency bin from f_c-b/2 to f_c+b/2. The term $e^{2\pi i f\tau}$ is not calculated for each frequency anymore, but only for the lowest frequency f_c-b/2 and for frequency step Δf, which is equal to the reciprocal of the time window of the Fourier transform. The terms for frequency bin n+1 follow from multiplication of the prior phase shift term with $e^{2\pi i f_n \tau} e^{2\pi i \Delta f \tau}$. The extra step is the calculation of the two exponential terms (only once), and the gain is that in the loop over the frequencies no exponential has to be calculated anymore.

These three steps optimize the computation for mine hunting sonars. However, notice that such optimization is case dependent and could be different for other cases, e.g. when the frequency or target characteristics are not comparable. For example, when the signal is extremely wide band, it becomes interesting to compute the impulse response of the target scattering, because all the frequency bins need to be computed. This means that the summation of Eq. (2.14) becomes a discrete Fourier transform, which is implemented as an FFT.

The 3D shape of the cylinder is modeled by a collection of scatterers with a regular grid spacing of $\lambda_{max}/10$. The order of magnitude of the number of discretization points for a mine-like object is around one million. The shape is perfectly smooth in this case. In practice, it was found that at the short wavelength scale of a few millimeters, an object cannot be assumed to be perfectly smooth. This is particularly true when the object has spent a substantial time sitting on the sea floor. Formally, the Kirchhoff approximation does not hold for rough surfaces due to the multiple reflections that appear, but for now these multiple and internal reflections are absent in the model. It is not straightforward to quantify this roughness within the model. In this model it is tuned with one parameter and verified with measurements of targets as shown by Quesson (2005). It was found that once this choice is made, incorporation of roughness into the model is rather easy. The roughness is incorporated as follows:

$$\mathbf{x_k}^{\mathbf{rough}} = \begin{pmatrix} x_k + \mathbf{N}\left(0, \chi/\sqrt{3}\right) \\ y_k + \mathbf{N}\left(0, \chi/\sqrt{3}\right) \\ z_k + \mathbf{N}\left(0, \chi/\sqrt{3}\right) \end{pmatrix}, \tag{2.15}$$

where $\mathbf{x_k}^{\mathbf{rough}}$ is the position of the k^{th} scatterer of the object with roughness and $\mathbf{N}\left(0, \chi/\sqrt{3}\right)$ is a normally distributed stochastic variable. This formula simply changes the position of all scatterers k by adding a normally distributed shift with zero mean and standard deviation $\chi/\sqrt{3}$. This roughness factor χ has been varied on different objects. The major changes in the acoustic response are an energy decrease in the contribution of corners, an energy decrease in specular reflections and an energy increase for the flat parts. The choice of a normal distribution on the positions is arbitrary, but tests with different approaches proved that this makes little difference. The tests included determining the effect of variations of the directions of the normal vectors, changes in the distributions and changing the scatter strength. It is interesting to note that increasing the roughness virtually has no effect for $\chi < \lambda_{max}/20$ and from this point onwards the effects reveal themselves quickly.

Modeling of a target response has been verified with measured data. The match was good, but there is room for improvement. The model is fully based on the fact that the target is an acoustically hard object. A material dependent reflection coefficient could be easily inserted, by adjusting the scatter strength of each target scatterer k. A more difficult improvement lies in the penetration of acoustic waves into the object. This would induce internal scattering. Another feature that is difficult to incorporate appears at typically low frequencies is the return of waves that are the result of interaction with the target, e.g. Lamb-type waves that travel around the target and travel back to the sonar later than the directly scattered signal. Such waves can be exploited for classification purposes, which is a whole field of research that is still ongoing and pursued by for instance Tesei (2002), Dragonette (1997) and Kirsteins (2004). For example, such waves arise when a fluid filled sphere is insonified and manifest as shell-borne wave that travel around the sphere. This feature shows high potential for classification, but is not modeled here. Nevertheless, finite element models are available in various research institutes, and can be used as a local model replacement or as a tool to model Lamb-type waves or scattering inside the target object.

Buried targets

Buried targets are treated similarly as targets in the water with slightly adapted travel times and amplitudes. Assuming a two layer system, the bottom penetration points of the ray from source/receiver to target are computed with Snell's law. The travel time is calculated using the sound speed in water c and the sound speed in the sediment c_s. Two-way Propagation Loss in decibels is subdivided into three parts, i.e. Absorption Loss AL, Spherical Spreading Loss SSL, again subdivided in the forward SSL_1 and the return path SSL_2, and Interface Loss IL:

$$
\begin{aligned}
\mathrm{PL} &= \mathrm{AL} + \mathrm{SSL}_1 + \mathrm{SSL}_2 + \mathrm{IL} \\
\mathrm{AL} &= \alpha_w c\left(\tau_1 + \tau_4\right) + \alpha_s c_s\left(\tau_2 + \tau_3\right) \\
\mathrm{SSL}_1 &= 10\log_{10}\left[\left(c\tau_1 \sin\theta_1 + c_s\tau_2 \sin\theta_2\right)\left(c\tau_1 \frac{\cos\theta_2}{\cos\theta_1} + c_s\tau_2 \frac{\tan\theta_2}{\tan\theta_1}\right)\Big/ \sin\theta_1\right] \\
\mathrm{SSL}_2 &= 10\log_{10}\left[\left(c\tau_4 \sin\theta_4 + c_s\tau_3 \sin\theta_3\right)\left(c\tau_4 \frac{\cos\theta_3}{\cos\theta_4} + c_s\tau_3 \frac{\tan\theta_3}{\tan\theta_4}\right)\Big/ \sin\theta_4\right] \\
\mathrm{IL} &= 10\log_{10}\left\{\left[1 - \frac{\left(\rho_s c_s \cos\theta_1 - \rho c \cos\theta_2\right)^2}{\left(\rho_s c_s \cos\theta_1 + \rho c \cos\theta_2\right)^2}\right]\left[1 - \frac{\left(\rho c \cos\theta_3 - \rho_s c_s \cos\theta_4\right)^2}{\left(\rho c \cos\theta_3 + \rho_s c_s \cos\theta_4\right)^2}\right]\right\} \\
&= 10\log_{10}\left[\frac{16\rho_s^2 c_s^2 \rho^2 c^2 \cos\theta_1 \cos\theta_2 \cos\theta_3 \cos\theta_4}{\left(\rho_s c_s \cos\theta_1 + \rho c \cos\theta_2\right)^2 \left(\rho c \cos\theta_3 + \rho_s c_s \cos\theta_4\right)^2}\right]
\end{aligned}
\tag{2.16}
$$

The attenuation coefficients in water (α_w) and in the sediment (α_s) depend on frequency and are given in dB/m. The formula for Spherical Spreading Loss when refraction is at hand is derived by Horton (1959). Interface Loss is calculated by double use of the widely-known formula for the reflection coefficient explained by Lurton (2004). The formula is directly derived from $\left(1 - R_i\left(\theta_1, \theta_2\right)\right)^2 \left(1 - R_i\left(\theta_3, \theta_4\right)\right)^2$, where R_i is the angle dependent reflection coefficient at the water-sediment interface. Interface Loss IL is calculated as a combination of the path to target and back to sonar. For these two formulae, for energy conservation, measuring one-way propagation loss in the sediment brings in an extra term c_s/c, because the decibel is related to pressure. When the source and receiver are in the same medium, the terms cancel. The symbols are explained in Figure 2-8. The interface incidence angles θ_1, θ_2, θ_3 and θ_4 are given by:

$$
\begin{aligned}
\cos\theta_1 &= z_s \Big/ \sqrt{\left(x_p - x_s\right)^2 + \left(y_p - y_s\right)^2 + z_s^{\,2}} \\
\cos\theta_2 &= z_t \Big/ \sqrt{\left(x_p - x_t\right)^2 + \left(y_p - y_t\right)^2 + z_t^{\,2}} \\
\cos\theta_3 &= z_r \Big/ \sqrt{\left(x_q - x_t\right)^2 + \left(y_q - y_t\right)^2 + z_t^{\,2}} \\
\cos\theta_4 &= z_t \Big/ \sqrt{\left(x_q - x_r\right)^2 + \left(y_q - y_r\right)^2 + z_r^{\,2}}
\end{aligned}
\quad . \tag{2.17}
$$

Finally, if normal incidence is considered, the reflectivity of the target is given by:

$$
20\log_{10}\left(\frac{\rho_t c_t - \rho_s c_s}{\rho_t c_t + \rho_s c_s}\right), \tag{2.18}
$$

where $\rho_t c_t$ and $\rho_s c_s$ are the specific impedance of target and sediment, respectively. If the contrast is low, common for buried targets, the target strength TS is reduced by this term. For the angles θ and the signal travel times τ, the location of the penetration point $\mathbf{x_p}$ is determined

(and $\mathbf{x_q}$ for return). This is realized with Snell's law given of Eq. (2.3) and trigonometry to the water-sediment interface. It results in four equations from which x_p, y_p, x_q and y_q are solved.

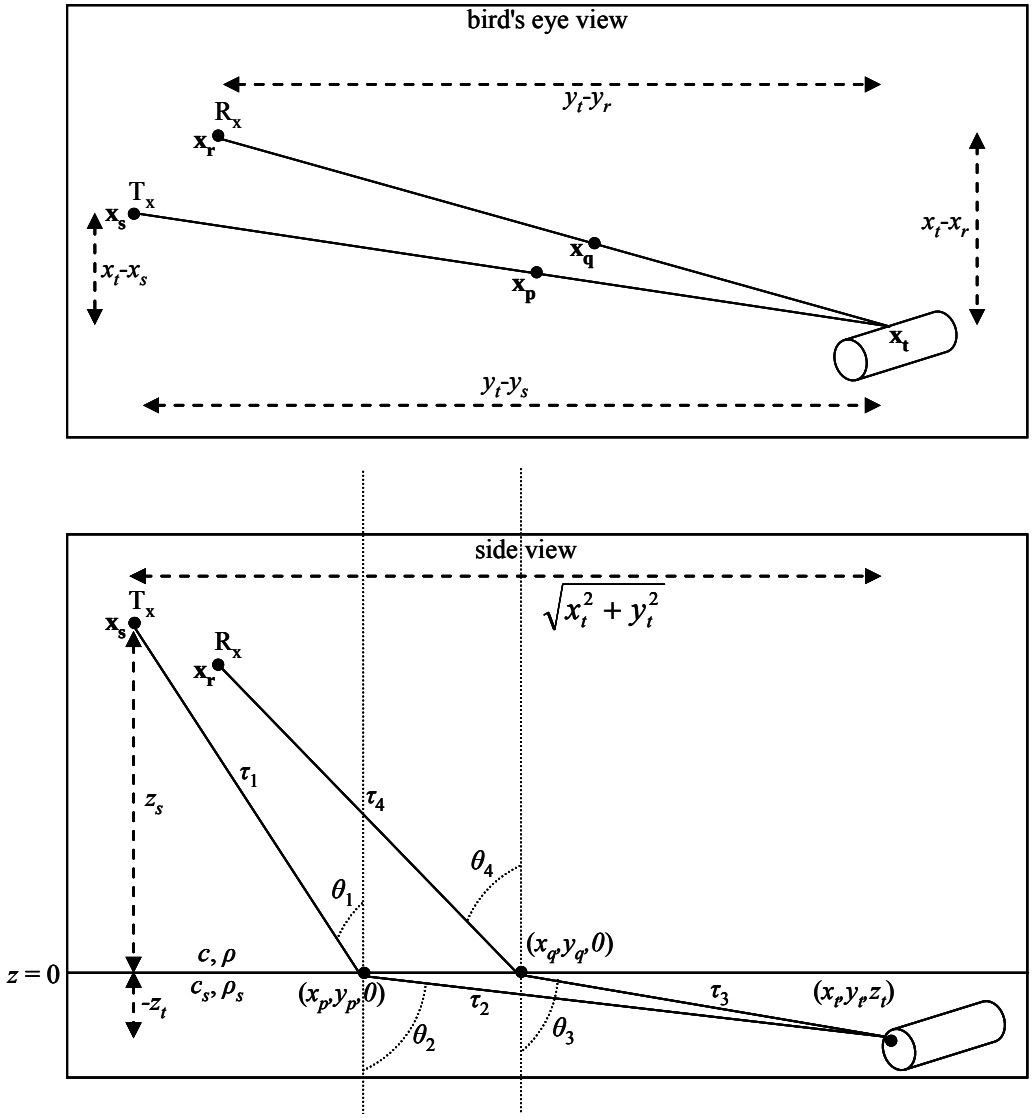


Figure 2-8 *Model for buried objects based on one sediment layer with sound speed c_s and density ρ_s. The travel times τ_1, τ_2, τ_3 and τ_4 are calculated directly from the geometry.*

$$\begin{aligned} c_s\sqrt{\frac{\left(x_p-x_s\right)^2+\left(y_p-y_s\right)^2}{z_s^{\,2}+\left(x_p-x_s\right)^2+\left(y_p-y_s\right)^2}} &= c\sqrt{\frac{\left(x_p-x_t\right)^2+\left(y_p-y_t\right)^2}{z_t^{\,2}+\left(x_p-x_t\right)^2+\left(y_p-y_t\right)^2}} \\ \left(y_p-y_s\right)\left(x_t-x_s\right) &= \left(y_t-y_s\right)\left(x_p-x_s\right) \\ c_s\sqrt{\frac{\left(x_q-x_r\right)^2+\left(y_q-y_r\right)^2}{z_s^{\,2}+\left(x_q-x_r\right)^2+\left(y_q-y_r\right)^2}} &= c\sqrt{\frac{\left(x_q-x_t\right)^2+\left(y_q-y_t\right)^2}{z_t^{\,2}+\left(x_q-x_t\right)^2+\left(y_q-y_t\right)^2}} \\ \left(y_q-y_r\right)\left(x_t-x_r\right) &= \left(y_t-y_r\right)\left(x_q-x_r\right) \end{aligned} \quad . \tag{2.19}$$

This system can be solved for x_p, y_p, x_q and y_q.

The signal travel times τ_1, τ_2, τ_3, and τ_4 are calculated from trigonometry applied to Figure 2-8:

$$\begin{aligned} c\tau_1 &= \left|\mathbf{x_p} - \mathbf{x_s}\right| \\ c_s\tau_2 &= \left|\mathbf{x_p} - \mathbf{x_t}\right| \\ c_s\tau_3 &= \left|\mathbf{x_q} - \mathbf{x_t}\right| \\ c\tau_4 &= \left|\mathbf{x_q} - \mathbf{x_r}\right| \end{aligned} . \tag{2.20}$$

2.4.2. Reverberation

As already shown in Figure 2-4, the reverberation in SIMONA is modeled in two ways, a deterministic way and a stochastic way.

The deterministic model
The deterministic model is based on a large number of point scatterers that are randomly distributed on the seafloor as visualized in Figure 2-9. This random position distribution is generated and then fixed for the entire simulation, i.e. all simulated sonar data are based on one and the same reverberation grid. The target strength of these scatterers is calculated from Lambert's law, but can be changed for more sophisticated models, e.g. as discussed by Urick (1975) and Abraham (2004). Lambert (1760) was the first to derive this law for optical applications and states that the scattering is proportional to the projection of the sea floor as seen from the receiver and proportional to the projection of the sea floor as seen from the source. In decibels Lambert's law can be written as follows:

$$I_s = I_i + \mu + 10\log_{10}\left(\sin\theta_{sm}\sin\theta_{rm}\right), \tag{2.21}$$

where I_i and I_s are the incident and scattered intensity in decibels, respectively. The scattered intensity is defined for unit scatter area and for unit range from the scatter area. The Lambert's parameter μ is also given in decibels and represents the bottom dependent scatter strength. In practice, this parameter ranges from about -40 dB for unconsolidated bottoms to about -10 dB for gravelly bottoms. The angles θ_{sm} and θ_{rm} the grazing angles corresponding to the source and receiver respectively.

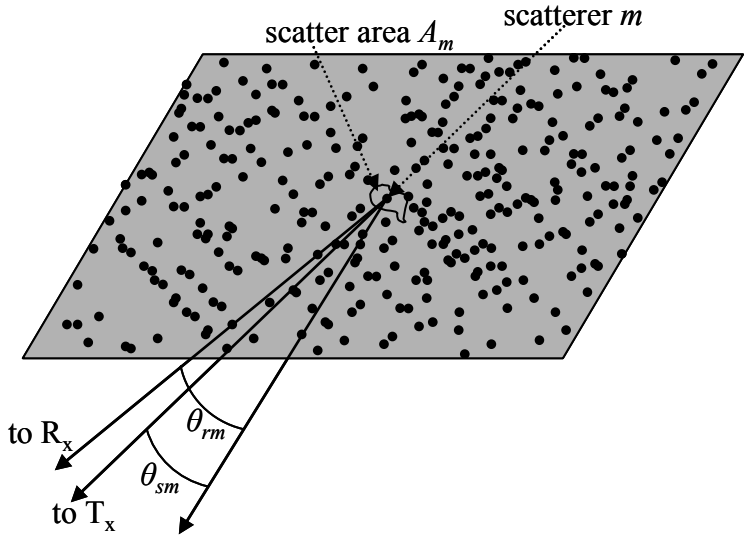


Figure 2-9 *Model for deterministic reverberation. A random grid is generated with point scatterers having consequential travel times and amplitudes based on Lambert's law.*

Because it is a coherent model, scatterers that are too close will interfere and an amplitude correction for the scatterer density is needed. These scatterers are treated as actual point targets, but with the possibility of variations in their position and amplitude. Every scatterer causes a signal arrival at the hydrophones and consequently, those arrivals are superimposed with the correct time delay. The superposition is performed with a fast computation of the impulse response, which is followed by a temporal convolution, which is applied in the frequency domain, because for the typically large number of scatterers this is computationally less expensive. The formula for the contribution of reverberation on the hydrophone data becomes a summation over all scatterers on the sea floor:

$$
\begin{aligned}
p(t) &= \sum_m \frac{\sqrt{2A_m \sin\theta_{sm} \sin\theta_{rm}}}{2} 10^{\frac{\mathrm{S+DI}(m)+\mathrm{PL}(m)+\mu}{20}} s(t-\tau_m) \\
\theta_{sm} &= \frac{z_s - z_m}{\sqrt{(x_s - x_m)^2 + (y_s - y_m)^2}} \\
\theta_{rm} &= \frac{z_r - z_m}{\sqrt{(x_r - x_m)^2 + (y_r - y_m)^2}}
\end{aligned}
\quad , \tag{2.22}
$$

where A_m is the representative scattering area defined by the ratio of the total sea floor reverberation area and the number of point scatterers. The factor is ½√2 due to the fact that the square root of the energy is proportional to the root mean square pressure. Lambert's law is included as in Eq. (2.21), which holds for scattered intensity per square meter. The directivity index DI depends on the scatterer m, which is zero when the scatterer is in the middle of the sonar beam as explained in Section 2.1.1. A typical acoustic result is shown in Figure 2-10 with the black curve.

Intermezzo: statistical distributions in sonar

Before further describing the stochastic reverberation model, this intermezzo is needed, which explains the application of statistical theory in sonar. The sonar equation, given in Eq. (2.5) is used to calculate the received signal level S. It is clear that the calculated value is an average, due to statistical behavior of each of the terms of Eq. (2.5) in real life. Parallel to this statistical signal behavior, the background is also subject to statistical behavior. The background is responsible for the generation of false alarms and may be dominated by noise or reverberation. This implies that statistical behavior is especially important for sonar performance prediction. To a lesser extent, it is also significant for development of signal processing methods.

The central limit theorem is often invoked to describe the statistical processes for the received sonar data. The noise for the received sonar data is commonly assumed to be an addition of a sufficiently large number of independent stochastic processes. The theorem then states that the probability density function is Gaussian or normal:

$$f_p(\upsilon) = \frac{1}{\sigma_\upsilon \sqrt{2\pi}} e^{-\frac{1}{2}\left(\frac{\upsilon}{\sigma_\upsilon}\right)^2} . \tag{2.23}$$

This means that then each noise data sample is normally distributed with a variance σ_υ^2 equal to the noise level. The hydrostatic pressure level is already subtracted from the data. Another distribution that is relevant for sonar statistics is the Rayleigh distribution. When the noise is said to be Rayleigh distributed, it means in principle the same, but one refers to a different stage in the signal processing. Sonar data are acoustic pressures, which fluctuates around a certain hydrostatic pressure. The sonar data are processed and at some point in the signal processing chain, referred to as the detector, a threshold is applied to the data. All samples above the threshold are detected and all samples below the threshold are ignored. The data samples are often represented by complex numbers by adding an imaginary part υ_2 that equals the Hilbert transform of the data υ_1. This representation of data samples ($\upsilon_1 + \mathrm{i}\upsilon_2$) called the analytic signal allows a simple conversion to amplitude and phase (in the form $A\mathrm{e}^{\mathrm{i}\omega}$). The amplitude (or envelope A) is usually considered in the sonar signal processing chain for detection. The distribution of this envelope or amplitude is calculated with the two independent normally distributed variables υ_1 and υ_2. The envelope is then obtained by $A^2 = \upsilon_1^2 + \upsilon_2^2$, which generates the probability density function for the envelope:

$$f_p(A) = \frac{A}{\sigma_\upsilon^2} e^{-\frac{1}{2}\left(\frac{A}{\sigma_\upsilon}\right)^2} . \tag{2.24}$$

The reverberation is also often assumed to be generated by a large number of independent scatterers, which also calls for the central limit theorem. However, reverberation level is usually modeled as being non-stationary, i.e. the standard deviation σ_υ varies with time.

The signal statistics, e.g. fluctuating targets, are not taken into account in SIMONA. Formally, the statistics are generated by each of the terms of the sonar equations. The statistics of the term propagation loss and target strength depend on the variability of many input parame-

ters. Knowledge about the statistics in the input parameters can be used by multiple simulations, which is beyond the scope of this thesis.

The stochastic model

The stochastic reverberation model in SIMONA consists of a calculation of the reverberation level RL versus time *t*. This time varying RL is first calculated by the sonar equation given of Eq. (2.5) and using Lambert's law given of Eq. (2.21) for TS. It is subsequently assigned with an appropriate statistical distribution. The model is based on an iso-velocity profile and a combination of multi-path signal arrivals similar to the model used by Abraham (2004), in which additionally the hybrid paths are modeled as described by Ellis (1994). These hybrid paths are the paths for which the way to the target is not the same as the way from the target, e.g. a direct path to the target and back to the sonar via a bottom reflection. Every time sample is now modeled as a stochastic process with variance $10^{\frac{\mathrm{RL}(t_i)}{10}}$. At this point, the choice for the distribution is still open. It may be a normal distribution, but it has been verified that a distribution derived from the *K*-distribution as discussed by Abraham (2002) better corresponds to measurements. The second moment, the variance of the stochastic process, is then equal to the energy RL(*t*) as found from the sonar equation, which is plotted with the red curve in Figure 2-10. For a zero-mean normal-distributed variable *N* with variance $10^{\frac{\mathrm{RL}(t)}{10}}$ this would result in:

$$p(t) = s(t) * N\left[0, 10^{\frac{\mathrm{RL}(t)}{20}}\right], \tag{2.25}$$

where the signal *s*(*t*) is convolved with the normally distributed noise, which is shown in Figure 2-10 by the blue curve. Thus, the black curve is the contribution of the deterministic reverberation and the blue curve is the contribution of the stochastic reverberation. Notice that the longer the signal *s*(*t*) is, the more energy is received by the hydrophones. The computation of RL(*t*) is based on the transmitted energy per second, i.e. it is the energy that returns to the sonar when unit energy is transmitted.

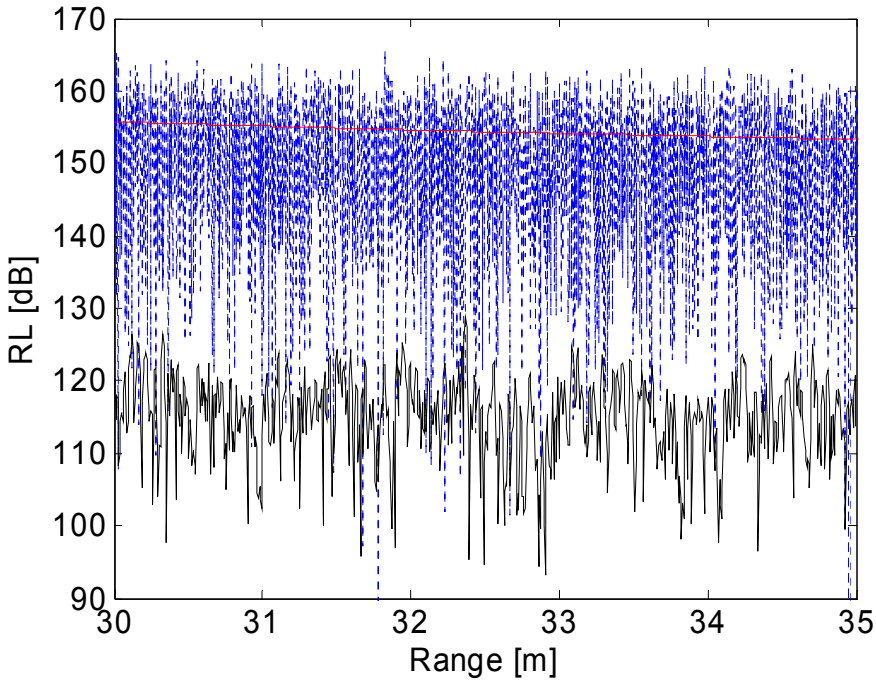


Figure 2-10 *An example of reverberation response. The dashed blue line is the stochastic model output based on the sonar equation (added with the red line). The solid line represents the deterministic part of the reverberation simulated by point scatterers with constant scatter amplitude based on Lambert's law. It is lower due to the limited reverberation patch on the sea floor.*

It is logical to use a combination of the two models, because in any SAS, sidescan or other sonar image it is easy to identify those deterministic (e.g. sand ripples, small rocks and the acoustic shadow) and stochastic (temporal variations) features of the sea floor. The combination of the two forms the total reverberation. It also determines the ping-to-ping correlation coefficients, which are important in synthetic aperture processing as will be shown in Chapter 5 and Chapter 6.

The two models may be used separately. Use of the deterministic model will result in a perfect coherence between different received signals. For instance, when a source transmits two times and source and receiver do not move, the received reverberation is identical. In practice, this is not the case, because the reverberation coherence is known to be time dependent. The most practical way to combine the output of the two models is performed with a weighted sum of the deterministic and the stochastic reverberation in order to insert the time dependent coherence. This means that the reverberation model has a tuning parameter, which determines how much the reverberation is stochastic or made from coherent scatterers on the sea floor. The parameter setting should be based on measurements, e.g. of the ping-to-ping correlation coefficients.

2.4.3. Target shadow

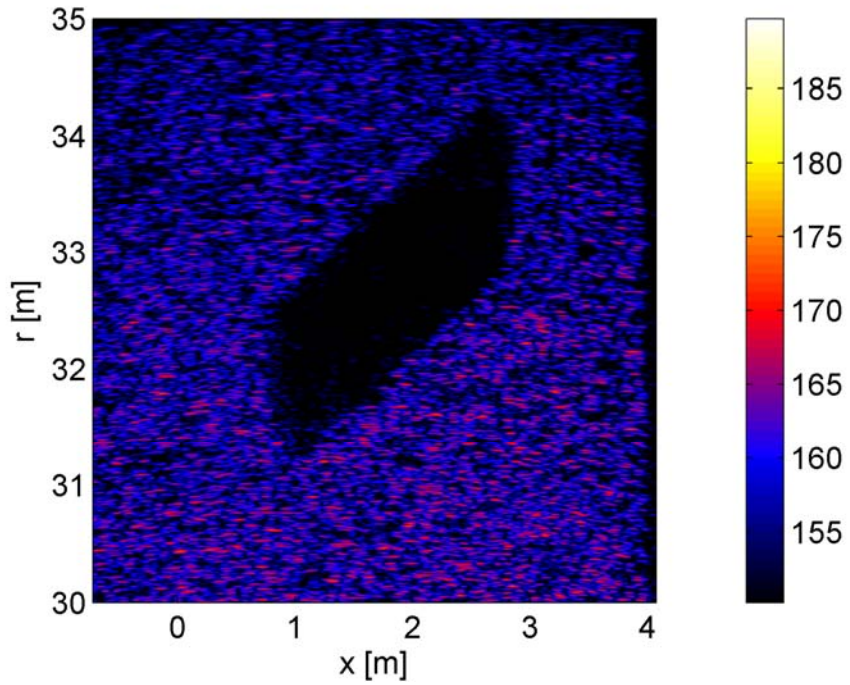


Figure 2-11 *An example of the reverberation with the acoustic shadow in the corresponding SAS image. The color scale is in decibels.*

When the target is large compared to the resolution, which is always limited by the acoustic wavelength, an acoustic shadow occurs in the reverberation field. Such a shadow is determined by the geometry and the target shape as visible in Figure 2-11. It should be noted that the color scale is not optimal for visualization of the details in this image, but is kept the same for the simulated images in this chapter to allow comparison. In a mine hunting sonar image, the shadow of the mine plays a major role for classification. The model for this is merely geometrical and acts on the reverberation pixels. For the acoustic paths from source/receiver to each target scatterer a projection on the sea floor is determined according to:

$$\mathbf{x}_{\text{shadow}} = \frac{1}{z_t - z_s}\begin{pmatrix} x_s z_t - x_t z_s \\ y_s z_t - y_t z_s \\ 0 \end{pmatrix}. \tag{2.26}$$

With this formula a three component vector $\mathbf{x}_{\text{shadow}}$ is found for the projected point on the sea floor. The z-value is always zero, and the x and y values are determined by the point target vectors $\mathbf{x_t}$ and the sonar position $\mathbf{x_s}$. A detailed analysis of the shadow and sonar processing in order to improve the shadow contrast in the sonar image will follow in Chapter 6. Subsequently, an envelope curve around these projected points is calculated. When a reverberation scatterer falls within this envelope, it is removed. This process is computationally expensive again, but can be relieved by a reduction in target scatterers depending on the sonar resolution. The shadow resolution does not need to be better than $c/(2b)$, from which a reduction in

number of target scatterers follows. The shadow is calculated for every source-receiver pair. This implies that the model includes the movement of the shadow along a (synthetic) array, which was described and utilized by Sabel (2005). The shadow in Figure 2-11 is also made with such a moving shadow and, therefore, there is a slight (almost negligible) blurring.

2.4.4. Multi-path

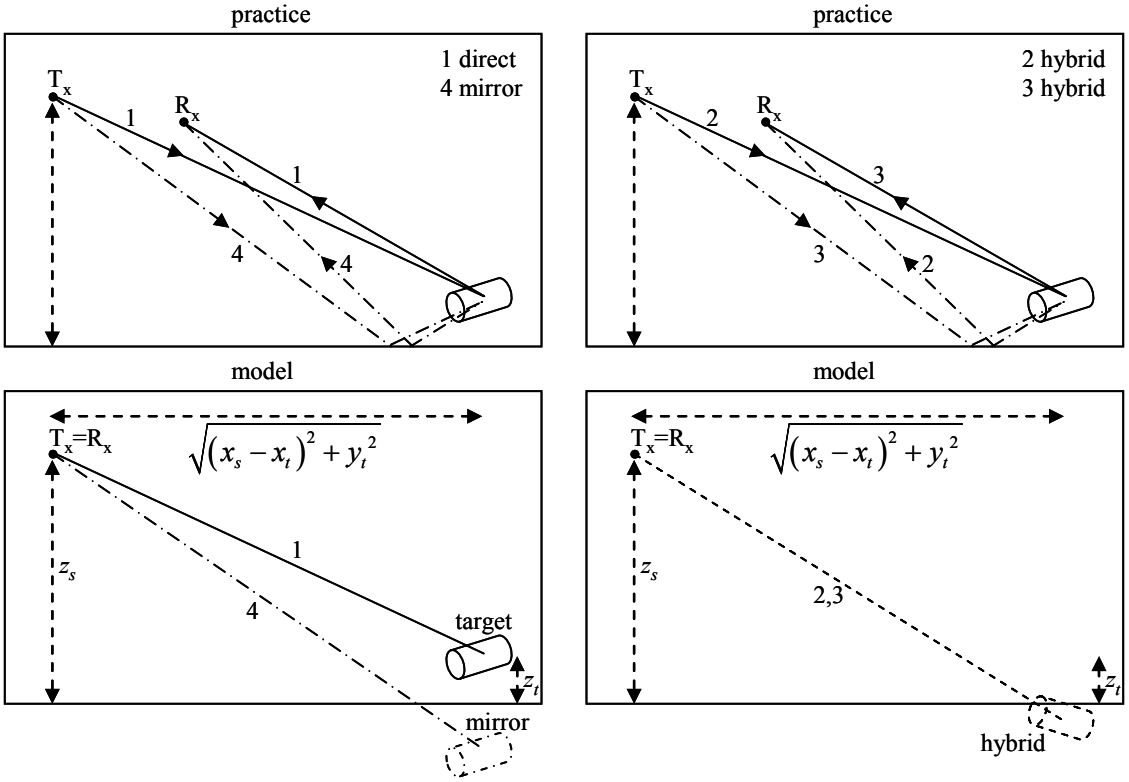


Figure 2-12 *The underlying multi-path model of SIMONA. The source T_x and the receiver R_x are assumed to coincide.*

Multi-path is the arrival of a signal at the hydrophones after the first arrival. It may occur due to reflection of the signal at the sea surface or at the sea floor, but can also be caused by bending of the acoustic rays via sound speed differences. Multi-path is a complex problem in sonar, since its effect on the sonar image depends on many parameters, which typically do not leave room for simplifications. The water surface and sea floor often act as an acoustic mirror, which causes the sonar to end up in an acoustic mirror hall as shown in Figure 2-12. Each signal may arrive many times with varying amplitude and possible varying Doppler. The paragraph on reverberation already included multi-path for the stochastic approach. As Abraham (2004) suggested, the statistical behavior of the reverberation depends on the combination of arriving multi-paths with a theoretical convergence towards a Rayleigh distribution.

In the introduction of this chapter, the simulator was explained to be based on source-target-receiver combinations. These three items have a position in 3D space and may move in time. For implementation reasons, the multipath arrivals are more easily modeled as if they arrive

from imaginary targets at a certain position known a priori. The positions of these imaginary targets have to be calculated from the geometry and a mirror assumption. The multi-path of the target is taken into account by introducing mirror targets. In the mirror model each target point is copied several times. A user-defined accuracy in decibels determines how many copies are needed. The position of each copy is determined with the formulas:

$$\begin{cases} z_{\text{mirror}} = 2h - z_t \\ z_{\text{hybrid}} = z_s + \sqrt{\left[c\left(\tau_{\text{mirror}} + \tau\right)/2\right]^2 - \left(x_s - x_t\right)^2 - \left(y_s - y_t\right)^2} \end{cases}, \text{ for surface reflection}$$
$$\begin{cases} z_{\text{mirror}} = -z_t \\ z_{\text{hybrid}} = z_s - \sqrt{\left[c\left(\tau_{\text{mirror}} + \tau\right)/2\right]^2 - \left(x_s - x_t\right)^2 - \left(y_s - y_t\right)^2} \end{cases}, \text{ for bottom reflection} \quad . \quad (2.27)$$

The travel time of the direct path is already available and is denoted as τ. The easy multi-path travel times are from the rays that are the same for the way to the target as for the way back to the sonar. These travel times τ_{mirror} can be calculated from Eq. (2.7) with the imaginary target position $\mathbf{x_t} = (x_t, y_t, z_{\text{mirror}})$, which is illustrated in Figure 2-12. The process starts with the bottom reflection of the target, then a surface reflection using the water depth h and then a bottom reflection and so on. For each reflection a mirror target is constructed and as visible in Eq. (2.27) also a hybrid target (in between normal and mirror target). This is the imaginary target that has a z-coordinate z_{hybrid}, which generates the travel time that is equal to the ray travel time towards the target and back to the receiver. For instance, the first hybrid target has a travel time equal to one direct path and a path via the bottom back to the sonar. The target strength of each mirror target is the same, except that the hybrid targets count double, because two ray combinations correspond to them. For instance, the path from sonar to target and back to the sonar via the bottom has the same travel time as the path from sonar via the bottom to the target and back to the sonar. Higher order multi-paths are attenuated by the propagation loss, because the corresponding travel distance increases with order. Additionally, the angle of departure and arrival at the sonar will differ from the direct path, which means that the value for the angle dependent Directivity Index may vary. In the simulator a threshold can be set, which stops the creation of mirror targets when their contribution falls below a certain level.

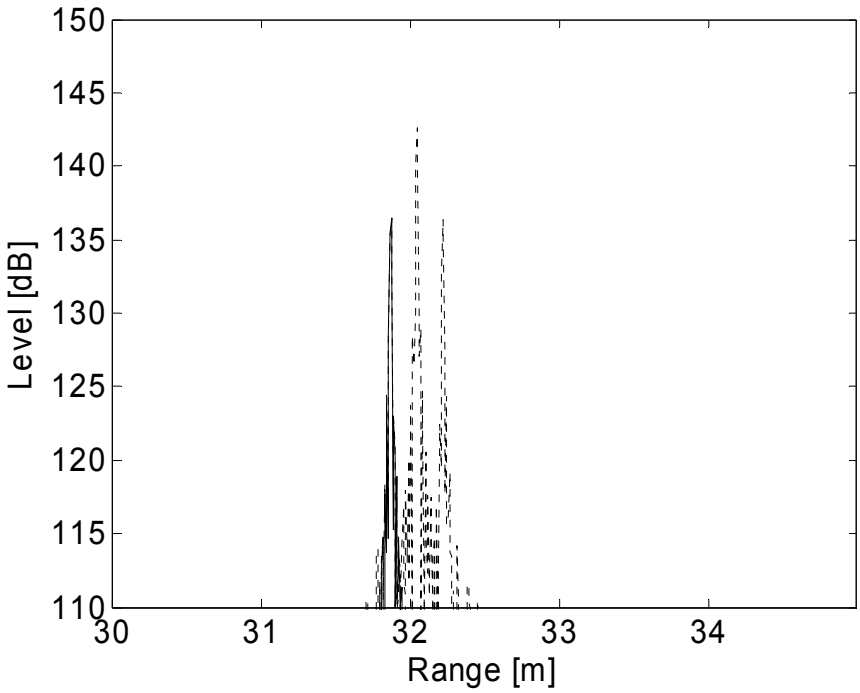


Figure 2-13 *Response of a point-like target with multi-path as a dashed line and without multi-path as a solid line. The sonar has a tilt angle of 22 degrees and the target is positioned an across-track distance (y) of 30 m.*

In Figure 2-13 the response of a point target is shown together with the response from a point target plus multi-path reflections. The sonar tilt angle is 22 degrees and the point target is positioned at an across-track distance y of 30 m, which results in a target range of about 32 m. The first arrival is the same and the second arrival is 6 dB higher, which is expected due to the double hybrid path contributions. The third arrival is the last visible multi-path, because the higher order paths are quickly attenuated by the vertical beampattern of the sonar and by propagation loss.

For an extended target the method is the same but the scatterers that form the target have to be flipped vertically according to the order of the multi-path. Notice also that the multi-path model can be applied to the point scatter reverberation of Eq. (2.22) that generates the reverberating sea floor.

2.5. Complete simulation for mine hunting

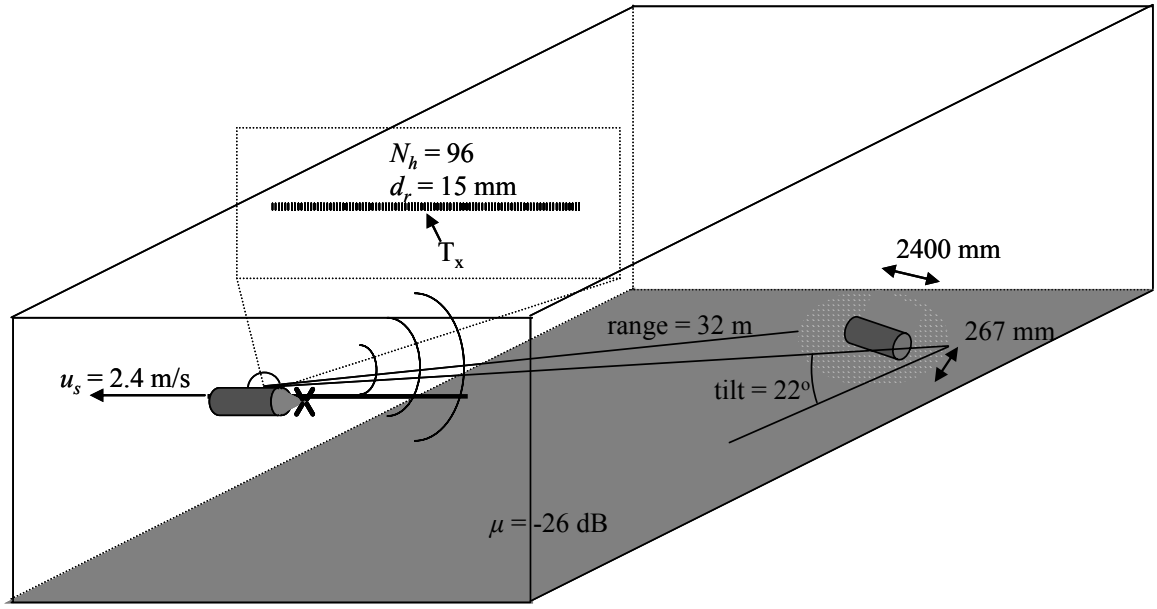


Figure 2-14 *Geometry of the complete simulation for mine hunting.*

All models discussed in the previous section are combined to form sonar data and images with a reasonable degree of realism. For computational reasons, the simulations are restricted to eight pings from the recently developed SENSOTEK sonar. This system is mounted on an AUV that is referred to as HUGIN. The AUV with sensor was built by Kongsberg Maritime AS and delivered in 2005. The ping repetition time T_p is 0.2 s, the transmit chirp signal runs from 60 to 110 kHz in 1 ms. The geometry of complete simulation example is depicted in Figure 2-14. The receiving array contains N_h = 96 hydrophones spaced at d_r = 15 mm and the source is in this case located in the middle of the receiving array. Between transmission and reception of the signal the platform has moved, which is accounted for in this simulation. The source level is set at 210 dB (re 1 μPa at 1 m). The sonar is sailing past the target with a velocity u_s of 2.4 m/s. The number of overlapping phase centers, specific hydrophone pairs that receive the same signal at different pings, is an important parameter in synthetic aperture sonar. The importance of overlapping phase centers was already briefly discussed in Chapter 1 and will be explained in detail in Chapter 5. It has an effect on the source/receiver separation and on the ping-to-ping correlation. The value for the number of overlapping phase centers can be calculated with N_h-$T_p u_s/(2d_r)$, which yields the number 32 for these simulations. The sonar tilt angle is 22 degrees, which puts the target in the middle of the vertical sonar beam. The beampattern is based on the frequency band of the signal and the size of the source and receivers. All beamwidths are 40 degrees at the centre frequency except the horizontal receiver beamwidth, which is 60 degrees. The proud cylindrical target of length 2400 mm and radius 267 mm rotated 45 degrees is positioned at an across-track distance of 30 m, which results in a target range of 32 m. The sea bottom consists of fine sand with a Lambert's parameter μ of -26 dB. The water depth is 15 m, which does not show in the simulations, because the attenuation of surface reflected multipath is high.

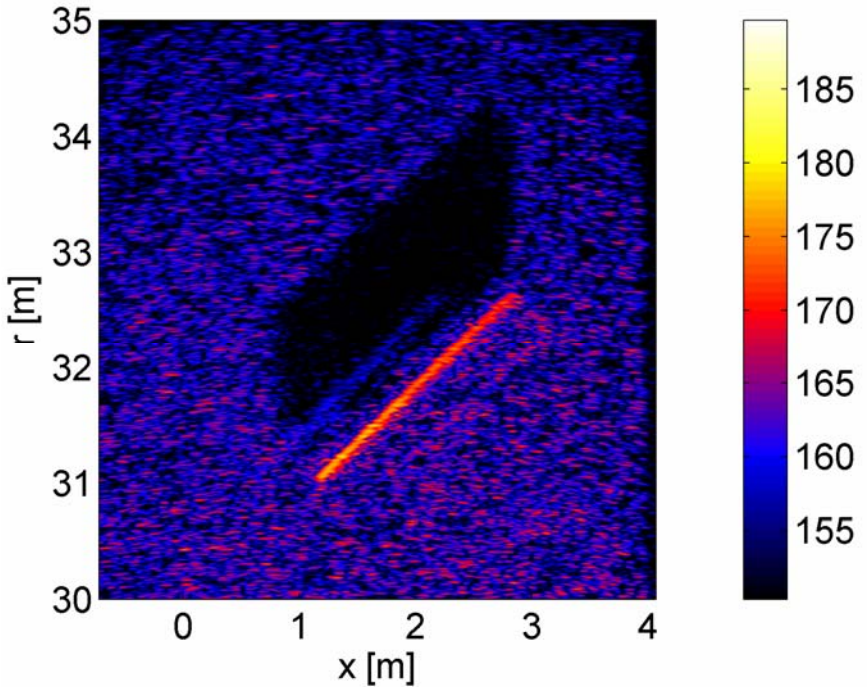


Figure 2-15 *Complete simulation of a proud cylindrical target on a fine-sand seabed without multi-path. The color scale is in decibels.*

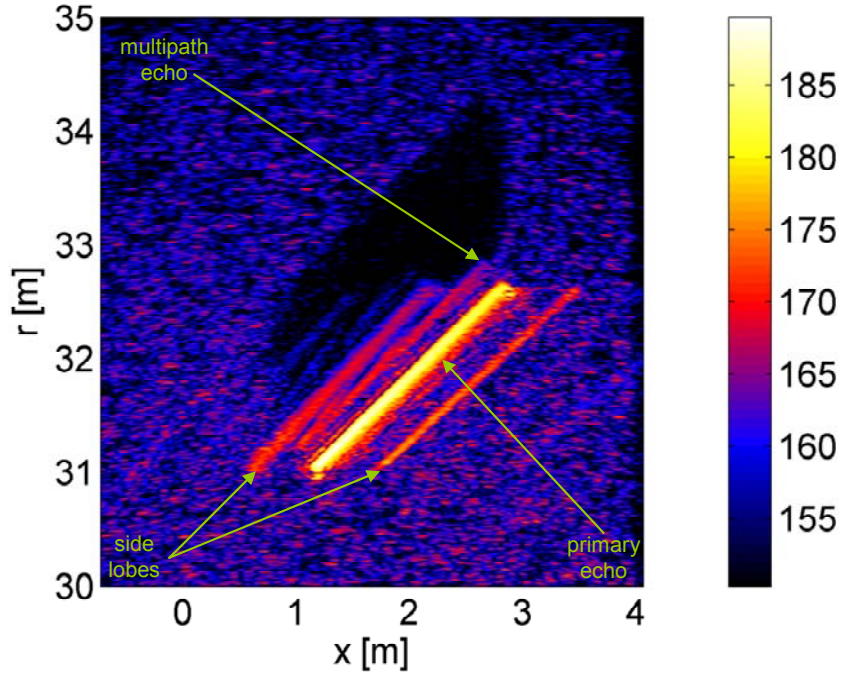


Figure 2-16 *Complete simulation of a proud cylindrical target on a fine-sand seabed with multi-path. The color scale is in decibels.*

The resulting SAS image of a complete simulation is shown in Figure 2-15 and Figure 2-16. Figure 2-15 shows the result without multi-path and therefore the target response is rather low. The level is low enough for exposure of the reverberation point scatterers just after the

target scatter, for instance at $(x,r) = (2,32)$ m. They arrive slightly later on the sonar because the strongest scatter from the cylinder comes from a part above the seafloor. A comparison of Figure 2-15 with Figure 2-16 leads to the conclusion that multi-path is an important feature in this case. The multi-path mainly consists of four acoustic paths, which are the same as in Figure 2-13. It also amplifies the signal from the cylinder accordingly, but the subsequent arrivals are not easily localized. Another striking feature is the appearance of the high sidelobes, which are especially visible in Figure 2-16. The signal-to-reverberation ratio is much higher and around 30 dB and the shadow is clearly visible. It can be concluded that the shadow is still sharp, but the sidelobes of the object have a somewhat distorting effect on the shadow. Since the spatial sampling satisfies the Nyquist criterion, the sidelobes are merely an effect of the imaging method used and disappear when applying an exact time-domain method. A verification of this is presented in the following section.

2.6. Measured synthetic aperture sonar data

The Norwegian Defense Research Establishment (FFI) has a long term research program in which the potential of SAS on AUVs is investigated. In this program the HUGIN vehicle is used with a real-time off the shelf SAS, the so-called EdgeTech described by Hayes (2004), on the one hand and a high performance SAS, the so-called SENSOTEK, on the other hand. The result of the previous section is now verified with a SAS image from the EdgeTech system, which was operated from this HUGIN vehicle. The measurement does not exactly match the simulation, but it is merely an example of the similarity between measured and simulated SAS images. Chapter 5 and Chapter 6 supply typical measurements of three other SAS systems.

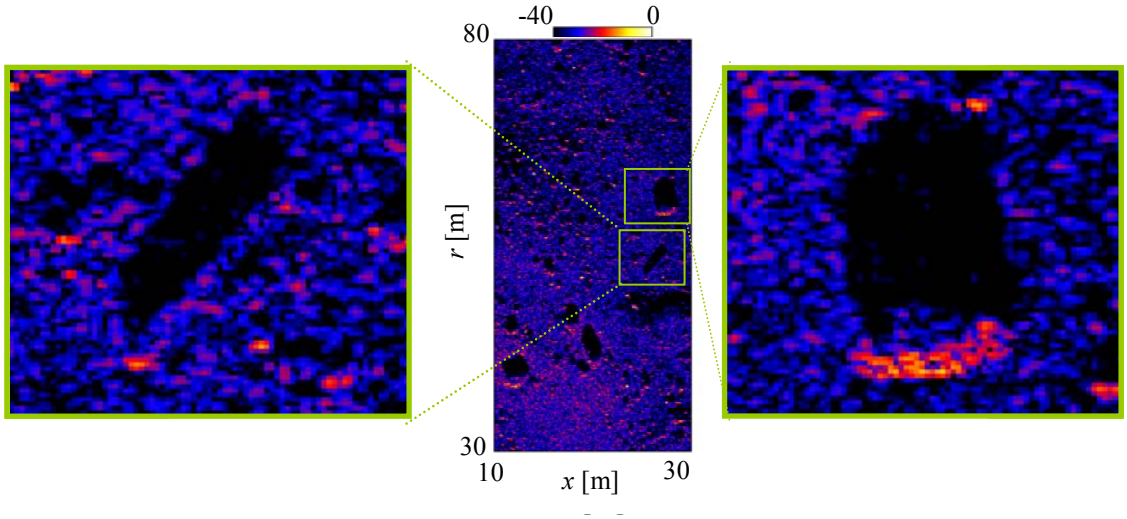


Figure 2-17 *Experimental SAS result for a case with many rocks scattered on the sea floor measured with the EdgeTech system and processed by FFI. Two patches are zoomed: the clear shadow of a cylinder of 4500×500mm on the left and a rock with high reflectivity on the right.*

This measured result, in a qualitative way, shows that the modeled approach is elegant and effective. A more quantitative analysis of simulated examples will follow in Chapter 5 and 6, but the different sub models that were discussed in the previous section are there. The left zoom of Figure 2-17 clearly shows the importance of the shadow in SAS images. This target is not visible itself due to the low target strength, but in the right zoom a rock with high reflectivity is shown. The reverberation is somewhat diffuse but besides this, clear reverberant highlights that are rather coherent appear (also from ping to ping). The multi-path model cannot be verified with this image, but a measured example will be seen in Chapter 6. Also the buried object model is not verified here, but measurements will be addressed in Chapter 5.

2.6.1. Use for signal processing development

Signal processing transforms the acoustic data matrix into a SAS image. The size of the input data equals the number of hydrophones, times the number of pings, times the number of samples, which in this case is $96 \times 8 \times 800 = 614400$. For digitalization with 16 bits per sample, this results in a data amount of just over a kilobyte. However, in practical situations this matrix is orders of magnitude larger, i.e. Gigabytes, because the number of pings, the integration length and the number of samples are typically much higher. Because the data rate is enormous, the signal processing has to be subdivided into three resolution levels. The first raw step is to generate a side scan image with moderate resolution. Parts in the image that require a higher resolution can be processed with the fast SAS imaging method called Stolt migration as discussed by Gough (1997). As illustrated in the previous section, for wide beam and long range cases, at some point the Stolt migration breaks down or requires computationally ex-

pensive pre-processing. At this point it is too early for a detailed treatise of this imaging method, but Chapter 6 is fully dedicated to the application of Stolt migration in SAS.

The model has been verified for one case in this chapter. Likewise, the model was evaluated for other cases, from other mine hunting systems to ASW. More evaluations and verifications lead to feedback into the model, which improve the model fidelity. It also enables the scientists and developers to go through the chain of signal processing modules and find the weak points and flaws. If one has access to such realistic model, one is able to generate sonar data time series with this model with flexibility for all input parameters. The time series of data serve as the input for the processing or imaging. The output of this is the sonar image. Contrary to the complete example that was used for verification of the model, it is often the straightforward and relatively uncomplicated simulations that provide insight. By simulating the point target response, it can be verified easily if the imaging performs adequately. The aforementioned SAS processing methods together with their assumptions can be applied to the sonar data in order to form a high resolution image. However, assumptions may give rise to errors in the image and it is necessary to know their influence beforehand. The most exact and most computationally expensive method, without any assumptions, can be applied to small patches around the targets. This computationally expensive method is a combination of time domain imaging and the enhanced shadow algorithm as described by Sabel (2005).

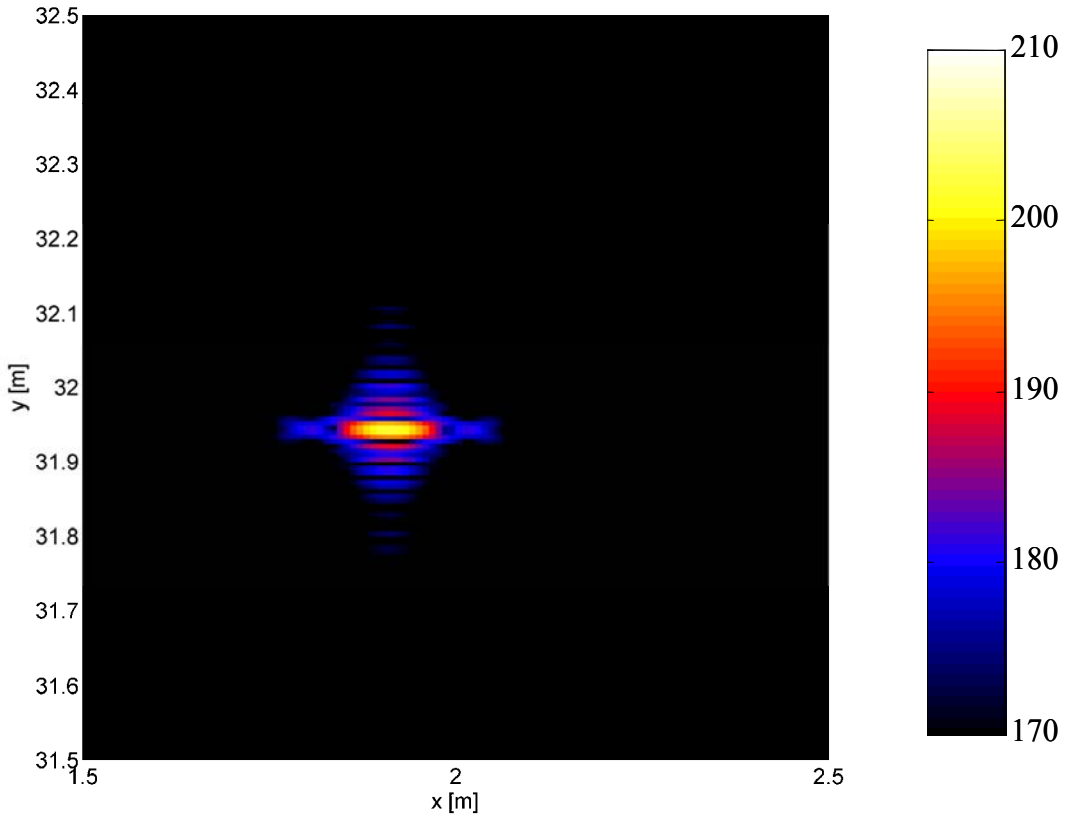


Figure 2-18 *Point target response with the same geometric settings as for the complete simulation. Source and receiver are coinciding, which is the ideal situation without motion.*

Figure 2-18 shows the response of a point target with the same geometric and acoustic settings as for the complete simulation of the previous section. The point target does not appear

in one pixel, because the aperture is finite and the bandwidth of signal used is limited as explained in Section 2.1.4. The signal level, resolution and side lobe behavior in this image can be compared with more realistic parameter settings. Chapter 5 and Chapter 6 will discuss the assumptions in the signal processing chain in detail. One of those assumptions is the replacement of source/receiver combinations by a midpoint. The performance deterioration due to the fact that source and receiver cannot be replaced by such a midpoint, or phase center, can be easily predicted in this way. It has to be noted that the apparent signal level of 210 dB does not mean that the total path loss equals zero. The signal processing chain includes for instance imaging, matched filtering, downsampling and bandpass filtering and does not have a normalization scheme in order to maintain a direct link with absolute acoustic pressure.

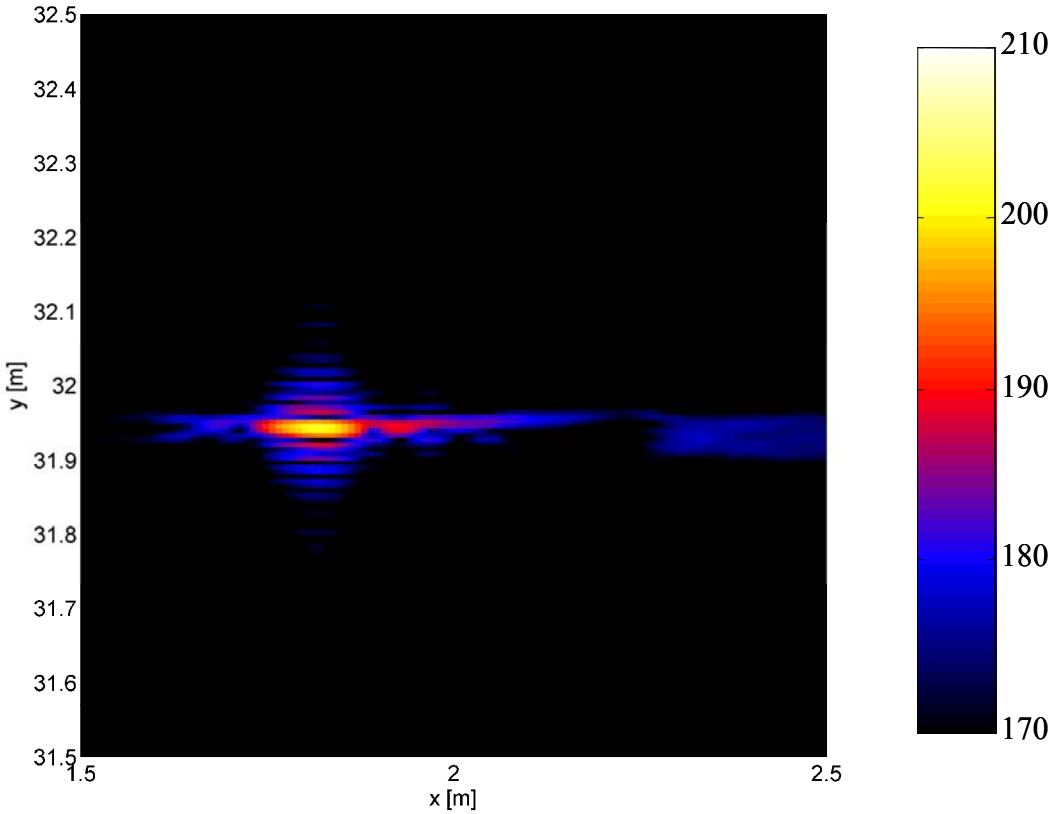


Figure 2-19 *Point target response with the same geometric settings as for the complete simulation. The sonar is moving and source and receiver are not at the same location, which limits the performance of Stolt migration.*

Figure 2-19 again shows the result for the case settings as in Section 2.5, but now with the processing method Stolt migration. There is a substantial difference with Figure 2-18, but it should be noted that it is a zoom. The application of Stolt migration to the simulated data requires the source and receiver to be closely together and a fixed position. This assumption is not straightforward and will be discussed in more detail in Chapter 5, which deals with the synthetic aperture signal processing chain. Besides high sidelobes, the target has also shifted somewhat along the *x*-axis, which is all caused by the motion of the receivers during the ping.

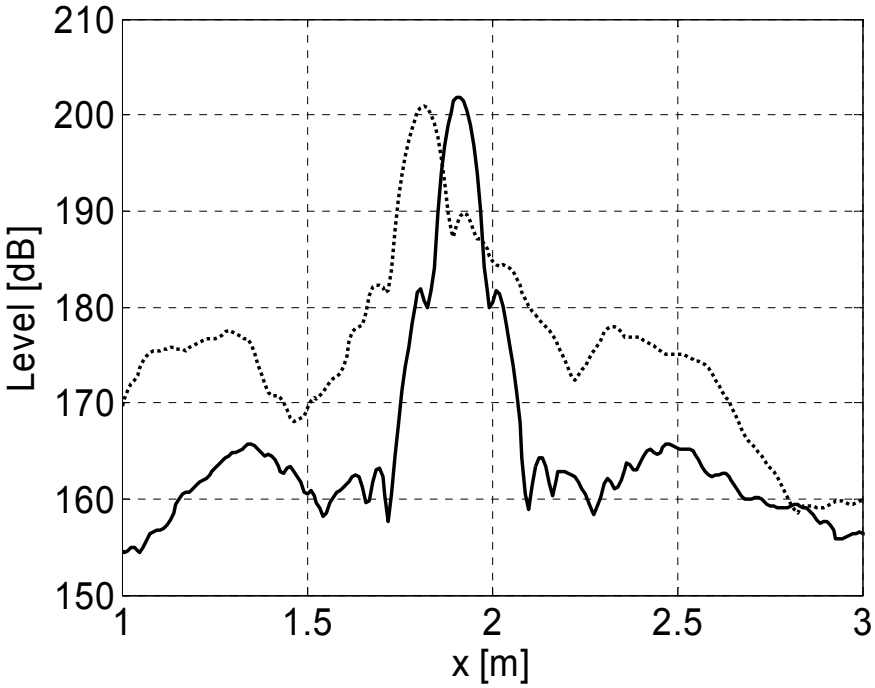


Figure 2-20 *The azimuthal pattern at the target range. The solid line is the ideal case with the source and receiver at the same position. The dotted line is the realistic case where the sonar is moving and a significant separation between source and receiver is induced.*

The difference in the comparison plot of Figure 2-20 is mainly caused by the motion of the sonar during the signal travel. The performance loss is about 1 dB in terms of signal level and the main side lobe increases with about 10 dB.

Near field effects

In general the term 'near field effects' is used when in a certain case one cannot assume the wave field to consist of plane waves. This may happen when a sonar is rather close to a target. Apart from simple attenuation, the response signal on the sonar is not the same at for instance two meters and three meters from the target (in the same direction). In other words, the target cannot be assumed to be a point target. When the sonar would move from 700 to 800 m, the response will be much more similar and at some point when the response does not change much anymore, the far field is reached. A similar effect appears for the sonar itself. When the sonar has a certain size, which is particularly the case for synthetic aperture sonar, there is a range where the wave field cannot be assumed to consist of plane waves. The signal processing has to account for this.

If the direction of arrival of a signal is determined with conventional beamforming on the receiving array, the geometric properties play an important role. The nature of the signal-arrivals depends on the positioning of the source and receivers, the signal frequencies and the target location. When the target is close or the sonar large, the situation becomes a so-called near field scenario. In such a situation one cannot assume the signal to arrive at the sonar as a plane wave, which has significant impact on the signal processing performance. The target

range (r) that separates this near field from the far field is called the Fresnel distance and is calculated with:

$$r = d_F^{\,2} / \lambda \,, \tag{2.28}$$

where d_F is the maximum separation between source and receiver. For the complete simulation, the Fresnel distance is approximately 28 m. When applying the Stolt migration algorithm to synthetic aperture sonar data, the input data are first converted to a data matrix equidistant in space and time (equidistant linear array of transceivers). The corresponding transceivers can be assumed to lie in the middle of the source and the receiver. Unfortunately, this assumption is not justified at close range. It was found that SAS processing with such an erroneous assumption introduces aliasing effects at certain positions in the image. A correction, which has its equivalent in seismics as the so-called normal move out correction, can be applied to the input data. The correction falls within the midpoint pre-processing (already used in Figure 2-20), but instead of taking the middle of the source/receiver combination as a midpoint, a position shifted to the back according to the wave-front curvature is employed. This assumption breaks down for ultra wide beam systems, because the wave-front curvature is not constant over the aperture. These and other pre-processing methods in combination with Stolt migration will be described further in Chapter 5, but the message here is that the simulator will be very helpful for development and testing of such methods.

2.6.2. Potential for classification

The complete simulation generates modeled images knowing all the properties of both geometry and sonar settings. This means that a tool is available to generate or complement a sonar image database that includes characteristics of the mine-like objects and the sonar specifications at the same time. Hence, this data base can be used for classification. The database can be made for all relevant objects, i.e. both man made and natural at varying conditions such as target range, water depth, aspect angle and grazing angle.

2.7. Specific features for the Anti-Submarine Warfare towed array sonars

The simulations for Anti-Submarine Warfare are less complicated and computationally less expensive. The computational bottlenecks in the simulator are the extended targets and scatterer based reverberation. The realistic example shown in this chapter needs a total calculation time of several hours on a Pentium 2 GHz system. A comparable simulation without reverberation and only a point target reduces the computation time to less than a minute, which is also a representative computation time for the ASW case. The target detail, even when scaling with respect to the frequency is taken into account, is much lower and shadows are generally not observed at all. The reason for this is that the submarine usually is not very close to the water boundaries and adding to this is the variable acoustic propagation due to inhomogenei-

ties and multi-path. Nonetheless, other features appear in the sonar image as is shown by Robert (2005). In the case of mine hunting, the noise is relatively low. In mine hunting cases, a reverberation-limited scenario can usually be achieved as was defined in Section 2.1.4. For ASW this is not always true, because the required transmitted energy would be too high to achieve a reverberation-limited case. Therefore, often, besides signal and reverberation, ambient noise can be observed in the sonar images of an ASW sonar. The noise modeling can be separated into directional noise from ships (passive targets) and omni-directional noise (sea noise and flow noise).

Passive targets are assumed to transmit a continuous signal, which would not be expected from their name. The term passive refers to the sonar case rather than the target and when the sonar is passive, it means it is only listening and not transmitting. The received signal of such a passive target is modeled with a signature $S_P(f)$ in the frequency domain. The phase shift and amplitude are calculated from the one way propagation. The discrete sound sources in SIMONA are referred to as passive targets as they involve one-way propagation. They are taken into account as (multiple) point sources that radiate a specific signal, at a given source level SL. This signal is defined by its normalized transmitted power level versus frequency, or target signature $S_P(f)$. Because the signal behavior is assumed constant within a simulated block of data, it was chosen to apply the travel times from the target to the receiver in the frequency domain: the received pressure versus frequency on the hydrophone $P_P(f)$ is then computed according to the formula:

$$P_P(f) = 10^{\frac{\mathrm{SL}-\mathrm{PL}}{20}} e^{2\pi i f r/c} S_P(f), \tag{2.29}$$

When passive contacts are ships, the target radiated pressure $S_P(f)$ consists in (colored) broad band noise combined with characteristic tonals. A typical example is the noise radiated by the tow ship of the sonar. In some other cases passive contacts such as marine mammals do not transmit a continuous signal, but a transient signal. The transients are then modeled by a time signal $s(t)$ defined by an analytic formula or with a specific wave file. $S_P(f)$is then the Fourier transform of $s(t)$ after zero-padding.

Noise is an important issue in Chapter 3. Ambient noise, or sea noise, is the result of biological, geological (earth movements, tides…) and environmental (rain, wind) noise, but also of industrial noise (shipping, oil-drilling platforms) as described by Urick (1975). The curves established by Knudsen based on sea measurements in deep water are used in SIMONA, but with a modification. ASW operations mostly take place in shallow waters where the Knudsen model based on deep water measurements needs to be adjusted. Actually, in shallow waters and at low frequencies, environmental noise is often quieter than in deep waters due to poorer propagation conditions. However, shipping and biological noise can increase the background noise level significantly depending on the location (in bays and harbors for example). Due to their nature and extreme variability, they are difficult to predict and have to be handled case by case. For environmental noise, however, a simple noise model can be used to derive the noise levels in shallow waters, from the deep water levels. Above 200 Hz, noise is mainly dependent on the sea state. The formulae for the noise amplitudes used in SIMONA are described by Robert (2005). The total noise is modeled by a combination of sea noise and flow

noise. Sea noise is assumed to be correlated for closely positioned hydrophones according to a spatial noise model that is described in detail in Chapter 3. Flow noise is assumed to be uncorrelated. In the simulator the sea noise is colored noise that depends on the sea state. Flow noise is also colored and depends on the tow speed. The flow noise level used in SIMONA is a function of the tow speed and the acoustic centre frequency and is derived from the experimental measurements presented by Beerens (1999). For frequencies higher than 10 kHz, additionally, Urick (1975) showed that thermal noise becomes important, and for frequencies higher than 100 kHz even dominant. This is accounted for in the simulations.

The *Doppler* effect is an important issue in Chapter 4. For ASW the received signal cannot always be assumed to be the same as the transmitted signal. Source, target, and receiver may move during the interaction with the signal. A model that accounts for the Doppler shift is added to the simulator. It is time consuming, because for every sample of the received data, the Doppler shift has to be calculated and applied to the acoustic data. The details of this are discussed in Chapter 4. Doppler effects become important when the sonar is moving with respect to the target. This relative velocity (v) induces a frequency shift Δf, which is given by the formula:

$$\Delta f = f \frac{c + v_{st}}{c - v_{st}} \frac{c - v_{tr}}{c + v_{tr}} - f = \alpha f - f \,, \tag{2.30}$$

where the shift depends on the speeds of the target relative to the source v_{st} and to the receiver v_{tr} in m/s. In the case of passive signals the quotient relative to v_{st} is irrelevant. If the shift Δf is much smaller than the reciprocal of the transmitted signal duration, the Doppler effect can be disregarded. This is the case in most mine hunting scenarios. However, for ASW and Torpedo defense, Doppler is significant and is often utilized in the processing. Proper Doppler modeling is therefore necessary. Notice that the Doppler shift can be time dependent. For example, during ASW platform maneuvers, the received signal may exhibit a time varying Doppler shift. The Doppler compression factor α is then computed for each sample and the signal is compressed accordingly.

Contrary to mine hunting, where normally standard waveforms like chirps and sinusoids are common, for ASW there is interest in *special waveforms* like tuned Doppler sensitive signals and reverberation suppressing waveforms as described by Doisy (2000) and van IJsselmuide (2003). The reason for this difference in resource signature is the significance of the Doppler effect. This effect can be used to determine the speed of the target instantaneously and can also be used to separate Doppler shifted echoes from the reverberation background. The difficult part in modeling the special waveforms is the Doppler sensitivity in combination with the fact that sometimes no analytic expression exists for the waveform. This requires a discretization of the waveform with high oversampling in order to generate the data correctly. The details can also be found in the article of Robert (2005).

2.8. Summary and conclusion

This chapter describes the sonar simulator SIMONA and the relevant theory on sonar that is used in the simulator and in the signal processing techniques to be investigated in the remainder of the thesis. The model has reached a stage of fidelity, which allows use for sonar performance prediction, signal processing development and generation of a high resolution sonar image database. It is clear that the underlying models for the acoustic shadow, reverberation statistics and multi-path are essential. The model is verified with a test case, which showed the influence of the different modules. This verification is concluded with a complete simulation for the SENSOTEK system employing all the modules. No measured sonar data of the SENSOTEK system was available, and therefore, data of a cylindrical object insonified by the EdgeTech system was used for verification. The side lobe behavior was predicted well and the measurement supplies a positive qualitative judgment of the underlying models.

The simulator that was described in this chapter was the starting point for the research presented in Chapters 3-6. Only in the following chapter the problem was directly tackled with the use of suitable experimental data and here the simulator plays a minor role. Chapter 4 deals with the Doppler effect and all methods were first developed and tested on sonar data generated with this simulator. Chapter 5 and 6 deal with the subject synthetic aperture sonar, for which a signal processing chain was developed from scratch with no availability of experimental data at the first stage of the research. Therefore, here it was a must to have this tool.

3. ADAPTIVE PORT/STARBOARD BEAMFORMING OF TRIPLET SONAR ARRAYS

3.1. Introduction

Chapter 1 already summarized the problems for sonars applied in the field of Anti-Submarine Warfare (ASW). The fact that operations are taking place in shallow coastal waters brings some problems, which are both a scientific and an operational challenge. The problem solved in this chapter is the discrimination between signals from the port and signals from the starboard side. The methods explained are developed with the aid of the simulator discussed in the previous chapter. For the testing, validation and performance measurement, it was not satisfactory to use simulated data. Because of the empirical nature of this topic, it was necessary to try the algorithms on sonar data collected at sea from many trials, of which two are discussed in this chapter. The work presented in this Chapter has a large overlap with the article of Groen (2005) in IEEE. The application of the signal processing methods is specifically performed as a part of this PhD research project. However, the beamformers presented are not novel and are obtained from literature. Where such literature is used, references are given. Furthermore, as also shows via the references, the research on triplets started before this PhD project in a continuing collaboration between TMS SAS (later named Thales Underwater Systems) and TNO. Additionally, the derivation of the formulae for theoretical performance was a part of this PhD project. Also, a major effort arose for the recording and analysis of experimental data. The attending of the sea trials and the application of the algorithms to measured data was part of the PhD project, but the trials were conducted with help of many people.

In this chapter, advanced port/starboard (PS) beamforming algorithms for a low frequency sonar system are designed, applied and validated. The two preferred methods to solve directly the PS problem are twin and triplet arrays. In the last decade the Underwater Acoustics group of TNO-FEL has analyzed both options. When processing the data of these systems, classical beamforming algorithms are not sufficient. Especially in the case of the triplet array, noise is correlated between the hydrophones in the array due to the small distance. For the triplet array van Mierlo (1997) started the research on spatial correlation. Noise correlation can be used in the beamforming to improve the sonar performance. Criteria of the processing that will be considered are array gain and port/starboard discrimination. From array theory, which can be found in Widrow (1985) and Nielsen (1991), different beamforming algorithms are suitable for triplet beamforming, i.e. a maximum PS rejection beamformer, a maximum gain beamformer, a best detection beamformer and an adaptive beamformer. In this chapter, performance of the system with application of these beamforming techniques is analyzed. It is important that the definition of the beamformers under investigation and the corresponding optimization criteria are clear and not ambiguous. Therefore, in the following Section, three desirable candidate beamformers are selected and defined accurately. Their names are optimum, cardioid and adaptive beamformer, respectively, in order to avoid very long and complicated

names. It should be kept in mind throughout the remainder of the chapter that these names are just labels and that one should realize that for example, the optimum beamformer is only optimum in a certain sense.

Single line array receivers are cylindrically symmetric and, therefore, cannot discriminate port from starboard. This is operationally very inconvenient and several attempts have been made to solve this notorious PS problem. Solutions can be found in the use of multi-line arrays, e.g. twin arrays by de Vlieger (1995), Allensworth (1995), Feuillet (1995) and Warhonowicz (1999) or directional sensors in a single line array by the company Thomson-CSF (1989), Berliner (1995) and Maksym (1996). The latter is superior from a handling point of view. In this thesis, PS beamforming of triplet array receivers, regarded as directional sensors, is investigated as solution.

A towed array consisting of hydrophone triplets is able to perform direct PS discrimination by using the small time-delay of signals received by the hydrophones on the P and the S side of the array. Doisy (1995), van Mierlo (1997) and Beerens (2000) presented the first studies on this ability in a series of UDT conference papers, in which they applied the so-called cardioid beamformer that gives high PS discrimination. It appeared that the specific PS beamforming for triplets is far from trivial. Since the ratio of array diameter to the acoustic wavelength is very small, the phase differences between the three hydrophones inside a triplet are small. This may lead to high signal loss by forcing to make PS rejection (the creation of a notch in the beampattern occurs by means of subtraction methods and may lead to losses in the ambiguous beam, especially near endfire). As long as the limiting noise is correlated: sea noise, tow ship noise, reverberation, as encountered in most operational conditions, this loss occurs also on the noise sources, and the net result of the PS beamforming is still a gain. But when going down in frequency or for high speed operations, flow noise may be the limiting noise, for which PS beamforming is not optimum.

In order to improve the signal-to-noise ratio, the use of optimum triplet beamforming is considered. In this beamforming the detection performance no longer depends on the correlations of received noise in the triplets. A decorrelation is achieved with help of a generalized noise correlation model, which is tuned by only one parameter and described by Beerens (1999). Different values for this parameter, however, result in different performance results. For instance, one can tune the parameter such that PS rejection is high or one can choose for a high signal-to-noise ratio. The former is attractive in a coastal area with strong directional reverberation. The latter is attractive in a deep water (omni-directional noise-limited) environment. Since these two optimum triplet beamformers are complementary, it is wiser to let the beamformer itself determine its optimum in a given environment. Therefore, an algorithm for adaptive triplet beamforming was developed by Beerens (2000).

The adaptive triplet beamformer is an MVDR (Minimum Variance Distorsionless Response) beam-space adaptive algorithm described by Nielsen (1991), Owsley (1985) and Monzingo (1980). In this beamformer the inner triplet correlations are actually measured and for each steering direction and at each range cell the beamforming is adapted to the local environment. In this way PS discrimination is guaranteed in beams with directional coastal reverberation, while high signal to background ratios are obtained in offshore (noise-limited) beams. Whether or not this concept works in practice will be looked into carefully and a comparison of the adaptive beamformer with other triplet beamformers is the main topic of this chapter.

The strong demand for PS discrimination in sonar applications comes from Anti-Submarine Warfare. Modern diesel-electric submarines have become much quieter in the last decades. The radiated noise levels have dropped much faster than sonar technology has improved. As a consequence, the passive detection of submarines has become increasingly problematic. Moreover, torpedo ranges have much increased lately. Therefore, there is a strong need for long range active detection of submarines. Low Frequency Active Sonar (LFAS) systems are good candidates to fulfill this need. These sonars are towed systems, such that they are variable in depth and can be deployed in the most favorable acoustic layer. An LFAS consists of a powerful wideband source and a long aperture receiving hydrophone array, which is usually on the order of tens of meters. For many reasons the latter must be able to solve bearing ambiguity in one single ping. After the cold war ended, the area of interest for Anti-Submarine Warfare has shifted from the ocean to the coastal waters, and, hence, shallow water operations have become more and more important. In such environments the time and space to maneuver is often limited, such that time consuming tracking procedures are to be avoided. Furthermore, coastal reverberation should be rejected to have good detection performance in offshore bearings. The use of hydrophone triplets in a single towed array provides the ability to immediately solve the PS problem and is, therefore, very suitable for passive and active use in shallow water operations.
The research in this chapter has been performed within the framework of the second New Array Technology (NAT II) program. The aim was to develop new technologies for low frequency active towed array sonars in shallow waters. This technology concerns both the receiver, discussed in this chapter and by Beerens (2005), and the source, which is analyzed in Doisy (2000) and Doisy (2005). The co-operative research program was initiated by TNO-FEL and TMS SAS and sponsored by the Dutch and the French Ministry of Defense.

The hydrophones in the triplets are close compared to the wavelength of the signals, which brings physical limitations to the PS discrimination. Although at the end of the chapter, adaptive PS beamforming is chosen as the best candidate, it still means that the trade-off between gain and PS discrimination remains. If noise is present in the data, it is always beneficial to have a longer aperture, which was operationally not attractive for this chapter's application.

The remainder of this chapter is organized as follows. In Section 3.2 the three mentioned triplet beamformers are derived from elementary detection theory. A key issue, their theoretical performance in terms of gain and PS rejection, is studied in Section 3.3. The theoretical results are compared to experimental results, which were obtained in a series of sea-trials with the CAPTAS (Combined Active Passive Towed Array Sonar) triplet array, which is described by Beerens (2000). The two sea-trials were directed by TNO-FEL in co-operation with Thales Underwater Systems (TUS, previously TMS-SAS) and the Royal Netherlands Navy (RNLN). In 1997 the first trial was performed in a noise-limited environment in the Mediterranean. The noise background consisted of sea noise and flow noise, where the latter was varied in level by sailing at different speeds. This trial is discussed in Section 3.4. In 1999 a second trial was performed in a reverberation-limited environment in the Bay of Biscay. Here the shelf break caused a background of reverberation in all bearings. This trial is discussed in Section 3.5. The conclusions are presented in Section 3.6.

3.2. Triplet beamformers

In this section, the expressions for three types of triplet beamformers are derived. *Triplet beamforming* is performed in beamspace, i.e. the triplet array is treated as three single arrays (in one hose), to which first straightforward array beamforming is applied. This is a conventional delay-and-sum beamforming applied by phase shifting in the frequency domain. The output of this process is a set of three array beam patterns that are still ambiguous. The input for the triplet beamformer is regarded as three single-line array beampatterns, i.e. directional hydrophones in a triplet.

The aim of triplet beamforming is two-fold: to obtain *PS rejection* and to achieve *triplet gain* (additional array gain due to triplet processing). The former is usually more important than the latter. The three triplet beamformers that are studied are:
A. Optimum triplet beamformer;
B. Cardioid triplet beamformer;
C. Adaptive triplet beamformer.
The last one is adaptive in the sense that the beamforming coefficients depend on the acoustic data following Cox (1991) and van Veen (1991). The optimum and cardioid beamformer have fixed coefficients, both maximizing one of the two performance indicators as discussed by Beerens (2000): the optimum triplet beamformer aims at optimizing triplet gain, whereas the cardioid beamformer optimizes for PS rejection. Triplet gain is defined in the same manner as array gain, which is the signal-to-noise ratio after beamforming divided by the signal-to-noise ratio before beamforming. The PS rejection is defined as the ratio of the energetic response in the signal direction and the energetic response in the opposite direction.

The general form for the output $B(\theta,\varphi)$ of a triplet beamformer as a function of the steering angles θ and φ is:

$$B(\theta,\varphi) = \mathbf{h}^{\dagger}\mathbf{b}\,, \tag{3.1}$$

where $\mathbf{b}$ is the three component vector of the three single array measurements, and the vector $\mathbf{h}(\theta,\varphi)$ contains three beamforming coefficients, which are related to the triplet geometry using spherical coordinates as shown in Figure 3-1. The symbol † denotes the Hermitian conjugate. The coefficients of the vector $\mathbf{h}$ can be chosen in accordance with the various optimization criteria mentioned previously.

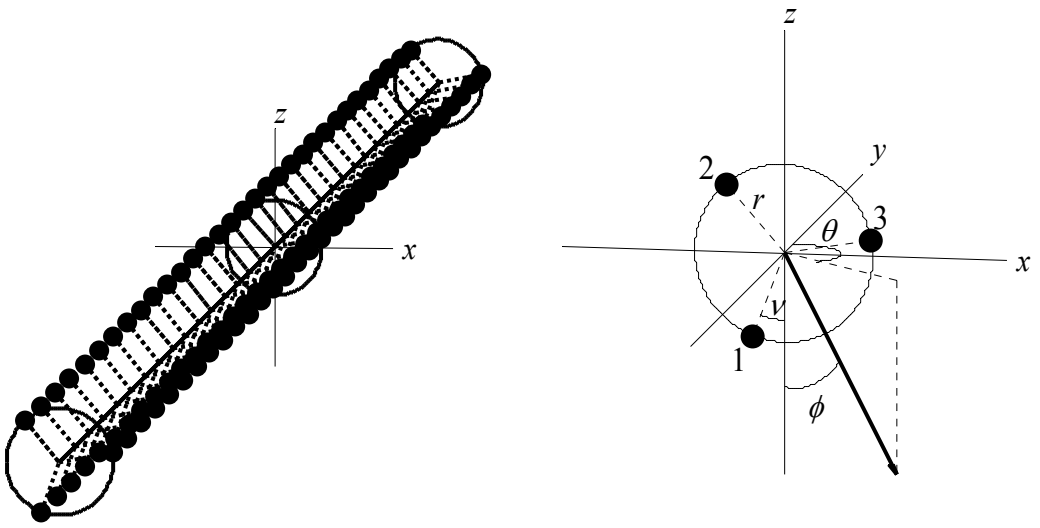


Figure 3-1 *Geometry of the hydrophone triplet.*
The angle θ, the azimuth, runs in the x,y-plane and the angle φ is the inclination angle.

The angle θ is the azimuthal angle in the *x,y*-plane from the *y*-axis with $0<\theta<2\pi$. The angle φ is the inclination angle from the negative *z*-axis with $0<\varphi<\pi$.

Because the recorded array data are converted to a directional triplet with the aforementioned single array beamforming, here it is sufficient to derive the equations for one triplet. The arrival time difference for a signal between one of the hydrophones of the triplet and the origin obviously depends on the angles (θ,φ). A target located in direction (θ,φ) yields a time difference:

$$\Delta t_j = \frac{r_t}{c}\begin{pmatrix}\sin\nu_j & 0 & \cos\nu_j\end{pmatrix}\begin{pmatrix}\sin\varphi\sin\theta\\ \sin\varphi\cos\theta\\ \cos\varphi\end{pmatrix}, \tag{3.2}$$

where $v_j = v+2(j-1)/3\pi$ and v the triplet roll, c the sound speed, r_t the array inner radius and $j \in [1,3]$ numbers the hydrophones in a triplet.
The triplet steering vector **d** lines up all the hydrophones signals for that specific direction (θ,φ) by means of a corresponding phase shift in the frequency domain. The three elements of this steering vector are:

$$d_j = \exp\left(2\pi i f \Delta t_j\right) = \exp\left[ikr_t\left(\sin\nu_j \sin\varphi\sin\theta + \cos\nu_j\cos\varphi\right)\right], \tag{3.3}$$

where $k = 2\pi f/c$ is the acoustic wavenumber and f the frequency.
Equations (3.2) and (3.3) are still exact for every angle of arrival (θ,φ), but the ray arrivals for the shallow-water long-range case are mainly aligned with the horizontal plane, except for the arriving tow ship noise. The assumption that the signals only travel in the *xy*-plane with $\varphi = \pi/2$ leads to the final form of the triplet steering vectors.

$$d_j = \exp\left(\mathrm{i}kr_t \sin\nu_j \sin\theta\right) \rightarrow \mathbf{d}(\theta) = \begin{pmatrix} \exp\left[\mathrm{i}kr_t \sin\nu \sin\theta\right] \\ \exp\left[\mathrm{i}kr_t \sin\left(\nu + \frac{2\pi}{3}\right)\sin\theta\right] \\ \exp\left[\mathrm{i}kr_t \sin\left(\nu + \frac{4\pi}{3}\right)\sin\theta\right] \end{pmatrix}. \tag{3.4}$$

For a conventional delay-and-sum beamformer, **h** = **d** is put in Eq (3.1). As the radius of the triplet array is small the noise received on the three hydrophones in a triplet is highly correlated. Therefore, a conventional beamformer performs poorly and it is favorable to consider a more general expression for a beamformer. A more general beamformer expression that takes other criteria into account is presented below.

To develop and evaluate the performance of the triplet beamformers, two performance criteria are used:

- the magnitude of the PS rejection:

$$r_{\mathrm{PS}} = \frac{B^2\left(\theta, \frac{\pi}{2}\right)}{B^2\left(2\pi\text{-}\theta, \frac{\pi}{2}\right)}, \tag{3.5}$$

where θ is the steering angle and where 2π-θ is the ambiguous direction to be rejected.

- and the triplet gain, which is the ratio of the gain in signal and gain in noise:

$$G = \frac{G_s\left(\theta, \frac{\pi}{2}\right)}{G_n\left(\theta, \frac{\pi}{2}\right)}. \tag{3.6}$$

The denominator G_n represents the amplification (gain) of the noise, which will appear to play an important role in determination of the optimal filter. Two ways can lead to high gain. Either the noise is suppressed or the signal enhanced.

A general expression for **h** is proposed by Nielsen (1991). As described in Appendix A, this formulation optimizes the probability of detection over the probability of false alarm in the case of a signal in noise.

The three triplet beamformers mentioned in the introduction are treated as special cases of this general form. The general expression is:

$$\mathbf{h}^{\dagger} = \frac{\mathbf{d}^{\dagger}\mathbf{R}^{-1}}{\mathbf{d}^{\dagger}\mathbf{R}^{-1}\mathbf{d}}, \tag{3.7}$$

where **R** is a symmetric correlation matrix of the form

$$\mathbf{R} = \begin{pmatrix} 1 & \rho_{12} & \rho_{13} \\ \rho_{12}^{\dagger} & 1 & \rho_{23} \\ \rho_{13}^{\dagger} & \rho_{23}^{\dagger} & 1 \end{pmatrix} \tag{3.8}$$

with correlation coefficients ρ_{12}, ρ_{13} and ρ_{23}. These correlation coefficients ρ are parameters that are a function of frequency and that can be chosen to optimize the beamformer for different optimization criteria.

This is a well-known result for optimum beamformers of arrays, which is derived in Owsley (1985) and Monzingo (1980). Decorrelation of the noise background is a technique whereby the signal-to-noise ratio is maximized by minimizing the noise rather than by maximizing the signal (as in conventional beamforming). In this formulation the choice of a triplet beamformer is now related to a noise correlation matrix $\mathbf{R} = \mathbf{R}_n$. The PS rejection r_{PS} is now calculated with:

$$r_{\mathrm{PS}} = \frac{B^2(\theta,0)}{B^2(2\pi\text{-}\theta,0)} = \frac{\left|\mathbf{h}^{\dagger}\mathbf{d}(\theta)\right|^2}{\left|\mathbf{h}^{\dagger}\mathbf{d}(2\pi-\theta)\right|^2} \tag{3.9}$$

and the triplet gain G is calculated with:

$$G = \frac{G_s}{G_n} = \frac{\left(\mathbf{h}^{\dagger}\mathbf{b}_s\right)\left(\mathbf{h}^{\dagger}\mathbf{b}_s\right)^{\dagger}}{\left(\mathbf{h}^{\dagger}\mathbf{b}_n\right)\left(\mathbf{h}^{\dagger}\mathbf{b}_n\right)^{\dagger}} = \frac{\left(\mathbf{h}^{\dagger}\mathbf{d}\right)\left(\mathbf{h}^{\dagger}\mathbf{d}\right)^{\dagger}}{\mathbf{h}^{\dagger}\mathbf{b}_n\mathbf{b}_n^{\dagger}\mathbf{h}} = \frac{\left|\mathbf{h}^{\dagger}\mathbf{d}\right|^2}{\mathbf{h}^{\dagger}\mathbf{R}_n\mathbf{h}} \tag{3.10}$$

using the signal from the steering direction $\mathbf{b}_s = \mathbf{d}$ and noise input vector $\mathbf{b}_n$.

This is a well-known result for beamformers and a general version of the derivation can be found in, for example, Nielsen (1991). In the following subsections, the matrix $\mathbf{R}$ will be filled in different ways. The choice for $\mathbf{R}$ can be seen as a tuning process. It is shown in Appendix A that the ratio between the likelihood of proper detection and wrong detection is maximized when the actual $\mathbf{R}_n$ is filled in for $\mathbf{R}$. How to determine $\mathbf{R}$ or choose it in a robust way, and what the impact on the two performance indicators is, is described in the following three subsections.

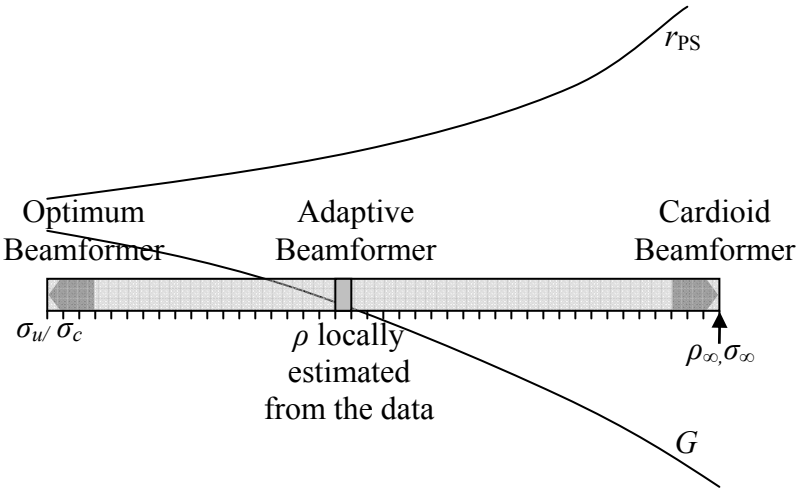


Figure 3-2 *The three triplet beamformers that are discussed depend on a tuning parameter σ (or ρ), which can be seen as a slide bar.*

3.2.1. Optimum triplet beamformer

The first triplet beamformer studied in this paper is just called *optimum triplet beamformer*. Optimum here means that the triplet gain is maximized by minimizing the gain in noise. Therefore, the background is assumed to consist purely of noise that is stationary with fixed spatial correlation. For this case a relatively simple expression can be derived from detection theory. In this section, detection theory, which is elaborated on in Appendix A, is applied to optimize the triplet beamformer against a background, which is a mixture of correlated (sea) and uncorrelated (flow noise).

For a given steering vector $\mathbf{d}(\theta,\varphi)$ at frequency f, the optimum filter in Eq. (3.7) only depends on the (inverse) triplet noise correlation matrix $\mathbf{R}_n^{-1}$. In van Mierlo (1997) a model for this noise correlation matrix is formulated. In this model two types of noise are incorporated: uncorrelated noise and correlated noise. The former is mainly flow noise. The latter consists of a collection of sea noise, tow ship noise, traffic noise, etc. As the triplet beamforming is performed in beam-space all these constituents can be regarded as directional noise and have similar correlation properties. The accompanying noise correlation matrix $\mathbf{R}$ can be decomposed as $\sigma_n^2\mathbf{R}_n = \sigma_u^2\mathbf{I} + \sigma_c^2\mathbf{R}_c$, where σ_u^2 is the uncorrelated, σ_c^2 the correlated and σ_n^2 total noise variance. The parameter $\sigma^2 = \sigma_u^2/\sigma_c^2$ is their ratio and the total noise correlation coefficient equals $\rho_n\sigma_c^2/\sigma_u^2 = \rho_n/\sigma^2$. The complete matrix has the form:

$$\sigma_n^2\mathbf{R}_n = \sigma_u^2\begin{pmatrix}1&0&0\\0&1&0\\0&0&1\end{pmatrix} + \sigma_c^2\begin{pmatrix}1&\rho_c&\rho_c\\\rho_c&1&\rho_c\\\rho_c&\rho_c&1\end{pmatrix} = \sigma_n^2\begin{pmatrix}1&\rho_n&\rho_n\\\rho_n&1&\rho_n\\\rho_n&\rho_n&1\end{pmatrix}. \tag{3.11}$$

The noise correlation coefficient ρ_n is modeled by:

$$\rho_n = \frac{\mathrm{sinc}\left(kr_t\sqrt{3}\right)}{1+\sigma^2}. \tag{3.12}$$

The $\mathrm{sinc}\left(kr_t\sqrt{3}\right)$-term is the theoretical spatial noise correlation function for sea noise ρ_c received on triplet hydrophones spaced at $r_t\sqrt{3}$ as derived by for example Nielsen (1991) and Urick (1975). In such model, it is assumed that the sea noise is omni-directional and can be calculated with an integral over the noise generated at the sea surface. The sea noise inside the triplets is highly correlated. The center frequency of the active band for CAPTAS is f = 1500 Hz. According to Eq. (3.12), for pure sea noise (σ^2 = 0) and a triplet radius r_t of 25 mm it follows that the noise correlation coefficient is $\rho_n \approx 0.988$. Although the previously mentioned noise correlation model is purely theoretical, it has been verified on real sea noise data by Beerens (1999). The experimental results were in agreement with theory. Therefore, it is concluded that this allows combining the three arrays such that a maximum gain against noise is obtained.

Noise parameter estimation
The complete model is tuned by only one parameter, σ^2, the ratio of flow and sea noise variance. To obtain optimum gain in practice, σ^2 should be estimated. For the CAPTAS array this parameter is about 0.1 (-10 dB) and often even less, depending on tow speed and sea state. For triplet arrays it is essential that the measured values for σ^2 are small, because flow noise negatively influences the triplet array performance, as will be explained in the following section based on the theory of van Mierlo (1997). The actual parameter to be used in the optimum beamformer can be estimated from empirical formulae (depending on wind and tow speed) or from real-time correlation measurements as carried out by Beerens (1991). The method of Beerens is used in this chapter. If the correct parameter value is used, the beamformer is optimized for array gain, provided that the noise correlation model is valid. This is the case only in environments in which noise is limiting detection performance.

3.2.2. Cardioid beamformer

It is possible to apply triplet beamforming in such a way that a cardioid directivity pattern is obtained as described by van Mierlo (1997). The formula for the beamformer that achieves this can be derived in several ways. The derivation that achieves this can be written down in different ways and for consistency here the approach with correlation coefficients like in the previous section is used.

In a cardioid beam pattern there should be zero sensitivity in the ambiguous direction, which means that infinite PS rejection is obtained. Without any other algorithm the beamformer can be derived now. This infinite PS rejection is achieved by zeroing the denominator of the expression for the rejection in Eq. (3.8), i.e. $\left|\mathbf{h}^{\dagger}\mathbf{d}\left(2\pi-\theta\right)\right| = 0$ has to be achieved. The matrix $\mathbf{R}$ in Eqs. (3.7) and (3.8) is now taken to be the signal cross-correlation matrix of the triplet. The correlation coefficients ρ will now optimize PS rejection. The equation that follows is:

$$\mathbf{d}^{\dagger}\begin{pmatrix} 1 & \rho_\infty & \rho_\infty \\ \rho_\infty & 1 & \rho_\infty \\ \rho_\infty & \rho_\infty & 1 \end{pmatrix}\mathbf{d}(2\pi-\theta)=0\,. \tag{3.13}$$

This equation can be evaluated using the trigonometric rules $\cos a = \frac{e^{ia}+e^{-ia}}{2}$ and $2\cos^2 a = 1+\cos 2a$ that hold for any angle a. It can then be written as:

$$\rho_\infty - 1 - (2\rho_\infty + 2)\cos\left(2kr_t\sqrt{3}\sin\theta\right) + 4\rho_\infty\cos\left(kr_t\sqrt{3}\sin\theta\right) = 0\,. \tag{3.14}$$

After some manipulation one can find that infinite rejection occurs for a special value of the correlation coefficient ρ_∞:

$$\rho_\infty = \frac{1+2\cos\left(2kr_t\sqrt{3}\sin\theta\right)}{\left[1+2\cos\left(kr_t\sqrt{3}\sin\theta\right)\right]\left[3-2\cos\left(kr_t\sqrt{3}\sin\theta\right)\right]} \approx \cos\left(2kr_t\sqrt{3}\sin\theta\right), \tag{3.15}$$

where the approximation can be made because $kr_t\sqrt{3}\sin\theta$ is small. This singular value is close to the correlation coefficient of a plane wave signal arrival at the array. The parameter ρ_∞ that is obtained using the cardioid beamformer can be associated with a noise variance σ^2 using Eq. (3.12). The associated noise model parameter σ_∞^2 is given by:

$$\sigma_\infty^2(f,\theta) \approx \frac{\mathrm{sinc}\left(kr_t\sqrt{3}\right)}{\cos\left(2kr_t\sqrt{3}\sin\theta\right)} - 1\,, \tag{3.16}$$

If this noise variance is equal to the real noise in the data, the optimum beamformer and the cardioid beamformer are the same. To get a feeling for the parameter values at which this occurs: for a target on broadside (θ = 90°) at f = 1500 Hz, PS rejection is maximum for ρ_∞ = 0.863, this gives σ_∞^2 = 0.145 (-8.4 dB), which is a realistic figure for towed array sonars. Off broadside the values are much lower and near endfire even negative values for σ_∞^2 would be required to obtain infinite rejection. This means that near end fire the two beamformers are mutually exclusive.

It is important to remark that these singular parameter values are generally much lower than the physical values of the ratio of flow and sea noise. This means that the gain is not optimum. Only for highly correlated noise mixtures (low flow noise), cardioid beamforming and optimum beamforming are similar. For high levels of flow noise, the triplet gain may even get negative, especially near endfire, as will be shown in Section 3.3. For given $\rho_\infty(\theta)$ from the cardioid beamformer the azimuth θ_0, for which the two beamformers are a noise background with ratio σ^2. This is true when $\rho_n(f) = \rho_\infty(f,\theta)$, given by Eq. (3.12) and (3.15), from which θ can be solved. As kr_t is small, both expressions are expanded in powers of kr_t and only retain terms up to order three:

$$\frac{1-\frac{\left(kr_t\sqrt{3}\right)^2}{6}+O\left(kr_t\right)^4}{1+\sigma^2}=1-\frac{\left(2kr_t\sqrt{3}\sin\theta_0\right)^2}{2}. \tag{3.17}$$

For the case of sea noise ($\sigma^2 = 0$) the θ_0 can be calculated with:

$$\sin^2\theta_0=\frac{1}{12}+O\left(kr_t\right)^2. \tag{3.18}$$

The term $\sin^2\theta_0$ is only dependent on kr_t in the second order. In the extreme case of sea noise the value becomes $\theta_0 \approx \text{asin}(1/12) = 17^o$. This means that for this type of systems the angle at which this occurs is not significantly dependent on frequency. Beerens (2000) suggested using the cardioid beamformer only near broadside and making a smooth transition to the optimum beamformer near endfire. This can be achieved by replacing negative values of σ_∞^2 by 0, which happens for a range of 17 degrees around the endfires. Such a 'relaxed cardioid beamformer' is applied in Sections 3.4 and 3.5.

3.2.3. Adaptive triplet beamformer

The two beamformers mentioned previously are each ideal for their own optimization criterion. Optimum beamforming gives good detection performance in all kind of noise-limited environments, e.g. deep waters. But optimum PS (cardioid) is required in areas, where coastal reverberation masks detection in offshore bearings. However, for an operator it is hard to determine which processor is most suitable in a specific environment, and it is preferable to have only one beamformer, which adapts to the situation.

To solve this problem, an algorithm for adaptive triplet beamforming is developed that optimizes the signal to background ratio. The background in this case is a combination of reverberation and noise in the beam (port and starboard). The adaptive beamforming uses actual estimations of the correlation coefficients of the beamformed data from the three arrays. These are substituted into Eq. (3.7). In this way the beamforming is optimized for the actual background.

There are, however, some drawbacks to adaptive beamforming. Adaptive beamforming is very sensitive to phase errors. If due to bad measurements (e.g. caused by electronic deficiencies or hydrophone positioning errors) the correlation coefficients are poorly estimated, the performance degrades dramatically; see for example van Veen (1991) and Cox (1987). For a successful application of adaptive beamforming several issues have to be addressed:

- integration time for the estimation of the covariance matrix,
- control of the condition number of the covariance matrix,
- frequency dependence of the covariance matrix,

These items are discussed next.

Covariance matrix
The adaptive triplet beamformer is built up in the same manner as the other two beamformers,

i.e. Eq. (3.7) and (3.11) are applied. The difference is that the correlation matrix **R** is now determined adaptively, i.e. it is derived directly from the actual correlation measurements rather than indirectly via a noise correlation model. Assuming perfect estimation of the actual covariance matrix, the following filter is applied:

$$\mathbf{h}^{\dagger} = \frac{\mathbf{d}^{\dagger}\mathbf{R}_1^{-1}}{\mathbf{d}^{\dagger}\mathbf{R}_1^{-1}\mathbf{d}} \tag{3.19}$$

The matrix elements for each bearing are computed as

$$R_{ij}(t,\theta) = \frac{\mathbf{b}_j^{\dagger}\mathbf{b}_i}{|\mathbf{b}_i||\mathbf{b}_j|}, \tag{3.20}$$

where $i,j \in [1,3]$ number the relevant single array. Here both the noise of Eq. (3.12) and the signal of Eq. (3.15) contribute to the correlation matrix. If only noise is measured in a beam, $\mathbf{R_1}$ will be the noise correlation matrix given by Eq. (3.11) and automatically optimum beamforming is applied. In practice it is better to replace the correlation coefficients by covariances, which are defined slightly different: $R_{ij} = \mathbf{b}_j^{\dagger}\mathbf{b}_i$. For a well-calibrated triplet array all three beam outputs will have equal level ($|\mathbf{b}_i| = |\mathbf{b}_j|$). In that case the covariance matrix and the correlation matrix are the same, but in practice arrays always suffer from small imperfections. The usage of the covariance matrix then has an auto-calibrating effect.

The computation of the covariance matrix elements takes place in the time domain. The great advantage of this time domain approach is that the adaptations to the rapidly changing environment can be made as a function of time, which would not be straightforward in the frequency domain. Reverberation from bottom structures may sometimes be only a few meters long and adaptations should follow up in much shorter time than the pulse duration. The disadvantage of this approach is an increase in computation time and memory usage, since now the triplet beamforming takes place after replica correlation with the transmitted pulse. This replica correlation (matched filtering) has to be executed three times (once for each array). Moreover, the frequency dependence of the correlation coefficients is neglected. The latter is discussed in the last part of this section.

Integration time

The choice for the integration times depends on the scenario. The integration time should be kept small for quick adaptations. In general, the stability of the adaptive beamforming increases when the integration time is longer. After some tuning, the integration time is chosen to be short, i.e. only a few ms (a few meters or less than 10 samples). This is in agreement with the expected size of the target. Since the target is included in the estimated covariances of Eq. (3.20), also in the direction opposite to the target, the target echo level will contribute to the estimated background field and raise the correlation coefficients. When a target signal is present, the correlation coefficients are much higher than when noise only is present. When the former occurs, the adaptive beamformer will automatically provide PS rejection. In this way optimum beamforming is applied in noise-limited conditions, whereas in case of strong reverberation, the correlation coefficients are high and the adaptive beamformer automatically tends towards a cardioid beamformer.

Inversion of the covariance matrix

In adaptive beamforming the covariance matrix has to be inverted, which is not trivial, as it is always close to singular. Especially for high signal-to-noise ratio, the matrix **R** converges towards the singular matrix $\mathbf{dd}^{\dagger}$. A measure for how well the matrix can be inverted is the condition number of the matrix (largest eigenvalue over the smallest eigenvalue). If the condition number is ∞, the matrix cannot be inverted. In theory, this situation will not occur for **R** if the integration time is long enough, but in practice measurement errors can disturb the picture. To obtain a reliable and stable output from the adaptive beamformer it is necessary to bound the condition number of **R**. A standard method to control the behavior of the condition number is to increase the diagonal elements of the matrix with a small value ε. This *diagonal loading* limits the condition number to the reciprocal of ε. In fact, this method yields a compromise, because a little conventional (delay-and-sum) beamforming is added to stabilize the adaptive beamforming. The loading ε should be as small as possible.

$$\kappa = \mathrm{cond}\left\{\begin{pmatrix} 1+\varepsilon & \rho & \rho \\ \rho & 1+\varepsilon & \rho \\ \rho & \rho & 1+\varepsilon \end{pmatrix}\right\} = \frac{1+2\rho+\varepsilon}{1-\rho+\varepsilon}, \tag{3.21}$$

where now $\rho = (|R_{12}|+|R_{13}|+|R_{23}|)/\mathrm{trace}(\mathbf{R})$ is the average correlation coefficient. To look at the effect of ε on the condition number (final best accuracy of the output), an example $f = 1500$ Hz is shown in Figure 3-3. The condition number is shown as a function of bearing, for which the sea noise and signal correlation coefficients are calculated with Eq. (3.12) and (3.15). The curves show the condition number when dealing with sea noise and the condition number when dealing with reverberation (signal). The dotted lines show the condition number versus bearing, when no adaptations are made (the gradient is high at 10 degrees from endfire). The dashed lines represent application of diagonal loading with $\varepsilon = 3.10^{-3}$. The solid lines represent the method of cutting the condition number, when it becomes too high. This method is computationally very unattractive and gives similar results as diagonal loading.

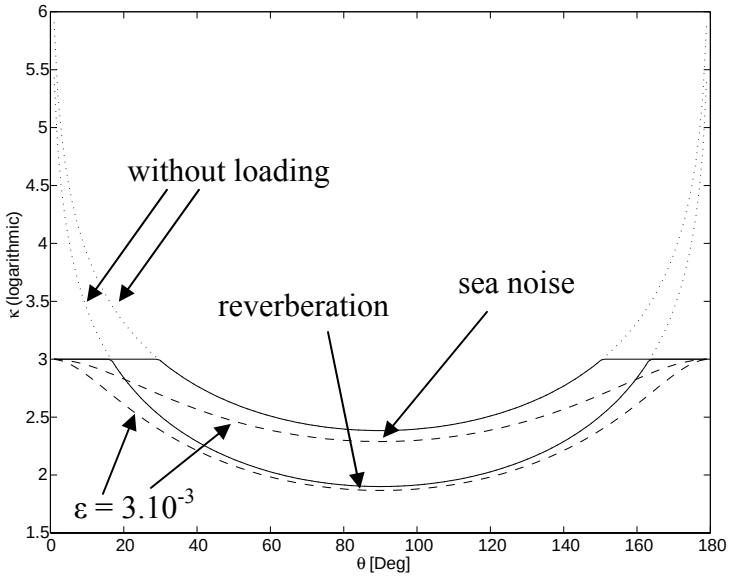


Figure 3-3 *Effect of diagonal loading on the condition number of the correlation matrix.*

Frequency dependence of the correlation coefficient
To get back to the variation of the correlation coefficient in the frequency band, it is now shown that this effect is even lower than the required diagonal loading. Since $kr_t\sqrt{3}$ is very small, the correlation coefficient for sea noise can be approximated with a third order Taylor expansion:

$$\rho = \operatorname{sinc} kr_t\sqrt{3} \approx 1 - \frac{\left(kr_t\sqrt{3}\right)^2}{6} \tag{3.22}$$

The variation of the correlation coefficient in the band (width b) should not exceed the variation ε due to loading:

$$\Delta\rho = \frac{\mathrm{d}\rho}{\mathrm{d}f}\Delta f = \frac{\mathrm{d}\rho}{\mathrm{d}k}\frac{\mathrm{d}k}{\mathrm{d}f}\frac{b}{2} < \varepsilon\,. \tag{3.23}$$

Substituting Eq. (3.22) and using $k = 2\pi f/c$ yields:

$$\frac{2\pi^2 f r_t^2 b}{c^2} < \varepsilon\,. \tag{3.24}$$

The bandwidth in which the frequency dependence of the correlations is still negligible follows when the values for the CAPTAS system given in Section 3.2.1 and $\varepsilon = 3.10^{-3}$ are filled in:

$$b < \frac{\varepsilon c^2}{2\pi^2 f r_t^2} \approx 400\,\mathrm{Hz} \tag{3.25}$$

This means that for the system settings in this chapter it is valid to apply time domain triplet beamforming. For still higher bandwidths the band can be cut into sub bands, which should be treated separately.

3.3. Theoretical performance

As described in Section 3.2, the performance indicators for the triplet beamformers are the magnitude of PS rejection and the triplet gain. To compare the three triplet beamformers, these performance indicators given by Eq. (3.8) and (3.6) are plotted versus bearing (azimuth) for the optimum and cardioid beamformer of an incident plane wave for a frequency of f = 1500 Hz. The noise is assumed to be Gaussian and white in the band of the signal. For a typical environment, a noise mixture $\sigma^2 = 0.1$ is assumed, which is a rather high value for a (well-designed) triplet array according to Beerens (1999). In the theoretical plots in Figures 3-4 this typical environment is shown with solid lines. The extreme situations with flow noise only and sea noise only are shown with the dotted and dashed lines, respectively.

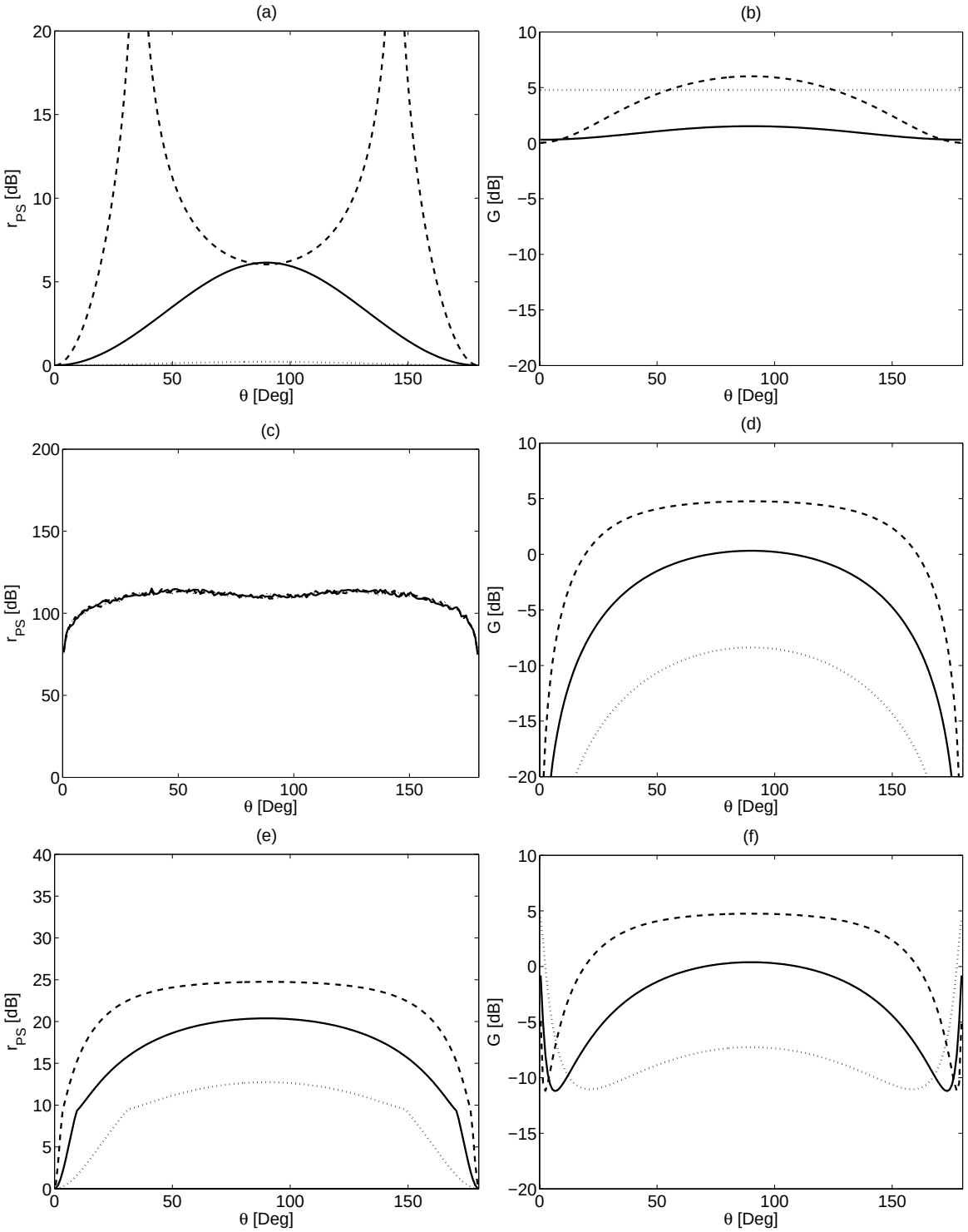


Figure 3-4 *Theoretical performance of the three beamformers. From top to bottom the performance of optimum, cardioid and adaptive beamformers is plotted, respectively. On the left PS rejection is shown versus bearing and on the right triplet gain versus bearing.*

Figure 3-4 shows the theoretical performance of the three beamformers with two performance indicators: PS rejection and triplet gain. When comparing, it should be noted that the *y*-axes of the plots are not equal, which was necessary for a clear visualization.

In the top panel of Figure 3-4 the performance of the optimum beamformer is shown. The PS rejection is 6 dB at broadside in sea noise, rises because σ^2 approaches $\sigma_\infty{}^2$, then drops again to 0 dB at endfire. In flow noise the PS rejection is less, but in the noise mixture the PS rejection is better and for some bearings even much better. The performance in flow noise is not alarming, since in practice the noise will always be a mixture. For the typical environment, the PS rejection is 6 dB at broadside and drops to 0 dB at endfire, which is enough for detection purposes. The PS rejection values are not impressive, but the beamformer is designed to obtain gain, which is achieved. Triplet gain is always positive and for the typical environment has a maximum of 1.5 dB around broadside.

The cardioid beamformer, shown in the middle panel (Figure 3-4), does indeed obtain infinite (machine precision) rejection. However, its gain performance is somewhat disappointing. For the typical environment near broadside triplet gain is 0 dB, but towards endfire it drops fast. In sea noise the performance is little better, but the performance against flow noise is poor. Here a loss appears in the order of 10 dB. This is a well-known fact from array PS beamforming; near endfire phase differences between P and S beams are very small and canceling the signal from one side will also reduce the signal from the other side. This is in contrast to flow noise, which always adds up if P and S beams are combined.

The general lesson is that for the non-adaptive beamformers there is a trade-off between gain and PS rejection. The cardioid beamformer provides infinite PS rejection, but poor gain, especially near endfire. The optimum beamformer provides sufficient gain, but has poor PS rejection. For proper detection and PS rejection one would like to have both. This is in theory achieved by the adaptive beamformer. For adaptive beamforming both the noise and the signal contribute to the correlation matrix. If only noise is measured in a beam, Eq. (3.20) will be the noise correlation matrix of Eq. (3.11) and automatically optimum beamforming is applied. However, if signal (or reverberation) is present in a beam the correlation coefficients rise and the beamformer starts to make more PS rejection. This PS rejection will not be infinite, but is limited by the signal-to-noise ratio. Therefore, its gain will outperform the cardioid beamformer. For adaptive beamforming, the triplet gain is deduced from Eq. (3.19) with

$$\mathbf{h}^\dagger = \frac{\mathbf{d}^\dagger \left(\sigma_s^2 \mathbf{d}\mathbf{d}^\dagger + \sigma_n^2 \mathbf{R}_n\right)^{-1}}{\mathbf{d}^\dagger \left(\sigma_s^2 \mathbf{d}\mathbf{d}^\dagger + \sigma_n^2 \mathbf{R}_n\right)^{-1} \mathbf{d}} \tag{3.26}$$

corresponding to the spatial filter estimated in a situation where signal (of magnitude $\sigma_s{}^2$) and noise are present in the estimation of the covariance matrix. Substituting in Eq. (3.6) yields the following expression for the triplet gain:

$$G = \mathbf{d}^\dagger \mathbf{R}_n^{-1} \mathbf{d} \tag{3.27}$$

This expression is the same as for optimum beamforming, as to be expected, since the response of the MVDR adaptive beamforming in the steering direction of the target is independent of the presence of the target. The theoretical performance of the adaptive beamformer in terms of triplet gain and PS rejection as a function of bearing angle θ is shown at the bottom panel of Figure 3-4. The gain would obviously be identical to Figure 3-4a and the PS rejection would be around twice the level (in decibels!) shown in Figure 3-4e. The plots are calculated with the formulae for gain and PS rejection in Eq. (3.8) and Eq. (3.6), but the matrix

$\mathbf{R}_1 = \sigma_s^2 \mathbf{d}\mathbf{d}^\dagger + \sigma_n^2 \mathbf{R}_n$ is replaced by its modulus $\left|\sigma_s^2 \mathbf{d}\mathbf{d}^\dagger + \sigma_n^2 \mathbf{R}_n\right|$. Thus, the theoretical performance is based on the correlation only and not on the phase shifts that the matrix introduces. The reason for this is three-fold:

1. Physically, as explained in Appendix A, the use of a matrix $\mathbf{R}_1$ in the triplet beamforming creates new single-line input data, which is an uncorrelated version of the original data. Subsequently, the vector **d** is applied for the beamforming. When a signal is present, $\mathbf{R}_1$ develops into a complex matrix, which decorrelates and sums the three signals and, subsequently, allows the vector **d** to combine the new signals again. The travel times of the signal are used twice in this way, which is not preferred.
2. The theoretical performance of the adaptive beamformer is expected to be a trade-off. It is supposed to trade (possibly infinite) PS rejection for signal-to-noise ratio by means of triplet gain.
3. The proper measure to quantify the performance of any sonar is not by means of array gain or PS rejection but by means of the detection performance itself. Such performance should be measured statistically with the probability of detection and the probability of false alarm. Obviously, there is a coupling between the measurement methods, which is usually known, but here it is argued that for the case of adaptive beamforming it is not. Unfortunately, this is a rather comprehensive procedure and for the simulations and experiments analyzed in this chapter, measuring the detection performance in this way was not viable. However, the preliminary analyses that were conducted clearly showed that the theoretical performance was much less than expected from Eq. (3.26).

The PS rejection definition previously mentioned is limited by the output SNR. The plots have been obtained with an input SNR of 20 dB. Around broadside, the PS rejection is high (close to the maximum required, which is the SNR), but in a small sector around end-fire, PS rejection decreases (it is not required there anyway). Triplet gain is always positive.
Therefore, in theory, the adaptive triplet beamformer seems to be making PS discrimination combined with positive gain. This is due to its ability to perform steering dependent processing: in the steering direction of the target, an optimal combination with respect to noise is performed, while in the ambiguous direction, the target is seen as a jammer and is rejected until its level is equal to the noise level at processing output. Performance on sea-trial data is reported in the next section.

The PS rejection definition previously mentioned now includes the noise contribution and it is limited by the output SNR. The plots have been obtained with an input SNR of 20 dB. Around broadside the PS rejection is high (close to the maximum required which is the SNR), but in a small sector around endfire PS rejection decreases (it is not required there anyway). Triplet gain is mostly positive, except very near endfire where just enough SNR is kept for proper detection.

Therefore, in theory the adaptive triplet beamformer seems to be making PS discrimination without strongly negative gain (even positive gain in case of low flow noise). In practice the application of adaptive beamforming is not always so easy. The estimation of the correlation matrix is not perfect and the performance will depend on this. Therefore, it is necessary to test the performance on sea-trial data.

3.4. Sea trial results in noise

3.4.1. Experiment set-up

In 1997 experiments have been conducted in a noise-limited environment in the Mediterranean. The aim was to assess the performance of a triplet array with respect to the topics PS discrimination and detection as a function of target bearing, frequency and tow speed. An experimental triplet array (the CAPTAS array) was towed behind Her Netherlands Majesty's Ship (HNLMS) Tydeman, an oceanographic research vessel of the RNLN. An artificial target (the TNO-FEL echo-repeater) was towed behind Research Vessel Planet. All experiments have been carried out under good weather conditions. To vary the flow noise levels, experiments have been performed at four different tow speeds: 6, 9, 12 and 15 knots. During the experiments, the target sailed through all the bearings at a fixed range of approximately 7 nautical miles.

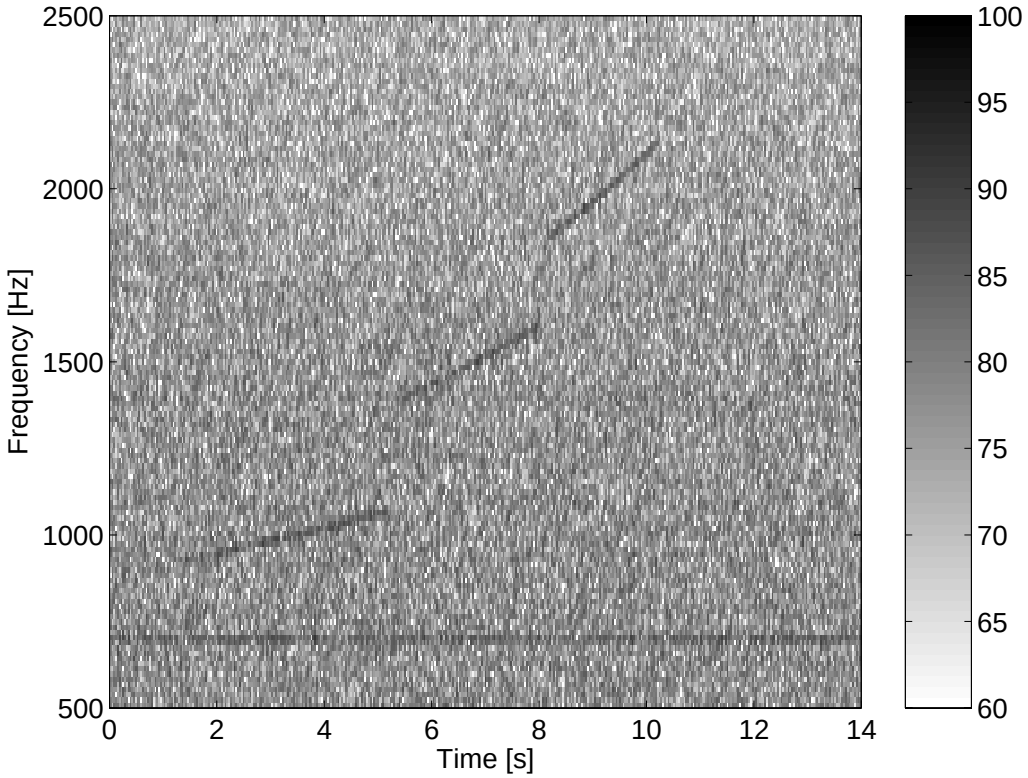


Figure 3-5 *Hydrophone reception of the 4 HFM sweeps during 15 knots experiment.*

The transmitted waveforms were Hyperbolic Frequency Modulated (HFM) sweeps around frequencies 1000, 1500, 2000 and 2750 Hz. The signals have a bandwidth of 100, 230, 300 and 500 Hz, respectively and a duration of 1.5, 1.2, 1.0 and 0.7 s, respectively???. The last has been left out of the analysis, because in addition to aliasing, it did not show different results from the 2000 Hz sweep. The bandwidth time product and bandwidth frequency quotient are kept constant for the four sweeps to ensure comparable matched filter gain and frequency variations. A *t-f* plot of the reception of the sweep at hydrophone level is depicted in Figure

3-5. Three of the four (low frequency) sweeps and a tow ship tonal (≈ 700 Hz) are visible in the first 10 seconds. The detection performance of the CAPTAS array is analyzed in different bearings, at different frequencies and for various noise mixtures as a result of this set-up.

3.4.2. Processing chain

The processing of the CAPTAS system is realized in a hardware part and a software part. A block diagram of the full chain is shown in Figure 3-6.

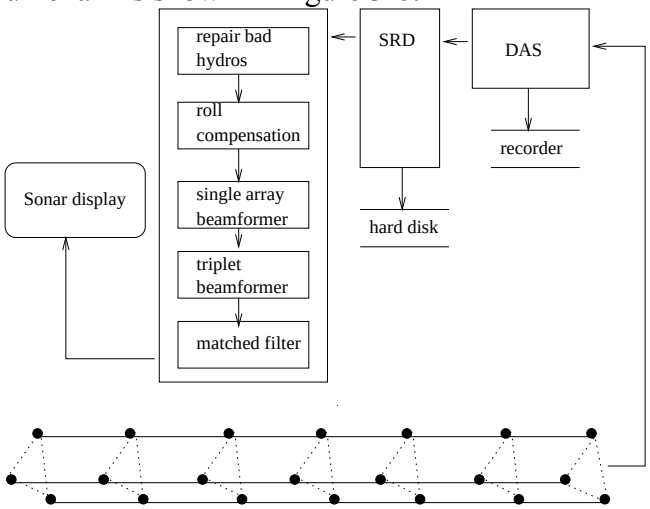


Figure 3-6 *Overview of the processing chain in CAPTAS. Before signal processing in software, the data are acquired on the Data Acquistion System (DAS) and are downsampled in the Sample Rate Decimator (SRD).*

The hydrophone signals are digitized and filtered in hardware in the array. They are received on the wet end and distributed in the Data Acquisition System, from which the raw data are recorded and downsampled in hardware. The downsampled data are now ready for further processing with software. First, the hydrophone data are checked and calibrated (bad hydrophones are replaced by interpolations of their neighbors). This is necessary, as a few hydrophones that do not operate correctly might destroy the output of the array completely, especially when adaptive beamforming (or array shading) is applied. After this the hydrophone signals are interpolated on the circle to compensate for triplet roll. Two roll sensors in the CAPTAS system measure the roll at the front and the aft of the array. From this the roll for each triplet is derived assuming roll progresses linearly over the array. From experience it is known that the roll of the triplets is measured accurately enough (sensor accuracy ~ 2^{o}) for proper acoustic processing. This roll stabilization is necessary to be able to apply single array (FFT) beamforming to the three straight arrays. After this the triplet beamforming is applied, followed by the matched filtering. For the adaptive beamforming the two latter processes are interchanged; matched filtering is performed prior to adaptive triplet beamforming.

3.4.3. Experiment results

The results of a 12 knots experiment are presented below. Experiments at other speeds did not show a very different picture, because there is a relation between flow noise and tow ship noise, both of which increase with tow speed. Due to the good weather conditions sea noise was not dominant. This meant that the noise correlations did not change very much over the experiments. Since this is the case, the tow speed dependence is not further analyzed here. The analysis focuses on variation with frequency and bearing.

In the Figures 3-7 to 3-9 the experimental results for the performance indicators of the different triplet beamformers as a function of bearing are shown. Results of the optimum beamformer are denoted by stars (*), of the cardioid beamformer by circles (o), and of the adaptive beamformer by squares (□). On the left, the PS discrimination and on the right the gain performance is depicted. The PS results are compared to theoretical results for the corresponding frequency and noise mixture. For the gain the theoretical maximum (correlated) and the minimum (uncorrelated) values are plotted. These theoretical curves are dotted and dash-dotted respectively.

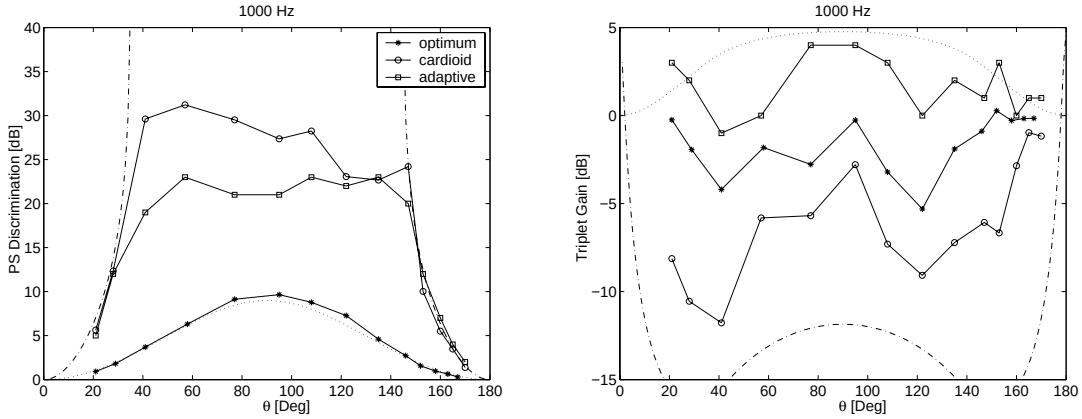


Figure 3-7 *Experimental performance at 1000 Hz. On the left PS rejection is shown versus bearing and on the right triplet gain versus bearing. The theoretical performance for the cardioid beamformer in the actual noise mixture is shown with the dash dot curve. The theoretical performance for the optimum beamformer in the actual noise mixture is shown with the dotted curve.*

In Figure 3-7 the results for 1000 Hz are shown. The optimum beamformer (*) does not have a high PS rejection: only a maximum of 9 dB at broadside. This is in accordance with the theoretical curve. PS rejection of the cardioid beamformer (o) is very high, some 30 dB, and is limited by the signal-to-noise ratio. The adaptive beamformer (□) performs as well as the cardioid beamformer in PS discrimination. The adaptive beamformer has an even higher gain than the optimum beamformer.

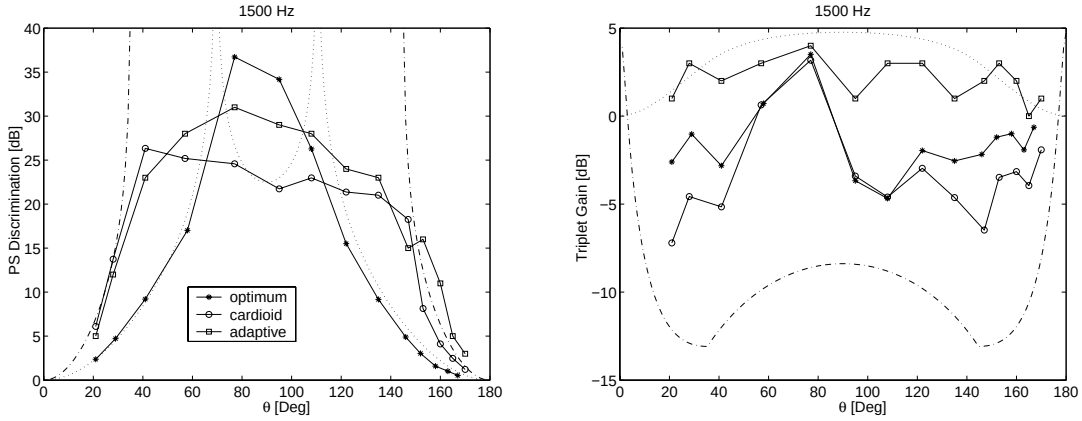


Figure 3-8 *Experimental performance at 1500 Hz. On the left PS rejection is shown versus bearing and on the right triplet gain versus bearing. The theoretical performance for the cardioid beamformer in the actual noise mixture is shown with the dash dot curve. The theoretical performance for the optimum beamformer in the actual noise mixture is shown with the dotted curve.*

In Figure 3-8 the results for 1500 Hz are shown. The rejection of all beamformers near broadside is more or less the same: over 20 dB. For endfire the optimum beamformer performs a little less well. The fact that optimum and cardioid beamformer perform similarly is caused by the fact that the measured value of the parameter σ_m^2 is very close to the singular value σ_∞^2. Since the correlated noise is dominated by tow ship noise during the experiment, the frequency dependence can be explained. At higher frequencies flow noise levels drop faster than tow ship noise, which was also concluded by Beerens (1999). In gain the optimum and cardioid beamformers also perform similarly (the optimum beamformer is only about 1 dB better than the cardioid beamformer). The adaptive beamformer performs almost equal to the cardioid beamformer in PS discrimination and is slightly better in gain than the other beamformers.

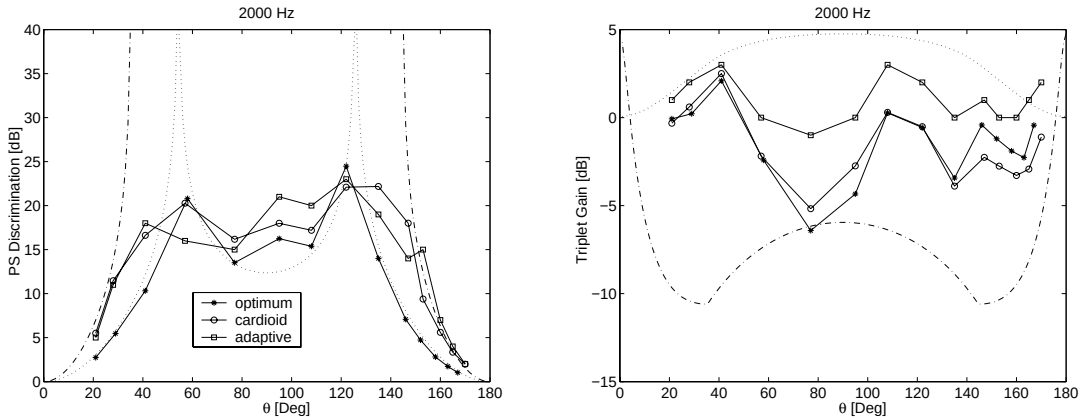


Figure 3-9 *Experimental performance at 2000 Hz. On the left PS rejection is shown versus bearing and on the right triplet gain versus bearing. The theoretical performance for the cardioid beamformer in the actual noise mixture is shown with the dash dot curve. The theoretical performance for the optimum beamformer in the actual noise mixture is shown with the dotted curve.*

In Figure 3-9 the results for 2000 Hz are shown. At still higher frequencies there are even less difference between the PS performances of the beamformers. All three have a PS rejection of

~ 20 dB at broadside. The gain of the adaptive beamformer is the best and is on average 2 dB better than the cardioid beamformer.

3.4.4. Discussion

Sea-trial data in several noise mixtures have been processed with three different triplet beamformers. Results of the experiments show reasonable agreement with theoretical results. The PS discrimination of the optimum beamformers follows the theoretical curves very closely and the gains are well within the theoretical maxima and minima. Of the three beamformers the adaptive beamformer performs the best. Its rejection is close to that of the cardioid beamformer and in cases where the SNR is limiting it performs sometimes even better. The PS discrimination performance of the optimum beamformer is relatively poor, in particular in the case of high flow noise (low frequencies and high tow speeds). This frequency dependence is explained with the varying ratio between wavelength and spacing in the triplets and also because of the varying noise correlation. Especially in gain the adaptive beamformer outperforms the others. The cardioid beamformer has a problem with gain near endfire and in flow noise dominated environments. The optimum beamformer does not suffer from these problems with gain. However, other than its name implies it optimizes only gain against omnidirectional noise, whereas in the real world environments noise is often directional. In such environments the adaptive beamformer performs better in gain.

3.5. Sea trial results in reverberation

Experimental set-up.
During the 1999 NAT II trials the objective was reverberation suppression. The trials have been conducted in the Bay of Biscay at the shelf break near La Coruña. The very steep slope guarantees high reverberation levels, which made this environment difficult. The aim of the experiments was to assess the performance of a triplet array in a reverberation-limited environment. In the trial a state-of-the-art low frequency active sonar was used. This was the TMS CAPTAS V1 (Sawari) system, which consisted of a transducer array with two Free Flooded Rings and a receiving CAPTAS triplet array. Both systems were towed by HNLMS Tydeman. Other platforms involved in the trial were a RNLN Walrus class submarine that served as 'target' and HNLMS Mercuur, which towed an artificial target. The transmitted sweep was a wideband HFM sweep (b = 500 Hz, f = 1500 Hz and T = 4 s).

Discussion of the data results.
In Figure 3-10 typical range-bearing plots of the underwater scene near La Coruña are shown. The three images are the output of the CAPTAS signal processing chain with the three beamformers. The images display acoustic contrast as a function of direction of arrival (bearing) and range. Clearly visible are nearby bottom features and reverberation from the shelf edge at the port side starting at 7 nautical miles. The detection of the submarine is made at $\theta = -90^{o}$ at a range of 7.2 nautical miles. The detection is hardly visible in the three range-bearing plots due to the high reverberation levels (the yellow and red clutter). After zooming, however, it can be found.

The upper panel of Figure 3-10 shows a plot where the optimum beamformer is used. The noise-limited region, present after approximately 9 nautical miles, is merely blue colored. The PS discrimination is rather bad, which in this case leads to a severe degradation of the overall detection performance. The performance degradation is so drastic, because high reverberation levels appear in the noise-limited seaward bearings. The plot shows that this beamformer fails in this environment, which was expected. It is explained with the dominance of coastal reverberation over noise, in the major part of the ping. This is further discussed in the statistical results of the performance indicators.

In the middle panel of Figure 3-10 the output from the cardioid beamformer is shown. The PS discrimination is very good (apart from the nearby bottom features, which come from below rather than from port or starboard). The gain over noise is not so good, which is not clearly visible here, but the noise-limited (blue) region is more blurred than the top image. In the lower panel of Figure 3-10 the adaptive beamformer is used. Here good PS discrimination and sharper contrast in the reverberation can be seen. The reverberation from below (near field bottom reverberation) is suppressed. Especially the performance for the adaptive beamformer near endfire is considerably better than the performance for the other two beamformers.

Nevertheless, it is hard to derive objective and statistically reliable results from the range-bearing plots. To get a better insight into the performance of the three triplet beamformers in reverberation-limited scenarios, several consecutive beampatterns of the target are depicted in a waterfall display in Figure 3-11. A waterfall display is a display in which the acoustic contrast after signal processing is shown versus the vertical axis time and the horizontal axis bearing. The resulting image may be refreshed with new information on the top and shifted downwards, which explains its name. It gives a convenient overview of all analyzed pings and the oldest ping is on the top in this case. During the analyzed experiment, the target moves from the forward bearings to the aft bearings in one hour. The ping repetition time was one minute and every second ping was processed. The target detections are automated and the accompanying target beampatterns are collected. The PS discrimination, side-lobe behavior and captured reverberation are visualized for the entire experiment.

In the upper panel of Figure 3-11 the application of the optimum beamformer is shown. PS discrimination is not very good and, therefore, reverberation (on the starboard side) is unnecessarily high. The middle panel of Figure 3-11 shows the cardioid results in this respect, which are better. However, towards endfire the levels are low, which is a well-known artifact of cardioid beamformers and was explained in Section 3.2.2. The endfire performance is the main problem of cardioid beamforming and should be improved.

The adaptive beamformer is shown in the lower panel of Figure 3-11. The results look very promising. The PS discrimination is high, the reverberation on the port side is low and the endfire region shows some energy.

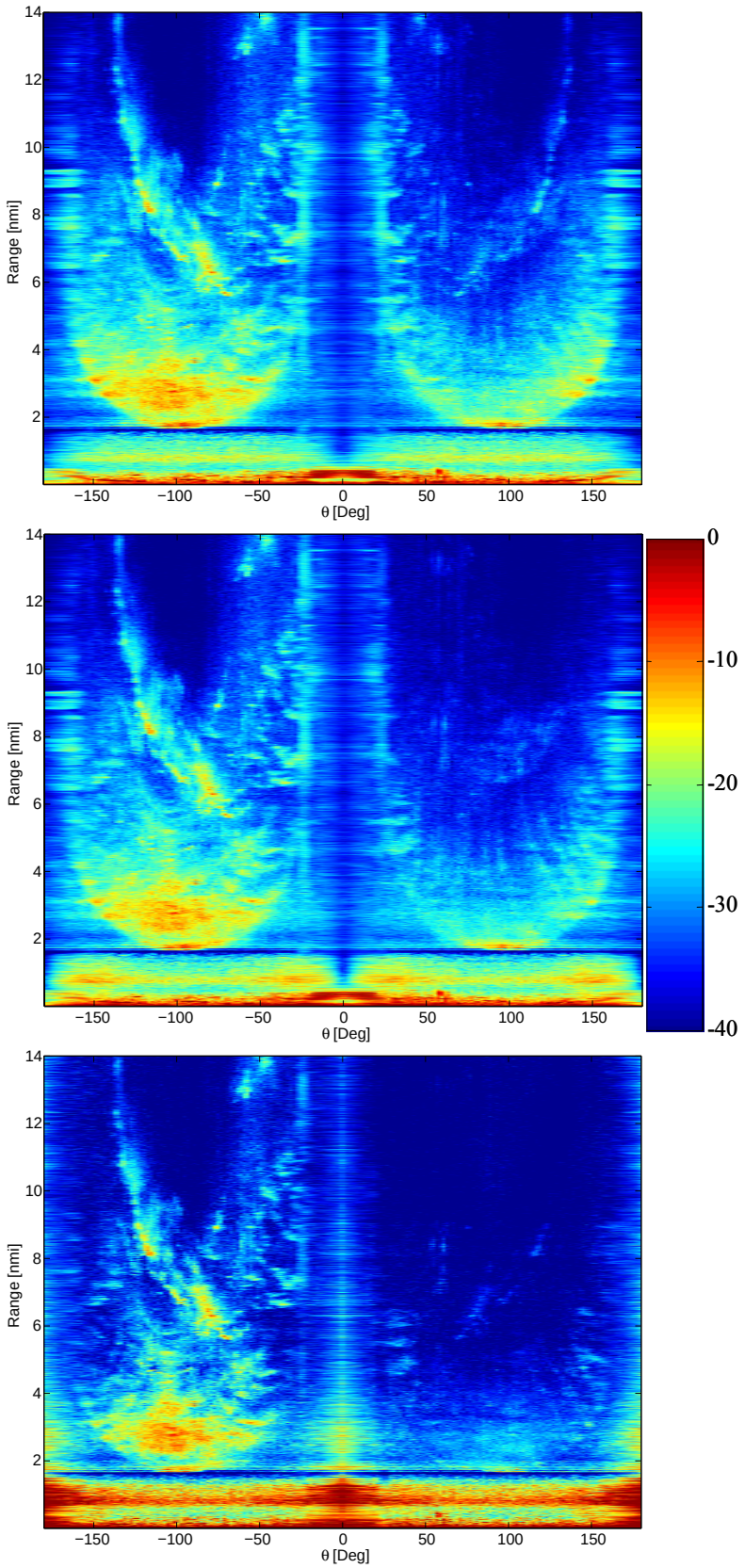


Figure 3-10 *Range-bearing plot of the optimum (top), cardioid (middle) and adaptive (bottom) beamformer. The color coding is based on a dynamic range of 40 dB and red represents the maximum level.*

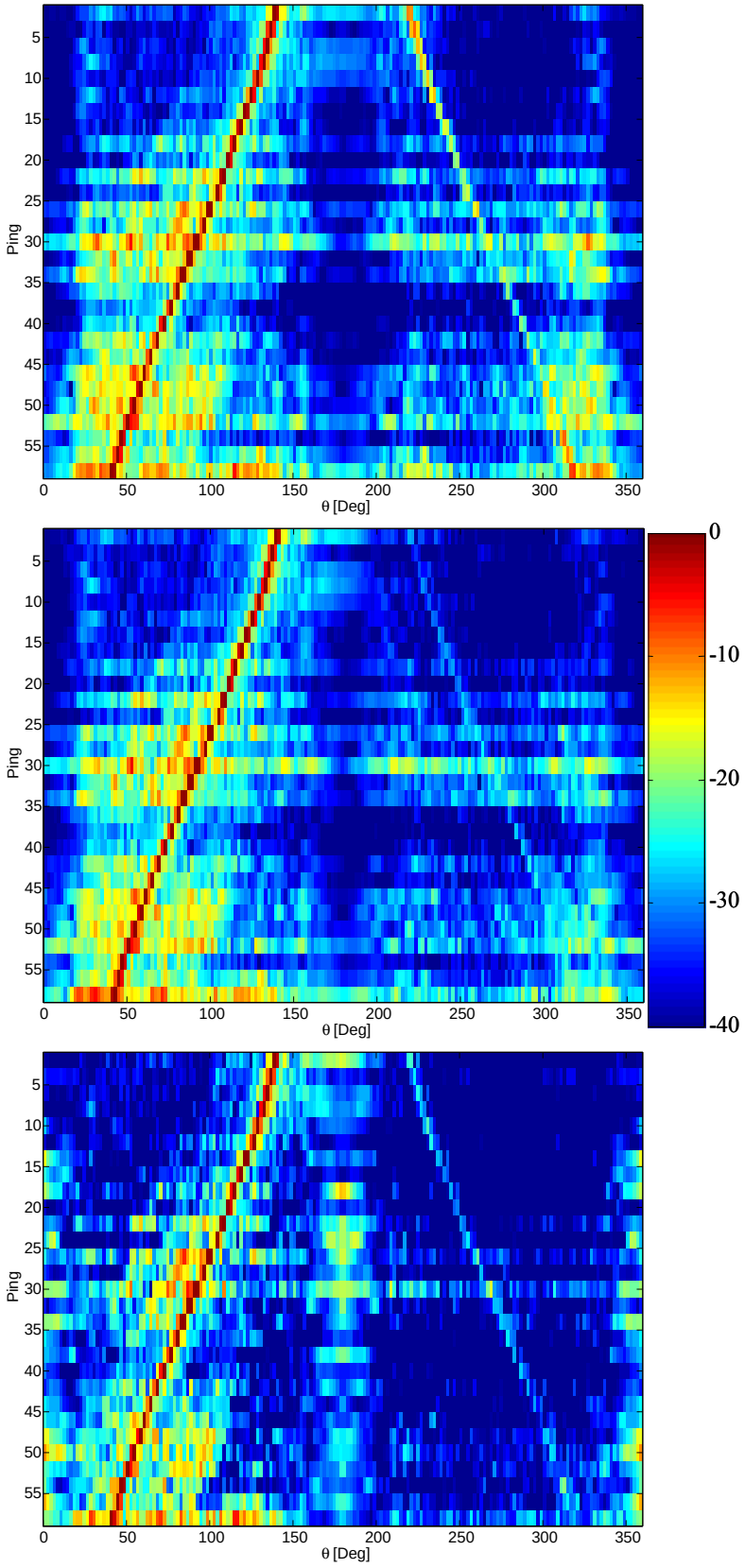


Figure 3-11 *Experimental beampatterns versus ping for application of the optimum (top), cardioid (middle) and adaptive (bottom) to the 9 knots experiment. The color coding is based on a dynamic range of 40 dB and red represents the maximum level.*

The experimental analysis is now concluded with the statistics of the performance indicators of the different beamformers at different tow speeds. Experiments performed at 6, 9, and 12 knots are shown in Figures 3-12 to 3-14. In the left plot the PS discrimination is depicted. The right plot shows the triplet gain, which is now the increase in signal to background ratio, because the scenario is reverberation-limited. The experimental values are shown as stars (*) for the optimum beamformer, circles (o) for the cardioid beamformer and squares (□) for the adaptive beamformer. In the left plot the theoretical formula for PS discrimination of Eq. (3.8) is overlaid. The theoretical formulas for gain are not shown here because they are valid for noise and not for reverberation as background. The correlation in the noise drops with tow speed for these experiments. This is explained with the rising amount of flow noise with tow speed and yields an expected worst performance during the 12 knots experiment.

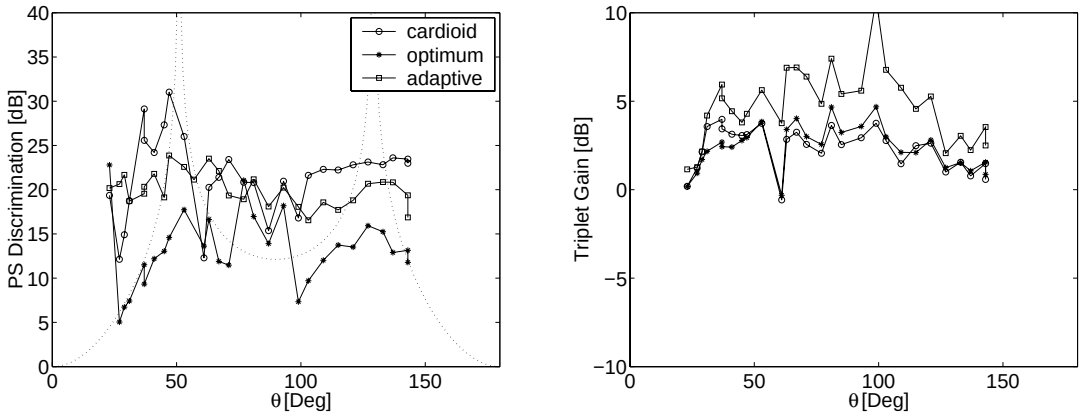


Figure 3-12 *Experimental performance in reverberation with tow speed of 6 knots. On the left PS rejection is shown versus bearing and on the right triplet gain versus bearing.*

Figure 3-12 shows the results of the 6 knots experiment. For all three methods rather high PS discrimination is obtained. Due to the very low flow noise levels, the noise correlation is reasonably high and the cardioid beamformer is close to the optimum beamformer. As both are almost similar and close to the overall optimum, the adaptive beamformer cannot beat the conventional beamformers in this case. The results are reasonably stable; the variation of both performance indicators over bearing is not very high.

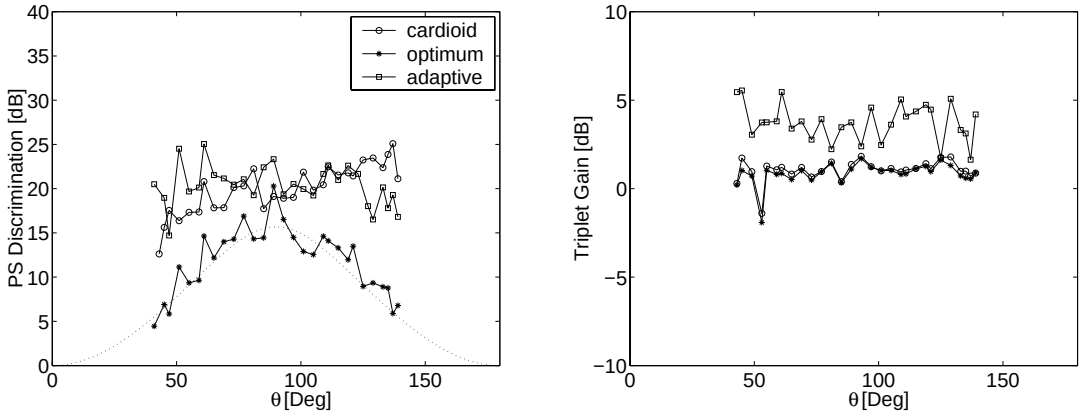


Figure 3-13 *Experimental performance in reverberation with tow speed of 9 knots. On the left PS rejection is shown versus bearing and on the right triplet gain versus bearing.*

Figure 3-13 shows the results of the 9 knots experiment. Due to the increased flow noise the correlation coefficients have dropped, which shows up in the lower PS discrimination of the optimum beamformer. The triplet gain of the adaptive beamformer is about 2 dB higher than the other two beamformers and also stable over the pings (and bearings).

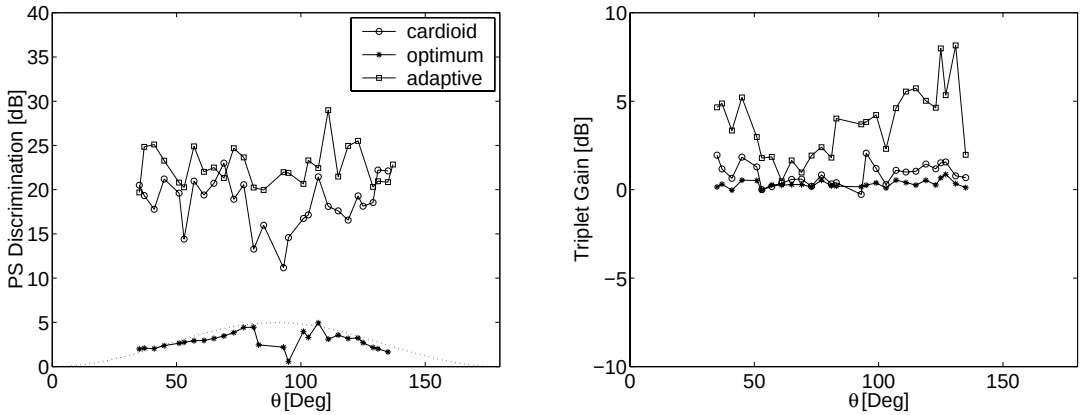


Figure 3-14 *Experimental performance in reverberation with tow speed of 12 knots. On the left PS rejection is shown versus bearing and on the right triplet gain versus bearing.*

Figure 3-14 shows the results of the 12 knots experiment. Flow noise levels now start to degrade performance of the conventional beamformers. The PS discrimination for application of the optimum beamformer has become very low (< 5 dB). The adaptive beamformer gives on average much (about 3 dB) higher triplet gain, but is less stable.

3.6. Conclusion

Detection and rejection performances of triplet beamforming techniques for active sonar in the limit of small diameter to wavelength ratio have been studied both theoretically and experimentally as a function of noise spatial correlation. The theoretical performance evaluation showed that the optimum beamformer does not supply enough PS discrimination and that the cardioid beamformer does not supply enough triplet gain. However, adaptive beamforming but also a mixed version of cardioid and optimum beamforming was shown to operate sufficiently well. Behavior on experimental data sets with different tow speeds, for targets at different bearing, and for sweeps at different frequency is investigated in both noise-and reverberation-limited environments. The final result is that triplet arrays processed with an adaptive triplet beamformer combine high PS discrimination performance with additional array gain in both environments. The PS discrimination reached 25 dB and is sufficient to reject even the most severe coastal reverberation. The additional array gain during the trials varied from 0-5 dB depending on the tow speed and promises better detection performance than equal aperture single arrays. The signal processing chain equipped with appropriate triplet beamforming even gives sufficient results for the upslope bearings, i.e. a small increase in performance with respect tot a linear array. It can be concluded that it is indeed possible to operate a triplet array in a shallow water environment.

4. DOPPLER CORRECTED ARRAY PROCESSING

4.1. Introduction

4.1.1. Background

The considered sonar system family in this chapter and in the previous chapter is the same. It deals with the Low Frequency Active Sonar (LFAS) used for Anti-Submarine Warfare (ASW). For the experimental data analysis, exactly the same system, CAPTAS, has been used. However, as will be shown in the theory and with the simulated results, the problem of Doppler is relevant for a wide range of systems. It is also good to notice the difference between this chapter and its predecessor. In the previous chapter, three single arrays were combined in order to find out whether a signal came from the port or starboard side. This single array beamforming was assumed to give adequate output. In this chapter the not-so-adequate scenarios for the single array beamforming are considered. Port starboard beamforming is a separate process and not regarded in this chapter.

The goal of an LFAS is to detect, localize and classify submarines. The active sound signal is typically generated by a powerful source that operates just below the cavitation threshold. The received data are recorded and are used as the input for the signal processing chain. Matched filtering and beamforming are the two most essential steps in the signal processing, naturally preceded by a pre-processing step to condition the hydrophone input data. The two methods were described in detail in Chapter 2. The processing for active towed array sonars usually gives energy as a function of range, bearing and Doppler velocity as most important result. On these images post-processing can be applied to perform detection, localization or classification automatically, but, at present, a large part of this is still in the hands of the sonar operator. This chapter concentrates on the kernel and leaves out the pre- and post- processing steps.

An LFAS consists of acoustic sources and receivers, which are subject to motion. This motion introduces errors in their expected or assumed positions. Because of these deviations, the output energy is shifted and smeared along the three aforementioned parameters. This chapter is dedicated to the application of Shape and Doppler Corrected Beamforming (SDCB) to tackle the problem of signal deterioration due to position deviations of the towed sonar. The actual problem boils down to processing loss of the towed sonar array due to the assumption that all hydrophones are on a straight line and have the same constant velocity. From experience it is known that in standard straight track operations this assumption is valid. However, when the tow ship makes a turn, the array follows and bends. Depending on several parameters, the effect on the processing result may be severe. Three effects contribute to this: deviation from the straight line, Doppler shift and Doppler spreading.

The topic Shape Corrected Beamforming (SCB) without correction for the Doppler effect is not new and has been investigated and published about, for example by Bouvet (1987) and Felisberto (1978). Both in literature and in operational systems the problem used to be treated in a static way, which will be described in more detail in the following section. The hydrophones were beamformed with a best estimate of their positions. The key problem here was to find the best estimation procedure. The most successful method for these hydrophone position estimates was the application of Kalman filtering on additional non-acoustic sensors, such as heading sensors added to the receiver array. The shape correction has already been investigated in earlier studies by for instance Ballegooijen (1989), Bouvet (1987), Felisberto (1978) and even estimation with the acoustic data themselves was tried by Bucker (1996). The topic that is addressed in this chapter is the application of Shape *and Doppler* Corrected signal processing to tackle the problem of loss in the signal processing during the maneuvers. The problem is processing loss in a towed array sonar due to the assumption that all hydrophones are on a straight line and have the same constant velocity. From experience it is known that in standard straight track operations this assumption is valid. However, when the array turns, this assumption is violated. Depending on several parameters, the effect on the processing result may be severe. Solutions for this degradation due to Doppler shift are accomplished by adapting the signal processing.

The operational survey speed for Anti Submarine Warfare, however, has increased. Moreover, the need for maneuvering with a sonar has increased. The topic Doppler and the combination with the so-called Shape and Doppler Corrected Beamforming have not been analyzed and are new fields of research. Another new feature of this chapter's research is the quantification of the sonar performance loss. These novel features were part of the PhD research. The expressions in this chapter are all novel and part of the PhD research unless a reference is given. The sea trials were attended by the author, but the measurements were accomplished with help from the Royal Netherlands Navy and TNO personnel. The application of the developed beamformers is performed as a part of the PhD research.

Different approaches for the compensation are investigated in order to determine the best treatment of the problem. In advance a clear separation can be made between the position estimation and the compensation. The estimation includes the extraction of hydrophone position and Doppler information from a combination of measurement and model. The requirements for the estimation and for the compensation methods will be discussed. Following the approach of SCB, again, the non-acoustic sensors will be used for the estimation process. The compensation method will affect the beamforming procedure. The analyzed methods have the same goal, but differ in the way of compensating for changes in Doppler shift and position in the signal processing.

4.1.2. Operational aspects

Regions for Anti Submarine Warfare (ASW) operations are more and more focused toward littoral water environments. This has many inconvenient implications for ASW sonar performance, e.g. reverberation, multi-path, reflections from coastlines, etc. It also means more

maneuvering for the tow ship of an ASW sonar. An example of a frigate sailing a turn at high speed is shown in Figure 4-1. In such a turn the towed sonar will typically follow the ship and even slightly cut the corner. This maneuvering causes the receiving array to bend with negative consequences for the array performance.



Figure 4-1 *Typical ASW scenario with a RN frigate in a high-speed turn.*

Negative effects on the processing performance due to Doppler shifts can be separated into two parts. The first effect is the variation of Doppler shift over the hydrophones in the towed array. The effect is caused by the array being bent, so that each hydrophone has a different course. This occurs during maneuvers and may cause problems in the signal processing. It is best explained in the frequency domain. When the signals of different hydrophones suffer from different Doppler shifts, non-corresponding signal frequencies will be combined in the beamforming process. The other effect that is considered is the change in Doppler during the time of transmission and reception of the signal. This implies temporal Doppler variations that cause Doppler spreading, which was already noted in the sixties, described in Kramer (1967) and Kramer (1969). The received signals are distorted and conventional beamforming and matched filtering will not make coherent matching possible, leading to processing losses. However, if the motion of the source and the hydrophones are known, both effects can be compensated for, either in the beamformer or in the matched filter.

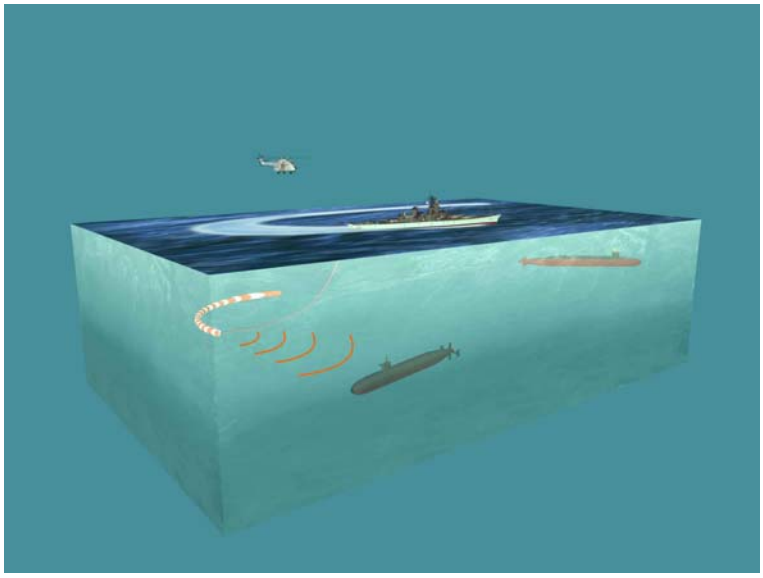


Figure 4-2 *Visualization of negative effects on sonar performance during maneuvers.*

Finally, it has to be noted that the verification of the methods on experimental data is somewhat limited. Although during the trials the system was towed in such a way that the Shape and Doppler deviations were appearing as clear as possible, it can be worse. An operational ASW frigate is able to maneuver much quicker and sharper. Moreover, the CAPTAS array is somewhat shorter than the state-of-the-art operational systems. It would be beneficial to do tests with such harsher scenarios.

4.1.3. Outline

In Section 4.2 a theoretical study is presented, in which the negative effects of shape deviations and Doppler shifts are quantified. The compensating algorithms are developed in Section 4.3. The requirements for the estimation accuracy of the sonar motion are discussed and analyzed in Section 4.4. The algorithms are tested on simulated data in Section 4.5. In 2002 and 2003 sea trial experiments were conducted with a real active target fitted with a locator source, which are discussed in Section 4.6 and 4.7. Final conclusions are given in Section 4.8.

4.2. Theoretical performance in a turn

This section will aim at a theoretical quantification of the performance loss in a turn. The performance loss is clearly dependent on the speed of the ship and the sonar. But also the frequency content and duration of the signal and turn rate will show to play an important role. In this section the performance loss is analyzed with signal energy loss due to the fact that the processing is not fully coherent when a sonar is in the turn. This loss is referred to as the maneuvering loss ML. It is defined by the ratio of signal amplitude in the case analyzed and the signal amplitude in the ideal case. The value of ML is always larger than one and is equals

one when the performance of the ideal case is met. The value of ML given in decibels is never positive, because the case can naturally not outperform the ideal case.

4.2.1. Error sources

A towed array during a turn of the vessel is considered and the effects of deviations on the processing are studied. Compared to a straight array (as assumed in standard processing), two differences can be identified:

1. Differences in hydrophone position (shape deviations);
2. Differences in hydrophone speed (Doppler).

Figure 4-3 shows that when assuming a stationary and straight receiving array, these differences give rise to phase errors in the received signals that may deteriorate the signal processing. Both errors are estimated in the remainder of this section. Parameters that are used throughout this chapter in both simulated and experimental data are chosen such that they correspond to a rough turn during an ASW operation. Without loss of generality the sonar track is assumed to be circular, similar to the approach of Gerstoft (2003). For the geometry a turn radius (R) of 500 m, a tow velocity (V) of 5 m/s and an array length (L) of 24 m is chosen. The acoustic properties are a signal duration (T) of 8 seconds, center frequency (f) of 1500 Hz, a bandwidth of 1000 Hz (100 Hz in the simulations) and a sound speed (c) of 1500 m/s. The transmit waveform is a so-called Hyperbolic Frequency Modulated (HFM) signal, which is described mathematically in Section 4.3.3.

4.2.2. Shape deviations

The general formula for maneuvering loss due to position errors ML_1 can be found by incorporating them in the general expression for the beamformer.

$$\mathrm{ML}_1 = \frac{N_h}{\left| \sum_{n_h=1}^{N_h} e^{\mathrm{i}k\left(\Delta x_h \cos\theta + \Delta y_h \sin\theta\right)} \right|}, \tag{4.1}$$

where θ is the actual bearing defined as in Figure 4-4, k the wavenumber ($2\pi f/c$), n_h the hydrophone index, N_h the number of hydrophones, and the position errors along and across the array, given by $\Delta x_h = n_h d - \frac{L}{2} - R\sin\left(\frac{2n_h d - 2d - L}{2R}\right)$ and $\Delta y_h = R\left[1 - \cos\left(\frac{2n_h d - 2d - L}{2R}\right)\right]$, where d is the hydrophone spacing.

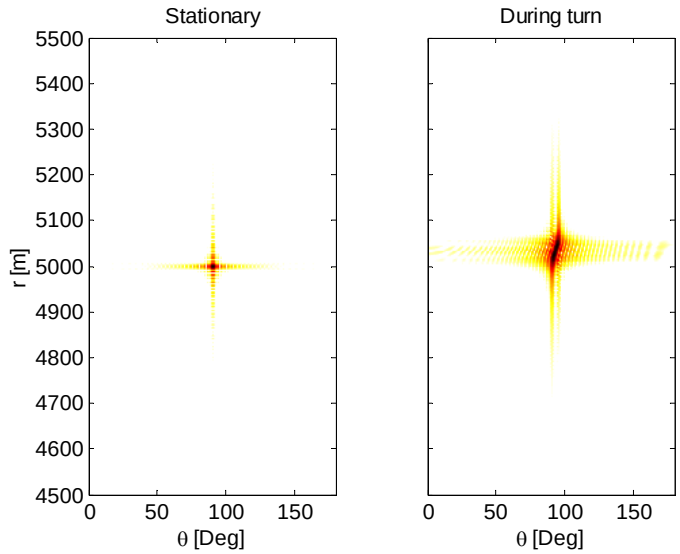


Figure 4-3 *Example of performance loss in a range-bearing plot. The stationary situation is shown on the left and a (non-compensated) turn on the right.*

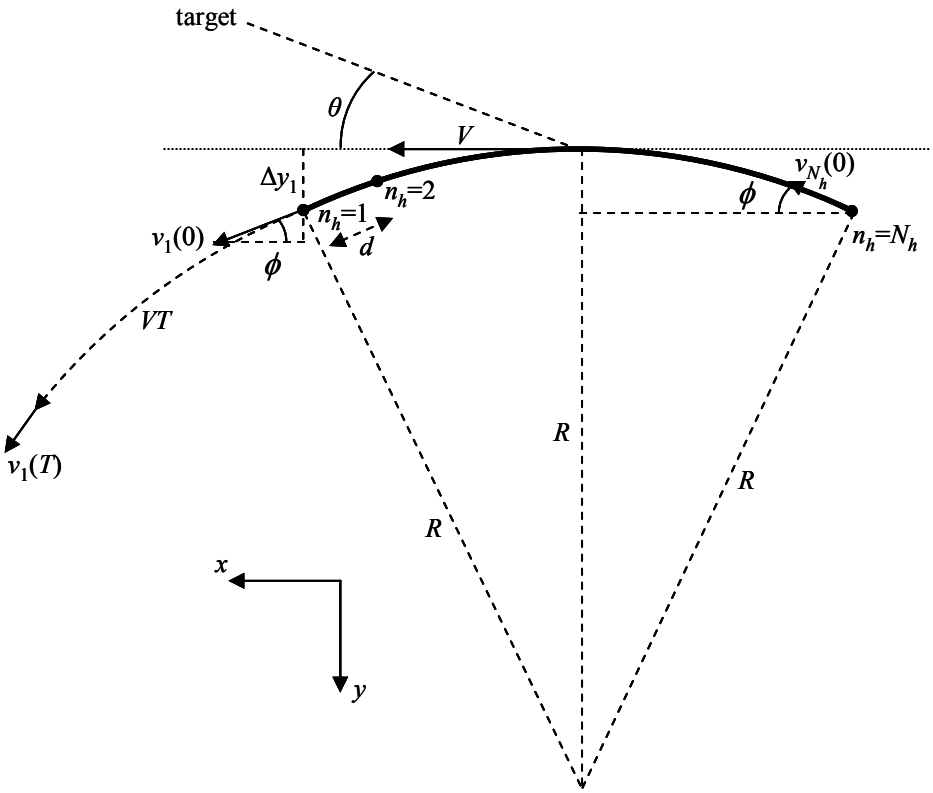


Figure 4-4 *Geometry of array during a turn with exaggerated curvature to point out the physical effects. Velocity and position deviations cause sonar performance degradation.*

To get insight into the physical behavior of the maneuvering loss, an infinitely long array that is covered with an infinitely dense array of hydrophones is considered. The Array Signal Gain

ASG_∞ of such an array is calculated, for the worst-case scenario (θ = 90 °). This means the summation of Eq. (4.1) is replaced by an integral over a variable l that runs over the array:

$$\mathrm{ASG}_\infty = \int_{l=-\infty}^{\infty} e^{\mathrm{i}kR\left[1-\cos\left(\frac{l}{R}\right)\right]}\mathrm{d}l\,, \tag{4.2}$$

The integral can be computed using the stationary phase relation:

$$\int_{-\infty}^{\infty} e^{\mathrm{i}k\xi(l)}\mathrm{d}l = \sqrt{\frac{2\pi}{k\left[\frac{\partial^2\xi}{\partial l^2}\right]_{l=l_0}}}e^{\mathrm{i}k\xi(l_0)}$$

with

$$\left[\frac{\partial\xi}{\partial l}\right]_{l=l_0} = 0 \,, \tag{4.3}$$

where the derivative at l_0 is given by $\sin(l_0/R)$, which easily translates into l_0 = ..., $-2\pi R$, πR, 0, πR,... Inserting one of these values of l_0 yields:

$$\mathrm{ASG}_\infty = \sqrt{\frac{2\pi R}{k\sin\frac{l_0}{R}}}e^{\mathrm{i}kR\left(1-\cos\frac{l_0}{R}\right)} = \sqrt{\lambda R}\,, \tag{4.4}$$

where $\lambda = c/f$ is the wavelength. Thus the array signal gain of an infinite circularly curved array is simply given by $\sqrt{\lambda R}$. An array of length L would give an array signal gain of L in the ideal case. This means that as soon as L becomes greater than $\sqrt{\lambda R}$, the maneuvering loss due to bending of the array, for $\theta = 90^\mathrm{o}$, is given by:

$$\mathrm{ML}_{1,\max} = \frac{L}{\sqrt{\lambda R}}\,. \tag{4.5}$$

The phase error with respect to the ideal straight array at the position along the array equal to $l = \frac{\sqrt{\lambda R}}{2}$, is given by:

$$kR\left(1-\cos\frac{l}{2R}\right) = \frac{2\pi R}{\lambda}\left(1-\cos\frac{\sqrt{\lambda R}}{2R}\right) = \frac{2\pi R}{\lambda}\left(1-\cos\sqrt{\frac{\lambda}{4R}}\right) \approx \frac{\pi}{4}\,. \tag{4.6}$$

This means that the phase at the end of an array of length $\sqrt{\lambda R}$ differs $\pi/4$ with the centre of the array. It can be argued that a hydrophone does not contribute to the array signal gain when

the phase difference is higher than this figure. It can be seen in Eq. (4.5) that the array length strongly influences the maneuvering loss ML_1. The maneuvering loss ML_1 is shown in Figure 4-5 versus operational array lengths and radii of curvature. The image represents the loss, which means that close to 0 dB, i.e. the white zone, one is in the zone of relatively good performance. It can be verified that the loss in a turn is negligible in most cases. Only for long arrays and very sharp turns compensation for this effect is necessary. The TNO-FEL Combined Active and Passive Towed Array System (CAPTAS) 32λ-array, which was used for collecting experimental data for this chapter, can be analyzed by looking at the surrounding area of the upper black cross. A 64λ -array, an operational system built by Thales Underwater Systems and currently in use by the Royal Norwegian Navy, can be analyzed by looking at the lower black cross/white circle. For arrays of such aperture ML_1 may become significant and even dominant.

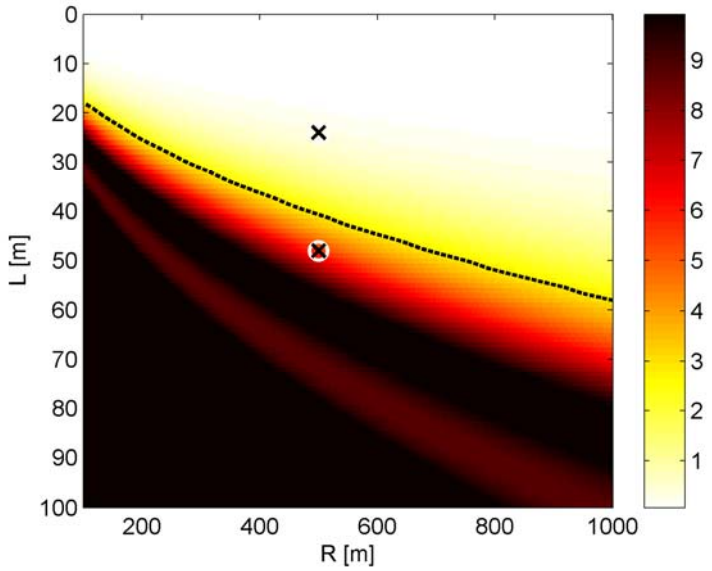


Figure 4-5 *Expected loss due to shape deviations (ML_1) on a decibel color scale. The dashed line represents the contour for a loss of 3 dB.*

4.2.3. Doppler shift

When a ship is towing a receiving array during a turn, specific Doppler effects arise. These Doppler effects generally manifest themselves in two different, separable ways:

1. Doppler shift: the Doppler shift changes with hydrophone
2. Doppler spreading: the Doppler changes with time

In this section the first effect is discussed and in the following section the second effect is discussed.

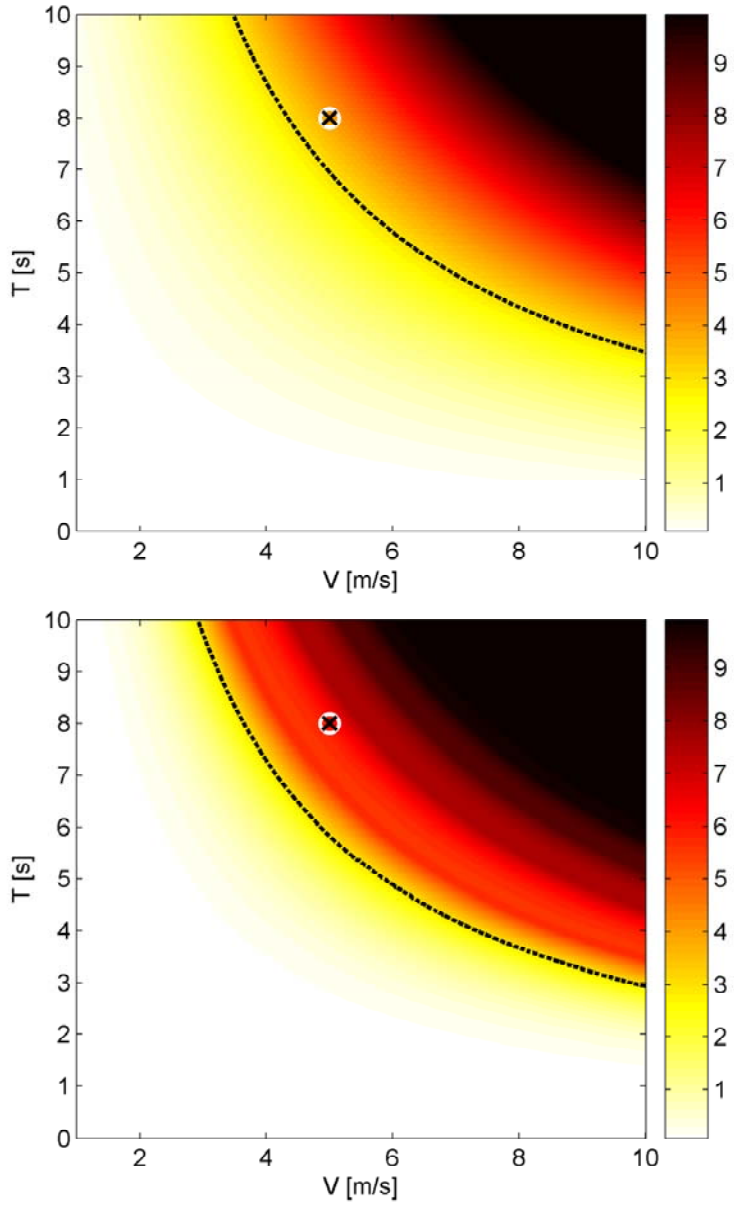


Figure 4-6 *Expected maneuvering loss due to changes in Doppler shift imaged on a logarithmic color scale. The top panel shows the Doppler shift effect (ML_2) and the bottom panel shows the Doppler spreading effect (ML_3). The dashed line represents a loss of 3 dB.*

The Doppler shift results in different frequency shifts according to the position and speed of the array. For a curved array that is positioned along a part of a circle, the velocity for the first and the last hydrophone is given by:

$$\mathbf{v}_1 = \begin{bmatrix} V\cos\phi \\ V\sin\phi \end{bmatrix} \text{ and } \mathbf{v}_{N_h} = \begin{bmatrix} V\cos\phi \\ -V\sin\phi \end{bmatrix} \text{ respectively,} \tag{4.7}$$

where for small angles $\phi \approx L/2R$. The maneuvering loss can be calculated by the integration of the loss terms per hydrophone. For this, first the frequency content is accounted for. This

loss per hydrophone can be calculated analytically by incorporating the frequency response $\sigma(\alpha, f, T) = \mathrm{sinc}(\pi f T(1\text{-}\alpha))$ of the one frequency signal. A signal with constant frequency f of duration T has a certain width when transformed to the frequency domain. When the Doppler shift is larger than this width, there is no coherence left. The acoustic energy will then fall in a completely different frequency bin. The second part accounts for the phase differences $\Delta\omega$ caused by the Doppler shifts, which are inserted into the exponential of the beamforming operation. The resulting contribution of each hydrophone is given by $\sigma(\alpha,f,T)e^{i\Delta\omega}$. The total loss due to Doppler shift ML_2 can then be written as the sum over the hydrophones:

$$\mathrm{ML}_2 = \frac{N_h}{\left| \sum_{n_h=1}^{N_h} e^{\mathrm{i}k\left(n_h d - 2d - \frac{L}{2}\right)\cos\theta(1-\alpha)} \sigma(\alpha, f, T) \right|}, \tag{4.8}$$

where α is the (target-receiver) Doppler compression factor given by:

$$\alpha = \frac{c + \mathbf{v}_h^{\mathrm{T}} \begin{pmatrix} \cos\theta \\ \sin\theta \end{pmatrix}}{c} = 1 - \frac{V}{c} \begin{pmatrix} \cos\dfrac{2n_h d - 2d - L}{2R} & \sin\dfrac{2n_h d - 2d - L}{2R} \end{pmatrix} \begin{pmatrix} \cos\theta \\ \sin\theta \end{pmatrix}, \tag{4.9}$$

where $\mathbf{v}_h$ is the velocity vector of hydrophone n_h. This vector is projected in the direction of bearing θ. Eq. (4.8) is depicted in the top panel of Figure 4-6 in decibels, for the CAPTAS system. The worst-case scenario for Doppler shift occurs at broadside. In the case that $R>>L$, a simplified analytic formula for $ML_{2,\max}$ can be derived. The maximum Doppler velocity difference for this angle is then well approximated by $VL/2R$. The hydrophone velocities at the far end of the array cause a Doppler shift of the signal, which for $\theta = 90^{\mathrm{o}}$ becomes:

$$\Delta f_{\mathrm{shift}} = VL / 2\lambda R. \tag{4.10}$$

It should be sufficiently smaller than the actual frequency resolution, which is:

$$\Delta f_{\mathrm{bin}} = 1/2T. \tag{4.11}$$

With Eq. (4.6) the length, which, when exceeded, results in hydrophones that no longer contribute to coherent beamforming. The length where the phase is stable is equal to $\lambda R/VT$. The maximum loss caused by Doppler shift is calculated by the ratio of L and this value:

$$\mathrm{ML}_{2,\max} = \frac{VLT}{\lambda R}. \tag{4.12}$$

4.2.4. Doppler spreading

The second effect comes from the moving hydrophones during the reception of the signals. This results in a frequency spreading in the hydrophone signals. To calculate the magnitude of

the effects, the scenario in Figure 4-4 is considered in order to further derive the theoretical formulae for these loss terms. Doppler spreading is caused by acceleration of the sonar and was analyzed by Kramer (1967) and Kramer (1969). If the Doppler shift is changing during the signal duration such an effect appears. To calculate the magnitude of this effect the scenario from Figure 4-4 is considered again. The maneuvering loss ML_3 is somewhat more complicated. Because of the non-stationary situation an integral over time t is calculated:

$$\mathrm{ML}_3 = \frac{T}{\left| \int_{-\frac{T}{2}}^{\frac{T}{2}} e^{\mathrm{i}\omega[1-\alpha(t)]t} \mathrm{d}t \right|}. \tag{4.13}$$

where $\alpha(t)$ is the Doppler compression factor and $\omega = 2\pi f$ is the angular frequency. The formula is evaluated on a computer by discretization of the integral. The result is shown in the bottom panel of Figure 4-6. Note that for this Doppler effect, it is important whether the system is active or passive. For passive sonars only Doppler effects due to velocity difference between receiver and target arise. For active sonar the Doppler effects that arise due to the velocity differences between source and target have to be considered in addition. The passive (one way) Doppler compression formula is given by Eq. (4.9) and the active formula by:

$$\alpha_{\text{active}}(t) = \frac{c - \mathbf{v}_h^{\mathrm{T}}(t)\begin{pmatrix}\cos\theta\\ \sin\theta\end{pmatrix}}{c + \mathbf{v}_h^{\mathrm{T}}(t)\begin{pmatrix}\cos\theta\\ \sin\theta\end{pmatrix}} = \frac{c\alpha(t)}{c - V\left[\cos\left(\frac{2Vt-T}{2R}\right) \quad \sin\left(\frac{2Vt-T}{2R}\right)\right]\cdot\begin{bmatrix}\cos\theta\\ \sin\theta\end{bmatrix}}, \tag{4.14}$$

where it is assumed that the source moves along the same curve during transmission as the hydrophone moves during reception. The worst-case hydrophone can also investigated with analytical formulae. This hydrophone is the one that is at the closest point of approach in the middle of the signal reception. Its velocity is given by:

$$\mathbf{v}(t) = \begin{bmatrix} V\cos(-\phi + Vt/R) \\ V\sin(-\phi + Vt/R) \end{bmatrix}. \tag{4.15}$$

Again, with the approximation $R>>L$, and for the worst case scenario, $\phi = VT / 2R$. The spreading in this case is well approximated by the velocity at $t = 0$ and $t = T$ (at broadside): $\mathbf{v}(0) = \begin{bmatrix} V\cos(-VT/2R) \\ V\sin(-VT/2R) \end{bmatrix}$ and $\mathbf{v}(T) = \begin{bmatrix} V\cos(VT/2R) \\ V\sin(VT/2R) \end{bmatrix}$. It has been shown that a signal with constant frequency undergoes a frequency shift when it arrives at a moving sonar. When the velocity vector of the sonar is not stationary during reception of the signal, the Doppler shift is not stationary either. It becomes a band of Doppler shifts, defined as the Doppler spreading. The corresponding speed difference that contributes to this Doppler spreading is given by $\Delta V = V^2T / R$. Such a speed difference causes a Doppler spreading of the signal that is given by:

$$\Delta f_{\text{spreading}} = V^2T / \lambda R. \tag{4.16}$$

Since it should be small compared to the actual frequency resolution of Eq. (4.11), an analytic formula for the worst-case scenario can be derived once more:

$$\mathrm{ML}_{3,\max} = \frac{2V^2T^2}{\lambda R}. \tag{4.17}$$

The Doppler shift effect in Eq. (4.12) showed a similar formula, the difference between the two effects being a factor L / VT. It should be noted that the Doppler spreading does not depend on the array length L. It is easily derived now that acceleration becomes dominant during a turn if more than an array length is sailed during the pulse duration. Note that in many operational scenarios the Doppler effects in Figure 4-6 are larger than the effects of shape deviations in Figure 4-5. Compensating for shape only does not seem adequate.

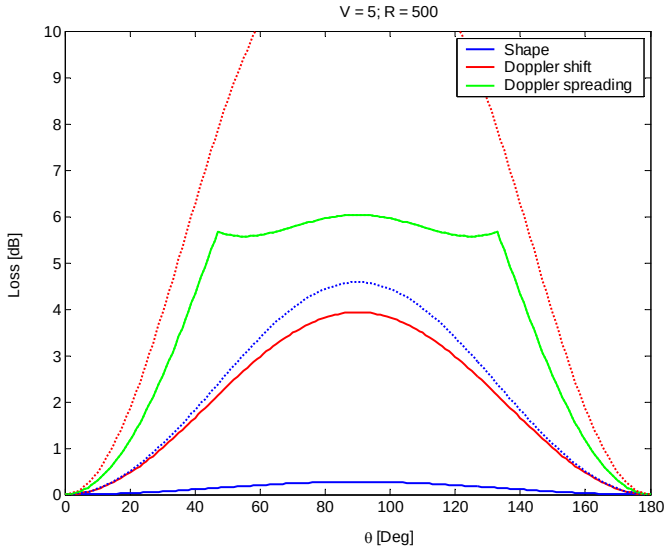


Figure 4-7 *Maneuvering loss as a consequence of shape deviations (blue), Doppler shift (red) and Doppler spreading (green) versus bearing for two LFAS arrays with a center frequency of 1500 Hz: 32λ (CAPTAS; solid lines) and 64λ (dotted lines). The tow speed V = 5 m/s and the radius of curvature R is 500 m.*

As a final exercise in Figure 4-7 all three terms of the Maneuvering Loss (ML) are plotted versus bearing. The first thing to notice is that for all three effects the loss is close to zero at endfire, and increases towards broadside. When the array is longer, the shape and Doppler shift effects are higher. The difference is so large that the Doppler shift effect becomes the dominant factor for a 64λ array in a turn. It shows again that the shape deviation loss is not important for the experimental CAPTAS array. The dashed green curve is not visible, because Doppler spreading is the same for both the CAPTAS and the 64λ array.

4.3. Compensation methods

This section describes the signal processing chain that is used for the experimental data analysis. The conventional parts of the chain will be replaced by more advanced Shape and Doppler compensation algorithms.

4.3.1. Signal processing chain

The beamforming is part of the signal processing. The structure of the signal processing chain is described in this section.

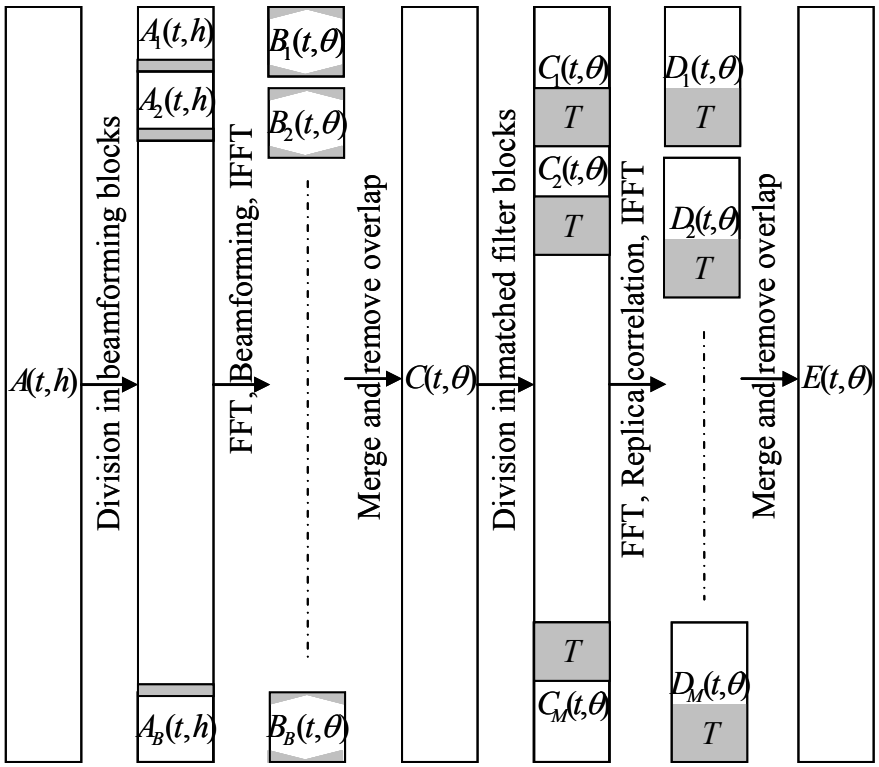


Figure 4-8 *Flow chart of the LFAS signal processing chain.*

Figure 4-8 shows that the process from acoustic data matrix to range-bearing image is a complex sequence of algorithms. The data received on the hydrophones are cut in time blocks. Division in data blocks is necessary in at least two stages in the processing, viz. the beamforming and the matched filtering. Typically, the beamforming blocks are much smaller than the matched filter blocks. The update rate of the beamforming is on the order of 10 Hz. The update rate of the matched filter is on the order of 1 Hz, but dependent on the signal duration. The processing chain starts with a matrix **A**, which represents the digitized hydrophone data of one ping. This matrix is divided into beamforming blocks $\mathbf{A_1}$ to $\mathbf{A_B}$. The update rate of this process is a tunable parameter. Subsequent blocks overlap slightly in time, because in the beamforming a time shift is applied to the data.

The next step is the beamforming of the data blocks, which is performed in the frequency domain. The overlapping data parts due to time shifting are shown in gray. At endfire the time shifts are larger and therefore a larger part of the beamformed data becomes invalid. Because the invalid parts are accounted for in advance, it is possible to glue them into a new large matrix, which represents the beamformed data of a ping **C**. The matched filter correlates the data with the replica signals in order to get the appropriate range resolution as described in Chapter 2. A similar procedure is now applied for the matched filter. The matrix **C** is divided into matched filter blocks $\mathbf{C_1}$ to $\mathbf{C_M}$. The blocks again overlap and the overlap size is equal to the pulse duration T. The update rate is again a tunable parameter and is equal to the reciprocal of the block size minus T. It is computationally attractive to keep the update rate as low as possible. The matched filtering is also performed in the frequency domain by means of multiplication with a replica signal. After cutting off the last T seconds the blocks are combined in the range-bearing data matrix **E**.

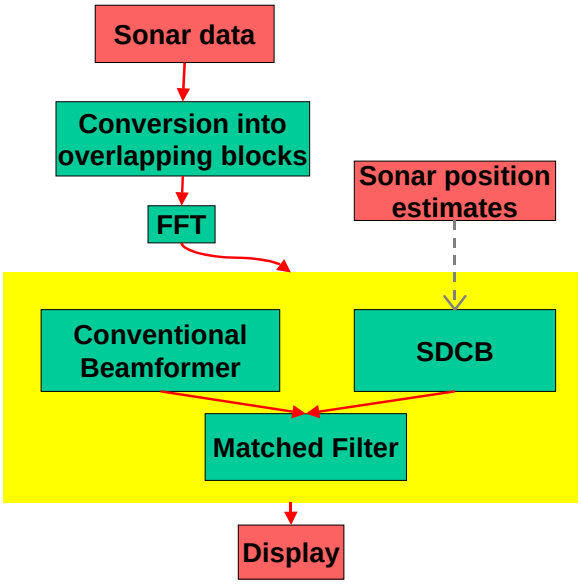


Figure 4-9 *LFAS signal processing chain.*

To summarize the complex structure, Figure 4-9 shows a simpler representation of the structure of the processing chain. The Doppler compensation is to be performed in the large block including the beamformer and the matched filter. After the beamforming and matched filtering, acoustic data as a function of range and bearing are sent to a display.

Beamforming is based on coherent summation of the received signal for their corresponding direction of arrival. This coherence is achieved with appropriate delay of the hydrophone signals. In beamforming, delay times between different hydrophones are compensated for. Delay times are phase shifts in a frequency domain approach. Beam, hydrophone and frequency dependent phase shifts are applied to the acoustic pressure P, which is a function of frequency f and hydrophone n_h.

$$Y(f,\theta) = \sum_{n_h=1}^{N_h} e^{-2\pi i f \Delta t_h(\theta)} P_h(f), \tag{4.18}$$

where the delay time is Δt, N_h is the number of hydrophones, θ is the beam and the output is the beamformed data steered in the direction of θ denoted by Y. The delay time depends on the hydrophone spacing d and the considered beam θ and the sound speed c. In this formula, normally, plane waves are assumed to arrive at an equidistant straight array that does not move during the time of the beamforming block. If the shape and attitude of the array is taken into account in the beamforming, the only variable that changes is the delay time for the hydrophone signal Δt_h. This compensation for sonar position is commonly known as Shape Corrected Beamforming; see e.g. Gerstoft (2003). For the considered scenario settings in this chapter, which are high-speed (10 kts) sharp (500 m radius) turns, SCB only solves a small part of the problem. A larger problem is Doppler variations that degrade the performance much more than shape/attitude deviations. These Doppler variations between hydrophones and over time can also be compensated for in the beamformer. This is the point where SDCB comes in. Although the theory is simple, implementation and use is not trivial. A lot of book-keeping is involved and the size of the beamforming blocks becomes crucial. Simulations have shown that a badly chosen update rate for the beamforming blocks results in the appearance of alias lobes in range; see Groen (2004).

During the investigation and development, many compensation methods were investigated. In this chapter three satisfactory algorithms are proposed, labeled with a number as follows:

1. Shape corrected beamforming
2. Stabilized beamforming and dynamic matched filtering
3. Shape and Doppler corrected beamforming (SDCB).

This was not a random choice. In this chapter, the effect of Doppler is analyzed, and therefore shape corrected beamforming was selected as the basis method. The third method, SDCB, compensates for all errors as long as the update rate is high enough. In Section 4.5, nevertheless, it is shown that the performance of Method 3 is equal to Method 2. Method 2, which leads to a minor change in the beamforming and the matched filter, has proved to be a good candidate for actual operational implementation.

4.3.2. Method 1: Shape corrected beamforming

When proposing different signal processing methods it is important to define a default method first, which in this case is shape corrected beamforming. This method is used as reference, when the sonar performance is measured. For shape corrected beamforming the shape and attitude of the array has to be known and accounted for in the beamformer. Normally, beamforming is performed on frequency domain data as already suggested in Eq. (4.18). When the shape and attitude of the array is taken into account in the beamforming, the delay time Δt is calculated with:

$$\Delta t_h(\theta) = \frac{\Delta x_h \cos\theta + \Delta y_h \sin\theta}{c}, \tag{4.19}$$

where the hydrophone positions are given by (x_h,y_h), $\Delta x_h = x_h - \bar{x}_h$ and $\Delta y_h = y_h - \bar{y}_h$. The beamforming is performed relative to a reference point, which is preferably the middle of the

array. It is here denoted by the mean position $(\bar{x}_h, \bar{y}_h)$. For the scenarios considered the output of this method is similar to conventional beamformer with the straight array assumption, which is in agreement with the previous section.

4.3.3. Method 2: Stabilized beamforming and dynamic matched filtering

The stabilized shape corrected beamformer is a Shape Corrected Beamformer with Doppler correction. Figure 4-1 clearly shows that the spreading manifests itself in both range and bearing. This method, Method 2, separates the two smearing problems and solves the bearing spreading with an adaptation in the beamformer and the range spreading with an adaptation in the matched filter.

The output of the beamformer is relative to North instead of the array heading. The assumption is that the array is rotating around its own center according to the measured motion. This method has the advantage that the existing processing chain only needs a small adaptation. The disadvantage is the fact that the Doppler effects are only compensated for partly, only in the bearing direction and not in the range direction. The formula for the beamforming is given in Eq. (4.18) and the delay time is now calculated with:

$$\Delta t_h(\theta) = \frac{1}{c}\begin{pmatrix}\Delta x_h & \Delta y_h\end{pmatrix}\begin{bmatrix}\cos\left(\theta - \operatorname{atan}\dfrac{\Delta y_h}{\Delta x_h}\right)\\ \sin\left(\theta - \operatorname{atan}\dfrac{\Delta y_h}{\Delta x_h}\right)\end{bmatrix}. \tag{4.20}$$

where the hydrophone positions are given by (x_h, y_h), $\Delta x_h = x_h - \bar{x}_h$ and $\Delta y_h = y_h - \bar{y}_h$. The vector $\begin{bmatrix}\cos\left(\theta - \operatorname{atan}\dfrac{\Delta y_h}{\Delta x_h}\right) & \sin\left(\theta - \operatorname{atan}\dfrac{\Delta y_h}{\Delta x_h}\right)\end{bmatrix}^{\mathrm{T}}$ represents the steering vector relative to North. When a true North display is used, the beamforming is automatically adapted to rotation of the array. This method is easy to implement and does not cost any additional computation time. The beamformer compensates the error in the bearing direction, but not in the range direction. This is due to the fact that the beamformer is a spatial operation on a time block of data, in which the signal travel times are assumed to be constant and only dependent on the angle. However, it is possible to correct for this remaining error in the matched filtering. The replica that is used in the matched filter is not the transmitted signal, but a bearing and time dependent adaptation of this, namely the expected received signal. The HFM signal is commonly used in LFAS systems and is defined by:

$$p(t) = \cos\left[\frac{2\pi T\left(f + b/2\right)}{b\left(f - b/2\right)}\ln\left(1 - \frac{b}{T\left(f + b/2\right)}t\right)\right]. \tag{4.21}$$

When this signal is transmitted from a moving source, reflected by a target and received by a moving hydrophone, the response will be somewhat altered. Doppler effects will influence the received signal. The instantaneous Doppler is calculated from the tracks of source, receiver and target. The received signal is affected as if it were compressed or dispersed according to its instantaneous Doppler shift. The method is now based on this time dependent Doppler compression/dispersion on the discretized replica that is used in the matched filter. The replica is normally sampled with sample frequency f_s, which is the same as the sonar sample frequency. The Doppler effects are now compensated for by compression/dispersion of the time grid, i.e. as if the sample frequency is no longer constant. This means that for the new replica the discretization of the time $t_i = \sum_{k=1}^{i-1} \frac{1}{f_s}$ is replaced by $t_i = \sum_{k=1}^{i-1} \frac{\alpha(t_k)}{f_s}$, where α is instantaneous Doppler compression factor calculated with Eq. (4.9) or (4.14). The implications of the use of such distortion in a replica signal are discussed in detail in Appendix B.

4.3.4. Method 3: Shape and Doppler corrected beamforming (SDCB)

In this section the most general solution for the beamformer is discussed and tested. The approach is based on dividing the ping in short time data blocks, which are all processed and combined in an ideal sense. For each data block the hydrophones have their own positions. In the beamformer these positions are processed correctly, which yields that Doppler shift, Doppler spreading and smearing in the beams is compensated for. These parameters are clearly still limited by the update rate. When the update rate is too low, the spreading is not compensated for. On the other hand, the allowed computational load limits the update rate. In practice the beamformer works like the stabilized beamformer, but with a fixed reference point. The positions belonging to the beamforming blocks are input to the beamformer. The reference point for the beamforming is the middle of the array at the first beamforming block. All the next blocks are properly phase shifted to this reference point, which implies compensation for all motion. If the x and y-coordinates are based on latitude and longitude, the beamforming is implicitly relative to true North. The beamformer is a Shape Corrected Beamformer with correction for all Doppler. The array can move along an arbitrary track as long as it is known. Computational efforts do not increase, because only the delay times have to be updated as in Eq. (4.20). The used formula for the beamforming is as in Eq. (4.18). The delay times are now based on a reference point (x_0,y_0), which is the same for all the beamforming blocks of the ping and are calculated with:

$$\Delta t_h(\theta) = \frac{[x_h(t) - x_0]\cos\theta + [y_h(t) - y_0]\sin\theta}{c}, \tag{4.22}$$

where the hydrophone positions are given by $[x_h(t), y_h(t)]$. A disadvantage of this method that will show in Section 4.5, is the high update-rate required, because all Doppler problems have to be solved within the beamforming.

4.4. Required sonar track accuracy

Application of the described methods requires an estimation or measurement of the sonar track. It is important to know the requirements in order to be able to adapt the system to them. Assuming a circular track, the requirements can be calculated as a function of speed inaccuracy ε_V and inaccuracy in curvature radius ε_R. Eqs. (4.1), (4.8) and (4.13) can be used to calculate the three loss terms at certain velocity V and curvature radius R. Summing these three terms yields a value for the sensitivity of the Shape and Doppler corrected beamforming. Figure 4-10 shows the Maneuvering Loss after correction versus the inaccuracy in radius of curvature ε_R and velocity ε_V for the CAPTAS system. The three terms are shown separately in panel a, b and c and the total in panel d.

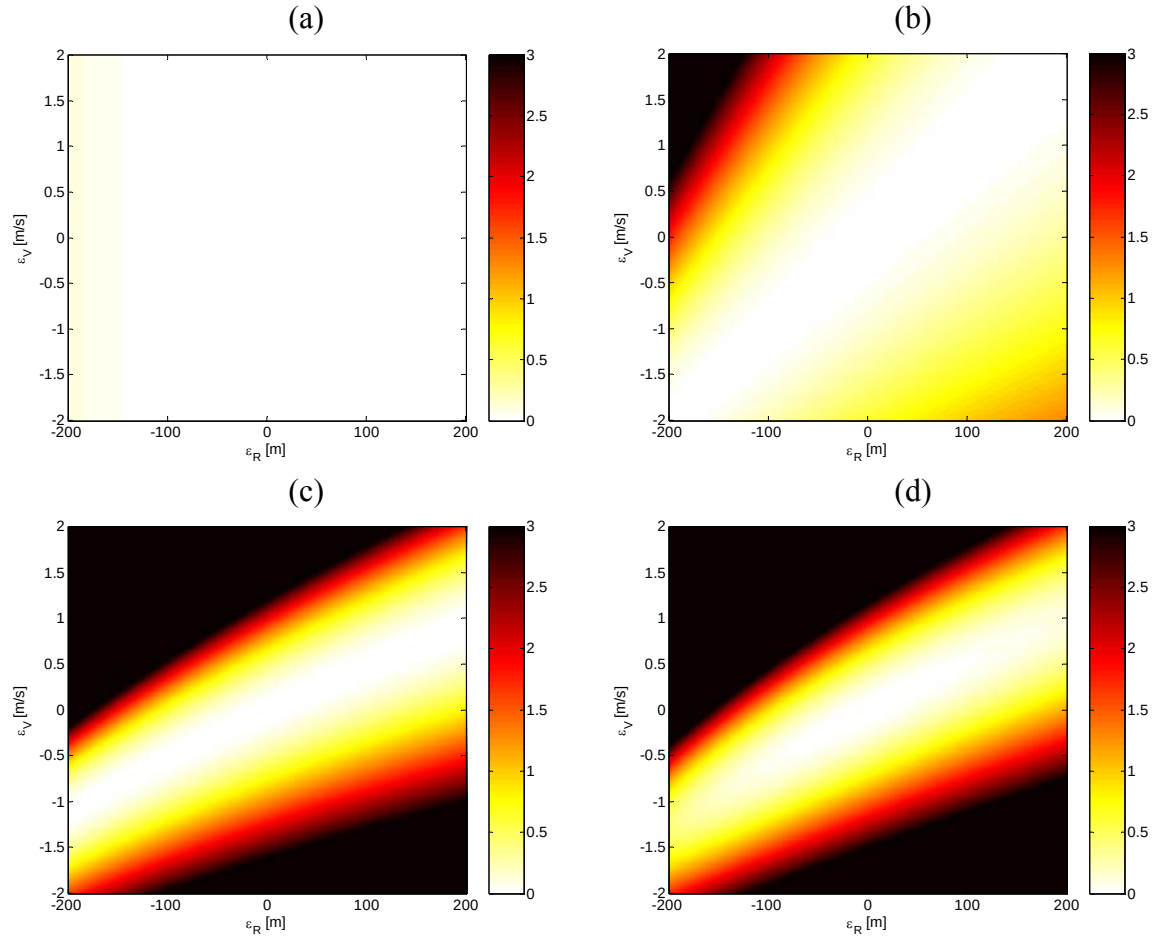


Figure 4-10 *Sonar performance sensitivity in a turn versus speed estimation inaccuracy ε_V and radius of curvature estimation inaccuracy ε_R with: (a) Shape deviation loss, (b) Doppler shift, (c) Doppler spreading, (d) Total loss. The result is calculated for a frequency of 1500 Hz, a turn radius of 500 m, a speed of 5 m/s and the settings of the 32λ CAPTAS array.*

Figure 4-10 shows the sensitivity of the performance versus ε_V and radius of curvature estimation inaccuracy ε_R. Panel a shows that the sensitivity for the shape deviation effect is negligible. Panel b shows the Doppler shift sensitivity is important and the Doppler spreading in panel c is even more important. It shows in panel d, the overall sensitivity, that the velocity

has to be known with an accuracy of about 1 meter per second and radius of curvature with an accuracy of about 100 meters. The sensitivity is not symmetric; it is better to estimate the velocity too low and the radius of curvature too large.

For the standard scenario, as described in Section 4.2.1, these formulae result in the images of Figure 4-10. In addition to this analysis, it is interesting to know what happens if the array is longer. A double length array is investigated similarly, which is depicted in Figure 4-11.

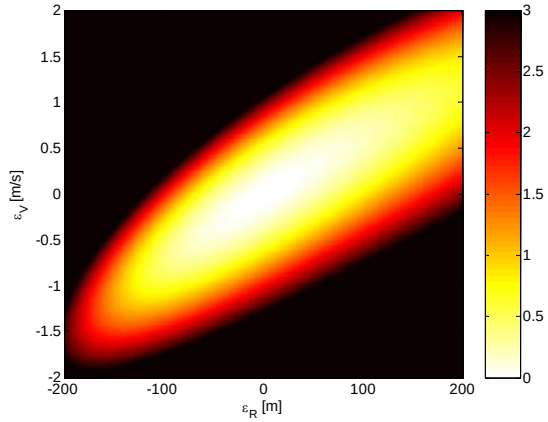


Figure 4-11 *Sensitivity of the sonar performance in a turn versus speed estimation inaccuracy ε_V and radius of curvature estimation inaccuracy ε_R. The result is calculated for a frequency of 1500 Hz, a turn radius of 500 m, a speed of 5 m/s and the settings of a (double length) 64λ array.*

Figure 4-11 shows the sensitivity for the double length array versus ε_V and ε_R. The overall sensitivity shows more of an ellipse shape (compared to the CAPTAS array in Figure 4-10), which is mainly caused by the increased Doppler shift.

The conclusion that can be drawn from this and a more elaborate analysis at different V, R, T, f and L is that the accuracy requirements are not very high. In all operational scenarios, the measured or estimated velocity needs to be within 1 m/s and the radius of curvature estimate within 100 m from the actual estimate. Both of these criteria can easily be met with simple means, e.g. the Global Position System (GPS) on the tow ship and/or heading sensors on the array. The most important sensors for the estimation of the sonar track are the heading sensors. The heading sensors would be used to calculate the radius of curvature with the following formula $R = V(t_1-t_0)(\psi(t_1)-\psi(t_0))\pi/180$. The accuracy required for the heading sensors can now be calculated with the knowledge on V and R and the way they affect the Doppler compensation methods. It turns out that, contrary to the results for position estimation for very long arrays, the Doppler compensation can be based on rough estimates instead of advanced sensor fusion and Kalman filtering as applied by Been (1996) and Gray (1993).

4.5. Proof of concept on simulations

In this section the different signal processing methods are tested on simulated data for the above mentioned standard turn. In the sonar data simulator SIMONA, described by Groen (2001), the relevant Doppler shift for every sample of the received data is taken into account. In Figure 4-12, the result of Method 2 is shown with the same simulation input parameters as Figure 4-3. The transmit signal is an HFM with T = 8s, f_c = 1500 Hz and b = 100 Hz. The transmit waveform is a so-called Hyperbolic Frequency Modulated (HFM) signal, which is described mathematically in Section 4.3.3. The left plot shows the result before application of the dynamic matched filter. It appears that the errors in bearing are solved. The right-hand plot shows correction for bearing errors in the beamforming and range errors in the dynamic matched filtering.

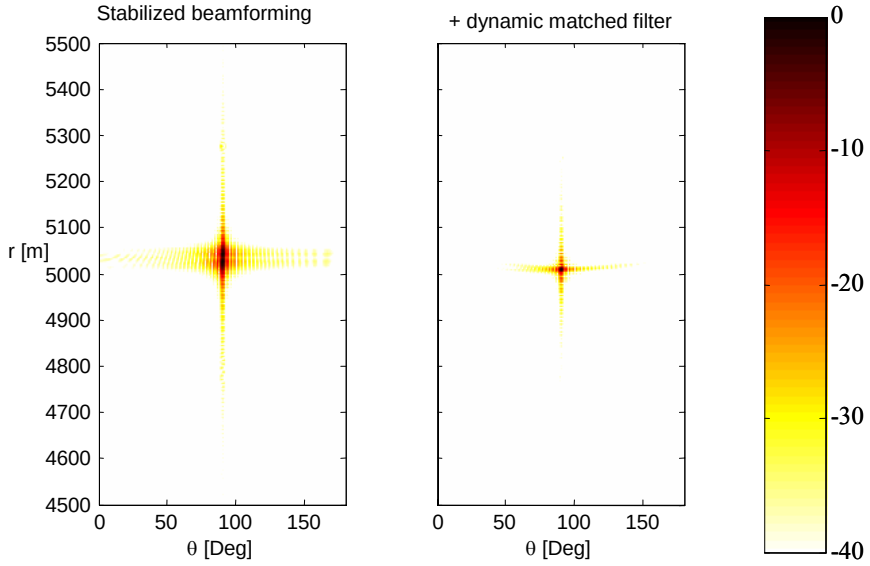


Figure 4-12 *Processing results of stabilized beamforming without and with dynamic matched-filtering. The images are in decibels and normalized with respect to the maximum.*

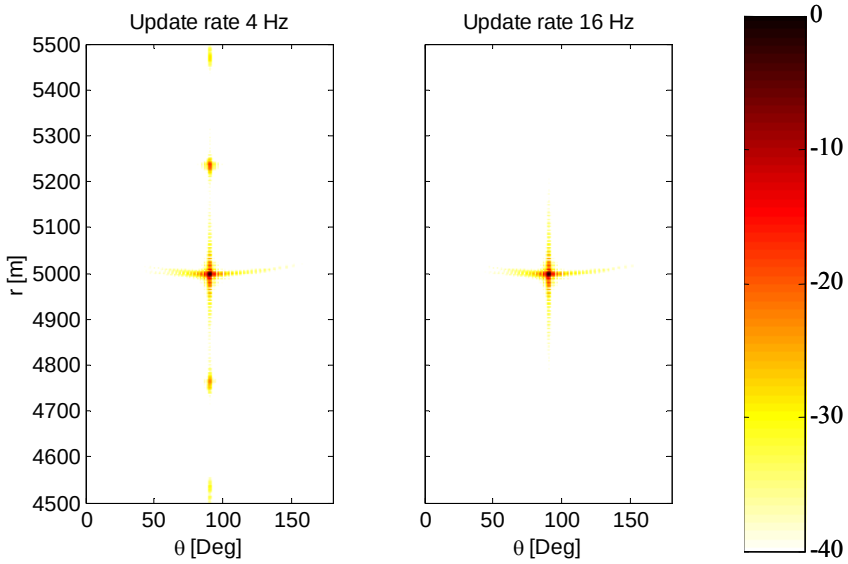


Figure 4-13 *Processing results of SDCB with different update rates. The images are in decibels and normalized with respect to the maximum.*

Figure 4-13 shows the results of SDCB, Method 3, with different update rates. The update rate has to be high enough, depends slightly on the geometry, and in this case is about 8 Hz. Formulae for the maneuvering loss Eqs. (4.8) and (4.13) also can be utilized for analysis of the update rate requirements. After all, within a processing block the Doppler is again assumed to be constant in time and over the hydrophones. An overview of the results on the different methods is given in Table 4.1 via the performance indicators maneuvering loss ML, angular resolution $\Delta\theta_{3dB}$, and range resolution Δr_{3dB}.

Table 4.1 *Quantitative analysis of processing results.*

Method	ML [dB]	$\Delta\theta_{3dB}$ [Deg]	Δr_{3dB} [m]
Ideal	0.0	2.2	6.8
Method 2 (without dynamic matched filter)	6.5	2.4	37.0
Method 2	0.3	2.2	6.6
Method 3 (4 Hz)	0.1	2.2	6.8
Method 3 (16 Hz)	0.1	2.2	6.8

4.6. North Sea experiments in 2002

In 2002 an LFAS trial was organized by the Netherlands, Norway and France. In spare hours five experiments were dedicated to the shape and Doppler corrected beamforming research. A Norwegian Ula class submarine served as a target. It had a source in its sail, which transmitted Continuous Wave (CW) and Hyperbolic Frequency Modulated (HFM) signals, which were received on a CAPTAS array (see van Mierlo (1997)) that was towed by Her Netherlands Majesty's Ship (HNLMS) Mercuur, the torpedo service vessel of the Royal Netherlands Navy (RNLN). Besides the acoustic data from the hydrophones, also other sensor measurements were recorded. In the towed array, roll, heading, depth and velocity (flow) sensors were

recorded. On board the tow ship, the navigation data (GPS among other things) was monitored and recorded.

4.6.1. Experiment description

During the trial three hours were reserved for Shape and Doppler corrected processing. First, it was the intention to prove the concept (starting with the easy case) with one-way propagation. Therefore, the normally silent submarine transmitted HFM signals from 1000-1800 Hz and CW signals at 2000 Hz. The parameter to vary was the signal duration, viz. 2, 4, 6, 8 and 10 s. The Closest Point of Approach (CPA) was at a range of about 3 nmi. Due to the wild maneuvering of both platforms, much closer would have been considered unsafe. The experiments have been conducted according to the plan in Figure 4-14.

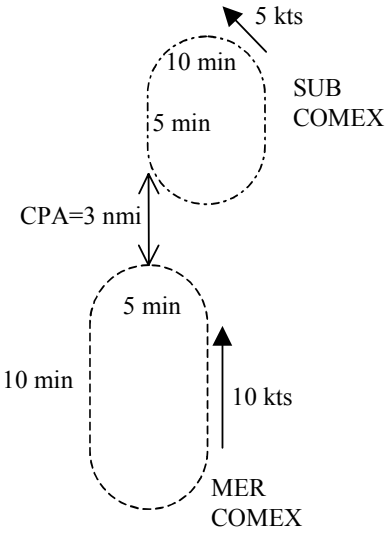


Figure 4-14 *Experiment set-up during 2002 trial off the coast of Norway.*

4.6.2. Environmental conditions

The local Sound Speed Profile (SSP) was frequently measured onboard the surface vessel. From these sound speed measurements an in situ estimate of the representative sound speed profile was constructed by means of a median calculation; see left hand panel of Figure 4-15. The late summer conditions result in a strongly downward refracting profile. For the sonar parameter setting as in the trial, severe bottom interaction is expected; see right-hand panel of Figure 4-15.

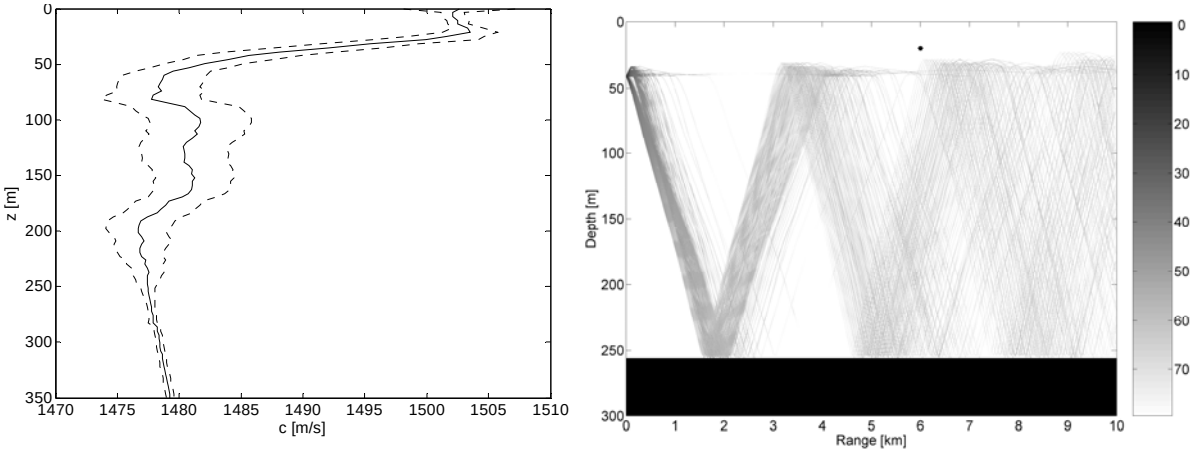


Figure 4-15 *The left plot shows the median SSP (solid line) with a measure for the variability during the 2002 trial by means of the standard deviation (dashed lines). The right-hand plot shows the associated propagation rays calculated with the TNO-FEL ray trace program "Stingray". The gray scale corresponds to the propagation loss in decibels.*

4.6.3. Signal processing results

Before all pings from different experiments are analyzed, first an in-depth analysis of one ping is performed. This is the ping in the first turn at the CPA, when the turn rate is maximal and the target is near broadside and the coherence loss due to propagation is minimal. In other words, this is *the* ping to prove the concept of SDCB. The analyzed signal is an HFM with center frequency 1500 Hz, bandwidth 800 Hz and duration 8 s. The target is located at a range of about 6000 m and a relative bearing of 80 ^{o}.

In Figure 4-16 the signal processing results are shown for shape corrected beamforming (left panel) and for the high rate SDCB (right-hand panel). In the left plot a range bracket around the target for the full 360 degrees is depicted, although for shape corrected beamforming it is almost symmetric. The target response is smeared out over bearing and range as expected. Unfortunately, it does not arrive once, but three or four times. To make it even worse the subsequent arrivals are also severely smeared out, much more than expected from the Doppler spreading. Furthermore, the tow ship is clearly visible at about 25 ^{o} and even its bottom reflection shows up at 60 ^{o}. In the right-hand plot an attempt is made to improve the results by application of SDCB. The beamforming update rate has been set to 8 Hz to ensure that no aliasing behavior would occur. These settings were validated with simulated scenarios. The starboard side (where the target was) has improved. The target signal is higher, and sharper in bearing. Additionally, the same can be seen for the tow ship noise. Unfortunately, the signals remain severely spread in the time/range direction, which is explained with the following text.

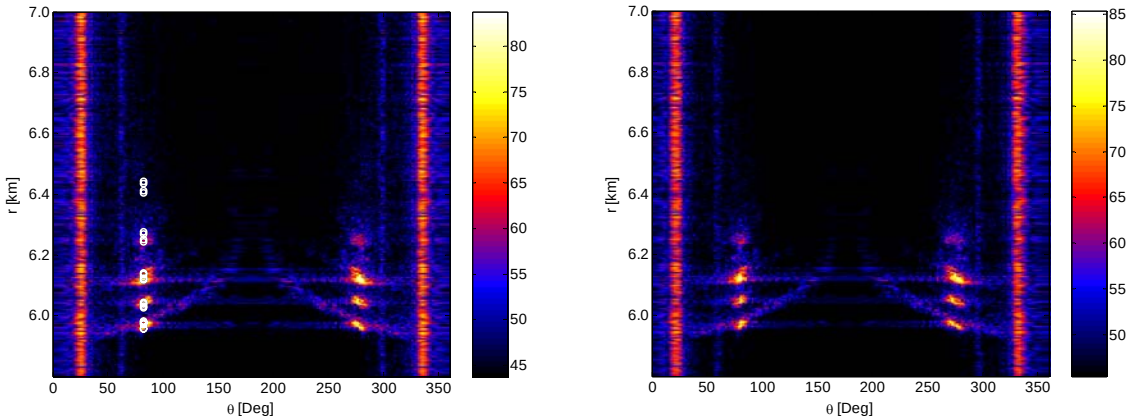


Figure 4-16 *Experimental signal processing result with shape corrected beamforming (left panel) and SDCB (right-hand panel).*

The expected multi-path structure is shown with the white circles overlaid on the left range-bearing plot in Figure 4-16 to indicate the severe bottom interaction. The multipath arrivals are calculated from simple geometry (based on a constant sound speed assumption). The used input parameters are acquired from the trial measurement and were a water depth of 256 m, a receiver depth of 41 m, a source depth of 10 m and a range of 6000 m. From these settings the conclusion can be drawn that the trial scenario is not optimal for analysis of shape corrected beamforming. In the beam direction, performance enhancement of SDCB is close to theory. However, in the range direction, no or very little improvement is seen with SDCB. The smearing in the range-bearing plots is only partly compensated for. The time smearing due the environment is clearly much larger than the time smearing due to Doppler variations. Due to this unfortunate stacking of disadvantages, the results are not typical. In other seasons, geometric settings or areas with harder bottoms the Doppler smearing will be dominating. From this experiment the important lesson is learned that even during the maneuvers described, other environmental issues may still be more important. In the following section a second experiment, which was planned with the knowledge of the first one, is described and analyzed. The solution to avoid environmental effects lies in an enlargement of both the depths of sonar and target. The direct path signal is then clearly separated from the rest.

4.7. Mediterranean experiments in 2003

During the analysis of the 2002 trial data, it appeared that another trial would be beneficial and give significant added value to the proof of concept of the methods. Therefore, in September 2003 another experiment was conducted with a different set-up based on the lessons learned. The experiment was part of the 2003 LFAS trial, which was conducted in shallow water Southeast of Sardinia. The experiment was conducted with the TNO-FEL LFAS system, consisting of a separately towed acoustic source (SOCRATES) and receiving array (CAPTAS); see Groen (2005). The system was deployed from the HNLMS Mercuur and the target was a Walrus class submarine that was equipped with an ITC2010 locator source.

4.7.1. Experiment description

The main criteria to decide on priorities in the definition of the experiment were as follows.

- As much statistics of sonar performance during maneuvers as possible.
- Passive and active recording such that they do not interfere or blank the sonar.
- Sail sharp turns (36 ^{o} per minute) at high speed (10 kts).
- Keep the risk of damage to the (dual-tow) system low.
- Avoid severe environmental effects like multipath and time spreading.

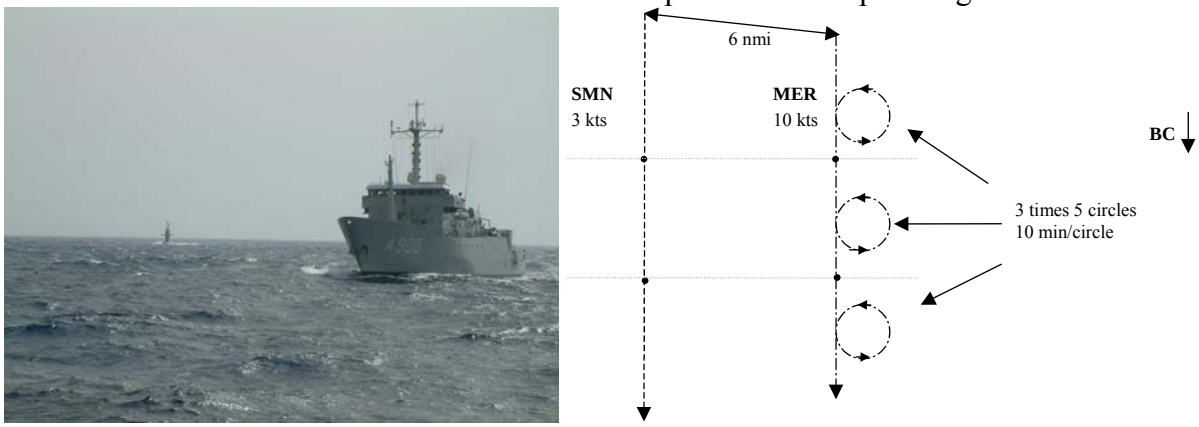


Figure 4-17 *Experiment set-up during 2003 trial off the coast of Sardinia. Participating platforms in the trial kindly made available by RNLN are shown on the left: the submarine and HNLMS Mercuur towing the sonar.*

During the experiment the weather was rather calm with a wind speed of 3 m/s in the direction North and Sea State 1. Just before the experiment decisions were made on the optimal geometrical settings. The CAPTAS receiving array was towed at an average depth of 110 m with a cable scope of 600 m. The SOCRATES source was towed at an average depth of 50 m with a cable scope of 200 m. The ship speed was 10 kts as planned. The average water depth was more than predicted from the sea charts. It was measured at 772 m. The SOCRATES source transmitted 1 – 2 kHz HFM pulses of 10 s duration at a level of 209 dB with a ping repetition time of 30 seconds. Due to extreme heating of the power amps this was increased to 60 seconds later on. The duration of experiment was three hours, in which the tow ship sailed five sharp 360 ^{o} turns three times in order to collect many pings during an actual maneuver. To our knowledge, this was the first time that a dual tow LFAS system was involved in such sharp high-speed maneuvers. Moreover, the findings for the optimal depth of the system conflicted with the mechanical and safety limitations of the LFAS system. Because of this high risk, it can be stated that a valuable data set has been acquired.

4.7.2. Environmental conditions

The trial was conducted with two surface vessels and a submarine that served as a target. On both surface vessels the local Sound Speed Profile (SSP) was frequently measured.

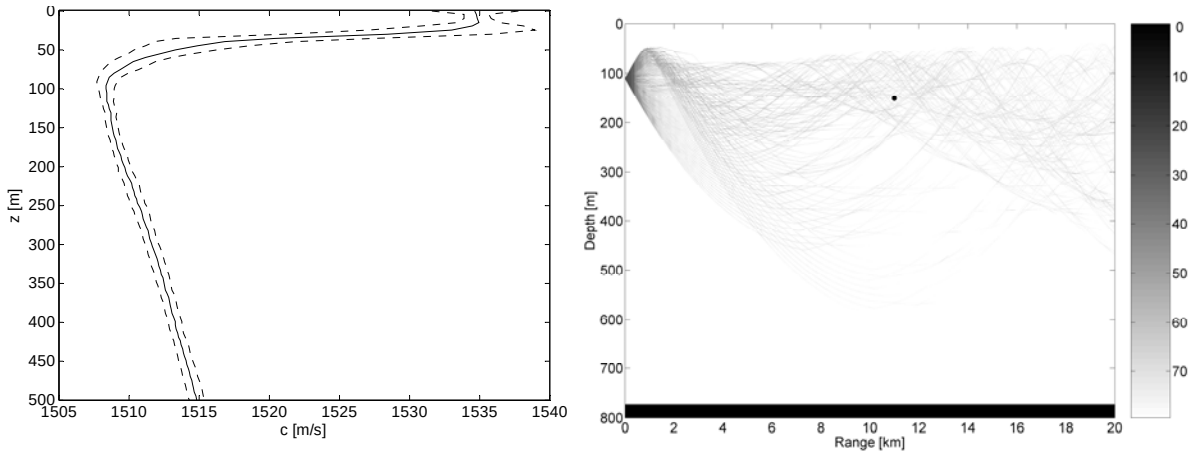


Figure 4-18 *The left plot shows the median SSP (solid line) with a measure for the variability during the 2003 trial by means of the standard deviation (dashed lines). The right-hand plot shows the associated propagation rays calculated with the TNO-FEL ray trace program "Stingray". The gray scale corresponds to the propagation loss in decibels.*

Since the results from the 2002 trial show its high importance, some additional research is conducted to analyze environmental effects on sonar performance. From numerous sound speed measurements an in situ estimate of the representative sound speed profile was constructed by means of a median calculation. Output of the ray trace program was found to give proper insight into the multi-path structure. The gray scale in the ray trace plot in Figure 4-18 represents the propagation loss. It appears that a direct path should exist in the acquired data. From geometry, it can also be shown that the first arrival can be separated from multi-paths.

4.7.3. Signal processing results

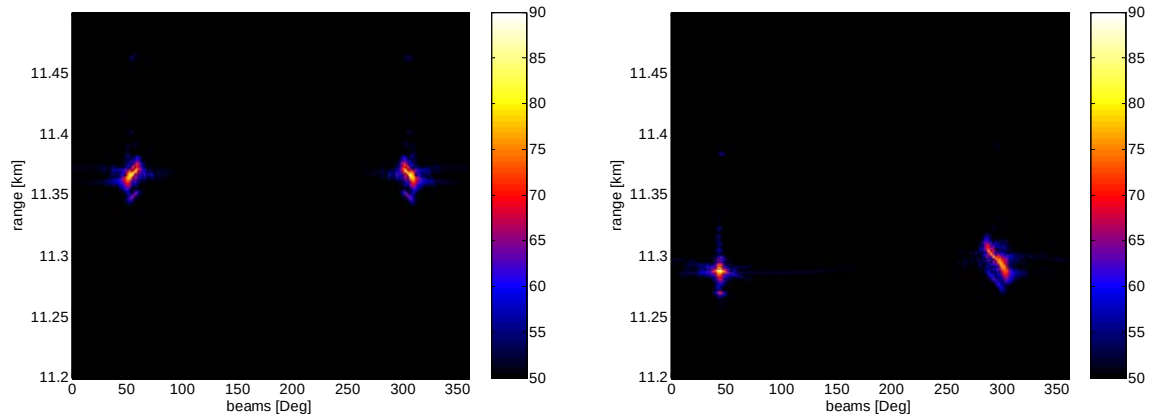


Figure 4-19 *Experimental signal processing result with shape corrected (left) and SDCB (right) on a locator ping.*

In this section two pings of the CAPTAS sonar system in a high-speed sharp turn are analyzed. The first one has a similar set-up as in the previous chapter. It means that the signal is transmitted from the submarine (a locator source) and received on the sonar array. It is ex-

pected that such a set-up supplies a clear insight into the mentioned effects because of the high signal-to-noise ratio and moderate distortion. Additionally, an active sonar scenario was conducted successfully. This is more interesting for operational purposes.

The results of the passive scenario are shown in Figure 4-19. The left range-bearing plot shows the shape corrected beamforming, which gives a clear view on the effects in the data. It is striking that the signal-to-noise ratio is much higher than in the previous trial. Moreover, the target is at a substantially longer range. In combination with the near absence of multi-path, this is in confirmation with the environmental study in the previous section. The results in the right-hand range-bearing plot show the results of the SDCB method. On the port side of the range-bearing plot, a clear improvement on the target is visible. The echo of the target is sharper and higher. The signal level with shape corrected beamforming is 80.9 dB and after SDCB it is 85.9 dB, which is significant. It has to be noted that the situation is ideal for such a processing loss recovery (radius of curvature was measured at 300 m at the array, a speed of 10 kts and a target bearing close to broadside). Finally, it is interesting to mention the port-starboard discrimination that is induced by the turn (and correct processing). In this case, it is measured at 7.2 dB. Finally, it should be noted that the application of SDCB implies a shift in range, from 11.36 km to 11.29 km. This is explained by the different reference points for the beamformer and is not relevant for the further analysis.

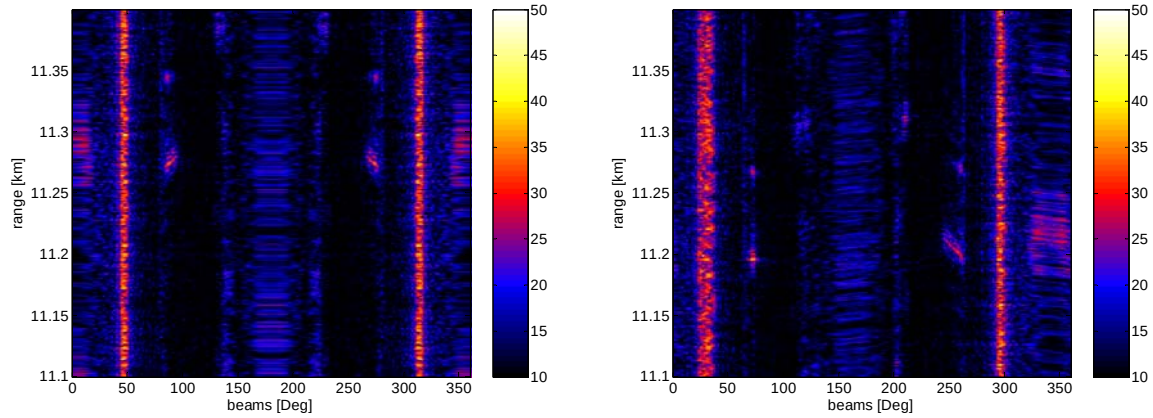


Figure 4-20 *Experimental signal processing result with shape corrected beamforming (left) and SDCB (right) on an active detection.*

Figure 4-20 shows the active results with shape corrected beamforming in the left range-bearing plot and SDCB in the right-hand range-bearing plot. This is one ping later than the passive scenario of Figure 4-19. The propagation appears to be sufficient for detection at a range of 11 km (before any post processing). The tow ship is now visible at 50 degrees and even its bottom echo at 80 degrees, which partly coincides with the target echo. In the right-hand plot, again, the target on the port side appears much better in terms of signal level and smearing. The measured signal levels are now 35 dB without and 40 dB with SDCB. The loss recovery appears to be about the same as in the passive case. Nevertheless, these remain statistics of one sole ping.

To verify the effects that were encountered, a simulation was performed with the same parameters as in the experiment. The results of this simulation are shown in Figure 4-21. The

left plot shows the symmetric image of shape corrected beamforming and the echo smearing looks similar to Figure 4-20. Also the image on the right shows a high similarity. However, the loss recovery, which is equal to the theoretical recovery of 8.6 dB, is higher now. This is due to the fact that the signal echo is also distorted due to other effects during its travel. The submarine is not a point target, and, moreover, propagation is not always a smooth process.

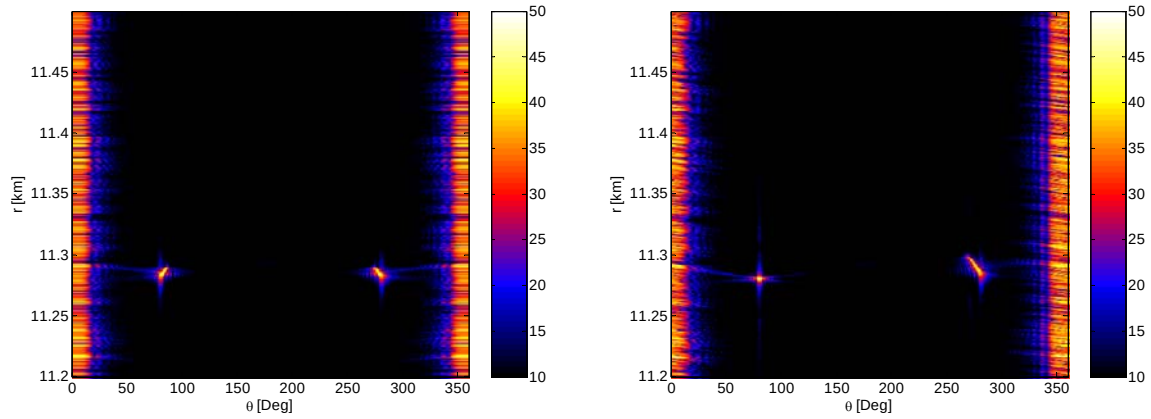


Figure 4-21 *Shape corrected beamforming (left) and SDCB (right) applied to simulated data set with the same properties as the active experimental ping.*

Statistical performance analysis

The statistical analysis is performed for all the recorded pings. Three performance indicators are evaluated from 157 locator pings and 181 active pings:

1. Range resolution
   For the range resolution, a cluster-based algorithm was used. It is determined by making a 2D cluster in the range-bearing plot, which determines the target. In 2 directions the far edges correspond to the beamwidth and "range" width. The 3 dB-beamwidth and "range" width were found to be a good representative for the bearing and range resolution.
2. Bearing resolution
   The bearing resolution follows from the 2D cluster in the same way as the range resolution.
3. Signal gain
   The signal gain is derived from the signal peaks as found in the range-bearing plots.

In this section, both the active pings and the passive pings are analyzed. Method 3, which was explained in Section 4.3.4, has been verified in the same way, but is absent in the plots of Figure 4-22, Figure 4-23 and Figure 4-24, because the results are the same as for Method 2 which was explained in Section 4.3.3. Another verification that has been carried out is the separate presentation on the stabilized beamforming results on the one hand and dynamic matched filtering on the other hand. The gain in range resolution and the gain in bearing resolution is caused by the matched filter and the beamformer, respectively. A few differences between active and passive that are worth mentioning can be found in the results. First of all, active means a more complex propagation issue. The sound travels from the sonar to the submarine and back. Also, the target may not be a real point target, but slightly extended. The second, possibly advantageous difference is the fact that the Doppler spreading is higher due to the contribution of the source. Then a small final remark can be made about the theoretical

range resolution, which is a factor 2 better now. The target tracking itself was a rather difficult analysis, since the signal-to-noise ratio was not always high for a submarine at a range of 11 kilometers. In the following four figures of Figure 4-22, the first performance indicator is evaluated versus bearing and radius of curvature. This first indicator is the range resolution, calculated with the 3-dB "range" width. The conventional method is the first result of this analysis and is shown in the top panels a and b.

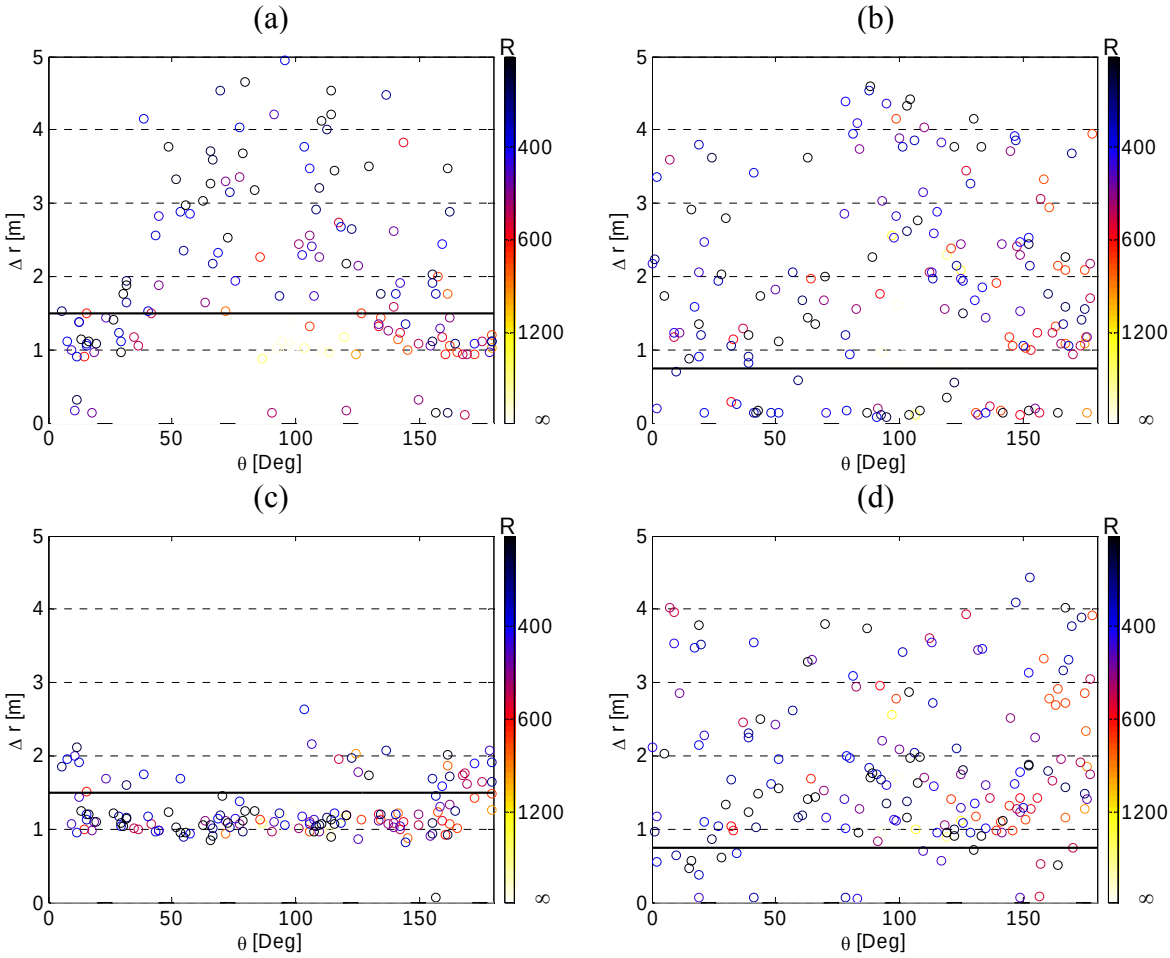


Figure 4-22 *Statistical analysis for passive (left) and active (right) pings with measured range resolution Δr_{3dB} for Method 1 (top) and Method 2 (bottom) versus bearing. The circle's color represents curvature radius of the array track. Theory is plotted with the solid line.*

Figure 4-22a shows the measured and theoretical range resolution (c/b) of Method 1 on the passive pings. The results are as expected. The range resolution worsens up to 4 times the theoretical value of 1.5 meter. The final result of the passive analysis is shown in Figure 4-22c where Method 3 is applied. Figure 4-22c shows an extremely good performance with respect to the range resolution. It is almost always better than theory, which can be explained with the slight underestimation due to scalloping loss and the sample frequency being on the same order as the range resolution. Additionally, there is no clear variation of the performance versus bearing anymore, contrary to the case where Method 1 is applied. This is the proof that the studied Doppler effects are responsible for a time spreading in the signal causing a resolution worsening. Unfortunately, the results on the right-hand side of Figure 4-22 are less convincing. Figure 4-22b shows the results with Method 1 and Figure 4-22d shows

the result of Method 3, which theoretically could lead to improvement. Unfortunately, there is no significant improvement and also statistically there is no reason for a success story. The time spreading is not caused by the motion of the sonar, but dominated by other effects like propagation and scattering. The range resolution shows an almost beam independent measurement scenario with large variations. For the active data set, the studied Doppler effects cannot have caused such measurements, so they can also not be fully compensated for as such. The only recognizable achievement is a clear improvement in the harsh pings that are black and near broadside. Both for the passive and active analysis, the difference of Method 2 and Method 3 are not worth mentioning and therefore the results of Method 3 are absent.

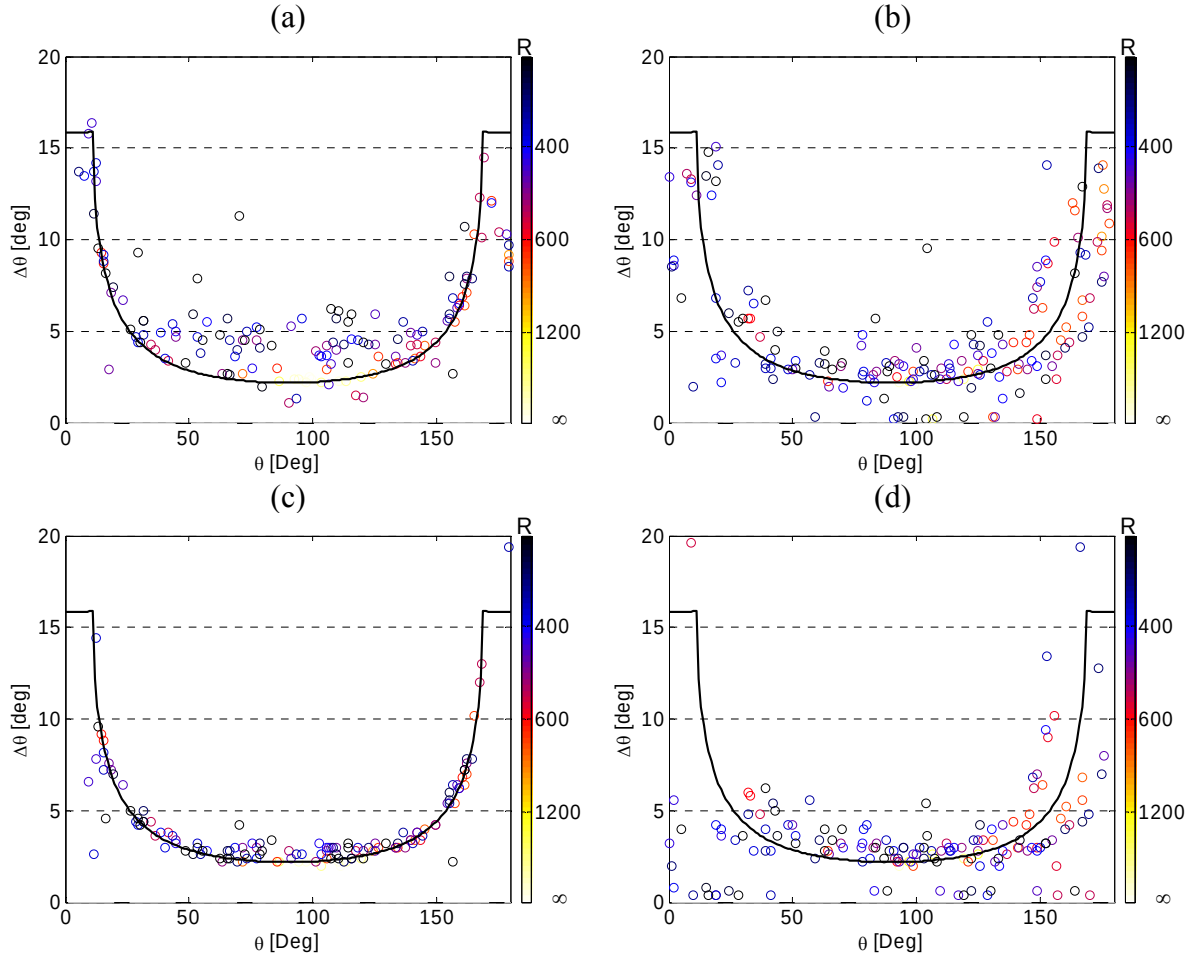


Figure 4-23 *Statistical analysis for the passive (left) and active (right) pings. The measured bearing resolution $\Delta\theta_{3dB}$ is plotted for Method 1 (top) and Method 2 (bottom) versus bearing. The color of the circles represents the curvature radius of the array track. The theory is plotted with the solid line.*

Figure 4-23 shows four plots of the behavior of the measured and theoretical values of the beamwidth versus target direction. Theory seems to be rather close to the measurements, but near broadside the measurements rise. This is expected due to the increased effect of Doppler shift. It is also expected and verified that most of the spreading in the bearing direction is solved with the stabilized beamforming and not with the dynamic matched filter. The comparison results for Method 1 (left) and Method 2 (right) are shown in Figure 4-23. It is clear for the passive data set displayed in plot c that the bearing resolution has improved signifi-

cantly and is close to theory. Moreover, the performance has also visibly improved on the active data set, which follows from a comparison between the plots on the right-hand side. In particular, the variation is somewhat suppressed. It should be noted that the measurements in the end fire region are somewhat unreliable due to the wide beam, low signal-to-noise ratio. In Figure 4-24 the signal gain of Method 2 over Method 1 is shown.

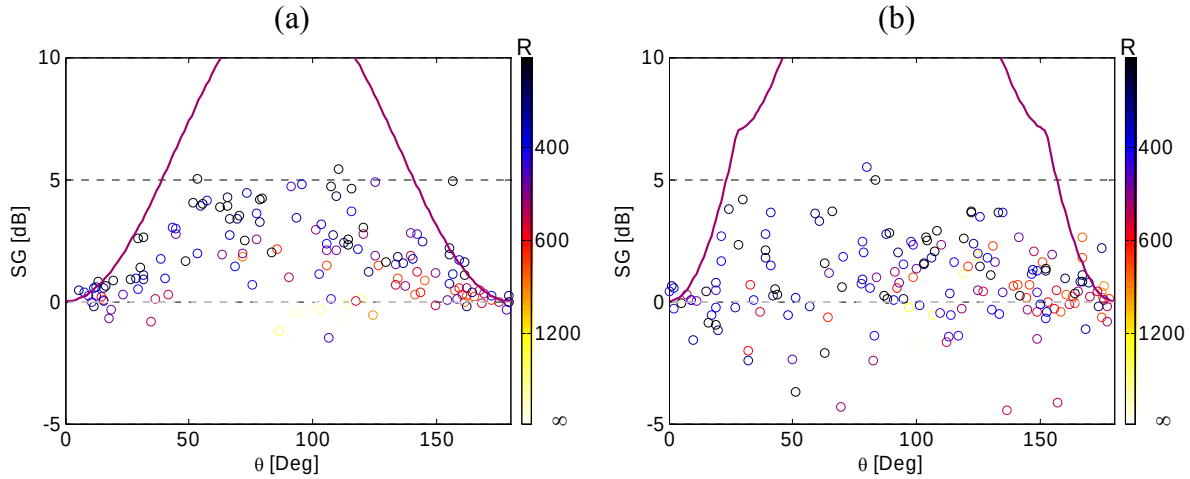


Figure 4-24 *Statistical analysis for the passive (left) and active (right) pings. The signal gain of Method 2 over conventional processing is plotted. The color of the circles represents the curvature radius of the array track. The theory is plotted with the solid line for a radius of curvature of 500 m.*

The passive analysis is shown in Figure 4-24a. The gain is higher near broadside than near endfire and is up to 6 dB. Apparently, the radius of curvature also affects the performance as expected from theory. The theory is plotted with the solid line in the appropriate colour (R = 500 m). This theoretical curve is relatively low, because this is a passive (single path) scenario, which means that the Doppler effects from the source are not present. The active analysis is depicted in Figure 4-24b and shows that the gain in signal appears to be positive in most cases and about halfway than what would be expected from theory. The gain is typically positive, but in 2 % of the cases the loss is significantly negative (<-3dB). Nevertheless, on average it is above zero and about 2 dB. However, it remains a somewhat disappointing result, but for explanation the reader is referred to the issues described in the beginning of this section. Figure 4-24b also shows that the gain depends on the target bearing, but there are large variations on the measured values. The theoretical expectations are higher, since both source and receiver cause Doppler spreading. The difference between theory and measurement is, nonetheless, also present and larger for this active analysis, because the Doppler effect alone does not monopolize all of the signal distortion.

The sonar performance was measured with several indicators, i.e. range resolution, bearing resolution and signal gain. The improvement on all indicators was similar for Method 2 and 3. At first glance the gain does not seem impressive. However, when taking into account the theoretical dependence on the angle of arrival (θ) of the signal and the curvature radius, the result appears to be acceptable. When the array is really in the turn and the target is near broadside, the signal gain is significant; about 4 dB.

4.8. Conclusion

In this chapter the effect of tow ship maneuvers on the sonar signal processing performance has been studied. The theory shows that without countermeasures both Doppler and position errors may give rise to serious performance loss in operational scenarios. The chapter provides formulae that quantitatively address the performance loss for arbitrary types of towed array sonars.

Three compensation methods have been described and successfully tested on simulated and experimental data. Conventional beamforming is based on the assumption of a straight array and constant velocity. Shape and Doppler corrected beamforming fully compensates for the motion effects during maneuvers. A first test of the algorithms on experimental data was performed on 2002 sea trial data. During this trial five SCB experiments were performed with a locator source and the CAPTAS array. Unfortunately, it appeared that due to the shallow positioning of the source and receiver and the late summer sound speed profile bottom interaction was rather severe. This interaction induces a time spreading larger than those expected from Doppler effects. As a consequence compensation for Doppler did not result in much loss recovery.

In 2003, again in late summer, a second data set was gathered in the Mediterranean. In these experiments a larger number of pings was collected, both in active and in locator mode. Moreover, the environment was monitored carefully and adapted for. Here, SDCB was successful on both the passive and active data set. The improvement with the compensation methods did not manage full recovery of the losses measured, which can be explained via the environment and additional motion inaccuracies. Fortunately, in the end, all described data sets, both in a passive and active sonar setting, proved the benefit of shape and Doppler correction algorithms during sharp high speed tow ship maneuvers.

The summarizing conclusion is that Doppler effects may induce significant maneuvering loss, but that with sophisticated processing this can be compensated for. This signal processing is relatively easy to implement, because the adaptation takes place in the beamforming algorithm and matched filtering algorithm used. These algorithms are modules in the signal processing chain and simply have to be replaced by the compensation methods described in this chapter. The gain can be several decibels in practical circumstances.

5. SYNTHETIC APERTURE SONAR PART I: SIGNAL PROCESSING WITH MOTION COMPENSATION

5.1. Introduction

In this chapter the mine hunting sonar research is presented. It can be read separately from the previous two chapters. However, the presented signal processing chain is developed with the simulator described in Chapter 2, and therefore, it is recommended to read Chapter 2 first. As a part of the signal processing chain, three imaging methods are analyzed and it is concluded that Stolt migration is the most suitable imaging method. This chapter gives a treatise on the complete signal processing chain, whereas the following chapter is restricted to the wavenumber frequency processing in general, and more specifically dedicated to the Stolt migration method. Both these chapters on mine hunting sonar signal processing are readable on their own. There is also some overlap due to the fact that the work was also published in separate articles. The research on synthetic aperture sonar in The Netherlands started from scratch with this PhD research. This implies that some of the methods and formulae are obtained from literature. When this is the case, references to the corresponding articles are given. The implementation of the synthetic aperture sonar signal processing chain and its application to sonar data, however, has been fully performed within this PhD research. This chapter and the following chapter show that novel findings are motion compensation techniques, imaging techniques and derivation of the theoretical performance expressions.

The performance of mine hunting sonar has not reached its physical limit by far yet. A significant improvement is the application of Synthetic Aperture Sonar (SAS). One of the bottlenecks in the signal processing of SAS data is the data flow and accompanying computational load. To solve this problem, scientists around the world are looking into the application of fast imaging algorithms, e.g. Gough (1997), Marx (2000), Fernandez (2000), Shippey (2001), Hawkins (1996) and Callow (2001).

Synthetic aperture techniques are investigated in order to increase signal gain and improve azimuth resolution. Spatial and temporal coherence and shape and stability of the sonar are the major limitations to SAS. The signal processing and the measurement of the SAS performance are discussed in this and the following chapter.

Modern mine hunting requires high-resolution sonars to detect small mines with low acoustic target strength. These sonars are increasingly used on Unmanned Underwater Vehicles (UUVs), to allow stand-off surveillance. Conventional sonars are limited in resolution by their real acoustic aperture and increased resolution would require prohibitively large receiving array. Furthermore, the absolute resolution deteriorates with range. SAS is generally recognized as the technique to solve these limitations.

As the sonar moves, the aperture is enlarged synthetically by coherent integration of successive pings, thus achieving a high range-independent azimuth resolution, see Hayes (1992). To achieve good images, many aspects need to be considered, such as phase errors due to sonar motion and propagation effects. The main goal of this chapter is to investigate, which signal processing methods are optimum for motion estimation, motion compensation and imaging. It is shown that the choice depends on the sonar system itself. The results presented here are derived for the state-of-the-art systems analyzed. However, the methodology is applicable to any SAS system and geometry.

The signal processing methods are a combination of optimal imaging and robust motion estimation. The synthetic aperture scenarios are on the edge of the so-called Fresnel zone, or acoustic near field, which was discussed in Chapter 2. As explained there, the boundary between the near field and its counterpart the far field is the Fresnel distance, which depends on the dimension of the sonar and the frequency used. It is the distance from which acoustic waves, transmitted or received, can be assumed to be planar. For the signal processing, dealing with a far field or a near field case is quite a difference, because for the latter wave front curvature has to be accounted for in the processing. This makes it interesting to identify optimal imaging algorithms with respect to computation time, memory used and imaging performance.

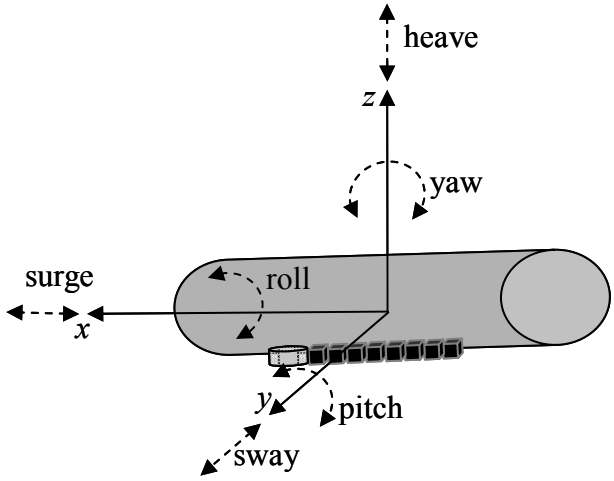


Figure 5-1 *Six degrees of freedom for a sonar mounted on a platform.*

Figure 5-1 shows the six degrees of freedom for the motion of the platform and the sonar mounted on it. The x, y and z directions are based on the geometric definitions in Chapter 2. The x-axis is defined in the direction in which the sonar travels. For the case of a varying sonar direction, the x-axis is naturally kept fixed and is, for instance, set in the sail direction of the sonar during the first ping. The y-axis is defined perpendicular to the x-axis and parallel to the sea surface. The z-axis is defined is perpendicular to the other two axes and points upwards. Sonar motion in the three directions is referred to as surge, sway and heave, respectively. The angles around the axes are called roll, pitch and yaw, respectively. The position of the origin can be chosen arbitrarily, and is usually defined as the center of the sonar.

The motion estimation problem is by no means solved conclusively yet and research is still ongoing, but already a combination of currently available methods gives a fairly robust and satisfactory result. Current motion estimation already increases resolution one order of magnitude in mine hunting. In this chapter five methods are considered for motion estimation:

1. Displaced Phase Center (DPC) is a (ping to ping) hydrophone data correlation method that estimates the surge, sway and/or yaw of the sonar.
2. Image Correlation (IC) uses correlations in successive ping images and the overall SAS image to estimate surge, sway and yaw of the sonar.
3. Contrast Optimization (CO) is a search algorithm to improve the overall SAS image contrast.
4. Phase Gradient Autofocus (PGA) creates highlights (point targets) in the overall SAS image and estimates the sonar position accordingly.
5. Navigation such as GPS and inertial navigation systems can be used to estimate the sonar positions.

Each method is has its drawbacks and, therefore, it is concluded beforehand none of the five is superior to the others. It should be noted that these methods do not have to be applied separately. Combinations of the methods are common and typically more successful than each method individually. Method five is the only method that is not sonar data driven, because it uses data from supplementary sensors. The other four methods are fully based on the acoustic data received by the sonar.

5.1.1. The synthetic aperture sonar signal processing chain

The work presented in this chapter is aimed primarily at mine hunting. However, the methods used are applicable to SAS in general. Sonar resolution can be measured in three dimensions: along-track (x), across-track (y) and height (z). Height resolution is commonly achieved with interferometry, which is outside the scope of this thesis. Across-track -or range- resolution is mainly the result of signal bandwidth in combination with pulse compression. Along-track resolution is the most relevant measure of SAS performance as it is mainly determined by aperture length.

Before the imaging is described, the overall processing is presented in Figure 5-2, from raw sonar data on the left to a SAS image on the right. The beamformer or imaging part is marked with the dashed background. The input for the signal processing chain consists of sonar data, parameters related to geometry, signal and array properties, and sonar track data. The sonar track data are derived either from external sensors or from the acoustic data by autofocusing or from both.

The first step is signal conditioning, which consists of hydrophone repair and equalization of the data. Bad hydrophones are detected by comparing cross-correlations and amplitudes. Each bad hydrophone is replaced by interpolation. Equalization is a normalization step over the received data, such that the received energy is the same for each channel. This is an important step for robustness of both the autofocus method and the beamformer.

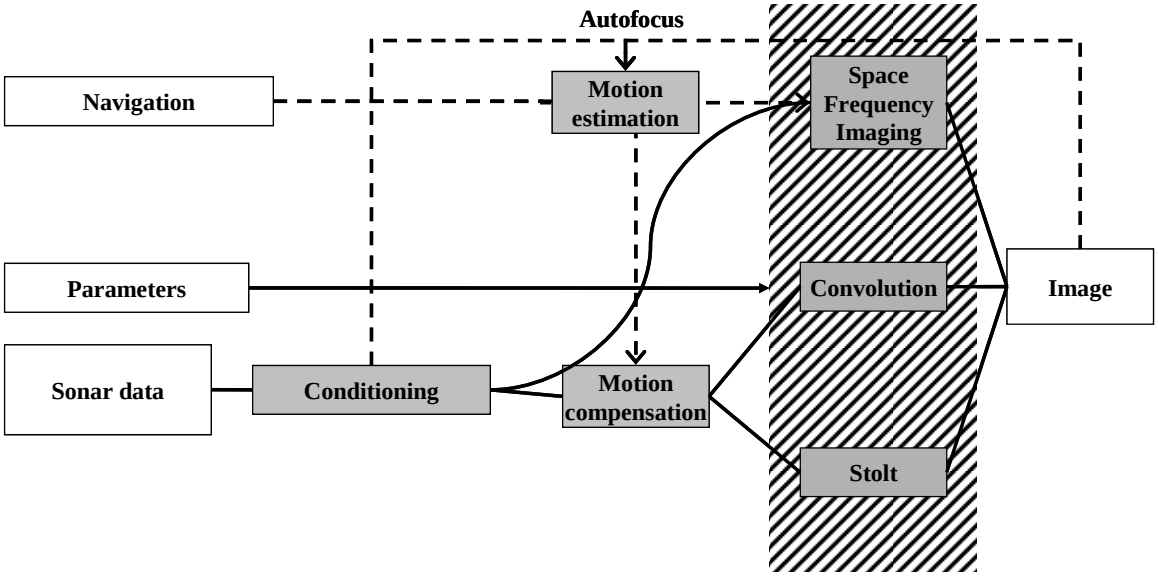


Figure 5-2 *Structure of the SAS processing chain. The dashed part is the kernel of the signal processing, i.e. the imaging. For the wavenumber frequency methods motion compensation prior to the imaging is required. Motion estimation is performed with the navigation data, acoustic hydrophone data and sonar image data.*

The evaluation on the algorithms is based on a finite set of scenarios and system types. This means that the conclusion for the choice in motion estimation, motion compensation and imaging method is based on this finite set as well. The multi-receiver sonar systems considered vary from about 10 kHz up to 200 kHz with beamwidths up to 40 degrees. Sonar mounted on a rail, underwater vehicles and a ship are analyzed. However, the remainder of this chapter might have to be reconsidered when dealing with the signal processing chain for strongly dissimilar geometries, systems or environments.

5.1.2. Outline

The remainder of this chapter follows the structure of Figure 5-2, starting with the shaded part, the imaging itself in Section 5.2. Many SAS imaging algorithms exist in literature, e.g. Gough (1997), Shippey (1998) and Bellettini (2000). A selected set of those imaging methods is analyzed here, namely Space Frequency Imaging (SFI), Convolution Imaging and Stolt Migration. All three prove to be useful for specific applications. The theoretical background of these methods and their performance in a simulated scenario are discussed in Section 5.2.1. Figure 5-3 shows the simulation geometry, where the sonar is a 32-hydrophone receiving array with a source in the middle. The performance of the different methods is analyzed in Section 5.2.2. Performance cannot be caught in one value and therefore different criteria are considered. One of the criteria for using a certain method is its interaction with motion estimation techniques as described in Section 5.3. Some experimental results are discussed in Sections 5.3.1 and 5.3.2. Section 5.4 describes two methods for motion compensation when wavenumber frequency methods are used. Conclusions and recommendations for future systems are presented in Section 5.5.

5.2. Imaging methods

The imaging method of the synthetic aperture sonar signal processing chain is defined by the part where the acoustic hydrophone data (hydrophone time series) are converted to sonar image data. The input data are acoustic pressures as a function of hydrophone n_h and ping n_p and time t. The output data, the sonar image, are amplitudes proportional to the acoustic contrast as a function of along-track position x and across-track position y. In this and the following chapter the coordinate y is used as across-track image coordinate, because the conversion from range to actual coordinate on the sea floor is merely a projection, and therefore, trivial.

Like in synthetic aperture radar and seismic signal processing, many dedicated imaging methods exist. The reason for this variety in imaging methods is the processing speed. Certain system specifications and geometrical parameters are usually within a certain parameter range. This allows assumptions in the signal processing chain. A clear example of this is the far field assumption, in which propagating acoustic waves are assumed to be plane waves.

The result of any digital signal processing chain is never exact, due to the fact that the computer has a certain precision and the data are collected and treated in a discretized form. For synthetic aperture sonar, the most correct, accurate and slowest imaging method is the time domain method that accounts for the exact travel times and amplitudes of the sonar signals. This method is only briefly investigated in this and the following chapter. The Fourier transform, or more specifically the Fast Fourier Transform (FFT), is a convenient tool to speed up the imaging. All three methods discussed in this chapter are FFT-based. It is investigated if the application of such FFTs is valid in the possible circumstances in which the synthetic aperture sonar is applied. Another convenience of the frequency domain is that one of the methods makes use of convolution. With convolution it is possible to search for features in the input data, e.g. hyperbolic signal arrivals on the hydrophones.

Because different sonars have different requirements, sonar designers develop their own dedicated optimal signal processing chain. There are many methods ranging from the slow time-domain to the fast chirp scaling method described by Raney (1994) and Banks (2000). There is, as often the case in signal processing, a trade-off between the runtime and assumptions made. Most applications tend towards the methods somewhere in the middle of this range, viz. Stolt migration and the slightly slower method of fast factorized back projection described by Shippey (1998) and Banks (2002). It is not the aim in this chapter to find the optimal imaging method, since this depends on the application and its requirements. The aim is to show the impact of geometrical variations such as sonar motion on the performance of the three imaging methods presented.

5.2.1. Theory: three approaches to the signal processing kernel

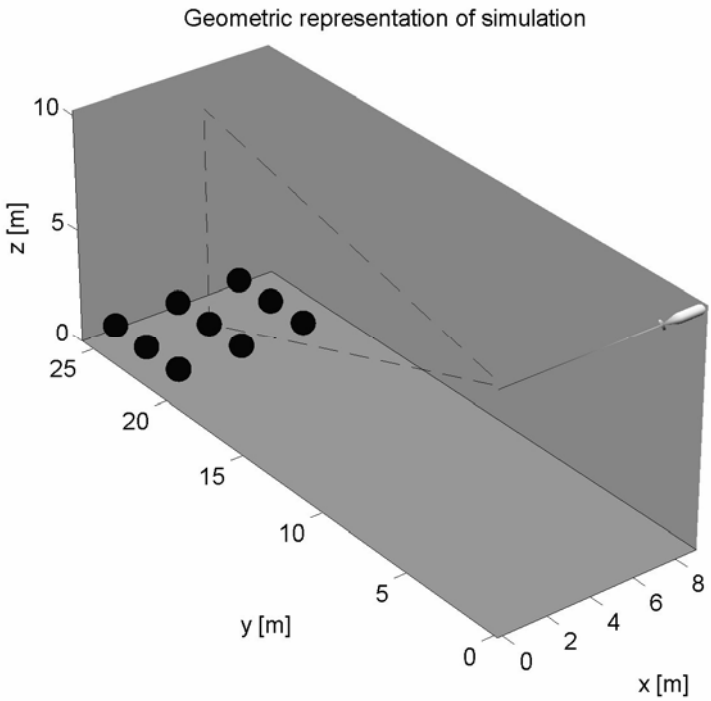


Figure 5-3 *SAS simulation geometry: a 32-hydrophone array moves in a straight line past a patch of sea floor with 9 targets.*

The kernel is defined as the part where the hydrophone data are transformed into an image. This is entirely based on the two-way travel times of the transmitted pulses. The simulation scenario from Figure 5-3 is used to explain the different methods and their behavior. The simulation consists of a 32-hydrophone receiving array moving 10 meters along a target field and collecting 64 noiseless pings of acoustic data. Imaging is the transformation of the measured pressure p into an acoustic contrast image g. For this process the Fourier transforms of p and g turn out to be convenient for both insight and computational speed. The pressure data that are measured by the sonar are denoted by $p(x_s,y_s;x_r,y_r;t)$, i.e. a function of source position (x_s,y_s), the receiver position (x_r,y_r) and time t. The imaging methods are derived for the 2D case, i.e. $z = 0$ or in the look direction of the sonar. The temporal Fourier transform of the acoustic pressure is denoted by a capital as $P(x_s,y_s;x_r,y_r;\omega)$. The spatial Fourier transforms, i.e. a transform from dimension x to wavenumber dimension k_x, are denoted by a $\tilde{}$ on top. The imaging methods that are applied in the wavenumber domain make use of a merge of source and receiver into so-called midpoints as explained further in this section. In that case the input parameters for the pressure $p(x_s,y_s;x_r,y_r;t)$ are reduced to $(x_m,y_m;t)$. The image g is a function of the image pixel position x and y.

In the theoretical part no distinction is made between the across-track coordinate y and the range r. This means that for the theory of the methods, the sonar to operate in the horizontal plane. In practice, this is not always the case, but the conversion from r to y is a simple pro-

jection of the image, which can therefore be omitted without loss of generality. The process of transforming the acoustic data to a sonar image is rather different from the methods in the previous chapters, which calls for a brief introduction on array focusing. Where it was beamforming in the far field, it is now array focusing or focused beamforming in the near field. The process is illustrated by the following intermezzo taken from the book of Lurton (2004):

Intermezzo: array focusing
When the array dimension is such that the near field condition is met (see Chapter 2), the acoustic waves cannot be assumed to be plane any longer, and beamforming is not optimal. One must then focus the array, by delaying the elements, to compensate for the differences in time of a spherical wave centered on the target according to Figure 5-4.

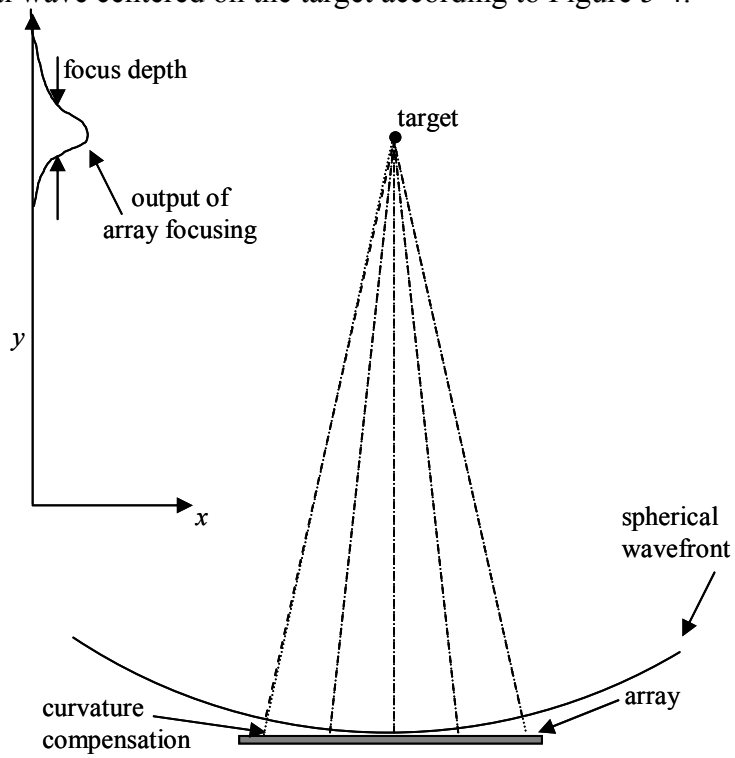


Figure 5-4 *Array focusing geometry. The signals travel times on the array can no longer be assumed linear. Array focusing on the target range compensates for this and results in a range dependent output.*

Focusing is only valid locally, around the focus range. The amplitude of the output signal decreases on each side. The domain of validity of focusing, the focus depth, is given by the spacing between the points at -3 dB around the focus range. This focus depth is an important topic in the remainder of this and the following chapter.

Space Frequency Imaging (SFI). This method processes the acoustic frequency domain input data P into frequency domain output image, or wave-field, G. Ping by ping the hydrophone signals are phase shifted according to the position of the image with respect to the position of the sonar. The focus range r_{focus} is assumed constant for the data-snapshot. In formula the procedure is as follows:

$$P\left(x, r_{\text{focus}}; x, r_{\text{focus}}; \omega\right) = \sum_{n_p=1}^{N_p} \sum_{n_h=1}^{N_h} e^{-i\omega\tau\left(n_p, n_h, x, r_{\text{focus}}\right)} P\left(x_s, y_s; x_r, y_r; \omega\right), \tag{5.1}$$

where $\tau\left(n_p, n_h, x, r_{\text{focus}}\right) = \frac{1}{c}\left\{\sqrt{\left[x - x_r\left(n_p, n_h\right)\right]^2 + r_{\text{focus}}^2} + \sqrt{\left[x - x_s\left(n_p\right)\right]^2 + r_{\text{focus}}^2}\right\}$ is the signal travel time,
n_p is the ping index,
n_h is the hydrophone index,
x_s is the along-track position of the source at ping n_p,
x_r is corresponding position of hydrophone n_h at ping n_p,
x is along-track image coordinate,
r_{focus} is the focus range (across-track distance),
c is sound velocity,
N_h is the number of hydrophones,
N_p is the number of pings, and
$\omega = 2\pi f$ is the angular frequency.
The general derivation of Eq. (5.1) is given in Appendix C. The pressure P in the frequency domain can be transformed back to time domain with an inverse Fourier transform:

$$p\left(x, r_{\text{focus}}; x, r_{\text{focus}}; t\right) = \frac{1}{2\pi} \int_{-\infty}^{\infty} P\left(x, r_{\text{focus}}; x, r_{\text{focus}}; \omega\right) e^{\mathrm{i}\omega t} \mathrm{d}\omega, \tag{5.2}$$

The output can still be seen as acoustic pressure versus time for each along-track position x. The image $g(x,y)$ is now obtained by mapping t on y. The expression for g valid for one focus range becomes:

$$\left[g\left(x, y\right)\right]_{r_{\text{focus}}} = p\left(x, r_{\text{focus}}; x, r_{\text{focus}}; \frac{2y}{c}\right), \tag{5.3}$$

This procedure to obtain the correctly focused $g(x,y)$ should be repeated with different focus ranges for all required y values. This obviously is computationally expensive, but results in an exact imaging. For these computational reasons, the choice has been made to use the image output of Eq. (5.2) for a certain time window of data, i.e. using samples at $y \neq r_{\text{focus}}$ as if they are correctly focused. The justification for this is discussed further in Section 5.2.2.

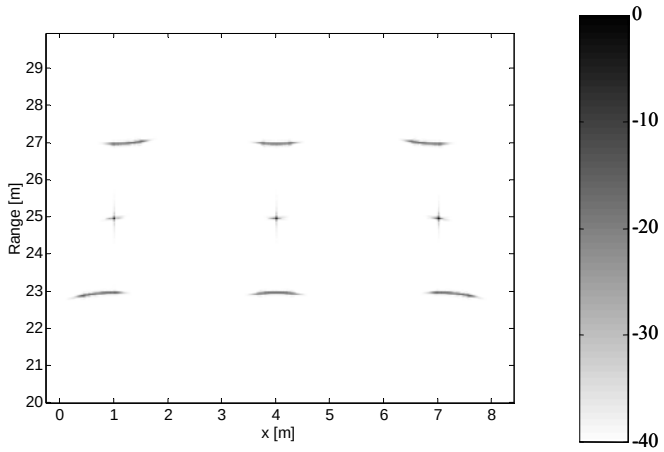


Figure 5-5 *SAS image obtained with Space Frequency Imaging*

Note that SFI supports arbitrary (synthetic) array shapes, where the sonar track is incorporated in the processing. This is indicated in Figure 5-2, where the sonar track information, i.e. the positions of the source and hydrophones for every ping, feeds directly into the beamformer. Figure 5-5 shows three sharp peaks at 25 m range and six somewhat smeared peaks. This smearing is caused by the use of a single focus range (on the target of the middle row in the image) and is discussed in Section 5.2.2.

Beforehand, it can already be concluded that the difference between SFI and the other two methods (Convolution Imaging and Stolt migration) come from the fact that no FFT is applied to the spatial (along-track) dimension. This means that motion compensation can be applied without assumptions on the directionality of the signal (see for further explanation Section 5.4). SFI is also flexible in terms of adding and removing a ping or a channel from the input data. This is convenient when the SAS processing is performed with a sliding window over the pings. It also turns out to have an impact on the image based autofocusing methods, e.g. image correlation autofocus. Image correlation is operated on the images individually in order to find the parameters, for instance yaw or sway, that optimize the total SAS image. When using SFI, there is no use applying an FFT over the pings, because one needs access to the individual ping data.

Convolution Imaging. If the acoustic input data can be assumed to come from a uniform linear array (ULA) of transceivers (transmit/receive elements), it is possible to use a wavenumber-frequency method. The positions x_m are the positions at which a transceiver is placed such that it can replace the corresponding hydrophone and source. Thus for every hydrophone/source pair a point is created for which the two coincide and would receive the same signal. For signals that come from far, the position of this transceiver, also called midpoint or phase center, is simply given by the middle of the two: $x_m = (x_r+x_s)/2$. Thus, here the notation $p(x_s,y_s;x_r,y_r;t)$ is replaced by $p(x_m,y_m;t)$. The main advantage of this approach is the computational speed, which is discussed in Section 5.2.2.

In practice, the ULA assumption often does not hold. Therefore, the input data must be aligned prior to imaging, using the sonar track information. This procedure is indicated in Figure 5-2 by the motion compensation box. This operation is required for both Convolution

imaging and Stolt migration. Once the data are properly aligned, Convolution imaging can be applied. First, a 2D replica $\left[p_0\left(x_m,0;t\right)\right]_{r_{\text{focus}}}$ is generated, which is based on the expected response of a target at x-coordinate equal to zero and focus range r_{focus}, which is a hyperbola in the case of a ULA. This replica is preferably calculated in the time-domain to avoid wrap around effects in either wavenumber or frequency according to:

$$\begin{aligned}\left[p_0\left(x_m,0;t\right)\right]_{r_{\text{focus}}} &= \frac{\delta\left\{t+\frac{2}{c}\left[\sqrt{x_m\left(n_p,n_h\right)^2+r_{\text{focus}}^2}-r_{\text{focus}}\right]\right\}}{\left[\sqrt{x_m\left(n_p,n_h\right)^2+r_{\text{focus}}^2}-r_{\text{focus}}\right]^2} \\ &\approx \frac{1}{r_{\text{focus}}^2}\delta\left\{t+\frac{2}{c}\left[\sqrt{x_m\left(n_p,n_h\right)^2+r_{\text{focus}}^2}-r_{\text{focus}}\right]\right\}\end{aligned}, \tag{5.4}$$

where δ is the Dirac delta function, which represents the impulse response. The final step to the amplitude independent replica is a step that is valid for an aperture small enough to have negligible amplitude variations. For SAS this is not always the case, but it is shown in Chapter 6 that taking into account the amplitude has another purpose, i.e. tuning of the image with respect to side lobes. Formally, amplitude attenuation, as given in the denominator of Eq. (5.4) has to be applied to this 2D replica, but this amplitude effect is found to be negligible for use in SAS. The acoustic image data can now be calculated as a 2D convolution carried out in the wavenumber frequency domain:

$$\left[\tilde{G}\left(k_x;\omega\right)\right]_{r_{\text{focus}}} = \tilde{P}\left(k_x,0;\omega\right)\cdot\left[\tilde{P}_0\left(k_x,0;\omega\right)\right]_{r_{\text{focus}}} \tag{5.5}$$

where k_x is the wavenumber and where the operator ˜ stands for the spatial Fourier operator. The notation with the capital G for temporal Fourier transform is used because the y-coordinate is associated with travel time t by $y = ct/2$. The sonar image pixels $\left[g\left(x,y\right)\right]_{r_{\text{focus}}}$ are found by two inverse Fourier transforms. Again, as for space frequency imaging, there is only one t with the correct focusing. Applying the constant sound speed assumption, y can be found by $y = ct/2$. But, as with space frequency imaging, the assumption is made that $g(x,y)$ is viable for a block of samples around r_{focus}. The important difference between the two is the intermediate step that transforms the input data to ULA data allowing the spatial Fourier transform.

Eq. (5.5) shows that the summations appearing in the space frequency imaging are replaced by FFTs, which has an important computational advantage. Figure 5-6 shows the image obtained with Convolution imaging, which does not differ much from Figure 5-5. This demonstrates the validity of the transceiver ULA assumption.

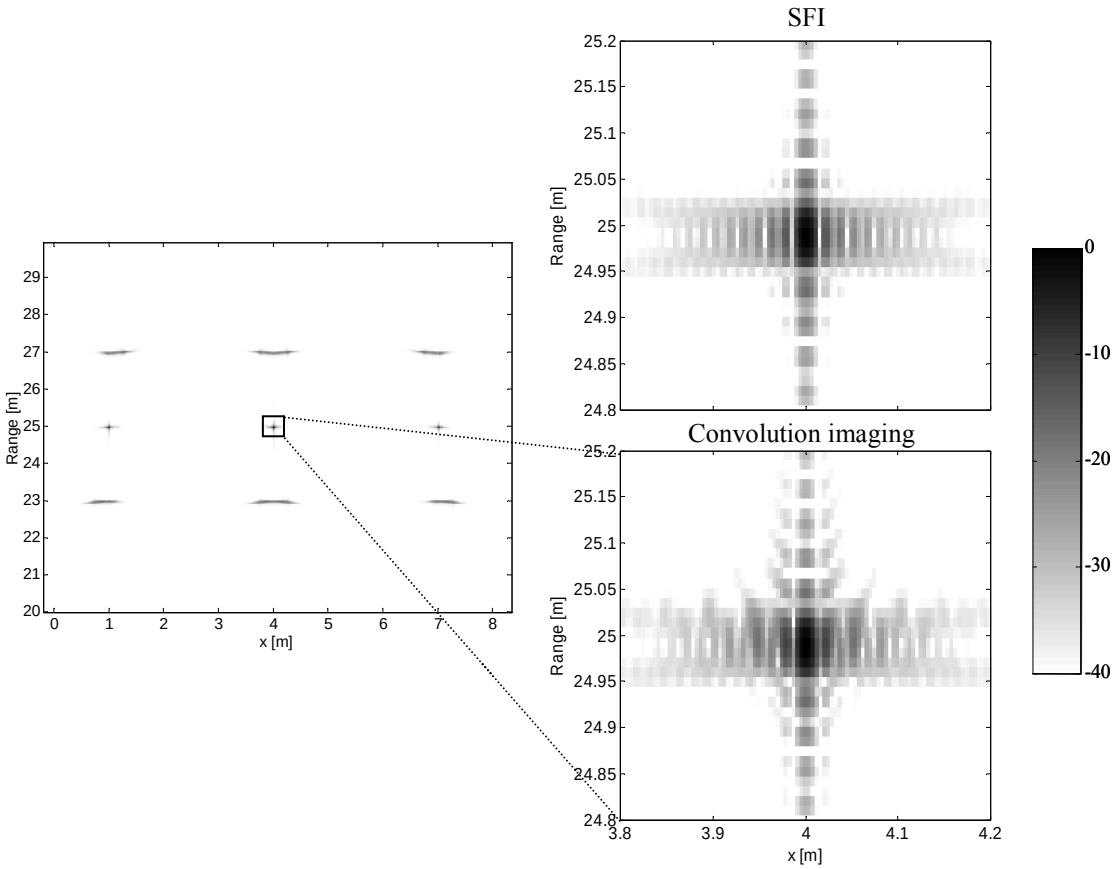


Figure 5-6 *SAS image obtained with Convolution imaging on the left hand side. The zooms on a well-focused target are shown on the right hand side for both SFI and Convolution imaging.*

When the details of the images with SFI and Convolution imaging are considered, some differences can be identified. The imperfections of Convolution imaging due to the ULA assumption are there, but are not important compared to the sidelobe structure that is present already.

Stolt Migration. The last imaging method considered is Stolt migration, which is applied in the wavenumber frequency domain as well, and therefore, shows a significant overlap with Convolution imaging. The general derivation of the method is given in Appendix C. First, the data are convolved with a replica focused on the closest range. Then the focusing in the image is realized, i.e. correct focusing for all pixels. This enhancement is achieved by means of an interpolation method in the wavenumber-frequency domain. Some extra computation time and memory usage is to be expected because of this interpolation, which is given by:

$$k_r = \sqrt{k^2 - 4k_x^2}\,, \tag{5.6}$$

where $k = \omega/c$ and the wavenumber coordinate k linked to time is replaced by the wavenumber k_r linked to range. Thus $\tilde{P}(k_x, 0; k)$ is replaced by $\tilde{P}_{\text{Stolt}}(k_x, 0; k_r)$ followed by the inverse

Fourier transforms in line with the description on Convolution imaging, but now $g(x,y)$ is found directly for all y according to:

$$g(x,y) = \int_{k_r=-\infty}^{\infty} \int_{k_x=-\infty}^{\infty} e^{-\mathrm{i}(2xk_x - yk_r)} \tilde{P}\left(k_x, 0; \frac{ck_r\sqrt{k_r + 4k_x^2}}{2|k_r|} \right) \mathrm{d}k_x \mathrm{d}k_r \,, \tag{5.7}$$

The details on imaging in the wavenumber frequency domain follow in Chapter 6, which is dedicated to these methods.

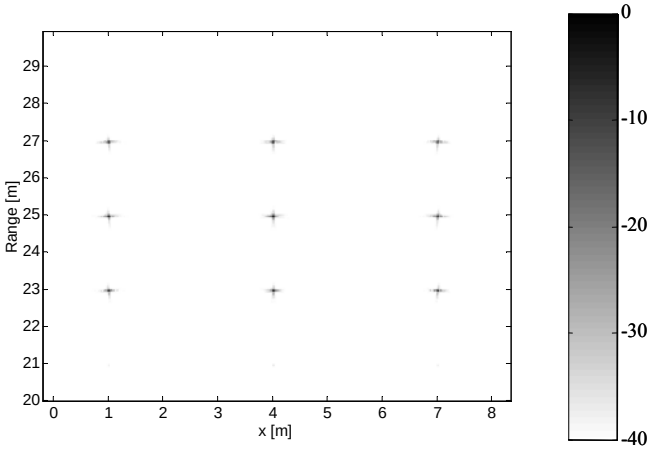


Figure 5-7 *SAS image: Stolt migration applied to simulated scenario.*

From Figure 5-7 it is clear that pixel-wise focusing is successful and all responses appear with the theoretical resolution as defined in Chapter 2. Inserting the values of b = 20 kHz, λ = 10 mm, r_{focus} = 25 m and L = 8 m results in $c/2b$ = 38 mm for the range resolution and $\frac{0.89\lambda r_{\text{focus}}}{L}\text{m} = 28\text{mm}$ as a good estimate of the azimuth resolution. The interpolation used here is linear with an oversampling factor of two. In the following chapter, the effect of using different interpolation schemes is analyzed in detail. It is shown in Chapter 6 that linear interpolation with oversampling factor two is sufficient for sidelobes and smearing behavior.

5.2.2. Considerations for imaging performance

Accuracy. In SAS processing it is important that the quality of the output image is not jeopardized by assumptions in the signal processing chain. Apart from motion errors, the imaging algorithm itself determines whether this is guaranteed. In this section three possible error sources are considered: fixed focus range, ULA assumption and interpolation. First, it has been mentioned in the previous section that errors are inevitable when a fixed focus range is used, i.e. with SFI and Convolution imaging. The wavefront curvature in the processing is set for the focus range, which results in an area around this focus range where the processing is valid. This area around the fixed focus range can be parameterized by the valid range window size, which is referred to as focus depth (Δr).

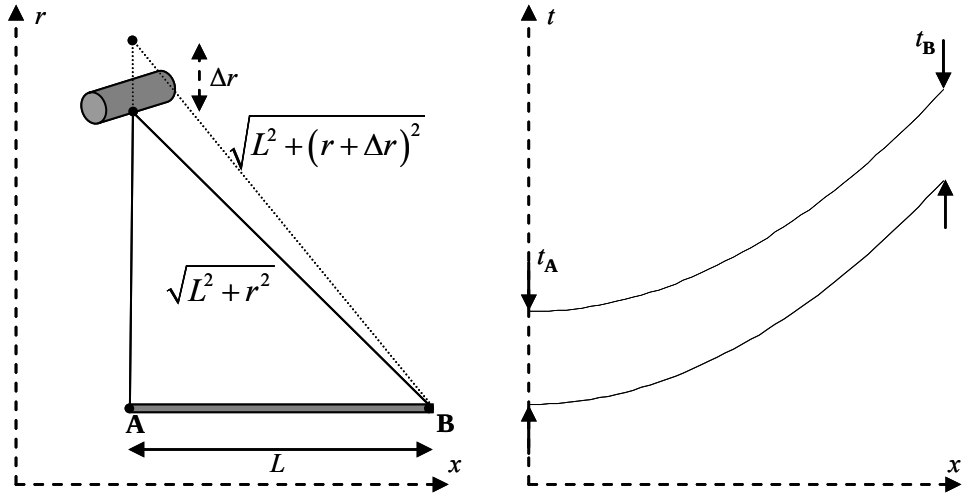


Figure 5-8 *Schematic overview of induced phase errors by an indicated focus range.*

In order to determine the properties of this valid region in the image, the worst-case scenario is analyzed by considering a target at one side of the insonified area and the two outer elements of the synthetic array, e.g. what is visible in Figure 5-8. The right plot of Figure 5-8 shows the travel times $t = 2r/c$ of the signals versus the x-separation between target and array position, which are hyperbolas. The difference in travel times for a target at range r and a target at range $r+\Delta r$ are $t_A = 2\Delta r/c$ and $t_B = 2\left[\sqrt{L^2+r^2} - \sqrt{L^2+(r+\Delta r)^2}\right]/c$, respectively. The criterion, similar to the stationary phase criterion of Chapter 4, which is used for determining the focus depth, is as follows. If a hydrophone delivers only half of its energy correctly to the final image due to an erroneous focus range then the focus depth is said to be the actual range minus the focus range. This focus depth is now defined by the difference in focus range that induces a phase difference equal to $\pi/3$. Thus t_A-t_B times c should equal $\lambda/6$, which results in the following equation:

$$\Delta r - \sqrt{L^2+(r+\Delta r)^2} + \sqrt{L^2+r^2} = \frac{c}{12f}, \tag{5.8}$$

from which an explicit expression for Δr can be derived:

$$\Delta r = \frac{c}{24f}\frac{c+24f\sqrt{L^2+r^2}}{c+12f\sqrt{L^2+r^2}-12fr} \tag{5.9}$$

This formula, shown in Figure 5-9, signifies bad news for most SAS scenarios. The focus depth is too small for practical use and smearing effects appear rather rapidly with SFI and convolution imaging, which can be verified by comparing the two images in Figure 5-5 with Figure 5-7. The values of f = 150 kHz, r = 25 m and L = 8 m result in Δr = 18 mm for the focus depth in the case considered. This means that the deterioration in performance becomes notable at ranges closer than 24.982 and beyond 25.018 m.

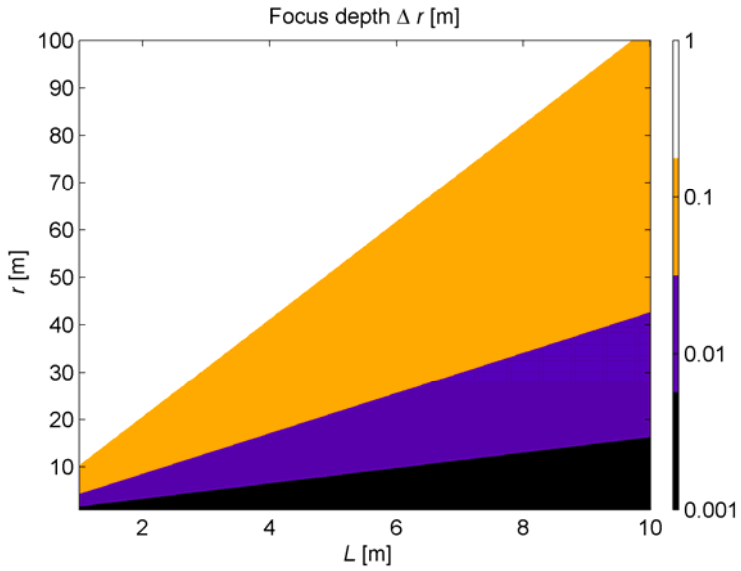


Figure 5-9 *Focus depth as a function of range and synthetic aperture length (f = 150 kHz).*

The second possible error source is the ULA assumption, which is necessary for the wavenumber frequency methods. This assumption also requires that a source/receiver pair is close enough to allow replacement by the midpoints representing a transceiver. This is similar to the far field assumption for the real aperture and is normally satisfied. In addition to this, the obtained monostatic pairs must be equidistant and on a straight line. Section 5.4 reports on the motion compensation that is applied to achieve this. Depending on the transmit-beamwidth (up to 40^{o}) this is successful up to deviations of more than ten times the signal wavelength.

The third and last effect on accuracy considered here is the interpolation used. Interpolation appears only in the Stolt migration. As shown in Eq. (5.6), it is applied in the wavenumber frequency domain, operating along the frequency dimension. The usage of Stolt migration and these interpolation schemes are discussed further in the following chapter.

Computational effort. The three methods have a different behavior with respect to the total computation time needed. The computations in the processing kernel roughly consist of the operations given in Table 5.1.

Table 5.1 *Operations for the three imaging methods.*

Method	Computational Operations
SFI	Two temporal FFTs, a spatial summation over the hydrophones/pings and an element-wise complex multiplication.
Convolution	Two temporal FFTs, two spatial FFTs and an element-wise complex multiplication.
Stolt	Two temporal FFTs, two spatial FFTs, an element-wise complex multiplication and interpolation.

It is known that an FFT is convenient to use for both correlation and imaging. Assuming that the amount of input data depending on the number of samples (N), the number of hydro-

phones (N_h) and the number of pings (N_p) are of the same order as the output data, the number of floating point operations is given by:

$$\begin{aligned} N_{\text{SFI}} &\sim 3N_h^2 N_p^2 N \log_2 N \\ N_{\text{convolution}} &\sim 3N_h N_p \log_2\left(N_h N_p\right) N \log_2 N \\ N_{\text{Stolt}} &\sim 6N_h N_p \log_2\left(N_h N_p\right) N \log_2 N + 5NN_h N_p \end{aligned} \tag{5.10}$$

where oversampling by a factor of two and linear interpolation (adding $5NN_hN_p$) is assumed for Stolt migration. From these theoretical formulae it can be concluded that convolution imaging is about a factor of 100 faster than SFI for the simulated scenario of the previous section. The computation time is also verified in the processing chain itself, which resulted in the numbers $T_{\text{SFI}} = 240$ s, $T_{\text{Conv}} = 20$ s and $T_{\text{Stolt}} = 100$ s. Apparently, in practice a factor 12 is achievable, because at a certain point not the FFTs but the replica generation is limiting. Figure 5-10 shows the computational load versus the number of pings, where it should be noted that the future is expected to bring about a typically larger number of pings (±500). It is clear that, especially for a large number of pings, SFI becomes less and less suitable.

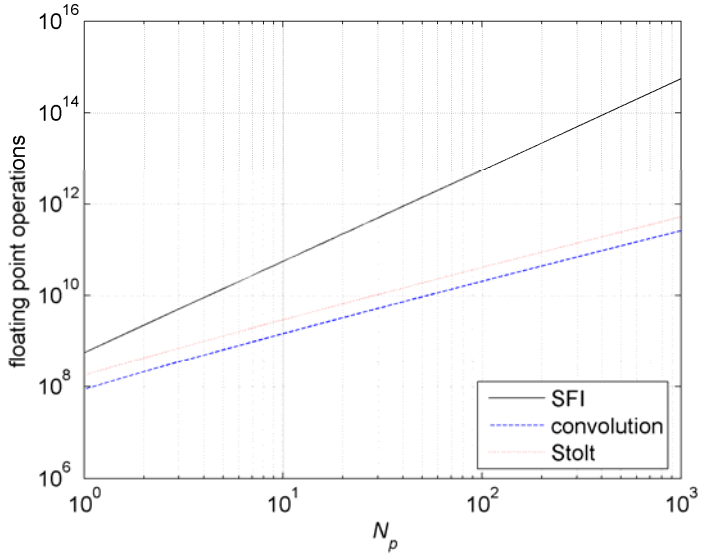


Figure 5-10 *Theoretical estimate of number of floating point operations for SAS imaging with the three methods investigated. The number of pings N_p is varied here and the number of samples N and the number of hydrophones N_h are fixed at 13333 and 32, respectively.*

Complexity. With respect to complexity Stolt migration is the least attractive. The method requires an investigation into the processing parameters, which is discussed in the following chapter. The algorithm is carried out in the wavenumber frequency domain and involves a 2D replica that needs to be prepared in this domain. Furthermore, the interpolation step itself requires tuning, i.e. the interpolation order and possibly oversampling. Because the data undergo four Fourier transforms, it is essential to control wrap-around effects. Last but not least, there is the feature of shading that can be applied to the data in all of the four domains (space, time, wavenumber and frequency), which has to be sorted out. The other two methods are straightforward and do not need any parameter tuning. Although difficult to implement and tune, Stolt migration is not complicated to apply, when the processing parameter settings are

investigated. A solution for this complexity is the main theme of the following. The complexity issues on oversampling, wrap-around effects, shading and optimal implementation are all solved in Chapter 6.

Robustness. All three methods are robust when the processing parameters are properly set. The performance can easily be verified on the simulated response of a point target, e.g. in terms of sidelobes and smearing. In practice, the robustness for SAS lies in the estimation of the motion, which is treated in the following section.

Flexibility. SFI is a convenient method regarding flexibility, because of its freedom in source/receiver positions. The ULA assumption is not needed and the method can be used for image correlation autofocus.

5.3. Motion estimation

Motion estimation is the step in the signal processing that results in an estimate of the sonar track and in practice has as output $x(t)$, $y(t)$ and $z(t)$ for the source and for each receiver. This estimate can be obtained from navigation data or from the acoustic data itself, or even from a combination of the two. This estimation process is very much system dependent, because it depends on the sonar motion measurement resolution. For instance, a high frequency sonar system benefits a lot from inclusion of the acoustic data in the estimation process, because the motion estimation resolution of the acoustics itself is directly related to the signal bandwidth. Another example is the use of the Global Positioning System (GPS), which is not always available under water. In principle, use of the acoustic data for such estimation is the preferred solution, since then, no additional sensors are required.

As mentioned in Chapter 1, autofocusing is estimation of sonar motion by using the acoustic data. The term autofocusing, in a literal sense, suggests a method that sharpens the image by means of the data themselves. Still, this does not provide a clear definition. It has to be mentioned here that in SAS literature the term autofocus is not always used in a unique way. In literature, autofocusing sometimes refers to the use of the sonar image data themselves to improve the image, but it is also used in a more general sense, i.e. the use of acoustic data to improve the image. To avoid confusion between the use of hydrophone data and image data, the term micro-navigation is introduced by Bellettini (2002). Nevertheless, all methods are an estimation based on the acoustic data and a pre-defined (focusing) criterion. An example of such a procedure is the correlation of data from coinciding midpoints of different pings, which ideally contain redundant data. The estimated parameters are the delay times (related to sonar track deviations) and the criterion is maximum correlation of coinciding received signals.

In this section, the estimated parameters from the autofocus procedure are always related to the sonar track. For mine hunting applications, estimation from the acoustic data is better than direct measurement from external sensors such as accelerometers. It can be accomplished in

many ways and finding the ultimate solution is still an important research topic around the world. Such ultimate solution is also expected to be very much system dependent.

Two methods are applied in this analysis: displaced phase centers (DPC) and Image Correlation (IC). DPC is a method that uses ping-to-ping correlation of overlapping monostatic transceivers to determine mutual displacements (as the aforementioned example). The method can be used to estimate

- Surge – DPC0
- Surge and sway – DPC1
- Surge, sway and yaw – DPC2

DPC1 and DPC2 are known to be subject to divergence as discussed by Bellettini (2000). Nevertheless, extension of the array based on these autofocus methods is known to be successful when the aperture enlargement is not too large. Moreover, for longer apertures the estimates can be improved with navigation data. The big advantage of the DPC methods is the fact that they are applied to hydrophone data, which makes them relatively fast.

Displaced Phase Center method for surge estimation

The first parameter to estimate is the along-track (x-) displacement of the array from ping to ping. Two matrices of digitally sampled acoustic data $p(n_p,n_h,t_i)$ and $p(n_p+1,n_h,t_i)$ are correlated to form a ping to ping correlation matrix $\mathbf{C}$ according to the formula:

$$\mathbf{C}\left(n_p\right)=\begin{bmatrix} c_{11}\left(n_p\right) & \cdots & \cdots & c_{H1}\left(n_p\right) \\ \vdots & \ddots & & \vdots \\ \vdots & c_{kl}\left(n_p\right) & \ddots & \vdots \\ c_{1N_h}\left(n_p\right) & \cdots & \cdots & c_{N_hN_h}\left(n_p\right) \end{bmatrix}, \qquad (5.11)$$

$$c_{kl}\left(n_p\right)=\frac{\mathbf{p}^{\mathrm{T}}\left(n_p,k\right)\mathbf{p}\left(n_p+1,l\right)}{\left|\mathbf{p}\left(n_p,k\right)\right|\left|\mathbf{p}\left(n_p+1,l\right)\right|}$$

where $\mathbf{p}(n_p,n_h)$ is a vector that contains all included time samples $p(n_p,n_h,t_i)$ and k and l are hydrophone indexes and run from 1 to N_h. The elements of the matrix $\mathbf{C}$ are built up with the correlation coefficients c_{kl}.

An example of a generated correlation matrix from experimental data is depicted in Figure 5-11. It should be noted that such correlation matrix is generally not symmetric. Typically the matrix shows a diagonal with high correlation coefficients. The offset from the main diagonal supplies the estimated value of the phase centers displacement. This value is directly coupled to the along-track motion of the sonar from one ping to another. This coupling is true under the assumption that:

1. The phase centers are positioned in the middle of the source and the receiver, which means that a plane wave assumption is used. The assumption breaks down when the receiver and source position are so far apart that the corresponding Fresnel distance encloses significantly in the correlation window. The Fresnel distance and near field effects were explained in Chapter 2 and are applicable to the plane wave assumption

here. If the relevant distance is less than the Fresnel distance, the wave front curvature has to be taken into account in order to find the correct midpoint position. Fortunately, for most operational systems this criterion is met, but otherwise additional compensating time delays are required.

2. The spacing of the phase centers is half the spacing of the original receivers, because the phase center is in the middle of the source and receiver. If the required grid shows gaps or is denser than the sonar settings supply, the estimated surge from correlation matrix **C** needs to be refined by means of an interpolation.

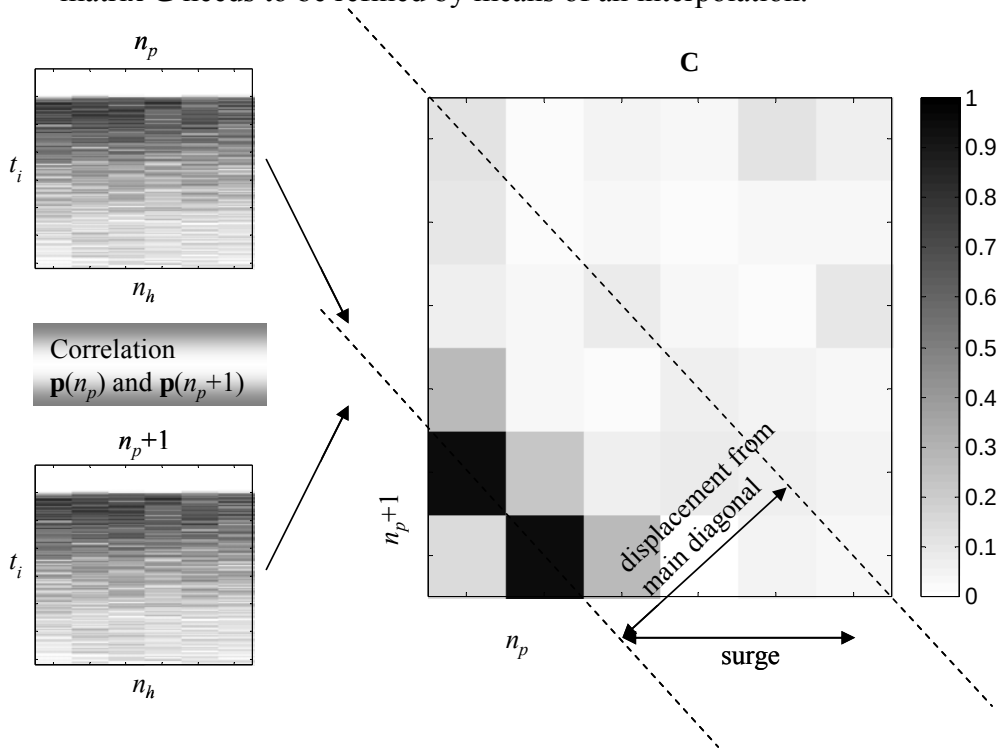


Figure 5-11 *Surge estimation with the Displaced Phase Center method.*

With the integration of the surge, an estimate for the along-track position $x(t)$ is found.

Displaced Phase Center method for sway estimation

This procedure estimates the sway for every ping. The input signals for the algorithm are the received data of the overlapping phase centers. In the case of Figure 5-11, this means two overlapping phase centers, i.e. two signals for ping n_p and two signals for ping n_p+1. The sway estimate now follows from the signal at ping n_p matched filtered with the signal at ping n_p+1.

$$\gamma_c\left(t,n_p,n_h\right)=\frac{\int p\left[t,n_p,n_h\right]p\left[t-\tau,n_p+1,n_h+\Delta h\left(n_p\right)\right]\mathrm{d}\tau}{\left|p\left[t,n_p,n_h\right]\right|\left|p\left[t-\tau,n_p+1,n_h+\Delta h\left(n_p\right)\right]\right|}$$

$$\Delta y_m\left(n_p\right)=\sum_{n_h}\left[\frac{ct_{\max}\left(n_p,n_h\right)}{2\left\{1-\max_t\left[\gamma_c\left(t,n_p,n_h\right)\right]\right\}}\left(\sum_{n_h}\frac{1}{\left\{1-\max_t\left[\gamma_c\left(t,n_p,n_h\right)\right]\right\}}\right)\right], \tag{5.12}$$

where γ_c is the output of the convolution between the signal at ping n_p and the signal at ping n_p+1, which is the correlation coefficient between the two as a function of time shift. The displacement of the midpoints from the ideal straight line, the sway, is denoted by Δy_m. The maximum of the correlation function is an estimate for the sway. The number of overlapping phase centers determines the number of estimates. These estimates are combined in a sum, weighted by their amount of correlation. For instance, when the correlation function γ_c peaks at $t = 0$, it means that the signal arrival of both pings is coherent and no sway (deviation from the straight line) is present.

Displaced Phase Center method for *yaw* estimation

When the yaw is estimated with a DPC method it is commonly referred to as DPC2 or DPC Antenna (DPCA). The estimation of yaw is based on the variation in $t_{\max}$ as a function of hydrophone in Eq. (5.12). The same result can be achieved by searching for a correlation peak in the beam or wavenumber direction. A correlation in the beam space would ideally also result in a peak with a high correlation coefficient. The width of this peak, e.g. the 3dB-beamwidth, is nonetheless wide and for broadside given by the second order approximation that was explained in Chapter 2: $50.8\ \lambda/L$ °. This value determines the accuracy of the ping-to-ping yaw estimate. Together with the sway estimates, this results in an accumulating error, which was studied by Bellettini (2002). This accumulation was found to be a severe drawback to the method when long apertures are considered. This method was therefore discarded in the following analysis.

Three important tuning parameters have to be considered when applying DPC:

1. The correlation window is an interval in range (or time) that is the same for the two pings. This interval should be chosen such that it gives the best estimates for surge and sway. When the interval is too small, the statistical content is not adequate and the estimates are not reliable. On the other hand, when the interval is too large, stability may not be guaranteed. Effects that contribute to this are medium instabilities (eddies), motion of the sonar during the ping and bathymetry variations causing uncertainties in the insonification plane of the sonar. The latter effect can be tackled by regularly updating the surge and sway estimates. In practice, the range window is estimated adaptively such that the resulting correlation coefficient(s) are optimal.
2. Thresholds to reject signals are necessary when processing actual sonar data. Malfunctioning of a single hydrophone may cause severe errors in the estimation. Two thresholds were implemented to avoid such situation. The surge estimates of all overlapping hydrophones are checked and when a surge estimate of a hydrophone deviates from the median of the estimates of the other hydrophones, this specific hydrophone is left out. For the sway non-physical estimates, for instance with extremely large motion, are also removed.
3. The order of interpolation for sway estimation is not set a priori. The input of the DPC method consists of acoustic data with a certain sample frequency f_s. As becomes clear in Section 5.4, this is not enough for a proper sway estimate. Since the computational effort is low because the interpolation is performed only on one correlation vector per ping, the order is set to 32.

The second method, *Image Correlation* (IC), is, as its name suggests, also based on correlation. The images of subsequent pings are correlated in two dimensions to estimate an x and y deviation. The obtained values are then related to yaw, sway and/or surge.

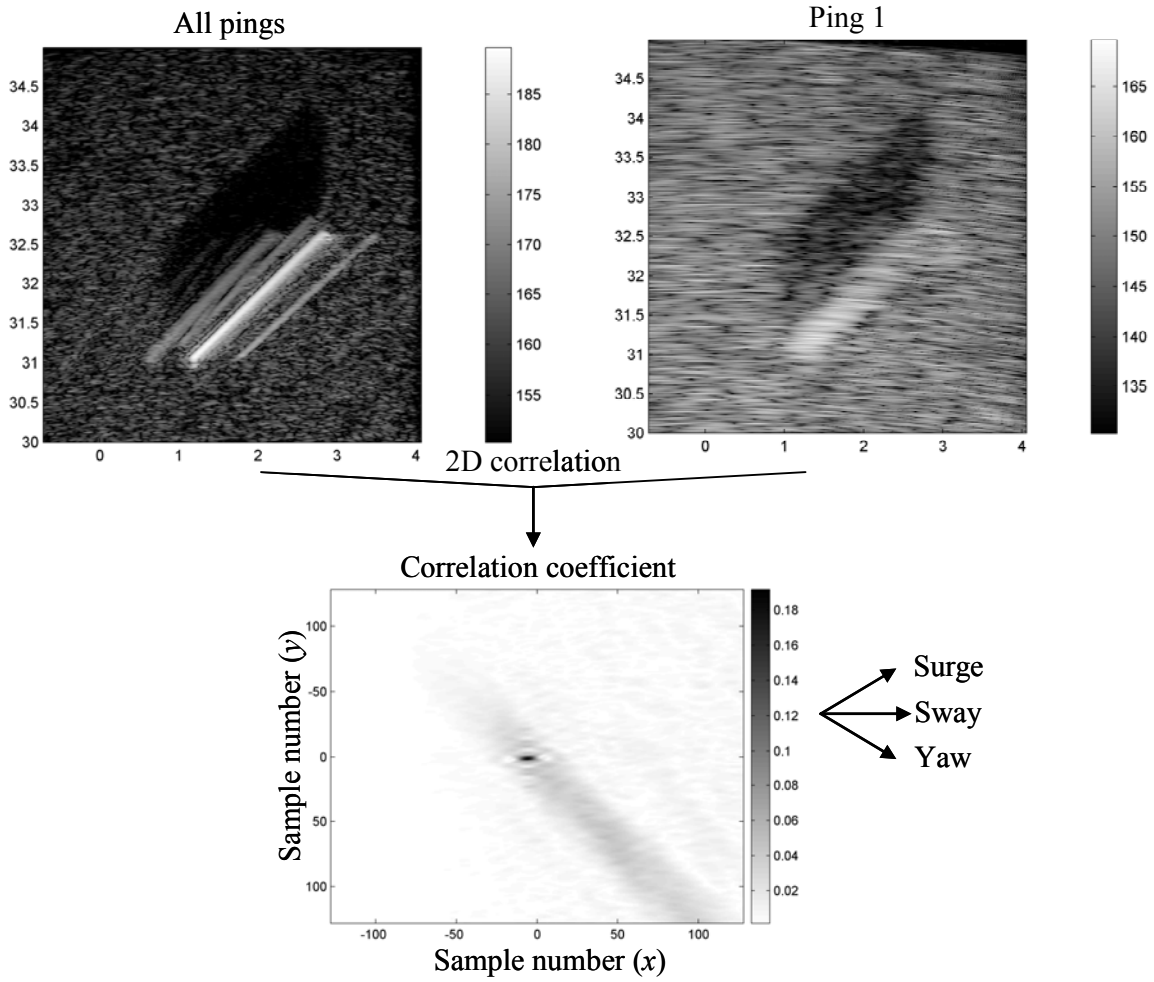


Figure 5-12 *Image correlation autofocus. A ping is processed separately and the result is 2D-correlated with the reference image. A peak appears where the ping result fits best. Surge, sway and/or yaw is derived from the 2D shift.*

As is clearly visible in Figure 5-12, image correlation process starts with a reference image. This can be the SAS image resulting from the prior pings or the SAS image of all pings without the ping under consideration. The considered (or current) ping is 2D convolved with this reference image, viz. correlated for all shifts in x and y. Naturally, the two images need to overlap completely. When the two images are identical, this procedure gives a peak with correlation value equal to one at the origin. However, the images are never the same, because the resolutions of the two are different. This means that in practice a clear peak, much lower than one, shows at the position that corresponds to the mutual shift between the two images. Assuming that this shift is caused by wrong motion estimation/compensation, a better estimate is now found with IC.

Additional computations. At first glance, it appears that autofocus is a step prior to and separated from imaging. When DPC is used the input data are correlated by means of an FFT. This FFT has to be applied anyway, which means that DPC has a small additional computational effort: only one temporal FFT. IC is a computationally more intensive method, which requires calculation of an image for every ping. This means that the total computational effort is multiplied by a factor 2 to 3.

Global or local autofocus. Contrary to DPC, which is a local method, IC can be applied to the whole data set, which yields more stable motion estimates. For example, one could first obtain a SAS image without autofocus or with DPC estimates. Then using IC on the SAS image and the underlying data one can estimate sway and yaw ping-by-ping. The preferred imaging for this autofocusing principle is SFI because of the ping-by-ping procedure. Such a process does not diverge and has a better resolution, because it is based on a stable and high-resolution image. It can also be repeated as an iterative method to further optimize the image.

5.3.1. Results on rail experiments

In 1999 rail experiments have been conducted by the French research institute Groupe des Etudes Sous-Marines de l'Atlantique (GESMA) and the British research institute Defence Evaluation and Research Agency (DERA). The trial consisted of a series of experiments, with different targets at various ranges between 25 and 100 m. After thorough analysis, e.g. described by Bellettini (2000) and Hétet (2000), the data have been kindly made available to TNO for analysis and algorithm development; see Groen (2001).

The results of this analysis consist of a comparison of different SAS images. In Section 5.2.2 it was shown that the results of SFI are almost equal to Convolution for this SAS system. Therefore, SFI is not discussed. One data set is chosen for analysis; a sphere at 23 m range, insonified with 20 kHz bandwidth CW pulses at 150 kHz. Two aspects in the processing are analyzed. First, Convolution is compared with Stolt Migration, followed by a comparison of DPC and IC autofocus.

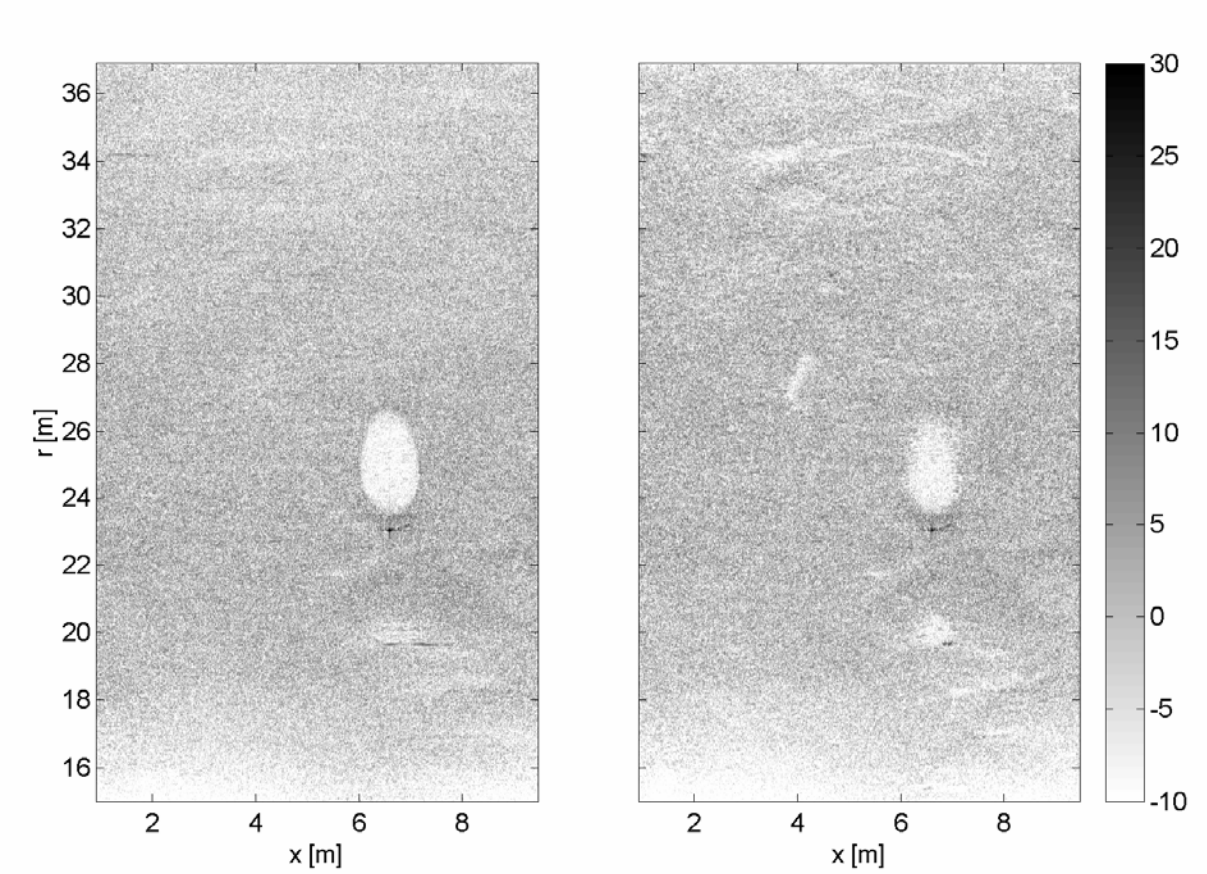


Figure 5-13 *Comparison of SAS images of the sphere at a range of 23 m. Single focus range Convolution imaging on the left and Stolt migration on the right.*

Figure 5-13 shows two SAS images from Convolution imaging on the left and Stolt migration on the right. The sphere is visible with a black spot at about $x = 7$ meters and $r = 23$ meters. The shadow behind it is visible between $r = 24$ and 27 meters. It is clear that the left image is correctly focused in a limited area around the sphere, where the right image is focused correctly for all ranges. However, the acoustic shadow behind the sphere in the left image is surprisingly sharp. This interesting effect is explained and exploited in Chapter 6.

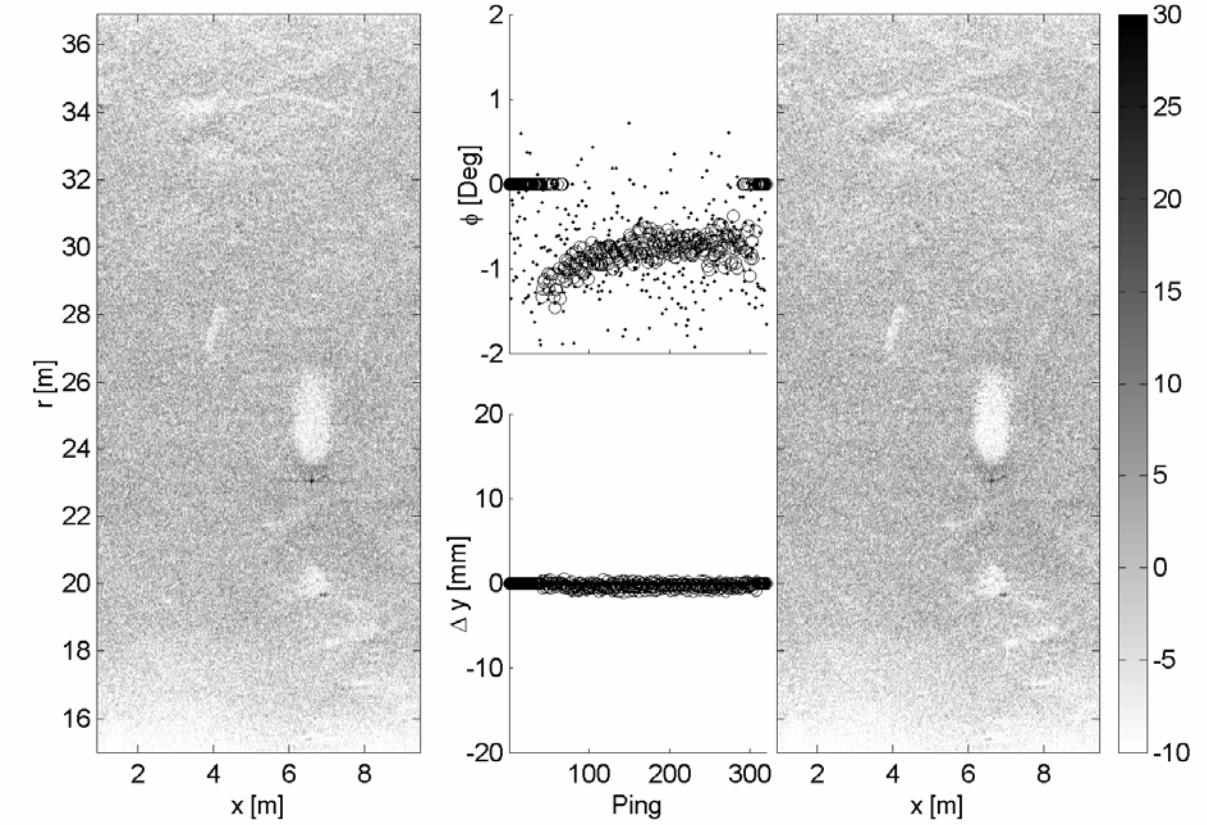


Figure 5-14 *Autofocus techniques applied to the data of the sphere at a range of 23 m. DPC on the left and IC on the right. In the middle the estimates for yaw (φ) and sway (Δy), with IC with the circles and DPC with the dots.*

Stolt migration is applied with different autofocus methods in the images of Figure 5-14. The left image is obtained with DPC and the right image with IC. The correlations used in DPC concern an area around the strongest reflector and also provide an estimate of the yaw angle φ. IC provides an estimate for both sway and yaw. The yaw estimate is much more stable with IC, but the images do not show much difference for this data set.

5.3.2. Results on experimental data with a ship mounted sonar system

The low frequency synthetic aperture sonar trial was conducted during ten days in September 2002 in the waters near Brest, France. Two sheltered locations with different bottom type were selected for placing targets; one near Morgat in the Bay of Douarnenez, depth about 25 m, the other near Rascas in the Bay of Brest, depth about 35 m. Each target field consisted of three metal cylinders and one fully buried dummy Manta mine. The cylinders ranged from proud and half buried to fully buried. The targets were placed by divers in the month preceding the trial. Additional to the target fields, three shipwrecks were measured at various locations in the same area.



Figure 5-15 *The mine hunting vessel HNLMS Hellevoetsluis (left) and the GESMA low frequency Synthetic Aperture Sonar (right).*

Before the trial, bottom coring was carried out at both trial locations and the cores were analyzed ashore. It appeared that the Morgat sediment is much more homogeneous (sand) than that in Rascas, which could also be observed during visual inspection. In Rascas, a dense layer of shells covered the somewhat muddy sea floor. The trial ship was the Alkmaar Class mine hunting vessel HNLMS (Her Netherlands Majesty's Ship) Hellevoetsluis, made available by the Royal Netherlands Navy (RNLN), of which a photo is shown on the left of Figure 5-15. This ship is equipped with a PAP (a remotely operated vehicle for inspection with an underwater camera), array stabilization system for the mine hunting sonars, two echo sounders, DGPS navigation and autopilot, and divers were on board for visual inspection of target burial. With the help of the RNLN maintenance service (SEWACO), a GESMA sonar was installed on the ship instead of the detection sonar. The ship's classification sonar was kept operational. For maneuvering, and especially during track following, active rudder and bow thrusters were sometimes used. Due to technical constraints, the sonar tilt angle was fixed at 32° from the horizontal. The wet-end part of the sonar is composed of the receive and transmit arrays in the front of a bronze container containing the electronic components. An Octans motion reference unit is fixed inside a cylindrical box, which is visible on the right of Figure 5-15. The receiver is composed with four PJ40 modules to form a linear array 80 centimeters long with 48 hydrophones. After amplification by a user controlled gain, each channel is synchronously digitized in a 16 bits ADC and recorded directly on carrier frequency. Sampling frequency was either 75 kHz or 100 kHz, for an operating frequency band of 15 – 25 kHz.

This section shows results for one (arbitrary) eastward experiment in the Morgat area, parallel to the target field followed by an example of sonar recordings of the shipwreck the 'Swansea Vale'. Figure 5-16 shows the recorded GPS track of the ship in blue dots and the target locations in red crosses. Obviously, the track is not entirely straight, which calls for motion compensation prior to SAS processing.

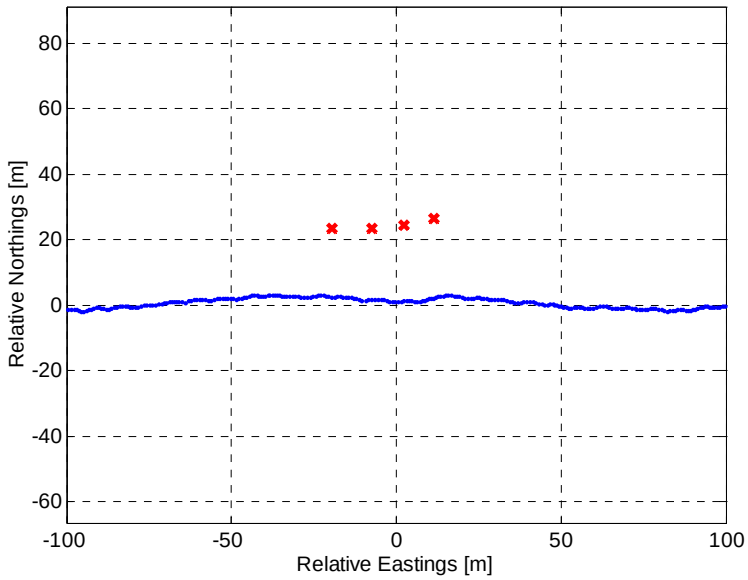


Figure 5-16 *Measured ship's track from GPS and target locations, Morgat target field.*

The earlier explained DPC (Displaced Phase Center) method of Bellettini (2000) has been applied to estimate sonar motion from the acoustic signals themselves. DPCA is an autofocusing, or micro-navigation, method that yields estimates of sonar surge and, optionally, sway and yaw, using the cross-correlations of overlapping midpoints between consecutive pings. It complements the motion reference unit measurements. The performance of DPCA depends on the magnitude of the correlation coefficients as shown by Bellettini (2002). To check this, the matrix of midpoint cross-correlations between consecutive pings was computed. Figure 5-17 shows this matrix for two specific ping numbers.

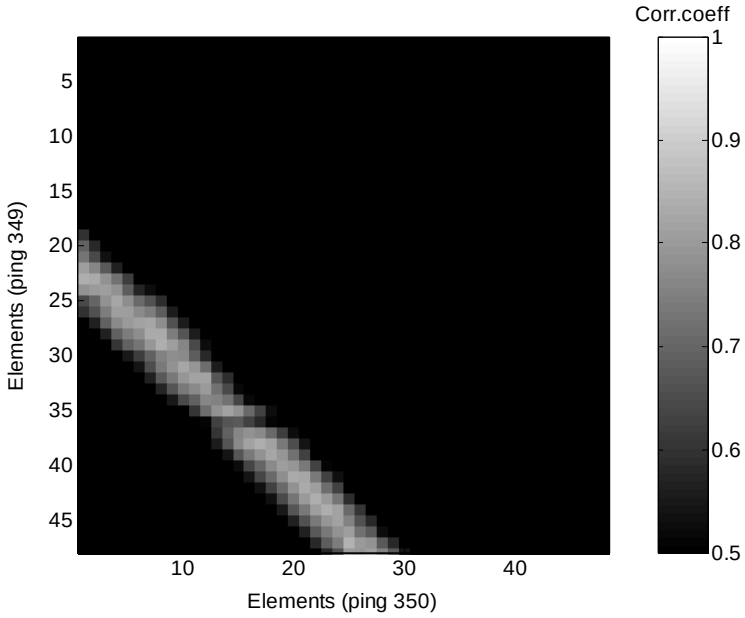


Figure 5-17 *Cross-correlations of overlapping midpoints in two consecutive pings.*

Figure 5-18 shows two graphs of surge (displacement in along-track direction for each ping) from DPC and sway (sideways sonar motion) estimated with DPC and Image Correlation (IC).

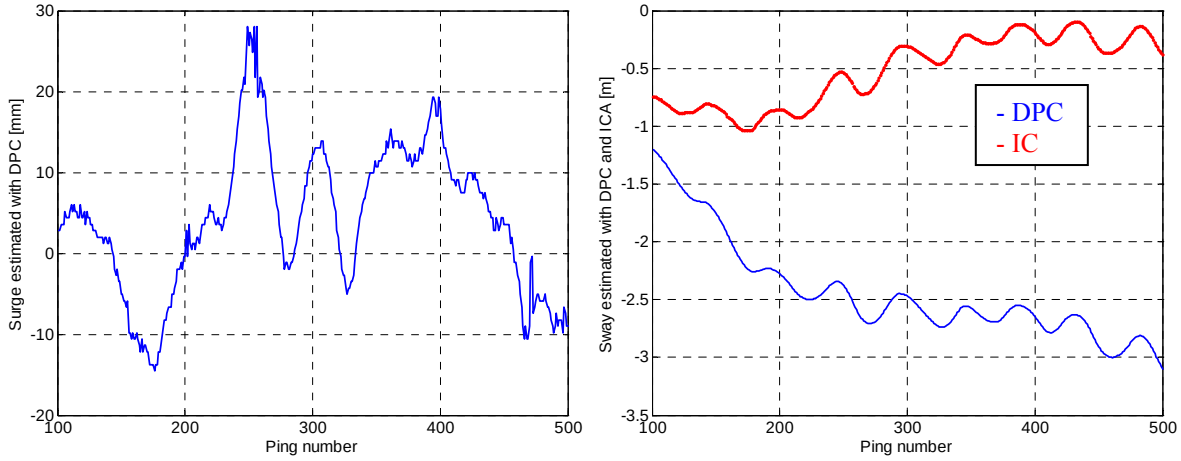


Figure 5-18 *Surge (left) and sway (right) estimated from the acoustic data using DPC and IC.*

It can be seen from the figures that the ship motion is indeed rather small. Nevertheless, the motion is large enough to have a severely degrading effect on SAS image quality if left un-compensated. The difference in motion between IC and DPC appears rather large after 500 pings, but both acoustic images are still of relatively high quality. This is explained by the track difference being close to a rotation only, which results in a constant displacement for all pixels in the SAS image. The other correlation based autofocusing method that was employed is IC, which was described in the previous section. The imaging result that was achieved with this method is slightly better than with DPC. We show the side-scan image (one beam per ping) and the SAS result with IC in Figure 5-19.

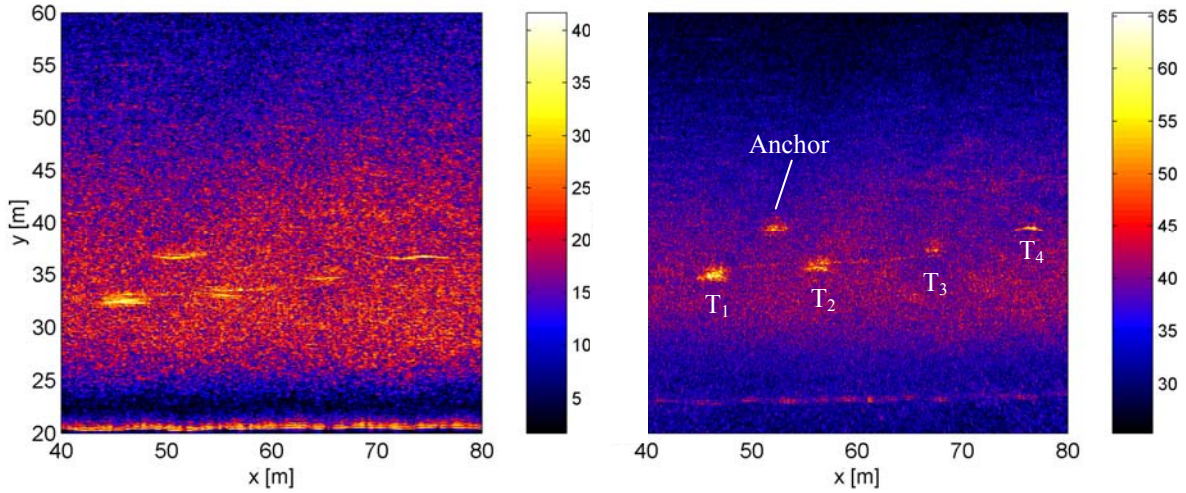


Figure 5-19 *Left: Side scan image for comparison. Right: SAS image, using Stolt migration and Image Correlation Autofocus. T_4 was temporarily marked with a reflector, hence the bright spot. The fifth reflection (between and little above T_1 and T_2) is an anchor from the diver's dinghy.*

Results with the shipwreck Swansea Vale

The cargo ship Swansea Vale was built in 1909 and sank in 1918 just outside the entrance of the bay of Brest after striking a submerged wreck. She was carrying wood from Bayonne to Dunkirk at the time. Her length was 71 m and her breadth about 11 m. The wreck's amidships is reasonably intact and upright, with boilers and engines still in place. The stern is also upright, with big holes. The seabed is flat and sandy with a lot of shells and strips of maerl (calcified seaweed).

The wreck proved to supply an excellent data set to point out the need for motion estimation and compensation, since it is more photo-like than the sonar images of the mines. The drawback of a data set of a wreck is that it is not a point target.

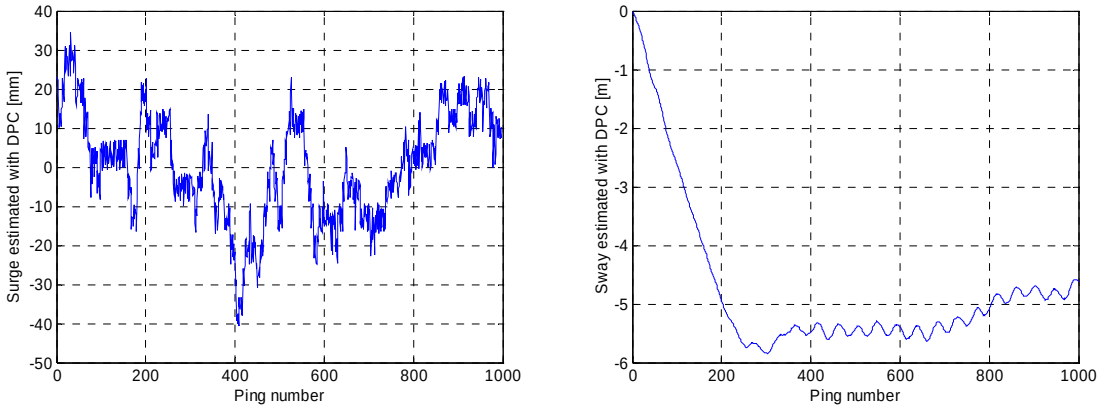


Figure 5-20 *Surge (left) and sway (right) estimated from the acoustic data using DPC.*

Figure 5-20 shows the estimates of the sonar track with the sway and surge output of the DPC method. The surge output shown is centered on zero, which would correspond to the average speed of the ship. The right hand plot shows the dynamic behavior of the ship, which was not completely on track at the beginning of the experiment. The automatic steering control system of the ship causes the sinusoidal behavior in both the surge and sway results. This experimental data analysis does not aim at a comparison between IC and DPC, but at a comparison between DPC and no motion compensation at all. Secondly, the integration angle β is investigated in combination with these DPC estimates. The integration angle is directly coupled to the synthetic aperture length and the range by $\tan(\beta/2) = L/(2r)$. This angle shows to be a suitable parameter for sensitivity analyses of SAS, and therefore, shows up frequently in the remainder of this chapter and Chapter 6.

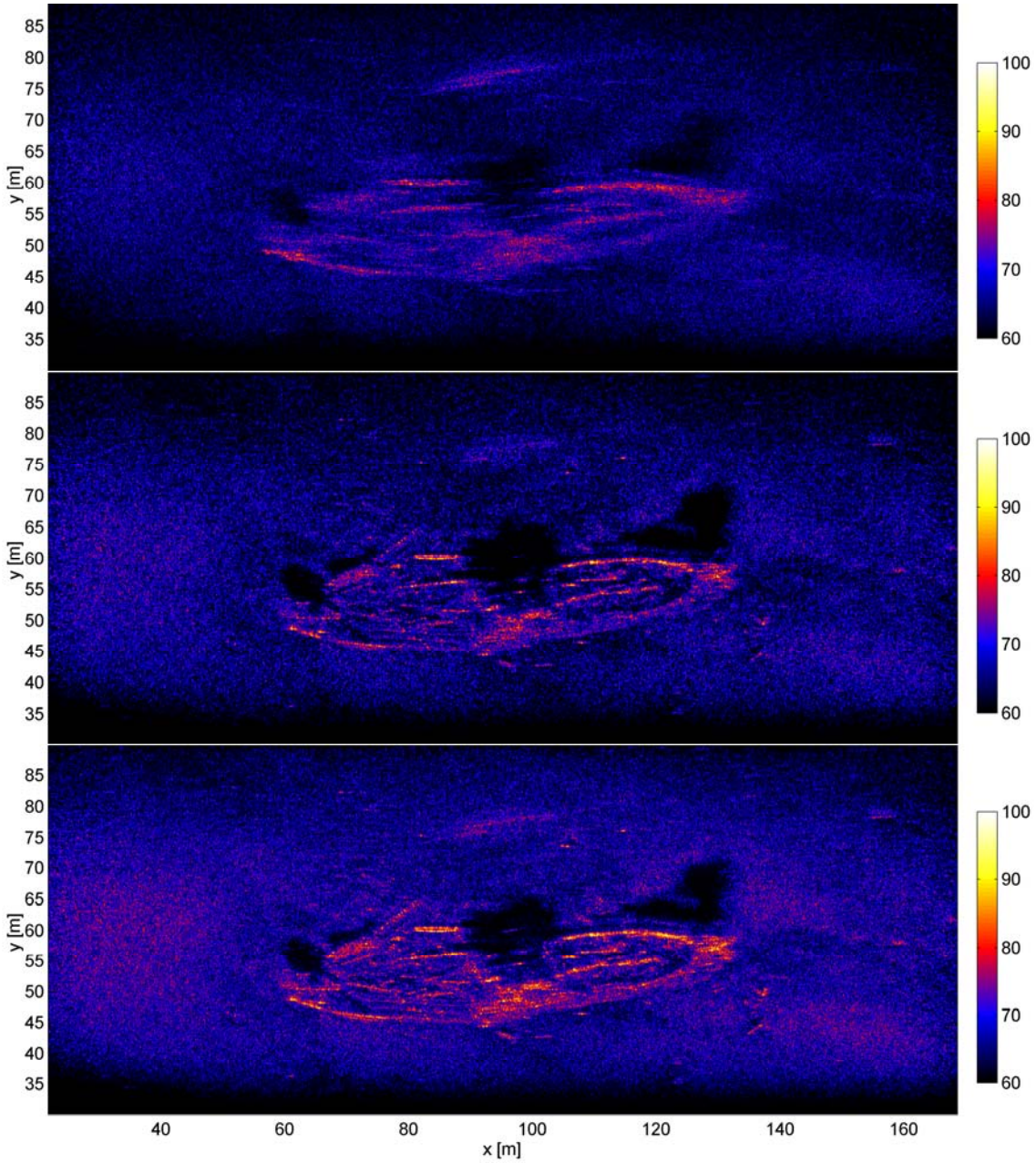


Figure 5-21 *Top: image of Swansea Vale wreck without motion compensation and an integration angle β of 30 °. Middle: SAS image, using Stolt migration and motion compensation with DPC estimates and an integration angle β of 15 °. Bottom: SAS image, using Stolt migration and motion compensation with DPC estimates and an integration angle β of 30 °.*

Figure 5-21 shows the uncompensated (top) and the motion compensated (bottom) SAS image for the Swansea Vale wreck with the same color scale. The difference is significant and it is clear that motion estimation and compensation is necessary for proper acoustic imaging. A rather clear image of the wreck is accomplished, which even shows a shadow at these low frequencies. A comparison by Hétet (2004) between high frequency and low frequency sonar images showed a different highlight behavior in the images. Apart from resolution, high frequency on the order of 100 kHz and low frequency on the order of 10 kHz undergo different

physical processes. The low frequency parts can reveal buried parts that are impossible to detect at the high frequencies. The scattering of the parts of the wreck also depend on the signal frequency.

The second issue is investigated by comparing the middle and the bottom image of Figure 5-21. The overall energy level is somewhat higher for $\beta = 30^{o}$. Also, when looking carefully, some features are apparent in the bottom image and not in the middle image, especially in the shadow areas. The clear shadows are on the other hand a benefit for the small integration angle. The difference in resolution is more difficult to assess from this qualitative comparison between the two images.

5.4. Motion compensation

Faster imaging can be achieved in different ways, but for each gain in speed usually a loss in flexibility or validity appears. The designer of a future operational SAS system needs to be aware of these trade-offs in order to make a well-considered decision on which signal processing algorithms to use. In this section the most promising candidates for SAS imaging are considered: wavenumber frequency domain processing methods. The main restriction of such methods is the requirement that the sonar track is straight and uniform due to the application of a spatial Fourier Transform. This restriction is analyzed and removed.

In order to investigate and meet the challenges with fast imaging methods, the Norwegian Defense Research Establishment (FFI) and TNO combined their knowledge, data and software. In this respect the key issue is the combination of valuable measurement data from a state-of-the-art underwater vehicle (HUGIN, see Figure 5-22), a realistic acoustic data simulator and the wavenumber frequency processing software. The accurate experimental navigation data supply the answer to whether or not wavenumber frequency methods can be applied to state-of-the-art AUVs.



Figure 5-22 *Deployment of the HUGIN AUV.*

After considering the validity of motion compensation in general, the analysis presented here consists of two parts. First, pure simulations are carried out to investigate the sensitivity of motion compensation to transmit beamwidth and sonar track. Secondly, realistic simulations are analyzed using measured sonar motion of the HUGIN AUV of FFI in Norway as a real life application (see Hagen (2001) and Hagen (2002)). This system is a logical choice for this analysis since it will be equipped with a SAS in the near future. It is already being used operationally for survey operations where side looking sonar plays a major role. To obtain high-resolution performance for such a sonar, synthetic aperture is the solution.

Note that the measurement with inertial sensors or estimation with autofocus methods of sonar motion is assumed to provide the input to the motion compensation. These aspects of motion estimation were studied in Section 5.3, and additionally by, e.g. Gough (1997) and Shippey (2001).

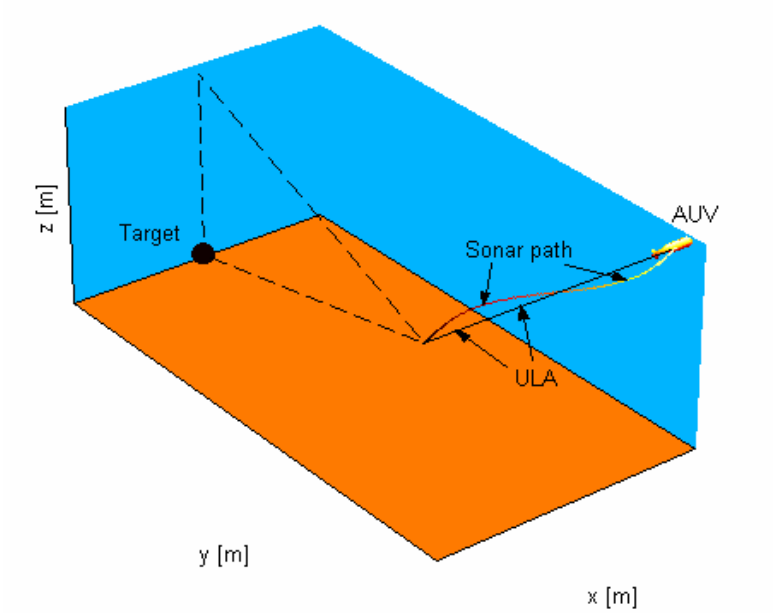


Figure 5-23 *Typical mine-hunting scenario: the sonar is traveling past a possible target along a path that is close to a straight line.*

5.4.1. Validity of motion compensation

Wavenumber frequency processing requires rectification of the sonar track as illustrated in Figure 5-23 to the aforementioned ULA. In this process, the received sonar signals are shifted in time to place them spatially in the ULA. In other words: the true SAS sonar trajectory is projected onto a virtual straight track. Theoretically, this time shift should construct the signal as received on the ULA from the measured signal. This is achieved by applying a time shift to the original hydrophone data based on the deviation from the straight line in the plane towards the target (area) as depicted in Figure 5-24.

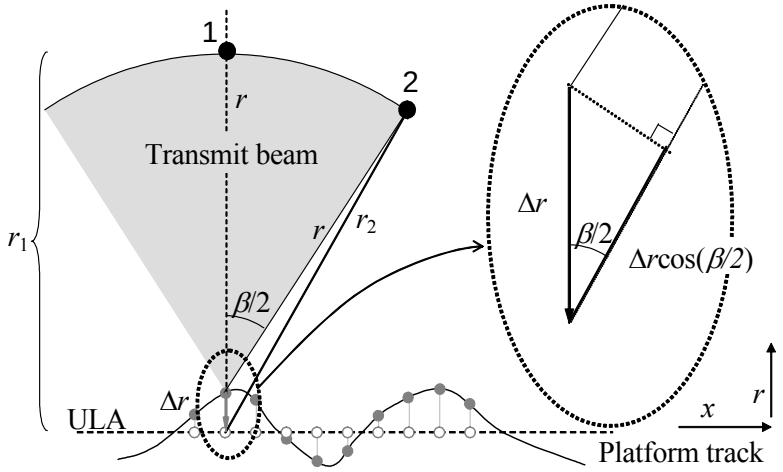


Figure 5-24 *Displaced and corrected midpoint positions and influence of shift Δy for target 1 in the center and target 2 at the edge of the beam.*

The projection on the ULA is carried out under the assumption that the applied time shift of the signals is the same for all the scatterers in the imaged area. This assumption is inherent to the method: from a recorded receiver a new receiver is created and thus the data extrapolated in one direction. At the end of this section methods are discussed that can overcome this issue. This assumption loses validity with increasing transmit beamwidth due to increased difference in angle of arrival of reflections from scatterers within the beam. Moreover, the validity diminishes with increasing deviations from the straight line. Figure 5-24 illustrates this effect schematically. The projection of the sonar track on the ULA corresponds to a displacement Δr. The angle β is the effective integration angle of the synthetic aperture, which is smaller than or equal to the source beamwidth. The range r_1 of target 1 from the current ULA midpoint equals $r_1 = r + \Delta r$. However, the range r_2 of target 2, which was originally at the same range as target 1, becomes $r_2 = r_1 + \Delta r\cos(\beta/2)$. Since target 2 receives the same time shift, the range error equals $\Delta r[1-\cos(\beta/2)]$.

5.4.2. Non-directional versus directional motion compensation

To account for the effect described in the previous section, an improved approach for the motion compensation investigated. Normally, the signal is assumed to arrive from the broadside direction, without taking the target direction into account. Therefore, this standard approach is from now on referred to as Non-Directional Motion Compensation (NDMC). This method can be enhanced with the knowledge of the geometry of the sonar track and the insonified area. The time shift is then based on the correct time delay for a certain target position in the SAS image, which is usually the middle for this analysis. This alternative method is referred to as Directional Motion Compensation (DMC), which is not necessarily better but establishes flexibility. For instance, one can choose to have optimal performance in a certain relevant part of the image or one can calculate the image several times with motion compensation for different target positions. The performance of DMC versus NDMC is investigated in the remainder of this document. This section presents further details of the two approaches.

Both NDMC and DMC are applied as phase shifts on the temporal Fourier transformed data before the spatial Fourier transform is applied. The Fourier transforms have to be applied anyway, so this does not slow down the computations.

The phase shift $\Delta\varphi$ for non-directional motion compensation is given by:

$$\Delta\varphi(n_p, n_h) = 2k\Delta r(n_p, n_h), \tag{5.13}$$

where $k = 2\pi f/c$ is the wavenumber, Δy is the in-plane deviation at ping n_p and hydrophone n_h, f is the frequency and c is the sound speed. DMC corrects for the angle γ between broadside and the direction of the middle of the imaged area:

$$\Delta\varphi(n_p, n_h) = 2k\Delta r(n_p, n_h)\cos\vartheta(n_p, n_h), \tag{5.14}$$

where ϑ at ping n_p is calculated from:

$$\cos\vartheta(n_p, n_h) = \frac{r}{\sqrt{\left[x_{\text{image}} - x_m(n_p, n_h)\right]^2 + r^2}}, \tag{5.15}$$

where x_{image}, r is the position of the middle of the SAS image and x_m is the position of the midpoint of hydrophone n_h at ping n_p.

The computation time for both methods is the same, i.e. only an element-wise multiplication with the frequency domain data. Both methods seem rather simple, but in practice it is the combination of motion estimation, motion compensation and imaging, which is the challenge.

5.4.3. Simulated scenarios

The effects on SAS image quality of time shifting due to known SAS sonar motion are investigated with simulations. To start the analysis, in this section the effect of deviations from the ULA is shown. Deviations are introduced and the SAS image without compensation is investigated. Deviations of several wavelengths are realistic, because they usually correspond to centimeters.

Twenty different scenarios have been simulated using the simulator SIMONA. The following parameters for the simulations are fixed: the signal is a 20 kHz bandwidth continuous wave (CW) pulse of .05 ms duration and centre frequency 150 kHz. The location of the source is at the centre of the 32 receiving elements, which are spaced by 10 mm or half the center wavelength. The deviation from the straight line is incorporated in the simulations as a sinusoidal motion. The motion takes place in the across-track plane (slant-range plane) directed to the target, which is the worst-case scenario. The sinusoid that describes the track consists of exactly one period and the amplitude is varied in five steps according to the wavelength sequence 0, $\lambda/10$, λ, 10λ and 100λ. Other types of deviation have also been analyzed, but

yielded no significantly different results. The source beamwidth is taken into account through the number of integrated pings, which is varied as 8, 16, 32 and 64 pings, respectively. The corresponding transmit beamwidths for the integrated pings are 6°, 12°, 24° and 46°. In the simulations, a single point target is simulated and no reverberation or noise is added. An example of the response for a highly non-straight sonar track is visible in Figure 5-25. It should be noted that the across-track motion is so severe that the signal approaches the lower bound of the image. The effect on the corrected signals in the bottom image materializes as a gap in the sidelobe behavior.

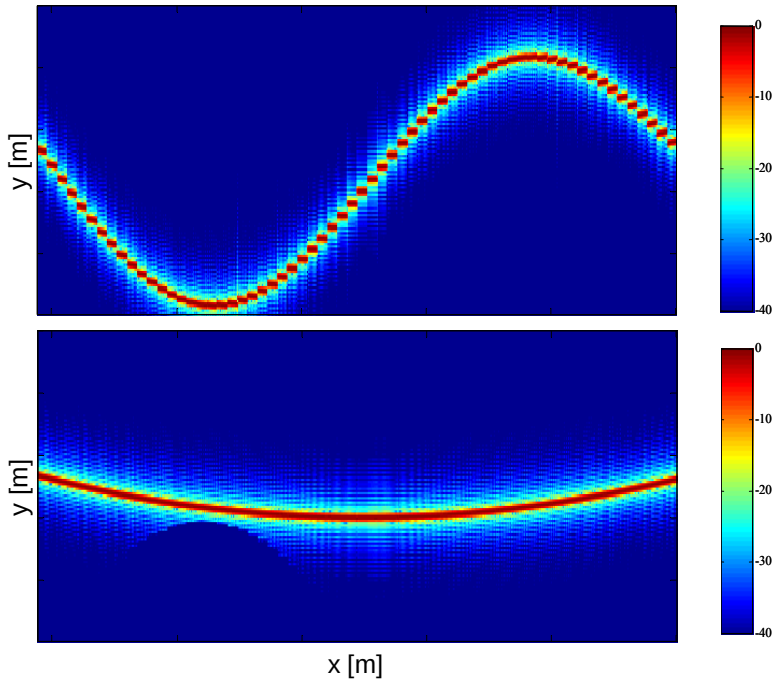


Figure 5-25 *Disturbed and corrected target response: input for SAS processing. Amplitude of deviation from the straight line is 100 times the wavelength λ.*

Figure 5-26 shows the SAS images with a dynamic range of 40 dB, with the maximum in black. For very large path disturbance, i.e. 100λ, the result is deteriorating significantly. However, the performance is acceptable for disturbances smaller than 100λ.

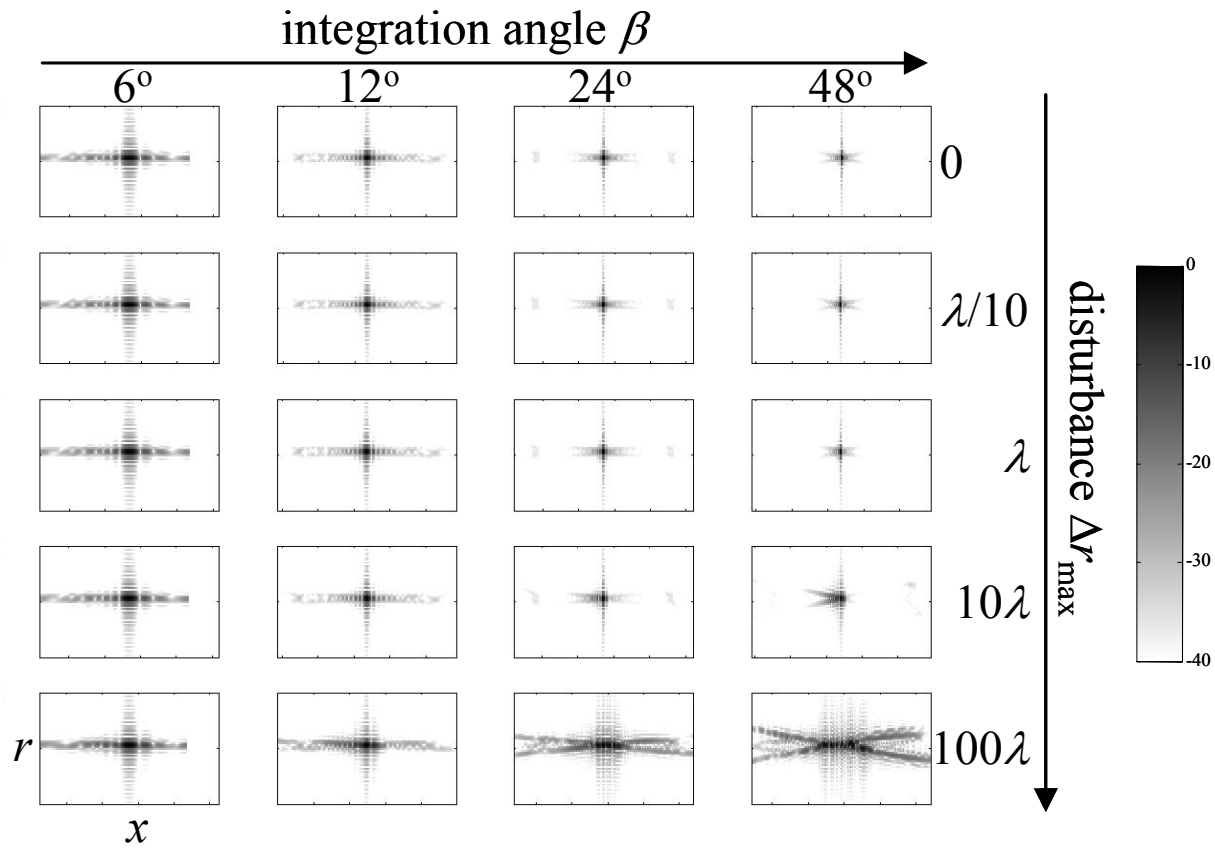


Figure 5-26 *SAS images (1 x 1 m) from wavenumber-frequency domain SAS without motion compensation for varying integration angle β (equal to the transmit beam) and disturbance amplitude.*

5.4.4. Application of motion compensation to simulated scenarios

In this section the results of the application of directional motion compensation (DMC) are shown. The method is compared with the original NDMC. Since DMC is optimal for only one along-track *x*-value (namely in the middle), it is necessary to analyze the validity of the method for the other *x*-values. Therefore, the simulated scenarios are adapted to have three targets: one in the middle and two at the sides of the transmit beam. The other simulation settings are exactly the same as in the previous case.

In Figure 5-27 and Figure 5-28 the resulting images after SAS processing are shown. In Figure 5-27 NDMC is applied. At first glance it is easy to see that the response of targets in the middle of the imaged area is not the same as at the side. Figure 5-28 shows the results of DMC. All SAS images are apparently sharper, but the result is certainly not perfect. The column most to the right corresponds to the largest transmit beamwidth. Due to the disturbance an alias band arises in the images and additionally the target responses are smeared out. The side targets are smeared out more than the middle target, because motion compensation is most accurate for the middle (in both methods). DMC proves to deal better with alias lobes and smearing. The other interesting striking difference appears in the last row, which repre-

sents the largest deformation (100λ). A lot of smearing in the target responses is visible for both methods, but the performance of DMC looks better.

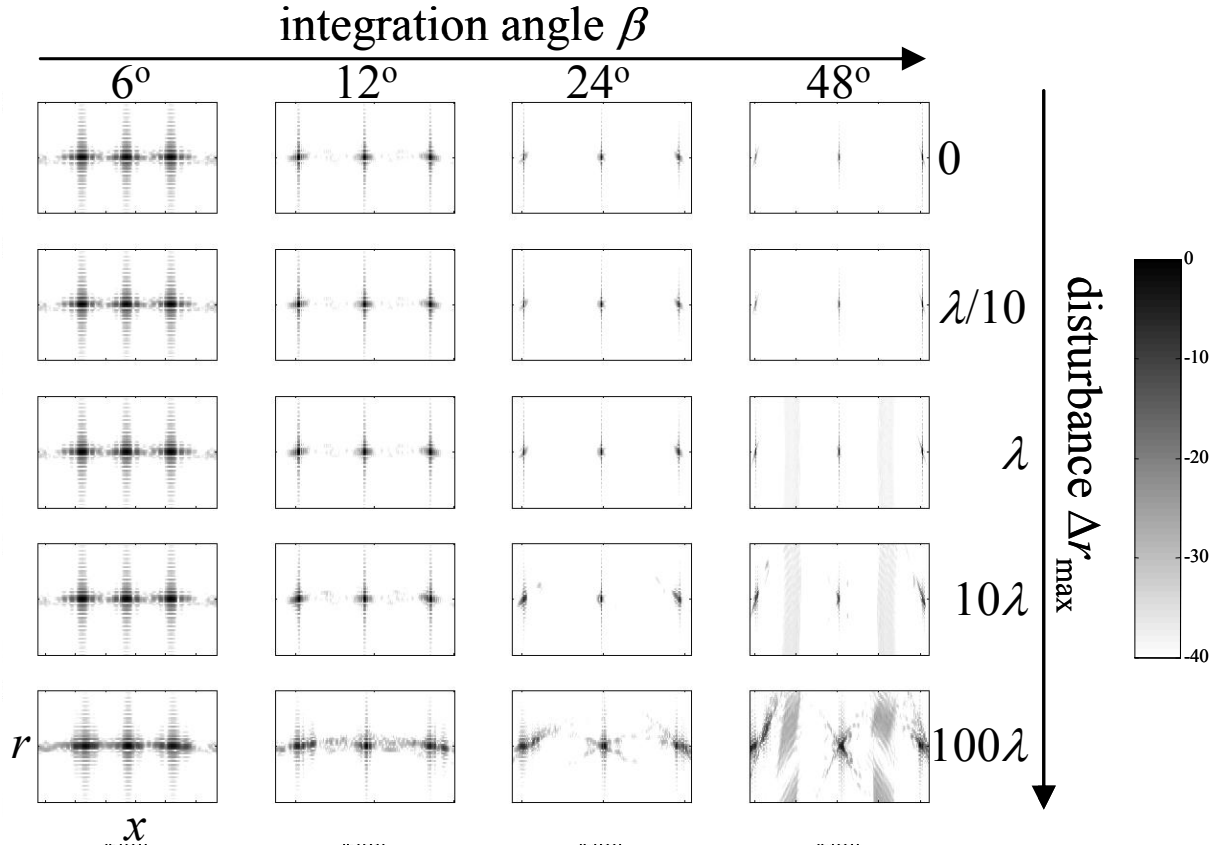


Figure 5-27 *Results from Non-Directional Motion Compensation (NDMC). In the 20 SAS images the disturbance amplitude and integration angle β are varied.*

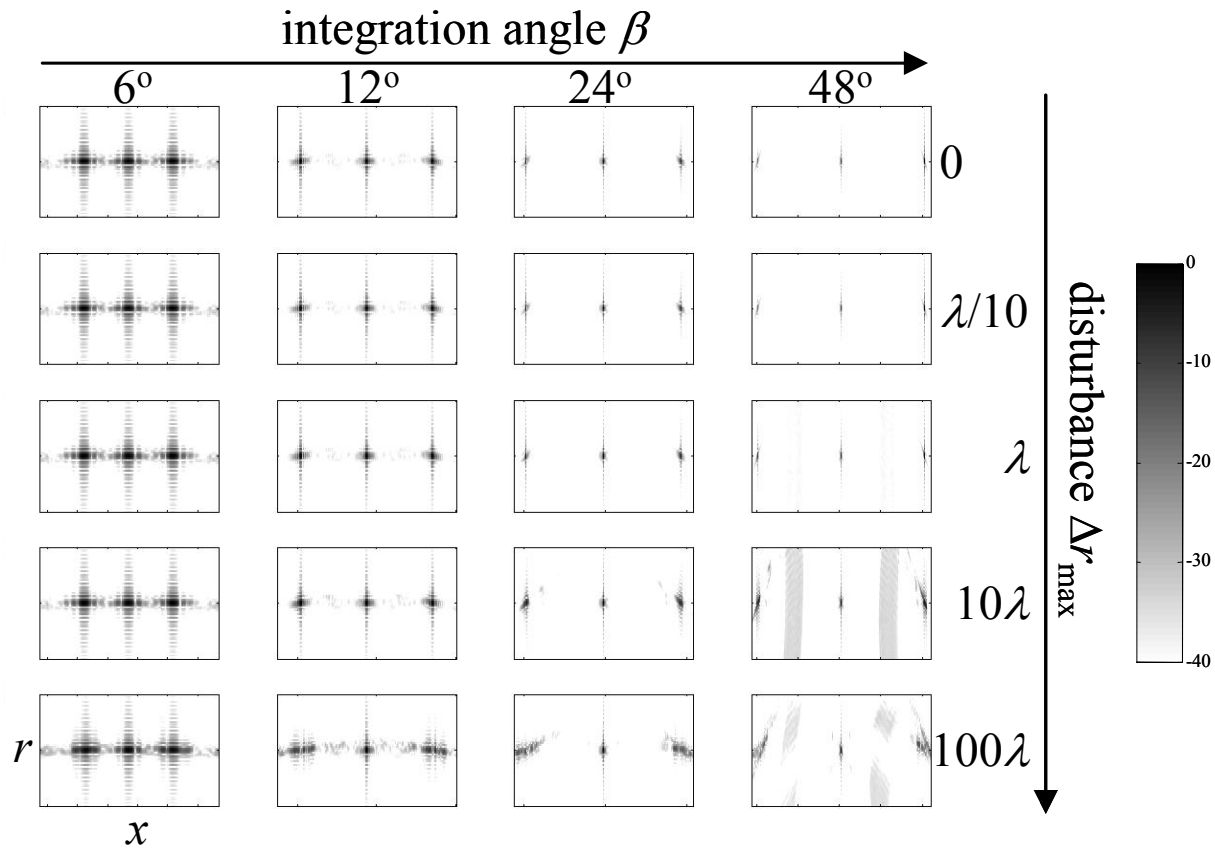


Figure 5-28 *Results from Directional Motion Compensation (DMC). In the 20 SAS images the disturbance amplitude and integration angle β are varied.*

5.4.5. Application to experimental data from the HUGIN vehicle

To test the validity of SAS wavenumber frequency processing in real life, a state-of-the-art Autonomous Underwater Vehicle (AUV) is used for a thorough investigation. In December 2001 a trial was conducted by FFI, where the HUGIN vehicle was deployed and recovered from the mine hunter KNM Karmøy described by Hagen (2002). After deployment, illustrated in Figure 5-22, the vehicle sails a track under water autonomously and surfaces afterwards. During the experiments non-acoustic data have been collected. Amongst others, the data consisted of latitude, longitude, depth, heading, roll and pitch. These data serve as input to SIMONA to simulate acoustic data from a sonar mounted on the HUGIN vehicle.

In the previous section a scenario has been sketched, which slightly differs from the simulation and processing in this section. The properties of the simulation with respect to acoustics are the following. The 64 transmitted pings are of the type CW/100kHz/0.1ms with a repetition time of 10ms. The target range is extended to a little more than 25 meters. According to the sensor data the AUV sails a path of about 11 meters for the selected part of the data. These acoustic properties are combined with the experimental non-acoustic data. First, a common scenario is analyzed, i.e. no drastic deviations from the straight line are present.

Secondly, the effects of a severe depth change, inducing large out of plane motion, are considered.

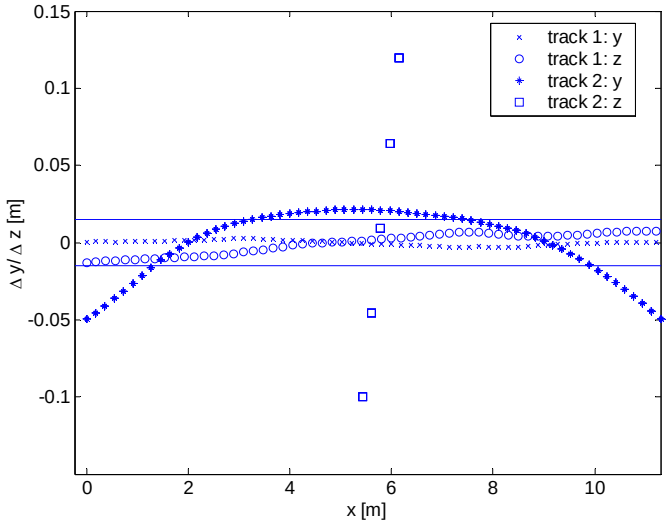


Figure 5-29 *Deviations from the ULA of the AUV. Both y and z deviations are show; λ is indicated by the two solid lines.*

Figure 5-29 shows the two tracks of the AUV, which are selected for the analysis. Of track 1 *y* and *z* are plotted versus *x* for every ping in x-marks and circles, respectively. The sonar is amazingly stable during this track and the deviations are within a wavelength, which is indicated by the two solid lines. The integration angle is about 25°, which places this simulation near the third column, middle row of the simulated images presented in Figure 5-26, Figure 5-27 and Figure 5-28. Of track 2, *y* and *z* are plotted versus *x* for every ping in stars and squares, respectively. During this track the sonar is rising rapidly, inducing large deviations both in-plane and out-of-plane. The deviation in z is much larger than a wavelength and is only partly shown, because the rest of the values exceeds the figure bounds. The transformation from *y* and *z* to in-plane and out-of-plane motion obviously depends on the grazing angle, i.e. the angle under which the sonar see the target vertically, that corresponds to the target range.

Track 1

Compared to the previous sections the simulated scenario here is much closer to a mine hunting operation. The object lying on the seafloor generates an acoustic shadow. This shadow moves according to the position of the sonar. The sea floor is modeled as 10000 scatterers, reflecting according to Lambert's law. This reverberation model, a part of SIMONA, was described in detail in Chapter 2. The resulting image in the left panel of Figure 5-30 indeed shows this shadow, but it is somewhat blurred.

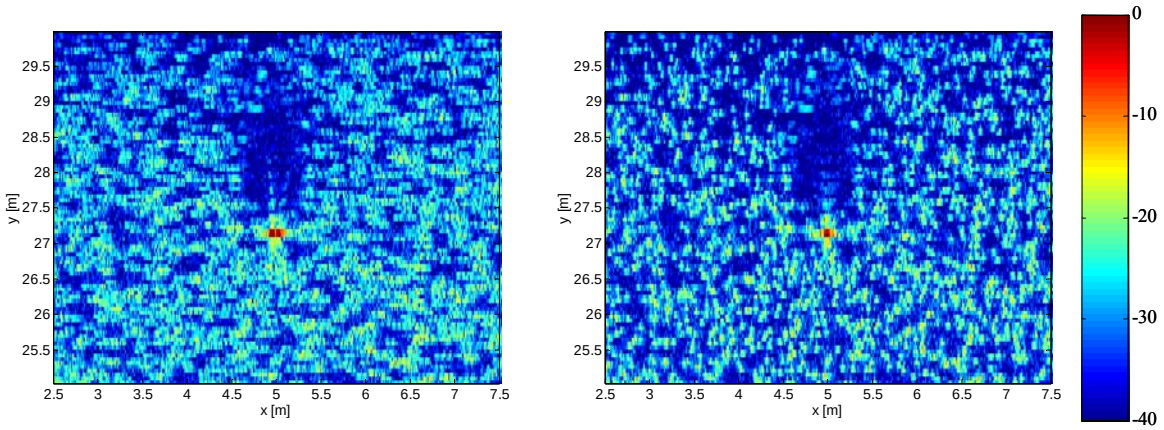


Figure 5-30 *SAS image with wavenumber frequency processing without motion compensation (left) and with directional motion compensation (right).*

After directional motion compensation the result has improved, which is visible on the right in Figure 5-30. Both shadow and target are sharper and the signal-to-interference ratio is higher. It can be concluded that motion compensation is a must for SAS on a state-of-the-art AUV, such as the HUGIN vehicle. Non-directional motion compensation is sufficient, but can be slightly improved by applying directional motion compensation.

Track 2

The example given above gives a rather favorable outcome of the SAS processing techniques. It appears that DMC is valid. However, to investigate how robust this method is with respect to severe deviations, a part of the data is analyzed, where the sonar travels upward instead of at constant depth. It is the worst-case scenario of the obtained data set. The sonar is rising approximately 2 meters in only 11 meters of displacement. Such a scenario is of course far beyond a stable operational track, but it can demonstrate the robustness of the proposed DMC technique. It is known that, depending on the geometry, the induced out-of-plane motion can deteriorate the imaging results significantly. Theoretical studies on compensation have already been performed, in the radar community e.g. by Jakowatz (1996). The left panel of Figure 5-31 shows the result without motion compensation. The effect of deviations is much more important than in the previous section. The performance of the SAS processing has severely degraded.

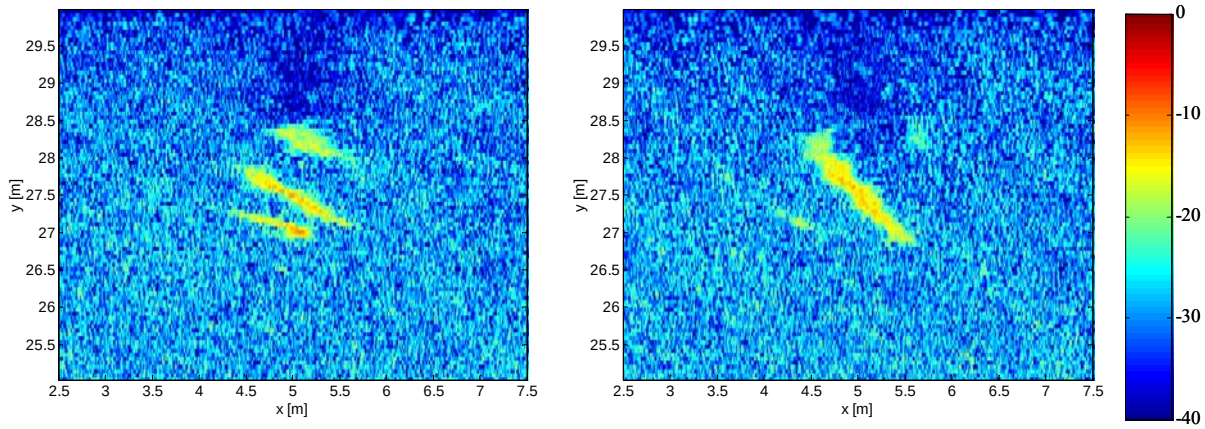


Figure 5-31 *SAS image with wavenumber frequency processing and no motion compensation (left) and DMC (right). The track of the sonar has both in-plane and out-of-plane deviations.*

When DMC is applied, it appears to be insufficient for this particular scenario. This is visible on the right hand side in Figure 5-31. The performance is a lot worse than the correctly compensated image in Figure 5-30. To tackle the problem of out-of-plane motion, an extension to NDMC and DMC is introduced. Both NDMC and DMC can easily be extended to cope with the problem. In the corresponding formulas in Eqs. (5.13) and (5.14), the variable Δr is replaced by a better estimate of the required spatial shift. This best estimate can be derived from the 3D wave equation with constant wave velocity.

$$\Delta r\left(n_p, n_h\right) = \left| \begin{pmatrix} y_m\left(n_p, n_h\right) \\ z_m\left(n_p, n_h\right) \end{pmatrix} - \begin{pmatrix} y_{\text{image}} \\ z_{\text{image}} \end{pmatrix} \right| - \left\langle \Delta r \right\rangle, \tag{5.16}$$

where the Euclidian norm is used to calculate the actual range. Note that the average deviation $\left\langle \Delta r \right\rangle$ is subtracted in Eq. (5.16), which is necessary to minimize the spatial shift, which in turn minimizes errors. In other words, it is best to lay the ULA in the middle of the sailed track and not at an arbitrary (far) position. What is important in this approach is the fact that the 3D approach implies that out-of-plane motion is accounted for automatically. The elevation angle, or elevation plane, of the sonar was assumed constant in the previous approach, but now it may vary. It should be clear that the closer the insonified area is the more out-of-plane motion affects the SAS performance.

The 3D extension is applied to the data set of track 2, which is shown in Figure 5-32. With this result it is proven that even for such an unstable path, motion can be compensated without enlarging the computational load. It should be noted that, theoretically, the processing could never perfectly match time domain SAS processing methods. Still, the assumption is made is that both elevation angle and azimuth are constant for a processing block for the motion compensation. This is why the ULA must be chosen as close as possible to the actual track, as in Eq. (5.16). Fortunately, the designer of a SAS usually has some freedom in choosing the dimensions of the data processing blocks. For example, one could subdivide the image in several small images that are all motion compensated in a sufficient manner. This obviously be-

comes computationally expensive rather quickly. At least, the knowledge is available now to determine the trade-off between performance and computational effort.

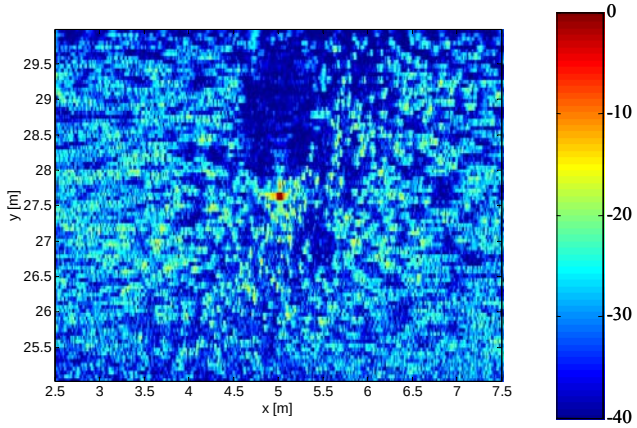


Figure 5-32 *SAS image with wavenumber frequency processing and 3D motion compensation. The track of the sonar has both in-plane and out-of-plane deviations.*

Figure 5-32 already shows that the assumptions are valid, even if the sonar motion is not stable. A detailed comparison reveals minor differences between Figure 5-32 and Figure 5-30. The most important one is the translation in y, which is only a shift because of the different tracks. But also the sharpness in Figure 5-32 is slightly less towards the sides of the image. One also can calculate these expected errors analytically as a function of the geometry. Formulas for validity of the motion compensation can be found in the following chapter.

5.4.6. Future ultra wide beam system issues

The motion compensation analysis in this section has shown that using DMC for an operational AUV-based SAS system is sufficient. In most cases, NDMC is even enough, and therefore, it is recommended as the default algorithm. Nevertheless, the performance depends on the geometry and the sonar properties. In general, the performance of NDMC degrades for systems with wider beams, i.e. longer integration angles. The performance of DMC does not show dependence on this beamwidth, but, as already apparent in the last example in Figure 5-32, it depends on the x-bracket of the output image. An image with x-values from zero to ten meter shows more performance degradation than an image with for instance values from two to six meter. The phase errors can be calculated using Eq. (5.13) for NDMC and Eq. (5.14) for DMC. Using the requirement that the phase error may not exceed $\pi/3$ the behavior of both methods can be visualized in one figure, which is computed with the difference of Eq. (5.13) and Eq. (5.14):

$$\Delta r < \frac{c}{12 f \left(1 - \cos\beta\right)}, \tag{5.17}$$

where β is the integration angle. This formula gives the validity bounds for NDMC. At the same time, it gives the maximum angle in the output image denoted with ϑ in Eq. (5.14)

when using DMC. The inequality is simply obtained by replacing β with ϑ in Eq. (5.17). Figure Figure 5-33 shows the inequality bounds for three different frequencies.

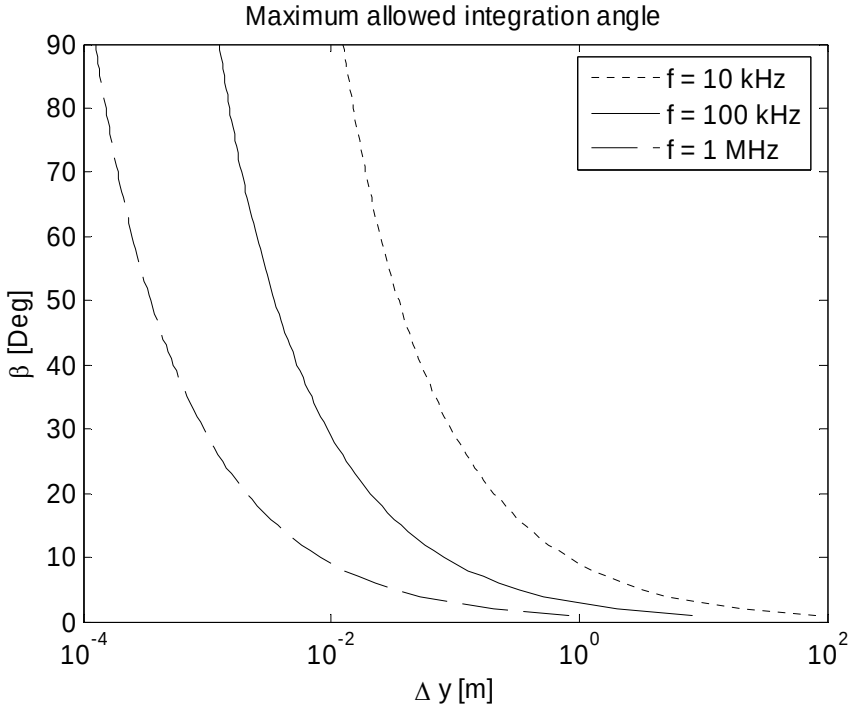


Figure 5-33 *Theoretical bounds for both motion compensation methods NDMC and DMC. The integration angle β is to be regarded as the angle in the image ϑ for the DMC method.*

As stated before, the considered SAS systems are safely on the left side of the bounding curve. However, the integration angle has improved and is expected to improve more for *future systems*. At some point, it may be necessary to apply even more advanced methods. All these more advanced methods have the disadvantage that the computational load increases. When wavenumber frequency imaging is still faster than the exact time domain method, it is recommended to choose one of these three approaches:

1. Switch to the aforementioned fast factorized back projection method.
2. The methods NDMC and DMC use one hydrophone as input for the computation of a new motion-compensated hydrophone. It is also possible to use multiple (or even all) N input hydrophones instead of one. In the limit, this procedure can be seen as an extrapolation of the wavefield. When the wavefield is known on a certain arbitrary array shape, the wavefield at some desired arbitrary array can be constructed. This approach has been tested on the SAS systems. The input and output (ULA) array positions should nevertheless be chosen as close as possible, so that the number N is reduced.
3. Process the images block-wise with DMC instead of one large image for the whole SAS integration angle. The images may be combined afterwards.

5.5. Conclusion

In this chapter the SAS signal processing chain is analyzed. For the three most important steps, motion estimation, motion compensation and imaging, the algorithms chosen are justified.

First, three methods, used for synthetic aperture imaging, are analyzed. None of the proposed methods is optimal for all performance criteria discussed. However, based on sonar parameters, geometry and the results from this chapter, a well-considered choice can be made on the most suitable SAS signal-processing kernel. Application to experimental data shows that the best quality is obtained with the Stolt Migration algorithm in combination with image correlation autofocus. But, because the computational load of image correlation is rather high and the added value compared to DPC relatively low, it is concluded that DPC is a good alternative. If navigation data are at hand, they are a good supplement for the yaw estimation.

Motion compensation is necessary when using wavenumber frequency synthetic aperture processing. Two methods have been described and analyzed in this report. The performance of Directional Motion Compensation (DMC), is always better than or the same as Non Directional Motion Compensation (NDMC). The calculation time and complexity are the same, so it is recommended to use DMC for motion compensation. One has to keep in mind that DMC has a limited validity range along the sonar track. If the image quality is jeopardized, the solution is to divide the images in (along-track) blocks, but this pushes the computational load at the same time. The DMC algorithms always operate with sufficiently high performance on the HUGIN data set except when large out of plane motion occurs. In such a case 3D motion compensation has to be applied.

The outcome of the research that is described in this chapter is valuable to any organization buying or building a SAS system. The primary result is the proof that wavenumber frequency imaging is suitable for operational sonar tracks, provided that the proposed motion compensation is used. Secondly, this statement is enhanced with the practical application of the methods on measured data of the state-of-the-art HUGIN AUV. This research can be applied to any operational sonar platform (AUV, towed vehicle or ship).

6. SYNTHETIC APERTURE SONAR PART II: WAVENUMBER FREQUENCY IMAGING

6.1. Introduction

In the previous chapter it was argued that Stolt migration is the best candidate for synthetic aperture sonar processing for both the state-of-the-art ship-mounted and vehicle-mounted sonars. It also mentioned that the method has its limitations. The main aim in this chapter is to reveal those limitations with respect to motion and focusing. To analyze this, theoretical formulae are derived, but the main support comes from the simulator, which was described in Chapter 2. The valorization of the novelty of the work presented in this chapter can be explicitly found in the part where the two imaging methods are combined in order to optimize sonar performance when shadows are present. The application and tuning of the different imaging methods, with both measured and simulated sonar data, was an important part of the PhD research. The formula for the imaging techniques that are obtained from literature are properly referenced when relevant. The experimental data described in this chapter were not measured by the author but supplied by third parties as mentioned in the acknowledgements.

Research on Synthetic Aperture Sonar (SAS) is not new, and its concept was already proven by Bucknam (1974) for instance, but it has reached a mature stage in the last decade. The major difference of SAS with conventional sonar lies in the signal processing, which merges signals from different pings correctly in order to form a high-resolution image. The applications of SAS are many, e.g. mine hunting, sea floor imaging, pipeline monitoring and sub-bottom profiling. These SAS applications are often based on interferometric sonar systems, which are described by Griffiths (1997) and Bonifant (1999). However, the R&D was mainly boosted by military applications, e.g. high frequency mine hunting. These high frequency applications usually entail a high ping rate, which makes synthetic elongation of the array an attractive candidate for resolution improvement. To have SAS operating satisfactorily, different problems have to be solved. Those problems lie on the one hand in the enhancement of the 'wet end' of the sonar, i.e. sonar quality, bandwidth and beamwidth, platform control, stability and use of additional sensors. On the other hand, a lot of effort is still put in enhancement of the 'dry end', i.e. the signal processing. Starting with relatively low bandwidth and low beamwidth, systems currently are in a transition phase from a stage of research to a stage of commercial development. For the SAS systems the main step in the signal processing chain is the *imaging*, also often referred to as the *beamforming*, e.g. by McHugh (1997). This step transforms the acoustic signals into the actual image. The other steps in the processing chain are the conditioning of the data, motion estimation and motion compensation. All these modules are nowadays well under control. Several imaging methods have been developed, some of them derived from radar and overviewed by Curlander (1991), Ulander (2000) and Keydel (1992), some others originating from seismics or reviewed by Upadhyay (2004). This chapter focuses on a specific way of imaging for SAS, which is wavenumber frequency processing. It aims at FFT-based signal processing without losing quality in the image in terms of blurring

(smearing of highlights), signal-to-noise ratio or contrast. Parts of the chapter are based on the work of Gough, Hayes and Hawkins, and are essential to recognize the new aspects presented. Those new aspects lie in the imaging kernel, which is the part where the element data are converted to image data in the wavenumber frequency domain. Focusing every image pixel correctly can be achieved with an interpolation step called Stolt migration.

Stolt migration is an imaging method for which the acoustic data are transformed from the time/space-domain to the wavenumber frequency domain, where it runs much faster than in the space time domain. The criteria that have to be met to be able to perform this 2D Fourier transform are presented in this chapter. These criteria are analyzed. Additionally, when the criteria are violated, compensation methods for pre-processing, with their limitations, are analyzed. The chapter shows that the important parameters in this sensitivity analysis are the integration angle and the signal wavelength. The convolution imaging described in the previous chapter focused on one predefined range. When using a fixed focus range an error emerges for the other ranges. This chapter shows that the convolution imaging is a special case of Stolt migration, in which the interpolation procedure can be omitted. Using Stolt migration in this way has given rise to a new classification method, which results in sharper acoustic shadows of the object. Despite of the high resolution on the object itself, a sharp acoustic shadow in the image is still considered to be a large advantage for image based classification.

The shadow of an object is a strong classification clue in naval mine hunting, as for instance described by Reed (2001) and Ciany (2001). An acoustic shadow appears at relatively short ranges (up to several hundred meters) in images from high resolution sonars, such as side-scan or synthetic aperture sonar (SAS), against a background of bottom reverberation. The quality of a SAS image is optimal for a certain integration angle or, equivalently, for a certain synthetic aperture length as a function of contrast and resolution. This means that image quality improves with integration angle up to this optimum. However, this does not hold for the shadow. The contour of a shadow becomes more blurred as the integration angle increases, because the shadow shifts according to the sonar position. This effect is similar to an optical shadow that is diffuse when an extended light source is used, such as a fluorescent tube, but sharp with a point source. The longer the light source (the optical equivalent of the synthetic aperture), the more blurred the shadow becomes. This chapter presents a simple, but novel, SAS technique that enhances the shadow from a detected object by compensating the blurring of the shadow in the image forming process. The technique will be demonstrated with simulated data that include this phenomenon of shadow dynamics along the synthetic aperture. Additionally, measured SAS images are analyzed in order to quantify the shadow contour improvement.

The outline of the chapter is as follows. First, the theoretical derivation of four signal processing techniques is given in Section 6.2. At the end of that section an overview of the pros and cons is given based on previous publications. An important issue here is range dependent focusing. In Section 6.3 the wavenumber processing is analyzed in more detail. The validity of the processing method with respect to sonar motion is derived analytically. Signal processing parameters, e.g. the 2D replica and the interpolation scheme, are thoroughly investigated in terms of side lobes and blurring. Optimal processing settings are derived in this way. Finally, the results of the methods are tested. A sonar data simulator, described by Groen (2005) and in Chapter 2, based on analytic expressions of diffraction was developed to analyze the geometric effects on the signal processing. The simulated data are generated for scenarios with realistic geometries and resemble the experimental data used.

The results on simulated data are shown in Section 6.4. Section 6.5 proves that convolution imaging is optimal to attain a clear and correct shadow. Elongation of the synthetic array blurs the shadow at some point. The theory on this blurring and corresponding compensation is derived. A combination of Stolt migration and convolution imaging is applied to optimize the images for classification. The results on experimental data are in Section 6.6. The processing is applied to both experimental data from a sonar traveling on a rail and data from a sonar in a towed underwater vehicle. In Section 6.7 a conclusion of the analysis is given.

6.2. Theory on synthetic aperture processing

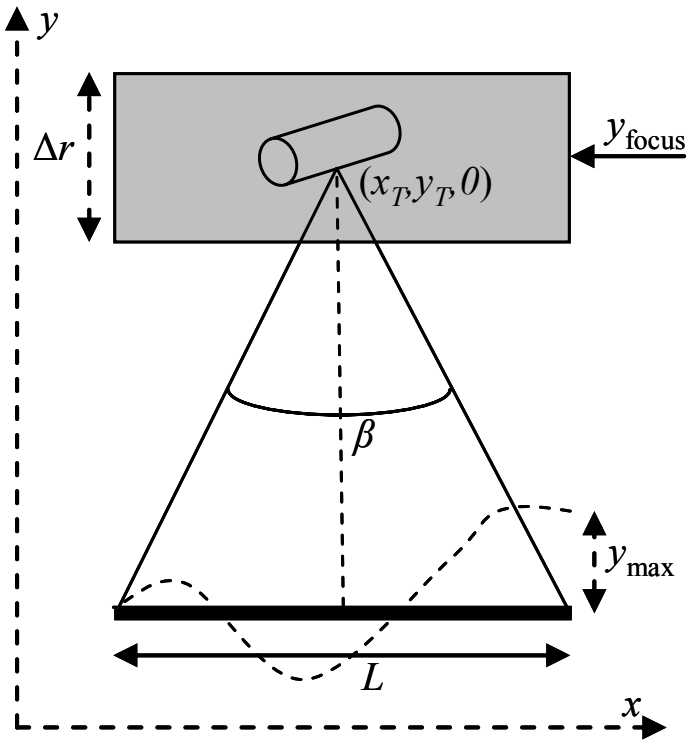


Figure 6-1 *Geometry for the SAS processing and its corresponding parameters. The gray part is the focus window.*

The derivation of the imaging techniques in this section runs parallel to those in publications from the acoustics group of the University of Canterbury, New Zealand, pioneers in wavenumber signal processing for SAS. Imaging techniques transform the received sonar data p to a SAS image g. The imaging methods are published by Gough (1997), Hawkins (1996) and Hayes (1992) for instance.

6.2.1. Space-time imaging

A straightforward method for imaging is space-time imaging (STI). As its name suggests, this method consists of a direct mapping of the input data f on hydrophone level to the output SAS image g. A general formula for calculating the acoustic pressure at an arbitrary point in space with the recorded data is derived in Appendix C. The relevant formula for space-time imaging without amplitude corrections is the end result of the first part of this Appendix:

$$g(x,y) = \int_{-\infty}^{\infty}\int_{-\infty}^{\infty} p\left[x_s, 0; x_r, 0; \frac{1}{c}\left(\Delta r_r + \Delta r_s\right)\right] \mathrm{d}x_r \mathrm{d}x_s \,, \tag{6.1}$$

where c is the sound speed, $\Delta r_s = \left|\mathbf{x_s} - \mathbf{x}\right|$ is the travel path length from source $(x_s,0)$ to (x,y) and $\Delta r_r = \left|\mathbf{x}_r - \mathbf{x}\right|$ is the travel path length from receiver $(x_r,0)$ to (x,y). The pressure p is integrated over the array of sources and receivers to form the image g.

The data are not measured by a continuous array of sources or receivers, and therefore, the discretized and finite length version of the imaging formula is:

$$g(x,y) = \sum_{n_p=1}^{N_p}\sum_{n_p=1}^{N_h} p\left\{n_p, n_h, \frac{1}{c}\left(\Delta r_r + \Delta r_s\right)\right\}, \tag{6.2}$$

where the input data are a function of ping n_p, hydrophone n_h and time t. These data are delayed in time according to the quotient of distance between sonar and image pixel (x,y). It has to be noted that it is this discretization that causes the typical behavior of a main lobe and side lobe for each imaged target. Without loss of generality, y is assumed to be the across-track distance in the direction of the target, which means that like in the previous chapter, y and r can be interchanged. Typically, the sonar has a certain height above the sea floor, which can be accounted for in the image by a simple coordinate transformation after all the processing steps described in this chapter. It should be noted that such an imaging step only operates on the phases and not on the amplitudes. As common in sonar operations, here the amplitude differences in the received data are not taken into account in the processing. The amplitudes are used in another way, i.e. for the topic of Section 6.3.5, which is tapering.

When this method is applied to digitized data, the data are either to be sampled in time with several times the Nyquist frequency or to be interpolated. Because of heavy computational effort involved in this method, it is not included in the performance analysis in this thesis.

However, efforts to reduce the computational load of the time domain imaging approach have been successful. A method used in SAR signal processing, referred to as fast-factorized back projection has shown to be worthwhile. The application of this method in SAS is described by Shippey (1998) and Banks (2002).

6.2.2. Space frequency imaging

Imaging is expected to be a lot more efficient when the Fast Fourier Transform (FFT) is applied to Eq. (6.2) similarly to Chapter 5:

$$P\left(x, y_{\text{focus}}; x, y_{\text{focus}}; \omega\right) = \sum_{n_p=1}^{N_p} \sum_{n_h=1}^{N_h} e^{-i\omega\tau\left(n_p, n_h, x, y_{\text{focus}}\right)} P\left(x_s, y_s; x_r, y_r; \omega\right), \tag{6.3}$$

and

$$\left[g\left(x, y\right)\right]_{y_{\text{focus}}} = p\left(x, r_{\text{focus}}; x, r_{\text{focus}}; \frac{2y}{c}\right), \tag{6.4}$$

where $r(n_p,n_h,x) = r_s(n_p,y_{\text{focus}},x)+r_r(n_p,n_h,y_{\text{focus}},x)$, $\omega = 2\pi f$ and f is the frequency. Unfortunately, this expression has a limited validity, because only one focus range, y_{focus}, can be taken into account for the concerned block of data in the FFT. The implications of space frequency imaging (SFI) on the SAS results are discussed in detail in Section 6.4.

6.2.3. Convolution imaging

Under special circumstances, to increase computational speed the use of two FFTs instead of one is allowed. The assumption that should be made here is the following: *the received acoustic data can be considered as if coming from a system with sources and receivers that form a uniform linear array (ULA) of midpoints.* Uniform and linear means that the source/receiver array is a line array that is spatially sampled at equal distances. This is rather limiting in terms of operational applicability, because such an SAS array type will never come into view. Fortunately, with pre-processing, it appears feasible to correct for most deviations of the ULA. Nevertheless, the array configuration still needs to meet the spatial sampling criteria as described by McHugh (1998), McHugh (1995) and Chatillon (2000). The ULA validity criteria and compensation methods to gain validity are not trivial and form an important part of the remainder of the chapter. The resulting formula for conversion of the acoustic input data to an image is a convolution, which is performed as an element wise multiplication in the wavenumber frequency domain:

$$\tilde{G}\left(k_x, \omega\right) = \tilde{P}\left(k_x, 0; \omega\right) e^{-2\mathrm{i}y_{\text{focus}}\sqrt{\frac{\omega^2}{c^2} - k_x^2}}, \tag{6.5}$$

where k_x is the wavenumber in the along-track (x) direction. Notice that the focus range y_{focus} has to be multiplied by 2 in the exponential, because of the propagation to the focus point and back. Fast Fourier Transforms replace the summations of Eq. (6.4), indicating that this comes out as the fastest method.

The method can also be considered in a different perspective. The received data are 2D correlated with an expected response of a point target located at the focus range, which has a hyperbolic shape as a function of x.

6.2.4. Stolt migration

The suggested method for SAS imaging is Stolt migration. The method is based on wave theory in combination with Fourier analysis and is widely used in seismic imaging; see Berkhout (1985) and Stolt (1978). It is also found successful in synthetic aperture sonar, as for instance described by Groen (2001) and also in radar, e.g. by Raney (1988) and Eichel (1089). Since the remainder of the chapter is dedicated to its application, the derivation of the method is now given in detail in Appendix C. It results in the formula:

$$g(x,y) = \int_{-\infty}^{\infty}\int_{-\infty}^{\infty} e^{-\mathrm{i}\left(2xk_x - yk_y\right)} \tilde{P}\left(k_x, 0; \frac{ck_y\sqrt{k_y^2 + 4k_x^2}}{2|k_y|}\right) \mathrm{d}k_x \mathrm{d}k_y , \tag{6.6}$$

where $k_y = \sqrt{\frac{\omega^2}{c^2} - 4k_x^2}$. As stated before, the input data form a matrix of acoustic pressures and can be written as a 2D case, i.e. as the acoustic pressure generated by a source at position $\mathbf{x_s}$ and a receiver at position $\mathbf{x_r}$. The method is similar to the convolution imaging and is also performed in the wavenumber frequency domain. The general derivation of the method is given in the second part of Appendix C. The important difference with convolution imaging is that Stolt migration focuses correctly for every across-track range (y) in the image and not just at the focus range.

The algorithm is based upon extrapolation according to the wave equation assuming constant sound velocity c as in Eq. (6.2), but then with a linear grid of transceivers. This wave field extrapolation is carried out in the wavenumber frequency domain, because of computational considerations; see Berkhout (1985). Thus, besides the pre and post processing steps that are discussed in the following section, the basis for Stolt migration is:

(1) Temporal and spatial Fourier transform
(2) Coordinate transform by means of Stolt interpolation
(3) Temporal and spatial inverse Fourier transform

Table 6.1 *Comparison of SAS imaging methods.*

	STI	SFI	Convolution	Stolt
Focusing	range dependent	fixed focus range	fixed focus range	range dependent
Assumption	none	one focus range	one focus range/ ULA	ULA
Speed	--	-	++	+
Accuracy	++	-	--	+
Flexibility	++	+	-	-
Autofocus	optionally combined	optionally combined	separated process	separated process

An extensive analysis on the comparison of the methods with respect to focusing, accuracy, speed and additional considerations is described by Bellettini (2000). In Table 6.1 an over-

view of the imaging comparison is given. In this table flexibility is referring to the ability to change the processing in time or spatially, e.g. ping by ping. FFTs jeopardize this flexibility. Each of the four methods proposed here may be the most suitable for a particular scenario.

6.3. Application of Stolt migration

6.3.1. Motion compensation

In Section 6.2.4 it was already mentioned that wavenumber frequency processing, and in particular Stolt migration, is based on the assumption that the formed synthetic aperture can be considered as a ULA of monostatic elements. In general, this is not the case and it is therefore necessary to analyze the effects of deviations from the ideal case. Also, the signal processing and imaging is 2D and not 3D, but generality is not lost for the motion compensation algorithms, because motion in the plane of arrival of the signals is dominant. It was shown in the previous chapter that severe out of plane motion may also need to be taken into account. Also, in practice the plane of arrival changes in time, i.e. the grazing angle decreases with time (range), which may affect stationarity of the motion estimation.

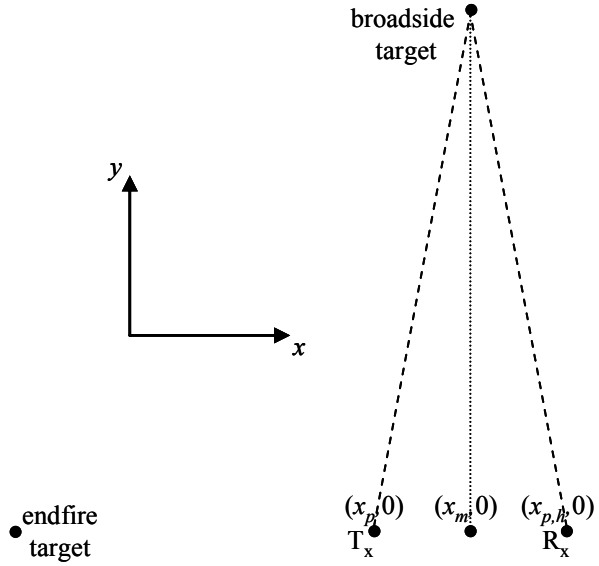


Figure 6-2 *In the ULA assumption the source receiver pairs are replaced by a midpoint.*

First, sources and receivers are not necessarily coincident. However, in wavenumber frequency processing, it is assumed that source and receiver coincide and can be replaced by a midpoint, the monostatic equivalent of the source/receiver pair, which acts as a transceiver. The replacement is only allowed for a long enough range and a small enough separation of source and receiver. Purely based on signal travel times, there is no difference between a signal of source/receiver pair T_x and R_x and a signal of a transceiver in the midpoint $(x_m,y_m) = (x_p,y_p)+(x_{p,h},y_{p,h})$. For a signal from a broadside target in (x_m,y) the signals have a slight phase difference $\Delta\eta$ equal to:

$$\Delta\eta = 2\pi \frac{\sqrt{\left(\frac{x_p - x_{p,h}}{2}\right)^2 + y^2} - y}{\lambda}, \tag{6.7}$$

The maximum phase difference should not be too large, for the validity of the ULA assumption. The requirement of $\Delta\eta < \pi$ gives:

$$y < \frac{\left(x_p - x_{p,h}\right)^2}{\lambda} - \frac{\lambda}{16}, \tag{6.8}$$

which is the same as the range that defines the near field of an circular object with radius that equals x_p-$x_{p,h}$. Introducing the worst case of the signal (the highest frequency $f_{\max}$) and ignoring the term $\lambda/16$ results in:

$$c\sqrt{x^2 + y^2} < f_{\max}\left(x_p - x_{p,h}\right)^2, \tag{6.9}$$

The scenarios under consideration in this chapter have a setup in which the near field range is less than a few meters, thereby satisfying this assumption.

Secondly, the sonar path is not necessarily a straight line. This topic is relevant, because it is known, for instance from Groen (2001) and Nielsen (1991), that deviations of more than a quarter of the wavelength are destructive for the coherent integration. This same issue also appeared in Chapter 4 with the shape and Doppler corrected beamforming for towed arrays. In practice, these deviations are at best in the order of centimeters. Therefore, the effect of the deviations is important for the signal processing. A correction referred to as motion compensation is applied to the data prior to the imaging to account for this effect as shown in Figure 6-3.

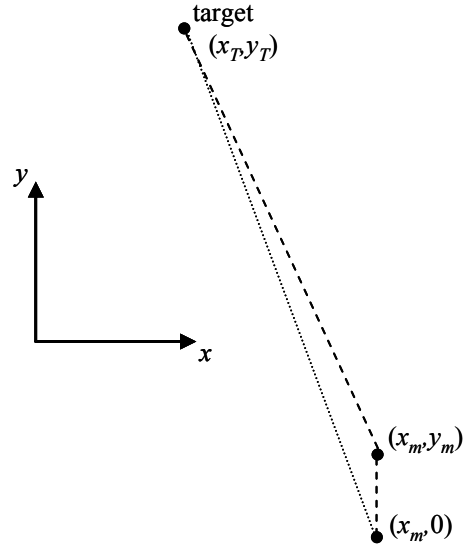


Figure 6-3 *When the midpoints do not lie on a straight line (y=0), a correcting phase shift has to be applied.*

The correction algorithm maps the received data to a new data set that would have been received by a ULA. The algorithm that is used for this is based on the assumption that a new midpoint consists of a delayed old midpoint that was not on the ULA:

$$P\left(x_m, 0; \omega\right) = P\left(x_m, y_m; \omega\right) e^{-\frac{2\mathrm{i}\omega y_m}{c}}, \tag{6.10}$$

In Eq. (6.10) an error is inevitable for signals that do not arrive from the direction along the line $(x_m,0)$ to (x_m,y). This phase error for these signals is calculated with $\frac{4\pi}{\lambda}\left[\sqrt{\left(x_T - x_m\right)^2 + \left(y_T - y_m\right)^2} - \sqrt{\left(x_T - x_m\right)^2 + {y_T}^2} - y_m\right]$. The worst case appears at the side of the source beamwidth (x_T-x_m=$y_T\sin\beta$). To quantify analytically the maximum deviation allowed, this worst case phase error, as in the stationary phase requirement of Gough (2000), is required to be less than $\pi/3$:

$$\sqrt{{y_T}^2 \sin^2\beta + \left(y_T - y\right)^2} - \sqrt{{y_T}^2 \sin^2\beta + {y_T}^2} - y < \frac{\lambda}{12}, \tag{6.11}$$

An explicit formula for the maximum deviation $y_{\max}$ be writing out the equality using Eq. (6.11) in order to investigate the performance sensitivity. Solving Eq. (6.11), yields that the ULA assumption is no longer valid when the initial deviation from the ULA is larger than:

$$y_{\max} = \frac{\lambda}{24} \frac{\lambda + 24 y_T \sqrt{\sin^2\beta + 1}}{\lambda - 12 y_T \left(1 - \sqrt{\sin^2\beta + 1}\right)}, \tag{6.12}$$

The implications for SAS scenarios are shown in Figure 6-4. The maximum allowed deviation mainly depends on the integration angle β. The synthetic aperture length L is related to β according to $L = 2y_T\tan(\beta/2)$. At the interesting ranges for SAS operations the sensitivity of $y_{\max}$ to the target range y_T is negligible and Eq. (6.12) simplifies to $y_{\max} = \frac{\lambda\sqrt{\sin^2\beta + 1}}{12\left(\sqrt{\sin^2\beta + 1} - 1\right)}$.

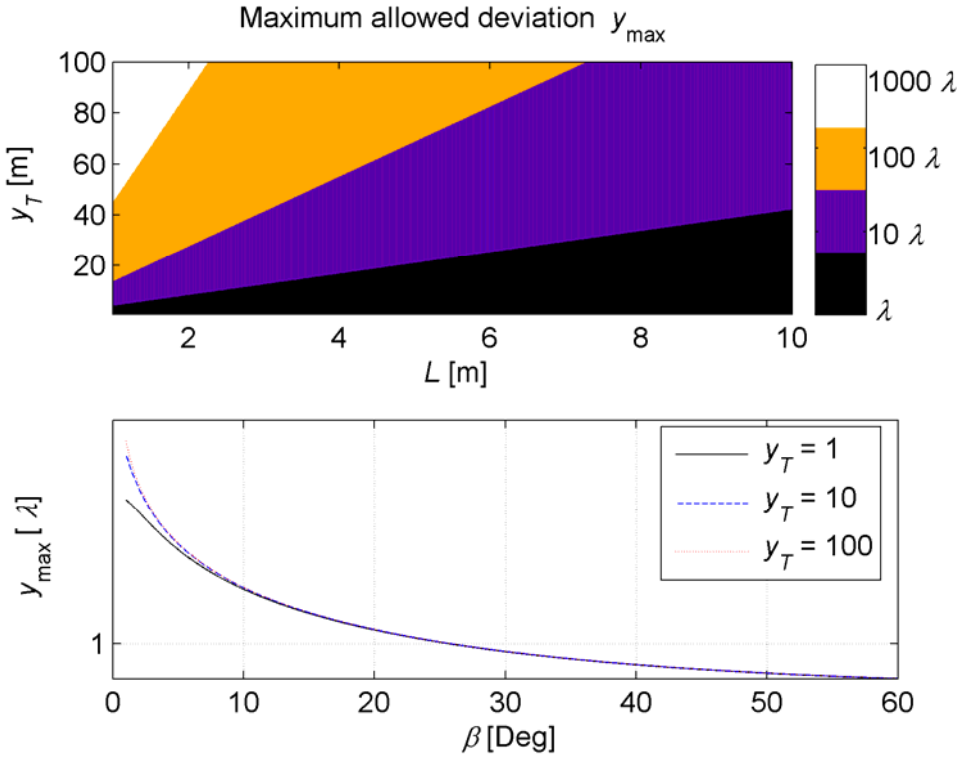


Figure 6-4 *Validity of linear motion compensation for ULA assumption. The results are given in wavelengths. In the upper panel the maximum allowed deviation is imaged on a logarithmic scale versus target range and synthetic aperture length L. In the lower panel the offset is plotted as a function of β at a range of 1, 10 and 100 m.*

6.3.2. Migration for a range window

Generally, Stolt migration is applied to a block of input data that does not start at the transmission time of the sonar, but at time t_0. Therefore, the data are pre-focused to the range $t_0c/2$, which results in correct focusing for the reflectors at the start range and (small range-dependent) hyperbolae for the remaining reflectors. This pre-focusing is referred to as start range migration, which is performed as an element wise multiplication in the wavenumber frequency domain. The procedure can be considered as bringing the measurement array closer to the target field by a range $t_0c/2$ and has its equivalence in seismics where it is referred to as redatuming. The data are then ready for the interpolation discussed in Section 6.3.4, which focuses the remainder of the image.

The procedure seems rather simple, but needs a somewhat closer look. The wavenumber frequency domain input data are multiplied element wise with the pre-fixed replica $e^{-2iy_{focus}k_y}$ according to Eq. (6.5). This replica represents the 2D (t,x) point target response at range $t_0c/2$ and $x = 0$. For implementation, convolution imaging is used and focused on $y_{focus} = t_0c/2$.
When this replica is transformed back to the time space domain, unfortunately, it shows some imperfections. Commonly in SAS, the integration angle is much smaller than 180 degrees. This means that the responses of the reflectors are only a part of the (infinite) hyperbola. Eq. (6.5) causes a cut-off effect that yields wrap around effects according to discrete Fourier the-

ory. The artifact can be avoided easily by constructing the replica p_0 in the space frequency domain by applying the phase shifts $\frac{\omega}{c}\left[\sqrt{x^2+\left(\frac{ct_0}{2}\right)^2}-\frac{ct_0}{2}\right]$:

$$P_0\left(x_m,0;\omega\right)=e^{\mathrm{i}\frac{\omega}{c}\left[\sqrt{x^2+\left(\frac{ct_0}{2}\right)^2}-\frac{ct_0}{2}\right]}, \tag{6.13}$$

This replica P_0 is then transformed to the wavenumber frequency domain replica $\widetilde{P}_0$ and convolved with the acoustic data. A quality comparison of the two replicas is given in Figure 6-5. On the left-hand side the replica as generated in the wavenumber frequency domain is shown, and on the right-hand side the replica as generated in the space frequency domain. The latter is also already band filtered in the same way as the acoustic data, which explains the sidelobes in the time domain.

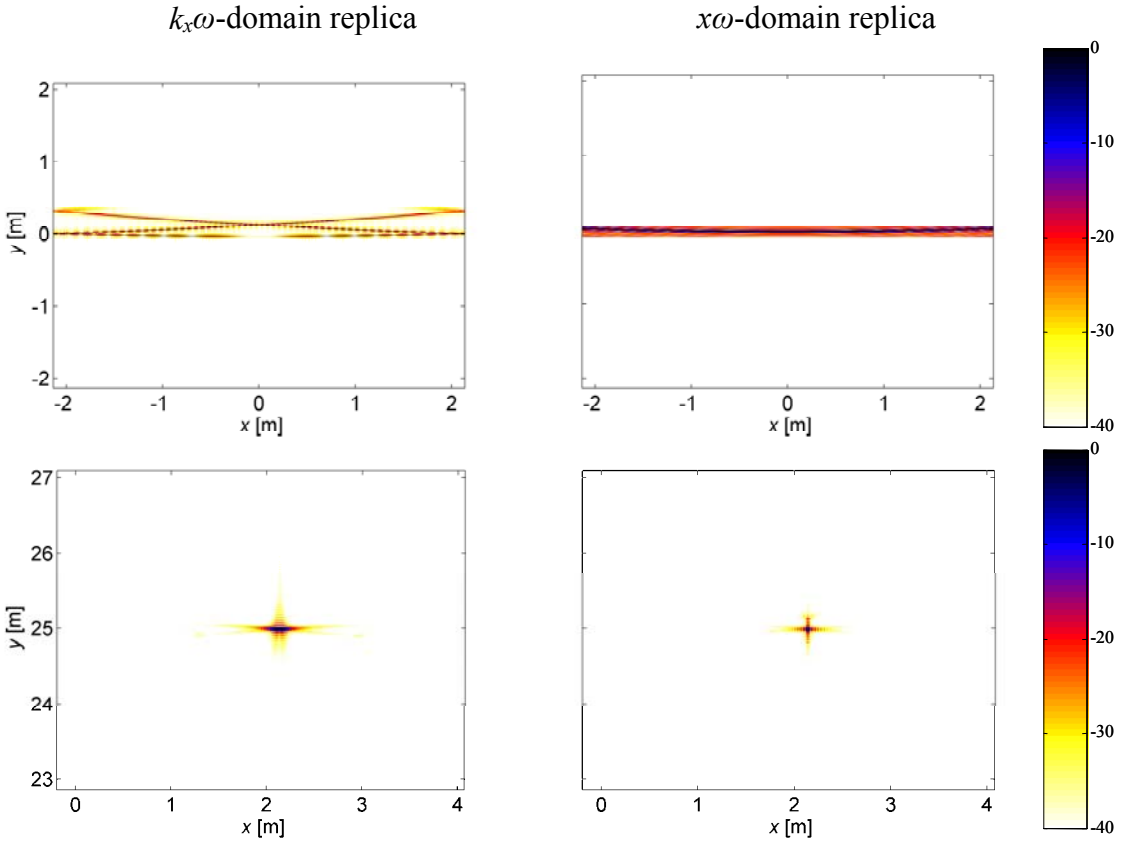


Figure 6-5 *Start range migration by means of convolution with 2D Point Target Response (PTR) generated in the wavenumber frequency domain (top left panel) or in the space frequency domain (top right panel). The lower panels show the effect on a point target image.*

The replica can be constructed prior to processing. The computations that are involved for real-time processing are minimal, namely an element wise multiplication of replica and data.

6.3.3. Limited domain processing

The bottleneck for the signal processing is the Stolt interpolation in the wavenumber frequency domain. This aspect, a combination of zero padding and interpolation, is discussed in the following section and is a continuation of the work described by Ekhaus (1997). Before performing calculations in the wavenumber frequency domain, it is efficient to find the relevant part of the data. In practice this is determined by the properties of the transmitted waveform, which are usually known (e.g. a chirp or a continuous wave pulse). In the frequency dimension, this relevant part is easily obtained from $f \in [f_c\text{-}b/2, f_c\text{+}b/2]$ with f_c the center frequency and b the bandwidth. In the wavenumber (k_x) direction, a similar relevant band can be found. The wavenumbers correspond to angles of arrival of the plane waves and usually these angles do not cover the entire range of $[-90^o, 90^o]$. The relevant part is given by:

$$|k_x| \leq \frac{\omega}{c} \frac{L}{\sqrt{{y_{\min}}^2 + L^2}}, \tag{6.14}$$

where L is the synthetic aperture length and $y_{\min}$ is the minimum range. If only this cone shape is used for the final imaging, it is beneficial for both calculation time and signal-to-noise ratio. The latter is easily verified, because only processing a limited range of frequencies and wavenumbers is comparable to a 2D-bandpass filter.

It should be noted that in this stage of the processing, L is still a tunable parameter. Narrowing the cone shortens the synthetic aperture according to Eq. (6.5).

6.3.4. Wavenumber frequency interpolation

As already noted in the former sections of this section, the crucial and computationally most expensive step in the process of acoustic hydrophone data imaging is the Stolt interpolation. The interpolation, which was first applied successfully in seismic imaging by Stolt (1978), is applied in the 2D Fourier transform of Eq. (6.2) assuming the ULA of transceivers. The data matrix P, dependent on k and k_x, is interpolated to a new coordinate system, given by:

$$\left(k_x, k_y\right) = \left(k_x, \sqrt{\frac{\omega^2}{c^2} - 4k_x^2}\right), \tag{6.15}$$

which was already derived in the previous Section 5.2. This interpolation appears to be the computational bottleneck in the signal processing, and thus, the interpolation scheme requires a careful design.

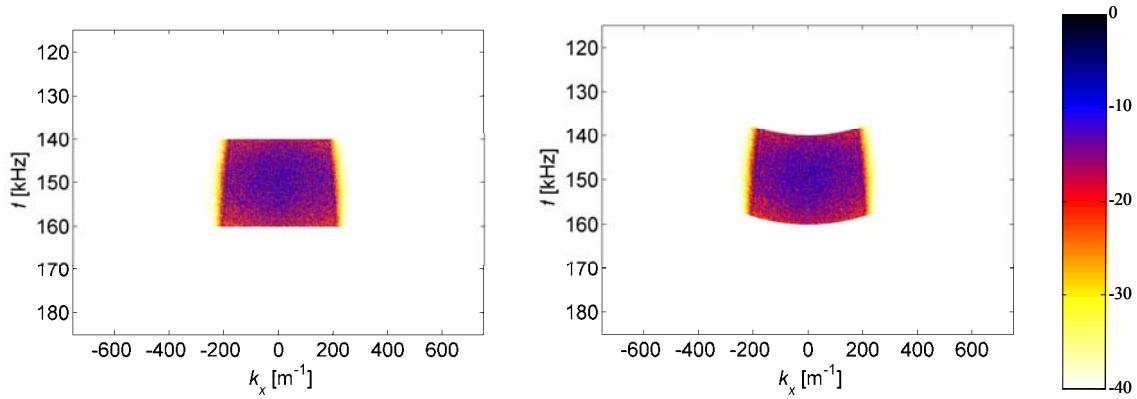


Figure 6-6 *Example of Stolt interpolation. On the left hand side the data are shown in the wavenumber frequency domain before Stolt interpolation. The acoustic energy is captured in an angle and band limited trapezoid. On the right hand side interpolation has been applied and the trapezoid is bent and covers a wider band.*

As a result, this focuses the energy correctly for all pixels in the image. The interpolation can be considered as a 1D operation (repeated for all k_x), since the second coordinate k_x is still present after the transformation.

Comparing the energy distribution before and after interpolation in the wavenumber frequency domain shows another property of Stolt migration. The shape starts as a trapezoid, which is defined by the signal bandwidth and the integration angle. After the coordinate transform of Eq. (6.15), this trapezoid is stretched, which is illustrated in Figure 6-6. This yields a virtual higher bandwidth and hence a better range resolution on top of the result of pulse compression. For preservation of energy, the coordinate transform also should be accompanied by a scaling factor, but it has been verified that this effect is negligible, because of the limited integration angle and frequency band.

For this step in the SAS processing some restrictions can be introduced with respect to accuracy. Operating on a discrete and finite data set, interpolation often involves some loss of accuracy. For this application the accuracy depends on the interpolation method and the sampling density of k. In other words, enhancement can be found in the use of a higher order interpolation method or in zero padding in the time domain. When the accuracy is not sufficient, two inconvenient effects appear. Ideal responses of point scatterers smear out and energy at the longest ranges fades.

To quantify and illustrate smear effects for a high-resolution SAS scenario, Figure 6-7 and Figure 6-8 show the results of different interpolation methods and zeropadding factors. The zeropadding factors used are 1, 2, 4 and 8 (where 1 means no zeropadding). The interpolation methods are nearest neighbor, linear on real and imaginary part, linear on phase and amplitude and cubic. The last is a piece-wise polynomial interpolation scheme as described by Fritsch (1980). The reason for analyzing two linear interpolation schemes is the difference in computational load. The effect of smearing is shown in Figure 6-7 with the response of a target at a range of 25 m on a 10-m long synthetic aperture. This simulated scenario can be considered as a scenario with a relatively large integration angle. The larger the integration angle, the more important the interpolation scheme gets.

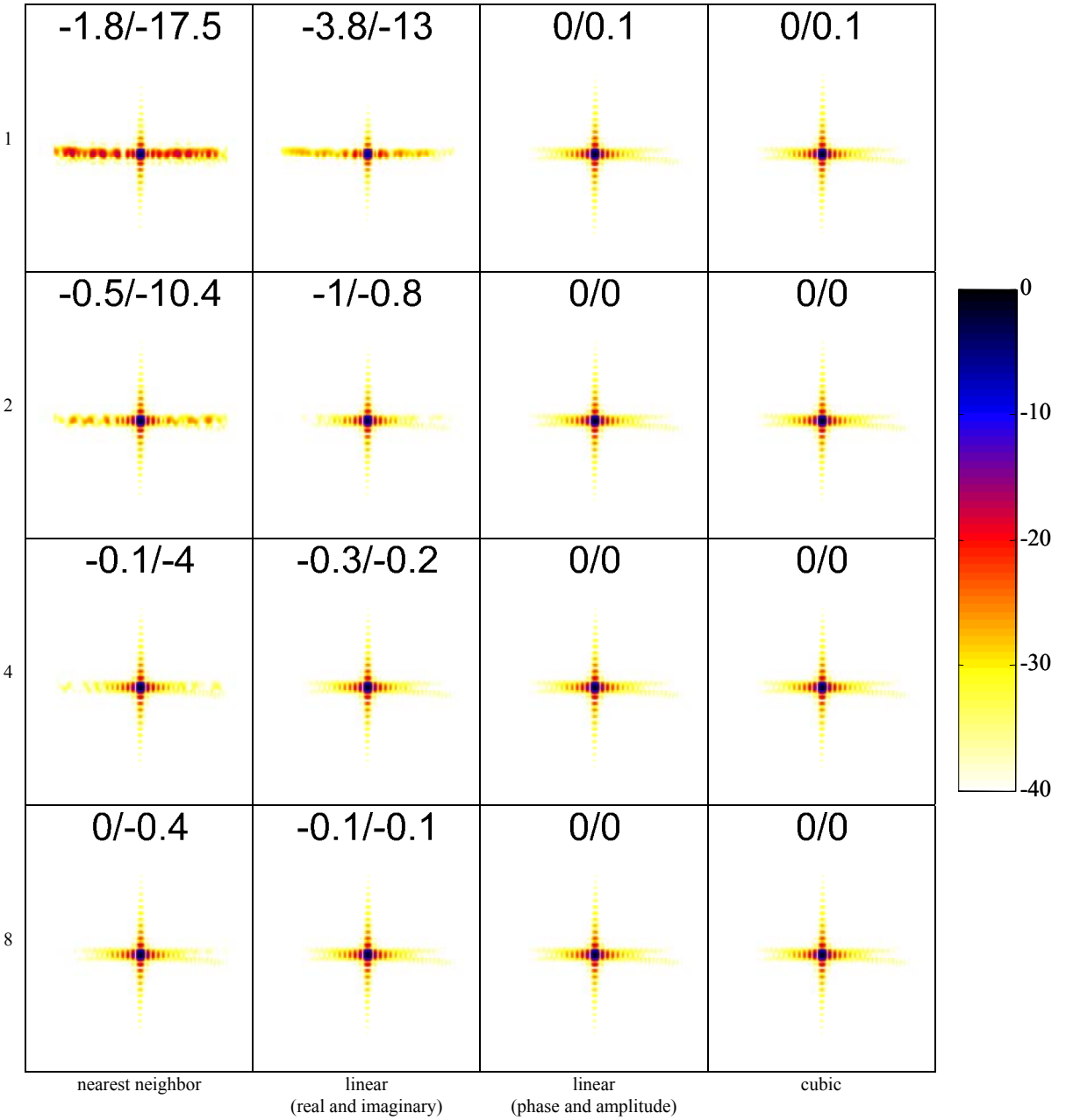


Figure 6-7 *Matrix of SAS images of a point target at a range of 25 m. Both the frequency zeropadding factors (1, 2, 4 and 8) and the interpolation method (nearest neighbor, linear on real and imaginary part, linear on phase and amplitude and cubic) are varied. The left value above the images is the maximum in the image relative to the theoretical maximum in decibels. The right value above the image is the total energy at the target range relative to the theoretical maximum. The images are a square zoom of 1 m^2 around the target..*

Another result of smearing is energy loss, which is first identified at the end of the range grid. Because the interpolation is performed on the range wavenumber axis, errors first manifest at the end of the grid. This is the same as insufficient interpolation in the time domain, which would first affect the high frequency components. Figure 6-8 shows this effect. The input for these figures is Gaussian noise hydrophone data. When Gaussian noise is inserted into the signal processing chain, one would expect Gaussian noise in the output SAS image. However, due to interpolation schemes, this is not the case. This loss of energy for the higher range samples due to insufficient interpolation is clearly visible. Nearest neighbor interpolation does

not lead to any losses in this respect. This is explained with the fact that no averaging is taking place in this interpolation. For the other methods at least two to four times zeropadding is necessary.

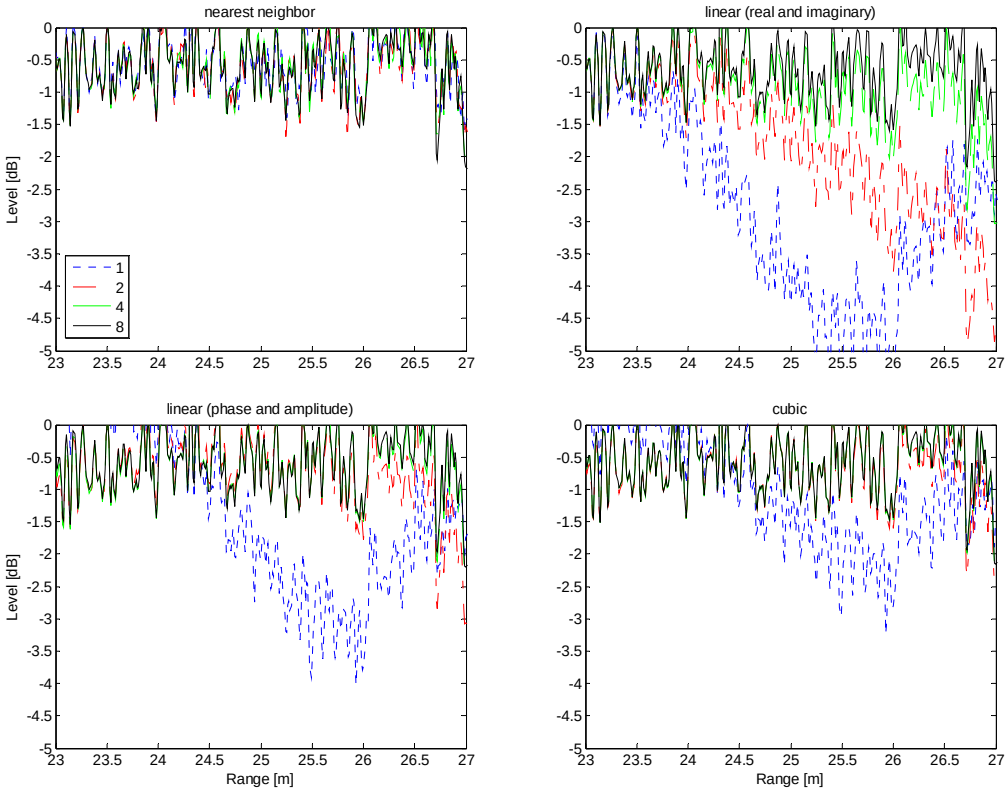


Figure 6-8 *Four plots of energy versus range of Gaussian noise input. Each plot represents an interpolation method with four frequency zeropadding factors.*

It can be concluded that a linear interpolation on the phases and amplitudes on twice zeropadded data appears to be a good choice in high frequency SAS processing, because it remains reliable with low computational costs. However, if enough computer memory is available, the four times zeropadded nearest neighbor method becomes more interesting. Cubic interpolation is computationally too expensive compared to the other methods. For time domain imaging, a higher order interpolation scheme is needed.

6.3.5. Tapering in different domains

The need for a taper in the processing arises if sidelobes are undesirably high. At the cost of resolution one can lower them to a suitable level. In contrast to signal processing in time or frequency domain, the result of such a taper is straightforward. This is easily understood in the following way. A taper in the time domain controls the resolution and sidelobes in the frequency domain and vice versa. This means that to be able to directly control sidelobes and resolution in the (x,y)-domain, the taper needs to be applied in the wavenumber frequency domain. Tapering can easily be applied to the cone shape as in Figure 6-6. A similar effect can be achieved by a 2D (t,x-domain) taper. A simple example is a taper along the synthetic aperture, which would indeed lead to lower sidelobes in the along-track direction, because wavenumber and x-position are coupled. This is nevertheless indirect and is not used further.

Note that under practical circumstances, acquisition-related tapers in both the wavenumber and frequency direction are already present in the recorded data. In both directions other effects are acting as a taper. Working with wideband waveforms the propagation loss depends on both frequency and range, and therefore, a physical (monotonically decreasing) taper is in the data. For the wavenumbers the directional characteristics of source and receiver and propagation loss play an important role in this respect. The source and/or receiver of a sonar usually have a directivity pattern that is not omni-directional in the view plane, which causes natural tapering over the acoustic aperture. For synthetic aperture applications it is beneficial to have both a wide beam source and receiver, because the synthetic integration length can be limited by these properties. As the sound travels further for angles further from broadside, the propagation loss increases monotonically, which provides an additional natural shading effect.

6.4. Results with simulated data

This section describes processing results achieved with two simulated scenarios. The main difference between the scenarios is the integration angle β. Section 6.4.1 clarifies the influence of β theoretically.

6.4.1. Influence of integration angle, theory

The investigation of geometry affecting the imaging performance concerns the traveled path of the sonar and its position relative to the region to image. The subjects of focusing and motion were already discussed in Chapter 5, but are now analyzed specifically for the wavenumber frequency processing methods, both theoretically and in practice on simulated data. With respect to the sensitivity of focusing it was shown by Groen (2002) and in the previous chapter that the focus depth Δr depends on the frequency f, the synthetic aperture length L and on the across-track position of the imaged object y_{focus}:

$$\Delta r = \frac{c}{24 f} \frac{c + 24 f \sqrt{L^2 + y_{\text{focus}}^2}}{c + 12 f \sqrt{L^2 + y_{\text{focus}}^2} - 12 f y_{\text{focus}}}, \tag{6.16}$$

A graph of this formula is shown in Figure 6-9.

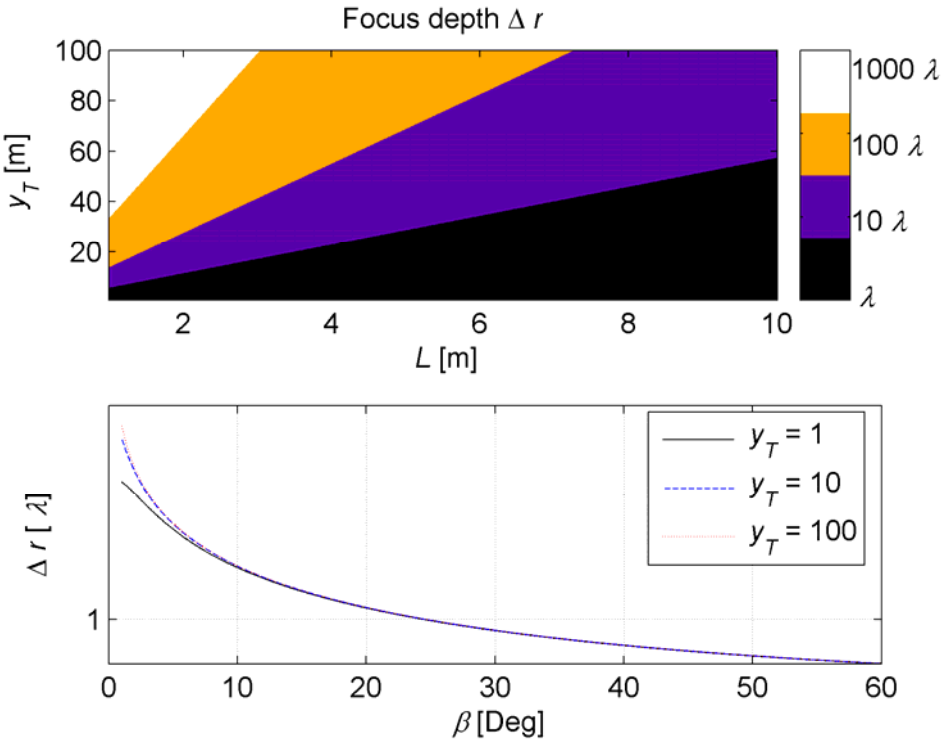


Figure 6-9 *The upper panel depicts the focus depth Δr in wavelengths versus synthetic aperture length L and range of the area of interest r. The lower panel shows the behavior of this parameter versus integration angle β, which can be expressed in the other two parameters and is shown for a range 1, 10 and 100 m.*

At the interesting ranges for SAS operations, β fully determines Δr. Overall, there is a remarkable resemblance between Figure 6-4 and Figure 6-9. Eqs. (6.12) and (6.17) are indeed similar apart from some constants and the tangent replaced by the sine. Rewriting Eq. (6.16) into an expression that is dependent on the wavelength λ and the integration angle β yields:

$$\Delta r = \frac{\lambda}{24} \frac{\lambda + 24\, y_{\text{focus}} \sqrt{4 \tan^2 \frac{\beta}{2} + 1}}{\lambda + 12\, y_{\text{focus}} \left(1 - \sqrt{4 \tan^2 \frac{\beta}{2} + 1} \right)}, \tag{6.17}$$

which is not equal to Eq. (6.12), but shows a similar behavior over the range for the parameters used. It should be noted that Δr is equal to $y_{\max}$ for small β, because then $4 \tan^2 \frac{\beta}{2} = \sin^2 \beta$. For the imaging performance, this formula implies that errors arise when the imaging method has a fixed focus range, such as with SFI and convolution imaging. As explained in the previous chapter, when the actual range differs more than Δr from the focus range, image blurring starts to occur. At the interesting ranges for SAS operations the sensitivity of Δr to the focus range y_{focus} is negligible and Eq. (6.17) simplifies to $\Delta r = \frac{\lambda L^2 + 2\lambda y_{\text{focus}}^2}{12 L^2} = \frac{\lambda y_{\text{focus}}^2}{6 L^2}$, which is a known result and is for instance mentioned by Lurton (2004).

6.4.2. Influence of integration angle, practice

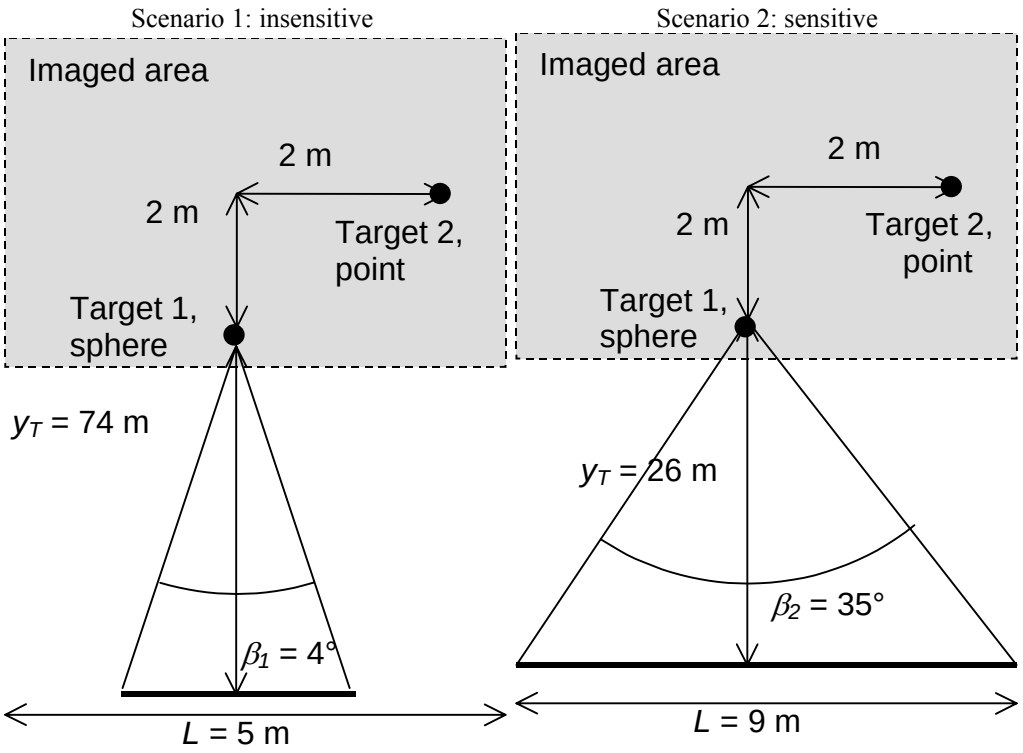


Figure 6-10 *Schematic illustration of the simulated scenarios.*

To investigate how a SAS image is finally affected by the geometry, two scenarios are investigated. The difference between the two is the integration angle, which is small in Scenario 1 ('insensitive') and large in Scenario 2 ('sensitive'). In both scenarios f = 100 kHz.

The 'insensitive' Scenario 1 is hardly influenced by the previously described geometry effects. The integration angle β = 4°, L = 5 m and the range of the sea floor patch to be imaged varies from 70 to 75 m. The simulation includes reverberation by means of point scatterers (10000 in total), a 1 m diameter sphere at 74 m and a shadow that is shifting according to the platform position. The simulation is repeated with the 'sensitive' Scenario 2, with β = 35°, L = 9 m and the range of the sea floor patch varying between 25 and 30 m. The resulting images are shown in Figure 6-11. One should realize that in practice the integration angle is fixed and limited by the transmission beamwidth.

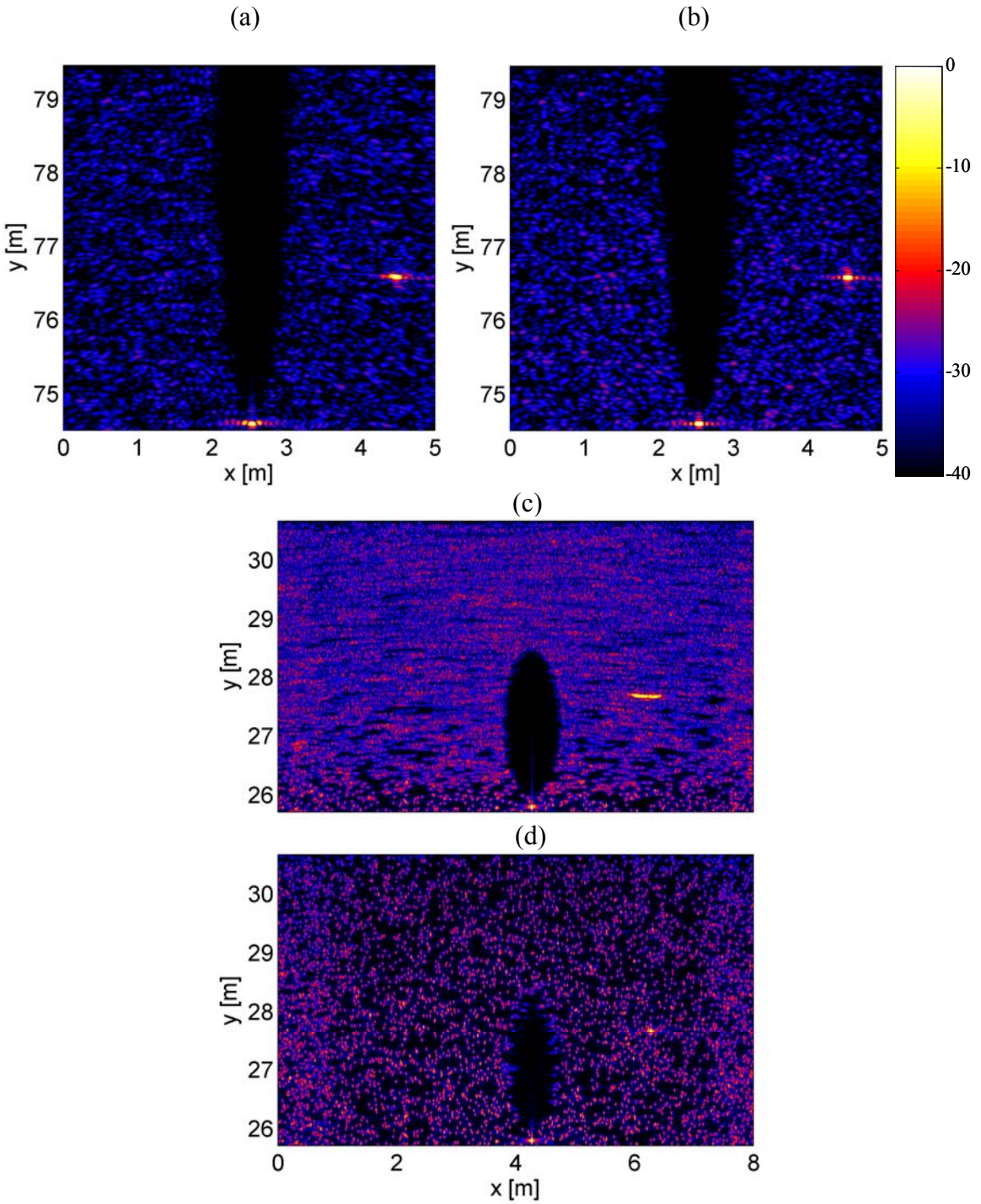


Figure 6-11 *The effect of geometry on SAS images. In contrast to the images a and b, the images c and d show a simulated scenario that is rather sensitive to focusing. The images a and c are obtained with convolution imaging focused at target 1 and the images b and d with Stolt migration.*

Several phenomena can be recognized in the images of Figure 6-11. The difference between the images a and b is rather small. There is a bit of smearing of the reverberation visible in the image b. In contrast to this, images c and d show a clear difference in reverberation and shadow. In image c the bottom scatterers are smeared and are not individually visible from about one meter from the chosen focus range, which is tuned to target 1. Furthermore, the

shadow is sharp in image c and blurred in image d. This phenomenon has been encountered both with real and simulated data in a similar manner. From the geometry, increasing shadow blur can be expected for increasing integration angle. Shifting of the shadow with the platform causes this. However, this shifting of the shadow is nicely compensated by the error in focus range. In other words: focusing on a point-like target sharpens the shadow behind it. Of course, in practice the focus range depends on the location of possible targets of interest.

6.4.3. Influence of platform motion, practice

The ULA condition is too severe in the application of synthetic aperture sonar. In operational situations, the aperture that is built up by translation of the sonar platform does not form a uniform linear array within the allowed deviations of a quarter of the acoustic wavelength. Hence a correction is needed, i.e. motion compensation is needed prior to imaging. The proposed correction method of Eq. (6.10) is based on phase alignment, which compensates the deviation from the straight line, as described in Section 6.3.1. To verify whether this compensation method is well suited to the operational demands of a common SAS system, the two scenarios are again used to show the effects of motion compensation. A sinusoidal deviation with amplitude equal to the center wavelength and period equal to the synthetic aperture length L is applied, to measure the effect of disturbance of the ULA.

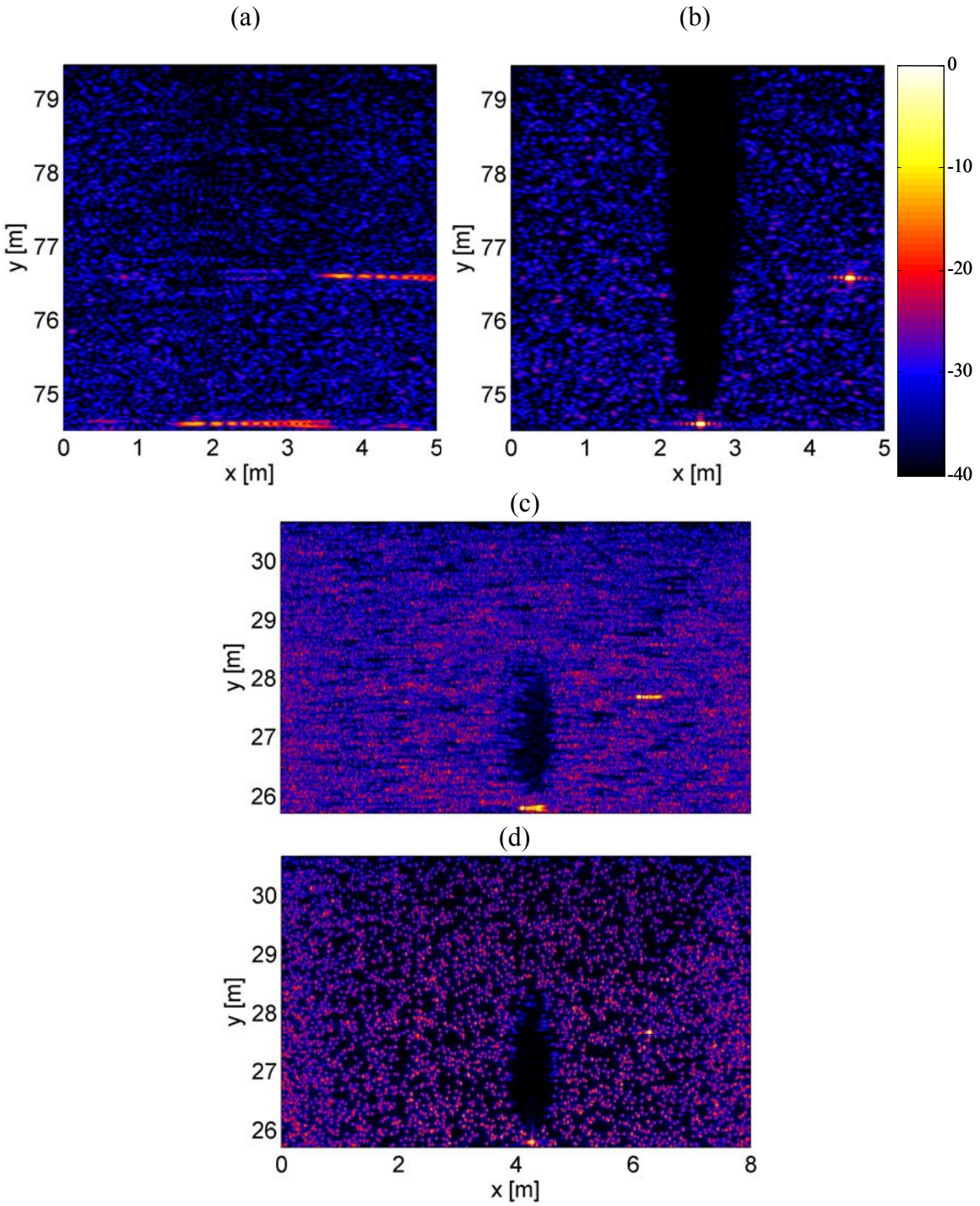


Figure 6-12 *The effect of deviations from the ULA on Stolt SAS images using Scenario 1, images a and b, and Scenario 2, images c and d.*

From Figure 6-12 it is clear that with these deviations motion compensation is a must. The result in the image a is especially dramatic. It can also be concluded that motion compensation repairs the degradation rather well.

6.4.4. Parameter sensitivity

Many parameters influence the quality of SAS processing. This section provides an overview of the most relevant parameters and their influence. Geometry effects have been discussed in the former sections. Here, parameters of the signal, propagation and processing are reviewed.

The transmission is defined by waveform, ping repetition time etc., and the receiver parameters comprise element spacing, number of elements etc. The influence of the waveform, generally defined by bandwidth, center frequency, duration and type, on the result of SAS processing is dominated by the frequency domain properties. The bandwidth itself proportionally influences the range resolution, and therefore, the influence for SAS is secondary. However, the frequency content of the signal is of great importance for the error sensitivity in the processing. Maximum allowed disturbances in focusing or geometrical errors are both proportional to the signal frequency, which is visible in Eq. (6.12) and Eq. (6.16). It is necessary to know the sound speed that is apparent during the propagation of the signal. However, analysis of both simulated and real data shows that the accuracy of measuring the sound speed is not a big issue for SAS processing. Of much greater importance is the path traveled by the sound, i.e. the range of the area of interest. After reception the signals are fed into the signal processing chain. The important parameters to choose in this stage are the integration (synthetic aperture) length or integration angle and the processing parameters (tapers, imaging type, filters, etc.).

In order to analyze quantitatively the effects of focusing and motion compensation, the beampatterns corresponding to Figure 6-11 and Figure 6-12 are plotted in Figure 6-13 and Figure 6-14, respectively. The beampattern was defined in Chapter 2, but it has to be noted that here the output is plotted as a function of x and not, as usual, versus bearing. This has no consequences for the results. As the simulations involve, besides numerous point scatterers, the insonification of two main targets, two plots are shown for each scenario. The response at the range of target 1 is shown in the figures on the left and the response at the range of target 2 is visible on the right. The beampatterns are shown for the four different cases:

(1) ULA, Convolution imaging, focused at target 1
(2) ULA, Stolt migration
(3) Deviated from ULA, Stolt migration without motion compensation
(4) Deviated from ULA, Stolt migration with motion compensation

The beampatterns in Figure 6-13 show (again) that focusing is not a major issue, but some losses can be expected for the secondary target. The result after motion compensation, visible with the dashed line is similar to having no disturbance at all.

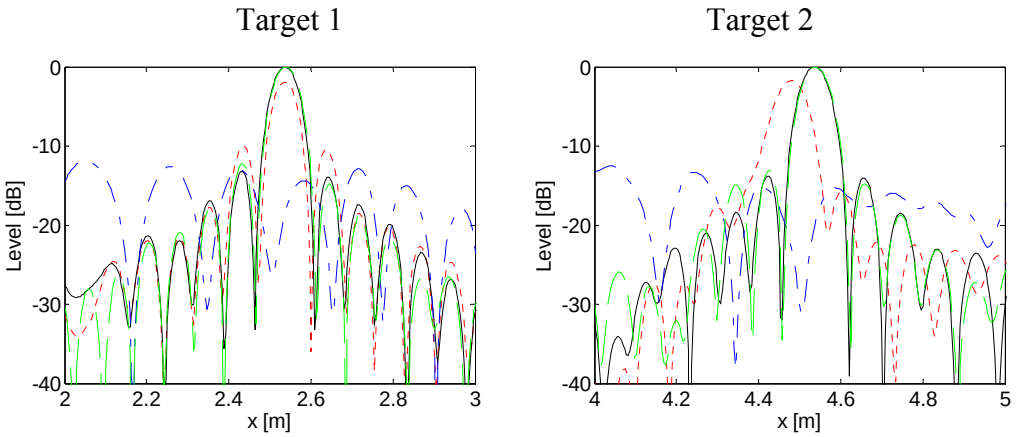


Figure 6-13 *Cuts at the target range on a scale of 40 dB of the 'insensitive' geometry (β = 4°). The four cases are plotted with black (1), red (2), blue (3) and green (4) curves. On the left the responses of target 1, which is positioned at the focus range, is shown. On the right the responses of target 2, positioned 2 m behind and next to target 1, are plotted.*

Figure 6-14 shows the results for the 'sensitive' geometry. For both target 1 and target 2 it is clearly visible that motion compensation and proper focusing are a necessity, otherwise the beampattern transforms to one with a very bad resolution (in fact the real aperture beampattern). After motion compensation some high sidelobes are still present, but the general behavior is acceptable.

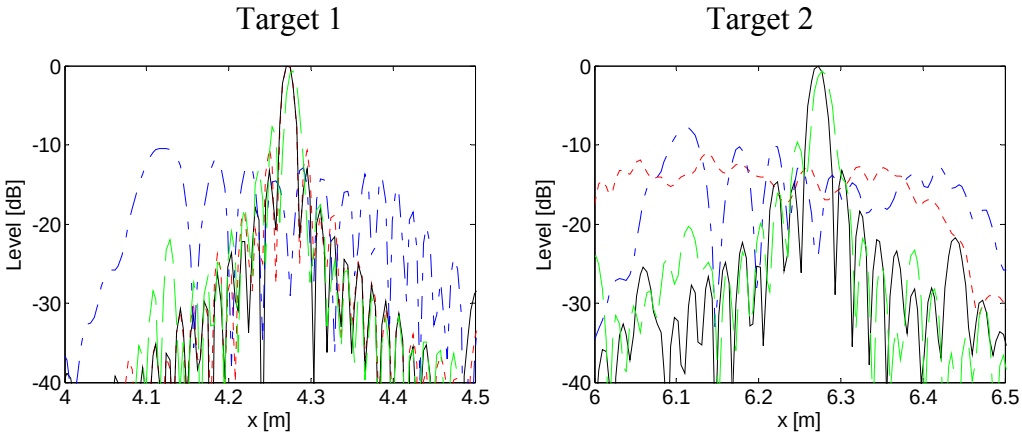


Figure 6-14 *Cuts at the target range on a scale of 40 dB of the 'insensitive' geometry (β = 35°). The four cases are plotted with black (1), red (2), blue (3) and green (4) curves. On the left the responses of target 1, which is positioned at the focus range, is shown. On the right the responses of target 2, positioned 2 m behind and next to target 1, are plotted.*

6.5. Shadow enhancement for improved target classification

The shadow of a target is a strong classification clue, because it supplies a lot of information on the shape of the target and is usually bigger than the acoustic response of the target. The shadow appears in the high resolution sonar images in a bottom reverberation-limited scenario. It is visible when the along-track resolution is better than the size of the object and

when multipath arrivals do not fill in the shadow too much. At longer ranges shadow classification becomes less trivial and at some point impossible.

The area behind the target that forms the shadow was already described and modeled in Chapter 2 and consists of the projected sea floor patch that is invisible for the sonar elements. Unfortunately, SAS uses an as long as possible aperture, which causes the area behind the target to shrink. This effect is similar to an optical shadow that is diffuse when a strip light is used, but sharp with a spotlight. The longer the light source (the optical equivalent of the synthetic aperture), the more blurred the shadow becomes.

This section proposes a method to solve this blurring. Naturally, first, a quantitative analysis of the blur in the sonar images proves the need for a solution. Second, the convolution imaging method is used in a special way for recovery of the shadow. This is followed by a analysis why this method recovers the shadow. Finally, the method is combined with the Stolt migration in order to achieve the best of both worlds.

6.5.1. Blurring of the shadow due to large integration angles

To be able to quantify the blurring effect, first an example is considered. A realistic scenario is chosen and with such geometry that the blurring effect is clearly present. This means short range, low grazing angle, small object, wide beam and a wide sonar band. The ping repetition time T_p is 0.2 s, the transmit chirp signal runs from 60 to 110 kHz in 1 ms. The sonar consists of one transceiver that moves past the cylinder target with a velocity of 44 mm/s, in order to meet the Nyquist sampling criterion. The source level is set at 210 dB. The sonar tilt angle is 6 degrees, which puts the target in the middle of the vertical sonar beam. The beampattern is based on the frequency band of the signal and the size of the source and receivers. All beamwidths are 40 degrees at the centre frequency except the horizontal receiver beamwidth, which is 60 degrees. The proud cylindrical target of length 1000 mm and radius 267 mm rotated 45 degrees is positioned at an across-track distance of 30 m, which results in a target range of 32 m. The sea bottom consists of fine sand with a Lambert's parameter μ of -26 dB. Notice that the scenario resembles the simulated example from Chapter 2, apart from the smaller target, the lower grazing angle and the transceiver configuration to avoid near field errors in the Stolt migration that were present there.

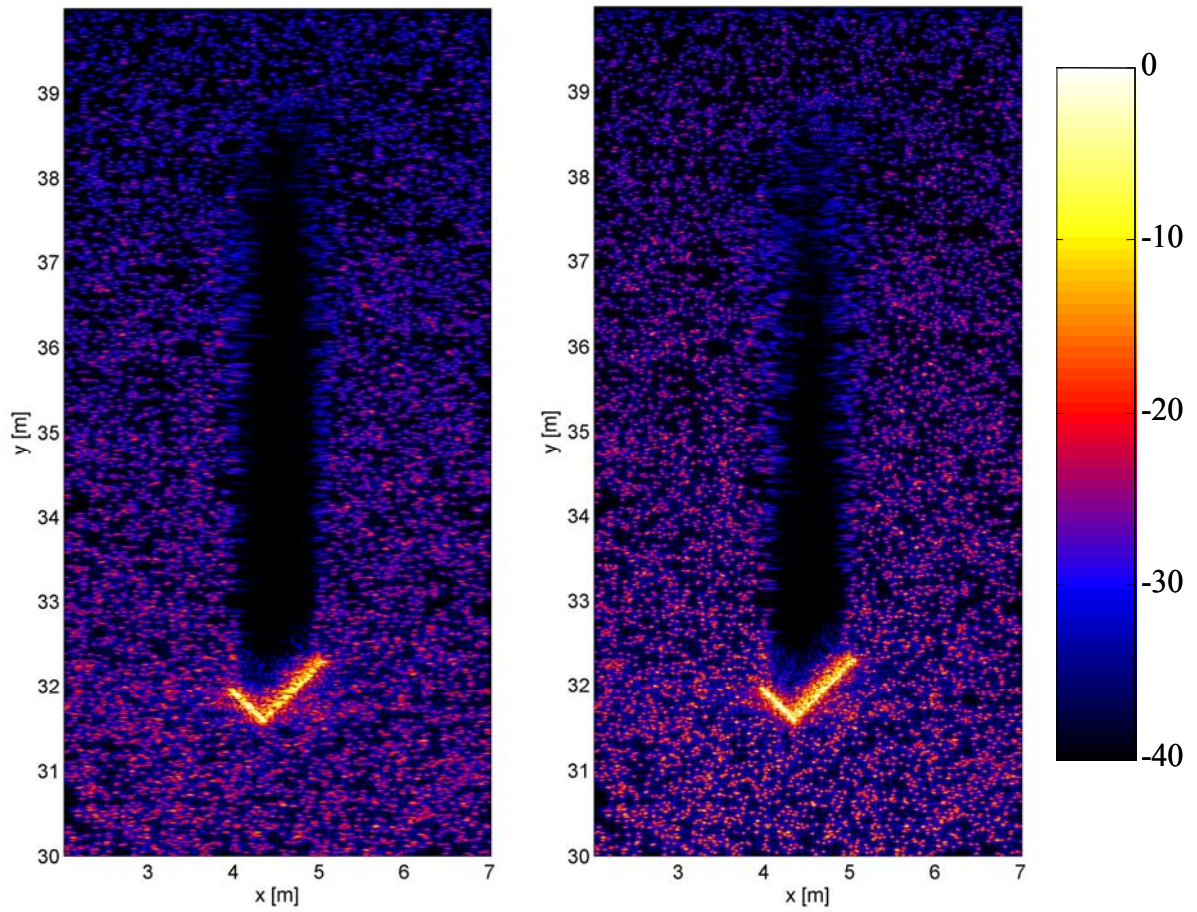


Figure 6-15 *Comparison of Stolt migration SAS images with different synthetic aperture length. The integration angle is 8 degrees in the left image and 16 degrees in the right image.*

Elongating the synthetic aperture is the same as increasing the integration angle. It causes the shadow to blur, diminish and changes its shape. Figure 6-15 clearly shows an improvement in resolution on the right hand side, i.e. the reverberation pixels and the cylindrical target are much sharper. Nonetheless, a large part of the shadow is filled in. Not only does this filled in part look bad in terms of resolution, but its energy level is somewhere in between those of the reverberation and the shadow. The result is a clear reduction in contrast and a shape that is far from what is expected from a cylinder.

Theoretical evaluation of shadow blurring

The analytical quantification of the shadow blurring is a difficult task for objects with an arbitrary shape. Therefore, a plate that stands on the sea floor parallel to the sonar track is taken as reference here. A plate with height h and width w also has the nice property that the edge of the shadow is always generated by the same part of the object, i.e. the plate edge. This also makes the plate the best-case example, because with most other objects additionally the shadow shape changes as a function of aspect angle.

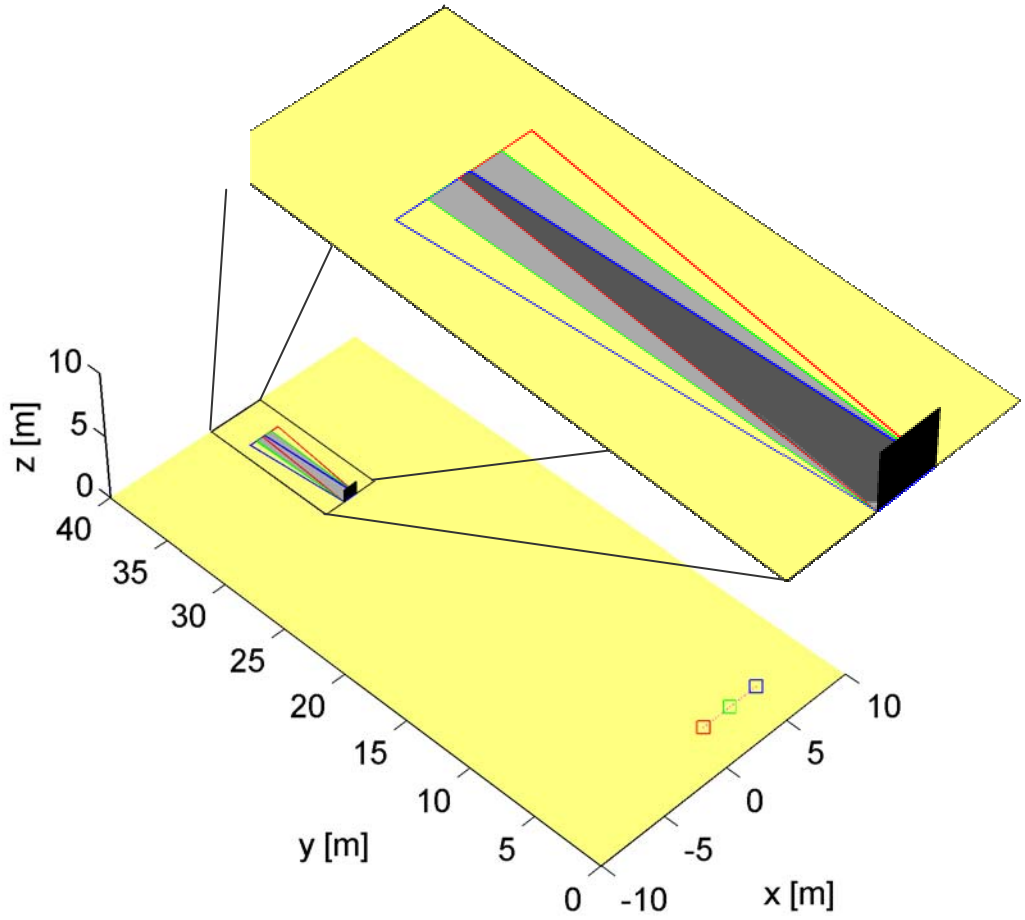


Figure 6-16 *Change of shadow as a function of aspect angle in the 3D geometry. Along the synthetic aperture the project shadow changes from the red through the green to the blue situation. Integration over the aspect angle from -β/2 to β/2 will leave only the dark gray part unaffected.*

Figure 6-16 shows the geometry of a SAS scenario with the same parameters as in Figure 6-15. The shadow formed by the utmost left ping (red) differs significantly from the shadow formed by the utmost right ping (blue). The zoom shows that more than half of the shadow is corrupted.

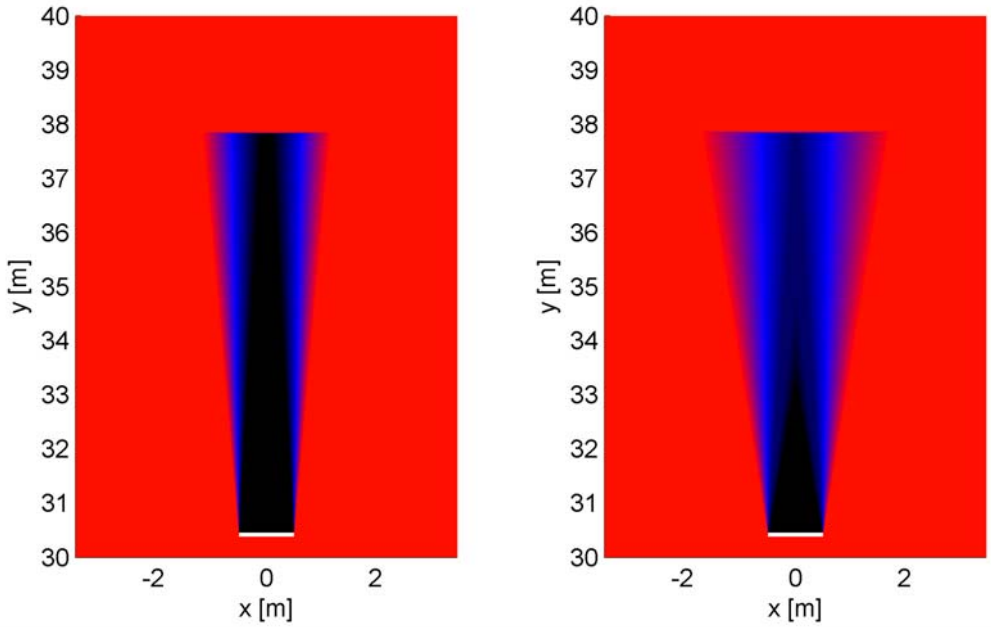


Figure 6-17 *Visualization of the resulting SAS images. The black part is the unaffected shadow. The blurred part extends from within the original shadow onto the reverberation. The shadow changes shape from square to triangle. The left hand image is calculated with β = 8 degrees and the right hand image is calculated with β = 16 degrees.*

Figure 6-17 illustrates the actual effect of blurring on the SAS image. The blurring first manifests itself in the along-track direction, but at an integration angle of 16 degrees the shadow length is also affected.

The blurred area of the shadow is referred to as A_{blur}, which is visible as the light gray parts in Figure 6-16. The first indicator that quantifies the shadow blurring ξ is the blurred area in the image divided by the expected affected shadow area formed by a plane wave:

$$\xi = \frac{A_{\text{blur}}}{A_0}, \tag{6.18}$$

in which the original (square-shaped) shadow area A_0 does not depend on the integration angle β, but only on the grazing angle γ. For a plate with height h and width w in Eq. (6.18):

$$A_0 = \frac{wh}{\sin\gamma}, \tag{6.19}$$

and in which A_{blur} is calculated by two formulae:

$$A_{\text{blur}} = \begin{cases} \dfrac{h^2 \tan\left(\dfrac{\beta}{2}\right)}{\sin^2 \gamma} & , w \geq 2h \tan\left(\dfrac{\beta}{2}\right) \sin\gamma \\ A_0 - \dfrac{w^2}{4 \tan\left(\dfrac{\beta}{2}\right)} & , w < 2h \tan\left(\dfrac{\beta}{2}\right) \sin\gamma \end{cases} \tag{6.20}$$

Notice that these areas are found in the SAS image and that they do not equal the projected area on the sea floor. In Eq. (6.20), the quantity $2h\tan(\beta/2)\sin\gamma$ becomes greater than w when the synthetic aperture is large enough so that the acoustic rays for high and low values of the sonar position x (passing on both sides of the object) start to overlap. The shadow shape then transforms from a carrot shape to a triangular shape. This is true for any object.

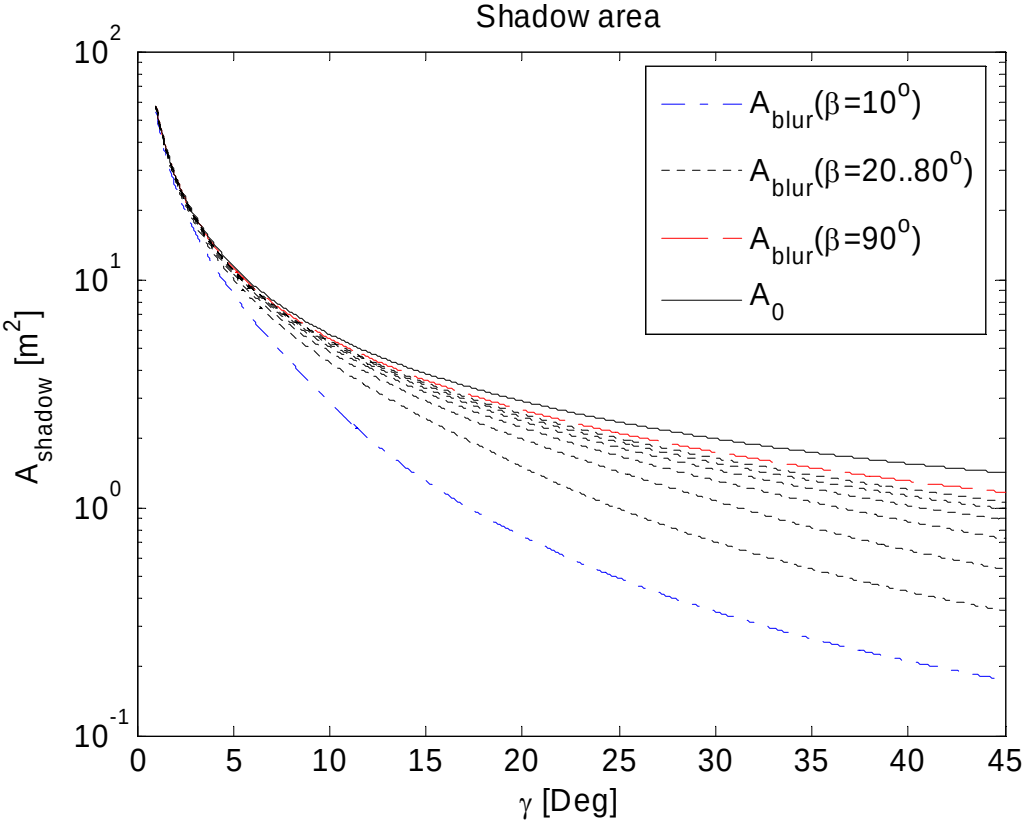


Figure 6-18 *Shadow area calculated for different grazing angles γ and different integration angles β. The areas A_0 and A_{blur} are shown on a logarithmic scale.*

Figure 6-18 shows the original shadow area A_0 calculated with Eq. (6.19), which decreases monotonically with grazing angle γ. It also shows a set of calculations of A_{blur} calculated at integration angles β varying from 10 to 90 degrees with steps of 10 degrees. For all cases the blurred area also decreases monotonically with grazing angle. The curves are continuous and differentiable despite of the fact that the curves are described with two formulae in Eq. (6.20). It is striking that in most cases the result is not favorable. The blurred area is a considerable part of the shadow.

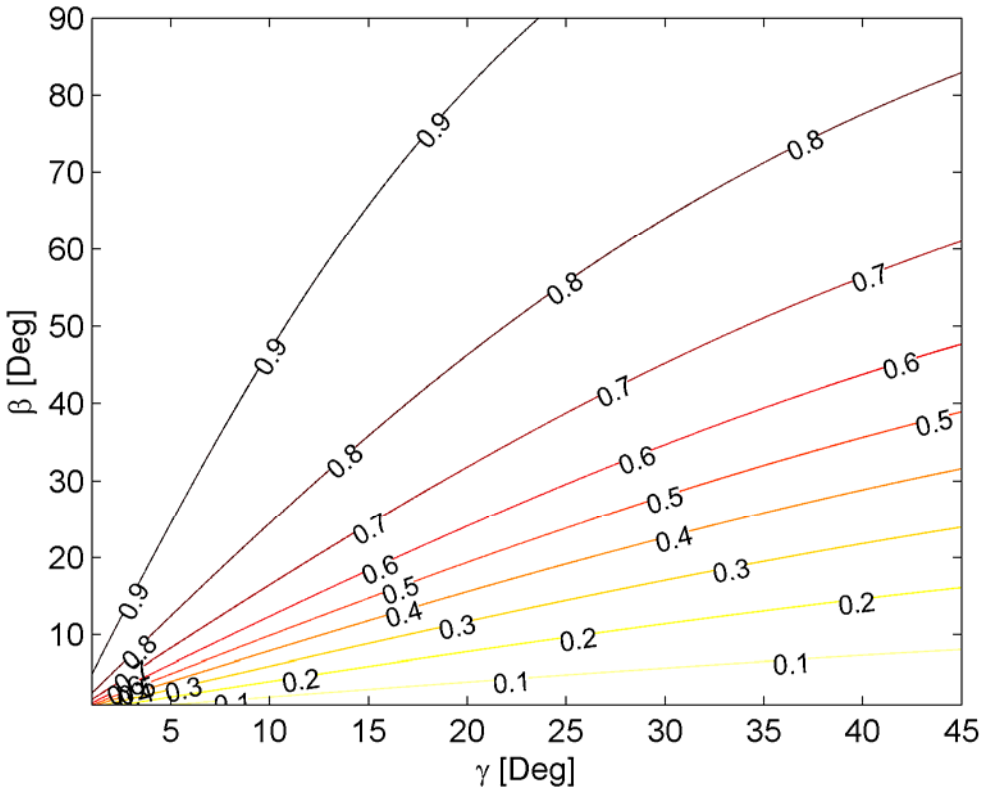


Figure 6-19 *Blur ratio ξ versus grazing angle γ and integration angle β. The blur ratio lies in between 0 and 1, where 1 represents the worst case, i.e. complete blurring.*

The ratio of the two areas as defined in Eq. (6.18) are shown in Figure 6-19 as a function of β and γ. The influence of β is clearly more important than the influence of γ. From this performance analysis it can be concluded that only small integration angles and high grazing angles supply a good scenario. A loss of 20 % of the shadow may already be unacceptable. For the state-of-the-art SAS systems severe blurring seems inevitable, since β is usually wider than 10 degrees.

The second indicator allows a stronger boundary criterion with respect to grazing angle, integration angle and frequency. The second indicator is based on the along-track shift Δx_{blur} of the shadow as appearing in the SAS image. Each projected point on the sea floor shifts along x as a function of aspect angle. Since this shift is changing with across-track position, the average $<\Delta x_{blur}>$ is considered. The average along-track shadow shift is calculated with:

$$\begin{aligned}\left\langle \Delta x_{\text{blur}} \right\rangle &= \frac{\sin\gamma}{h}\int_0^{\frac{h}{\sin\gamma}} \Delta x_{\text{blur}}\,\mathrm{d}r \\ &= \frac{\sin\gamma}{h}\int_0^{\frac{h}{\sin\gamma}} 2r\tan\left(\frac{\beta}{2}\right)\mathrm{d}r \\ &= \frac{h\tan\left(\frac{\beta}{2}\right)}{\sin\gamma}\end{aligned}. \tag{6.21}$$

From this equation a good criterion can be derived, by the requirement that the average shadow shift in the along-track direction ought to be within a resolution cell. The resolution cell was given by $c/(2b)$ in the range direction and $0.22\lambda/\tan(\beta/2)$ in the along-track direction (in terms of 3dB width). The criterion $\langle\Delta x_{\text{blur}}\rangle < \Delta x_{3\text{dB}}$ can then be expressed as:

$$\frac{h\tan\left(\frac{\beta}{2}\right)}{\sin\gamma} < \frac{0.22\lambda}{\tan\left(\frac{\beta}{2}\right)}, \tag{6.22}$$

or

$$\beta < 0.22\arctan\sqrt{\frac{2\lambda\sin\gamma}{h}}\,. \tag{6.23}$$

Notice that both the resolution and the shift contain a factor $\tan(\beta/2)$. These factors enhance each other in the criterion.

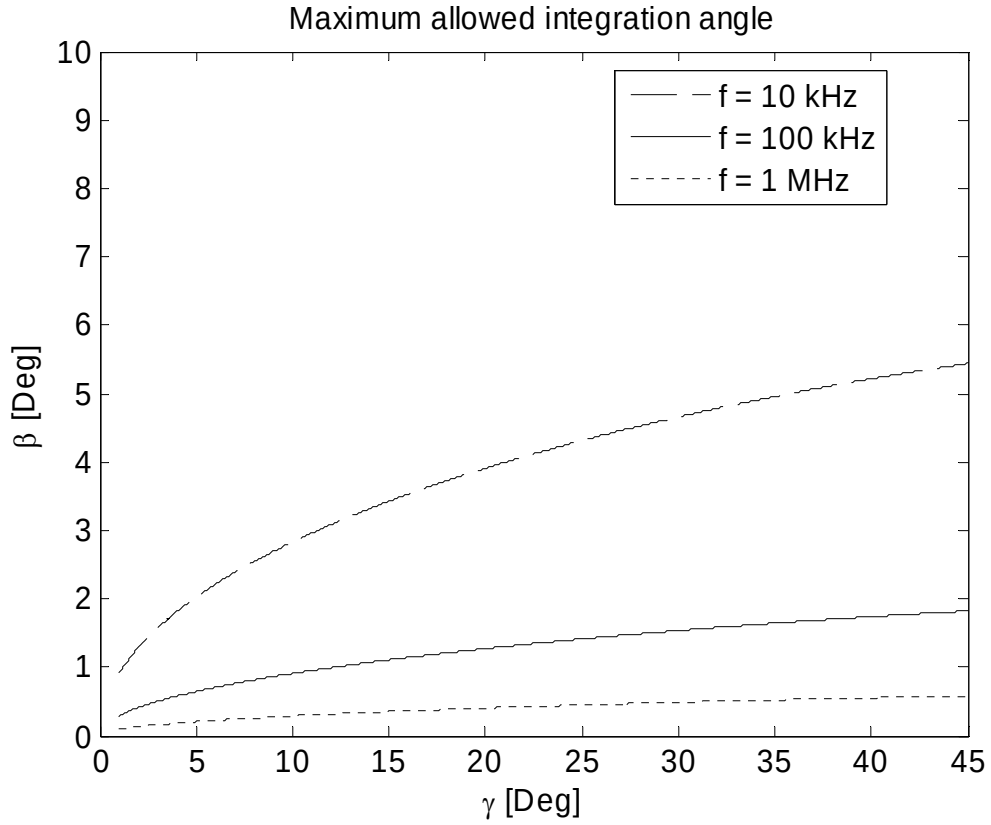


Figure 6-20 *Maximum allowed integration angle following the criterion that the along-track shadow shift may not surpass the actual resolution in that direction.*

Figure 6-20 shows the criterion for three different frequencies, which cover the whole band of mine hunting sonars. The allowed integration angle is always (much) smaller than 10 degrees. It may be concluded (again) that the shadow blur is significant, but that for very low frequencies the blur effect is not that severe.

6.5.2. Sharper shadows with convolution imaging

The idea for an enhanced shadow algorithm came from data analysis from several experimental data sets. It appeared that varying the focus range resulted in sharpening or defocusing of the shadow. This focusing of the shadow did not seem to coincide with a focus of the object or the rest of the image. The convolution imaging method was also tested on these data sets and it appeared that this method outperformed the Stolt migration method in terms of shadow contrast. For some time it was considered as just a remarkable effect and considered as one of the things that just come with experimental data. This section shows that it does not just come with experimental data, but that it can be explained and compensated for in an optimal way.

The explanation of this phenomenon is not trivial and two approaches are needed in order to find the solution.

Shadow motion along the synthetic aperture

First, the problem is analyzed with the projection of a point on the sea floor. This point represents a reflection point of the target, e.g. the top of a sphere. This point $(0, y_t, z_t)$ is projected on the sea floor at a position $(x_{\text{shadow}}, y_{\text{shadow}}, 0)$. This projection point moves depending on the sonar's observation position $(x, 0, z)$:

$$\begin{pmatrix} x_{\text{shadow}} \\ y_{\text{shadow}} \\ z_{\text{shadow}} \end{pmatrix} = \begin{pmatrix} -\dfrac{xz_t}{z - z_t} \\ \dfrac{y_t z}{z - z_t} \\ 0 \end{pmatrix}. \tag{6.24}$$

Notice that the y-coordinate of the projection does not depend on the x-coordinate of the sonar, i.e. it is generally constant over the synthetic aperture. The idea now is to try and make a hyperbola that fits the travel times of such a hypothetical shadow projection point. The travel times of the signal for the target and for the projected shadow point are given by:

$$\begin{aligned} t_t &= \frac{2}{c}\sqrt{x^2 + y_t^2 + (z - z_t)^2} \\ t_{\text{shadow}} &= \frac{2}{c}\sqrt{(x - x_{\text{shadow}})^2 + y_{\text{shadow}}^2 + (z - z_{\text{shadow}})^2} \\ &= \frac{2}{c}\sqrt{\left(\frac{xz}{z - z_t}\right)^2 + \left(\frac{y_t z}{z - z_t}\right)^2 + z^2} \end{aligned}. \tag{6.25}$$

Migration of the target is defined as the difference in travel time between the actual sonar position and the closest point of approach, i.e. $t(x = x) - t(x = 0)$. For the same geometric properties as in the previous section, at an integration angle $\beta = 16\ ^{\circ}$, the migration for the target point and the projected shadow point are shown with the dash dot line and the solid line in Figure 6-21, respectively. The migration curve of the projected point is even sharper than the target point curve, regardless of its longer range. The migration curve for a target point at the same closest point of approach, i.e. the expected migration at that particular distance (also used in the SAS processing), is shown with the dashed line.

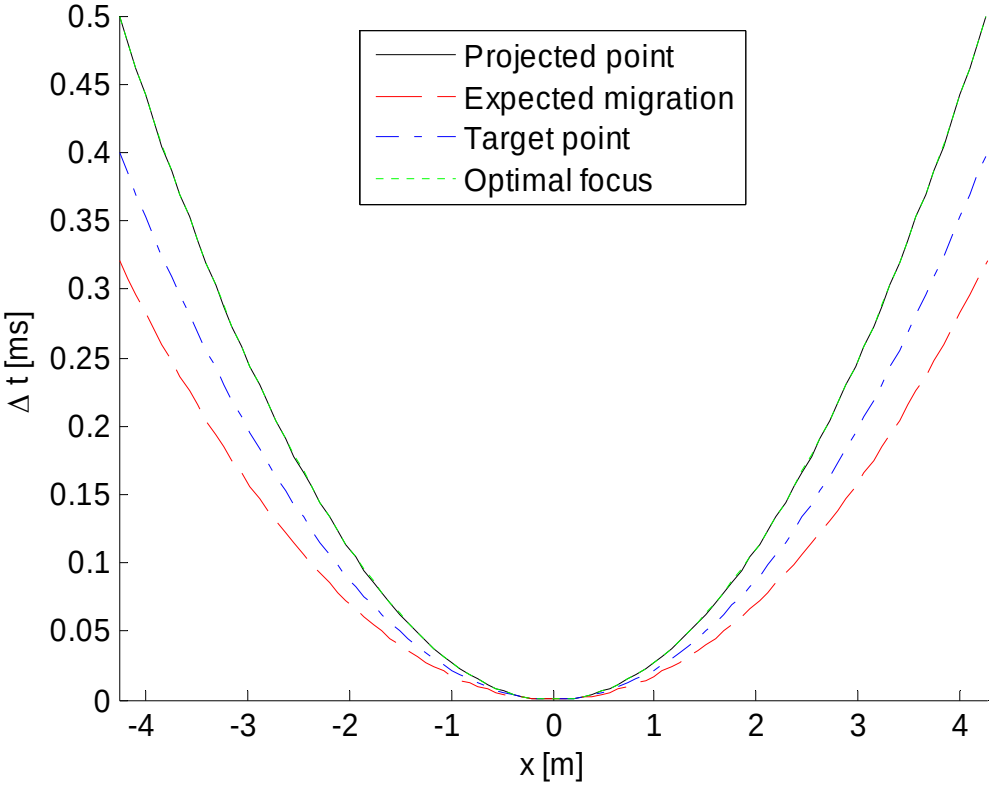


Figure 6-21 *Migration as a function of sonar x-coordinate for the projected shadow point (--), the expected migration for a normal stationary point at the same position as the shadow point (- -), the target point (- . -) and the hyperbola at an optimal focus range (. . .).*

The maximum migration of the target and the projected shadow point is defined as the travel time at the side of the beam minus the travel time at the closest point of approach. The closest point of approach occurs for $x = 0$ and the farthest point, at the side of the beam, occurs at $x = \sqrt{y_t^2 + (z - z_t)^2}\,\tan\frac{\beta}{2}$. The maximum migration for the shadow point is given by $t_{\text{shadow}}\left[\sqrt{y_t^2 + (z - z_t)^2}\,\tan\frac{\beta}{2}\right] - t_{\text{shadow}}[0]$. Focusing at a special range r_{focus} has exactly the same maximum migration. The equation to find the same migration is as follows:

$$\frac{c}{2}\left\{t_{\text{shadow}}\left[\sqrt{y_t^2 + (z - z_t)^2}\,\tan\frac{\beta}{2}\right] - t_{\text{shadow}}[0]\right\} = \sqrt{\left[y_t^2 + (z - z_t)^2\right]\tan^2\frac{\beta}{2} + r_{\text{focus}}^2} - r_{\text{focus}} \quad (6.26)$$

The explicit expression for the correct focus range is found by solving this equation. The result is:

$$r_{\text{focus}} = \frac{4\left[y_t^2 + (z - z_t)^2\right]\tan^2\frac{\beta}{2} - c^2\left\{t_{\text{shadow}}\left[\sqrt{y_t^2 + (z - z_t)^2}\,\tan\frac{\beta}{2}\right] - t_{\text{shadow}}[0]\right\}^2}{4c\left\{t_{\text{shadow}}\left[\sqrt{y_t^2 + (z - z_t)^2}\,\tan\frac{\beta}{2}\right] - t_{\text{shadow}}[0]\right\}}. \quad (6.27)$$

For the geometry considered, the target range was about 32 meters and r_{focus} is close to 24 meters. The difference between the two is substantial, but the difference between actual range of the moving shadow projection point and r_{focus} is even larger. This would mean that the difference in range between the image range and the focus range should be within focus depth, which was given by Eq. (6.17). If not, the (non-moving) reverberant scatterers blur the shadow, because they are poorly resolved and smeared out in the x- (and y-) direction.

For the aforementioned scenario, the optimal focus range for target points between zero and one meter above the sea floor is computed and plotted in Figure 6-22 with the solid line. Optimizing for the middle of the target implies a focus depth indicated by the dotted lines. More precisely, this means that every point scatterer that lies outside the region between the dotted lines is not well focused. 'Not well-focused' was defined as a signal loss greater than three decibels.

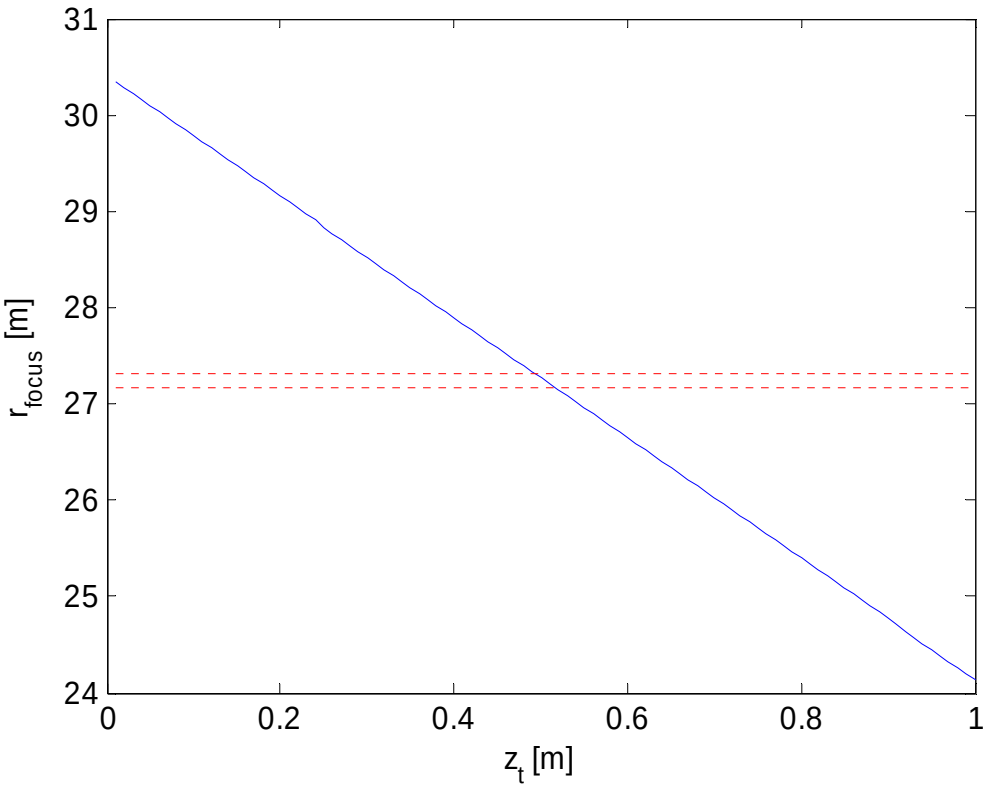


Figure 6-22 *Optimum focus range for the exemplary geometry versus target point height z_t. For a fixed focus range (in the middle), the focus depth is shown by means of the dotted lines.*

The focus depth is clearly not sufficient for this scenario. But, even worse, the optimal focus range calculated from Eq. (6.19), does not give ideal output images at all. The optimal focus range was found to be around the actual target range and the same for all points in the shadow. It is therefore concluded that this moving shadow point hypothesis, as presented in this section, does not sufficiently explain the sharpening of the shadows in SAS images. The next section will show an alternative approach, which will have more success.

Hyperbolae behind the target

The approach that is described now abandons the idea that a hypothetical shadow point is moving along the synthetic aperture. Instead, two fixed scatter points are considered, A and B. They are placed behind a plate, and where point A lies just outside of the plate's shadow area, point B is placed within the shadow region. They both have a response on the sonar. When the sonar's x-position is varied, the travel time for each point shows a hyperbolic behavior. The hyperbola for closer points is narrower. The signal is only received when the scatter points are within the sonar beam, i.e. for $x_s \in \left[x_t - r_t \tan(\beta/2), x_t + r_t \tan(\beta/2) \right]$. The scatter points are, nevertheless, also masked by the plate, for some values of x_s. This is where the case of point A becomes slightly different from the case of point B. The x values where signals from point A and B are masked:

$$\begin{aligned} x_s &\in \left[x_A - r_A \tan(\beta/2), x_A - \left(\frac{w}{2} + x_A \right) \frac{r_A}{\Delta r_A} \right] \\ x_s &\in \left[x_B - \left(\frac{w}{2} - x_B \right) \frac{r_B}{\Delta r_B}, x_B + r_B \tan(\beta/2) \right] \end{aligned}, \tag{6.28}$$

where $\Delta r_A = r_A - r_t$ and $\Delta r_B = r_B - r_t$ are the range differences with the target. The hyperbolae are depicted in the middle panel of Figure 6-23. Point A is shown with the dash dot line and point B with the dotted line. For both the visible area is solid.

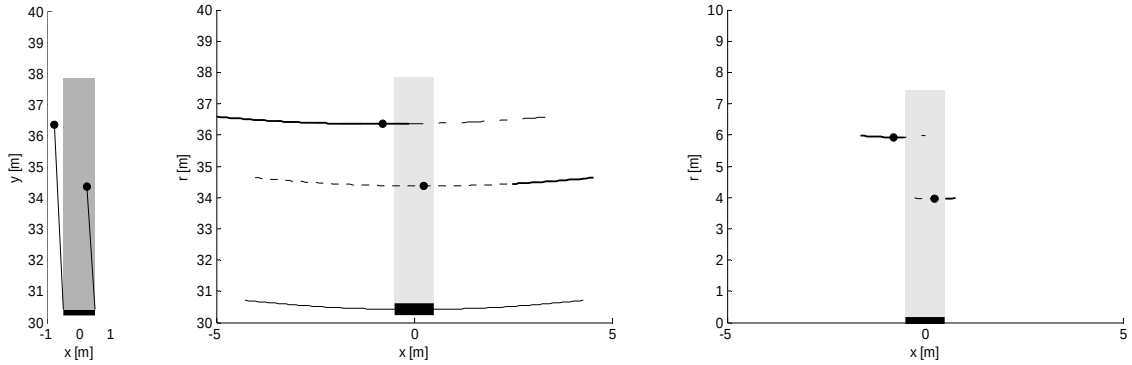


Figure 6-23 *Response for two fixed scatter points A and B on the sea floor. The left panel shows the 2D geometry with a point just next to the shadow and a point in the shadow. The middle panel shows the response of the two points and the target versus sonar position x. The right panel shows the response after convolution imaging with a focus range at the target.*

After Stolt migration, the hyperbolae transform into points. When the target range is used for focusing, the hyperbolae transform into a hyperbola that is described by:

$$\begin{aligned} r &= \sqrt{x^2 + \Delta r_A^{\,2}} \quad , x \in \left[x_A - r_A \tan(\beta/2) \frac{\Delta r_A}{r_A}, x_A - \left(\frac{w}{2} + x_A \right) \frac{r_A}{\Delta r_A} \frac{\Delta r_A}{r_A} \right] \\ r &= \sqrt{x^2 + \Delta r_B^{\,2}} \quad , x \in \left[x_B - \left(\frac{w}{2} - x_B \right) \frac{r_B}{\Delta r_B} \frac{\Delta r_B}{r_B}, x_B - r_B \tan(\beta/2) \frac{\Delta r_B}{r_B} \right] \end{aligned}, \tag{6.29}$$

where the x-window around the target is narrowed by a factor $\Delta r_A / r_A$ and $\Delta r_B / r_B$, respectively. It is as if the aperture is moved closer to the target and the remaining range causes the

remaining hyperbola with the same integration angle as before, as shown on the right hand side of Figure 6-23. The formulae can be simplified to

$$\begin{aligned} r &= \sqrt{x^2 + \Delta r_A{}^2} \quad , x \in \left[x_A - \Delta r_A \tan(\beta/2), -\frac{w}{2} \right] \\ r &= \sqrt{x^2 + \Delta r_B{}^2} \quad , x \in \left[\frac{w}{2}, x_B - \Delta r_B \tan(\beta/2) \right] \end{aligned} . \tag{6.30}$$

It is this equation that explains the sharpening of the shadow. Each point on the sea floor is defocused according to the range difference with the target. *Yet, the defocusing effect stops exactly at the edge of the shadow generated by that object.* Convolution imaging with a focus range on the target does the trick and, therefore, is recommended as a solution. The right-hand side of Figure 6-23 shows the Stolt migrated data with the dash dot line for *A* and the dotted line for *B*. Only the solid parts of the lines are actually present in the SAS image.

An elegant and simple method solves the blurred shadow problem. The only thing that remains is a test on simulated and experimental data. Figure 6-24 shows the simulated scenario of Figure 6-15 again, but now focused at 31 and 32 meters for the whole image. In both images of Figure 6-24, the shadow is much sharper. The sharpening is not very sensitive to the focus range used. The focus depth is also well visible as a band of well-focused reverberant scatterers. And, indeed, the shadow is much longer than this band.

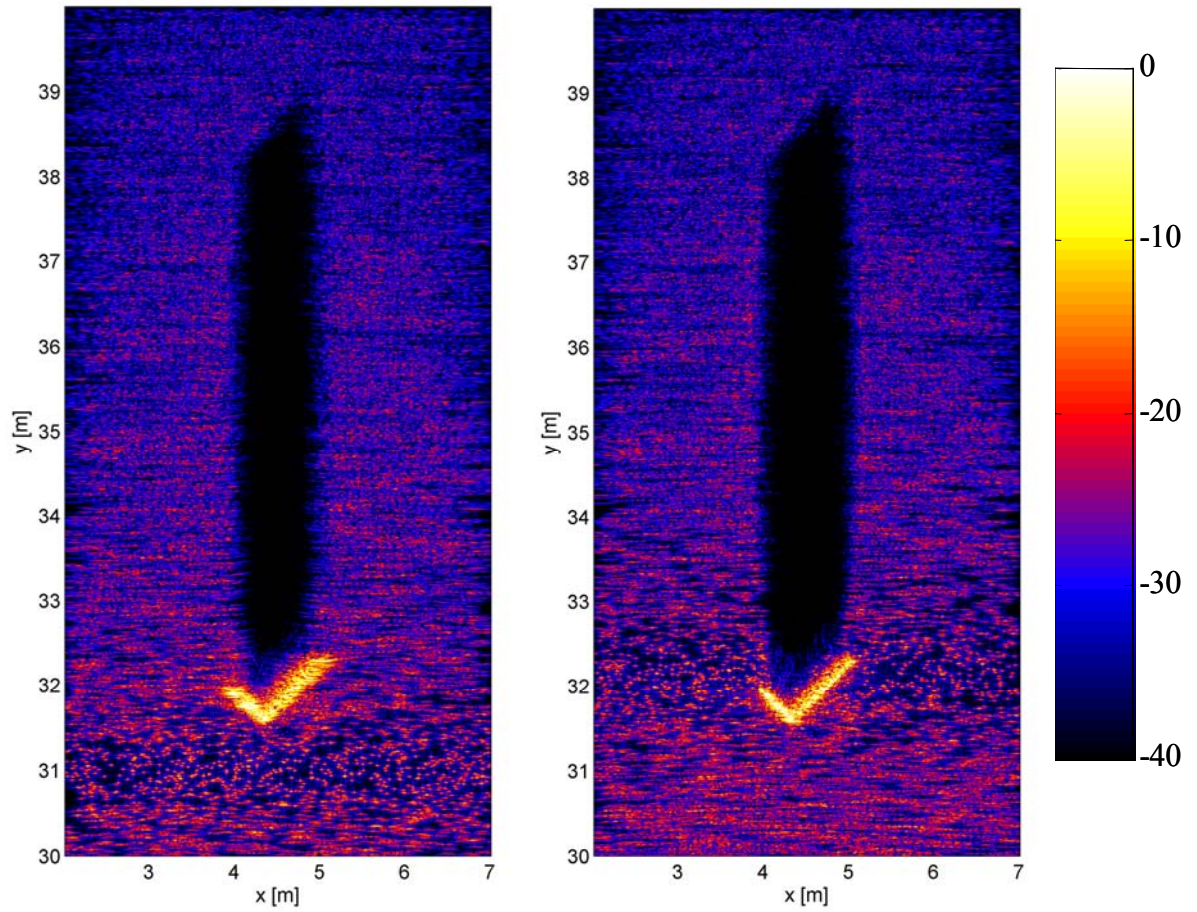


Figure 6-24 *Two simulated data results focused on a range of 31 (left) and 32 (right) meters.*

6.5.3. Combining convolution imaging with Stolt migration

A contour finding method was applied to both shadow areas. It first detects the target on the basis of signal amplitude. A contour is drawn along the boundary where the target scatter exceeds the threshold. From this contour the target width in the azimuth or along-track (x)-direction is determined. Then the lowest amplitude is searched in the region behind the target. From this starting point, marked by a cross in the left panel of Figure 6-23, a contour in the form of a convex contour is grown. A 'shadow threshold' is stepwise increased until the shadow width matches the expected width, which is equal to that of the target. The final contour is displayed in green. The right hand side panel shows a merge of the sharp shadow and the Stolt processing output as the right hand side panel of Figure 6-15. The merge is realized by cutting and pasting the shadow area from the convolution image (within the green envelope) into the Stolt image. The sharpened shadow reveals much better the rectangular cylinder shadow than the shadow from Stolt processing.

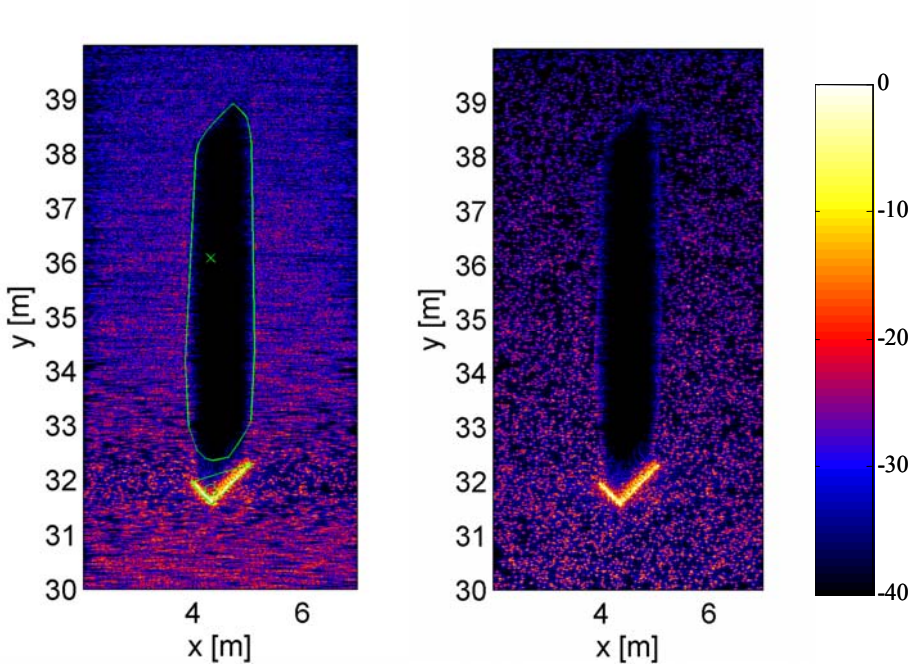


Figure 6-25 *On the left hand side the contour method is applied to convolution imaging output. On the right hand side the data are merged in order to form an overall sharp image (shadow + objects).*

6.6. Results with experimental data

To compare and verify their performance, the discussed SAS imaging methods are applied to two experimental data sets. The first concerns rail experiments with targets at different ranges. In this case, the deviation from the desired straight line is a minor issue. The second data set concerns a sonar mounted on an unmanned underwater vehicle (UUV), insonifying targets at a more or less single range. This is a more realistic scenario, but still the platform proves to be surprisingly stable.

In both cases deviations of the sonar have to be taken into account. First, the sonar positions are estimated with an autofocusing method. The chosen autofocus method is image correlation. However, it is not claimed here that this method is optimal. Autofocusing is, and will remain, the primary topic of research on SAS for the following years. Proposed methods are different for different frequency bands, scenarios and receivers (single or multi-element), see Bellettini (2000), Hétet (2000), Johnson (1995), Gough (2000), Sutton (2000), Callow (2001) and Fortune (2001) for instance. The optimal method(s) will not be developed until the SAS community agrees on a uniform way of comparison.

It was shown by Groen (2002) that image correlation autofocus gives a more accurate and more stable result to Displaced Phase Center (DPC) for multi-element receivers. However, DPC is more interesting for a computational point of view. The main advantages of image correlation are higher accuracy of the estimated parameters and no divergence with increasing number of pings. To apply this autofocus method robustly, parameter tuning is required, but this falls outside the scope of this thesis.

6.6.1. Application to rail data

In 1999, the defense research agencies GESMA (France) and DERA (United Kingdom) conducted rail experiments with the purpose of gathering data to show the capabilities of SAS in mine hunting. The data set has been analyzed extensively by several researchers, e.g. Hétet (2000), Groen (2001), Groen (2002) and Banks (2002). During the experiments a sonar traveled on a 10 meter long rail insonifying different targets at various ranges between 25 and 100 m. The sonar consisted of two receiving arrays of 32 elements and an acoustic source. Only data from the upper array are used for the analysis. Two experiments, denoted by experiment A and B, have been processed and analyzed. Experiment A concerns the insonification of a sphere on the seafloor at a range of about 25 m. The objects in experiment B are a sphere and a cylinder at a range of 75 m. The maximum integration time is 320 pings, with a repetition time of 3.34 s.

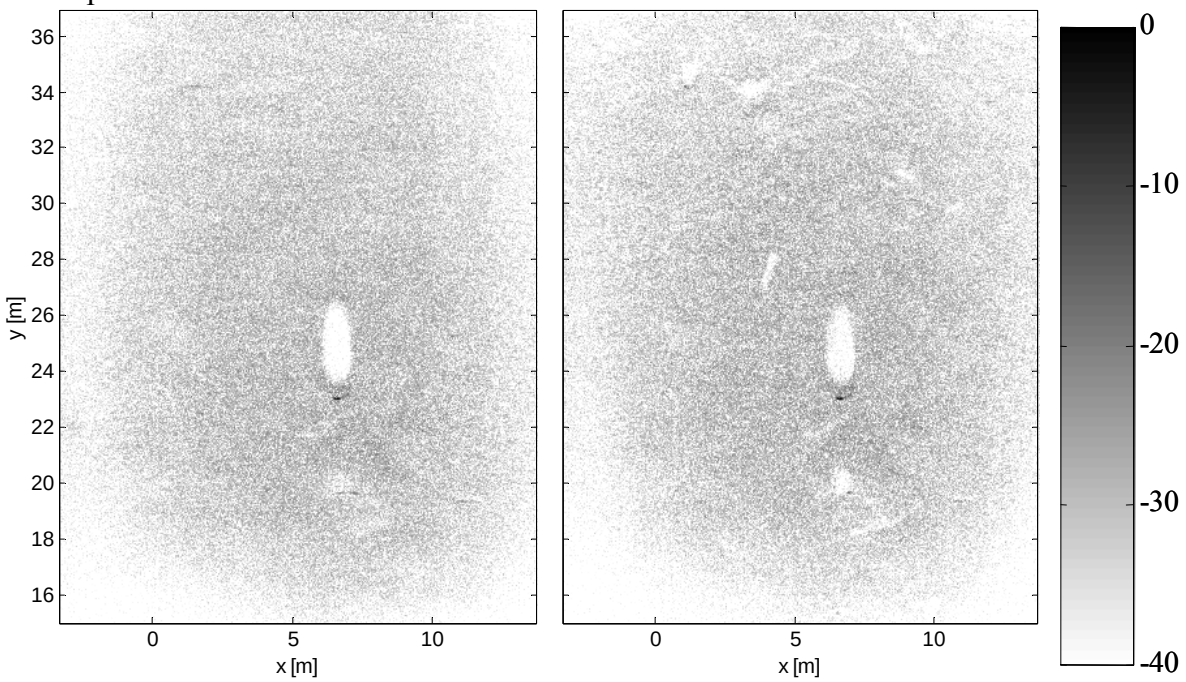


Figure 6-26 *Two resulting SAS images of experiment A. In the left image single-focus-range processing is applied, e.g. convolution imaging or SFI. In the right image correct-focus-range processing is applied, e.g. STI or Stolt migration.*

Figure 6-26 shows two SAS images of experiment A that result from convolution imaging and Stolt migration, respectively. Since the sonar was moving on a rail, deviation from the straight line is no problem. It was found that crabbing angle (yaw) estimation and compensation was sufficient. The processing is focused on the sphere, which is positioned at (x,y) = (6.6 , 23.1). The difference in sharpness of the shadow is similar to the simulated case in the previous section, which was explained in Section 6.5. Smearing is visible for ranges other than the focus range $y = y_{\text{focus}}$. The right image, processed with Stolt migration, shows a much sharper picture of the seafloor. Except for the shadow of the main target, many bottom features show up as shadows. An interesting feature is located at (x,y) = (6.9 , 19.7), which is an originally buried target that has emerged due to sea currents (scour).

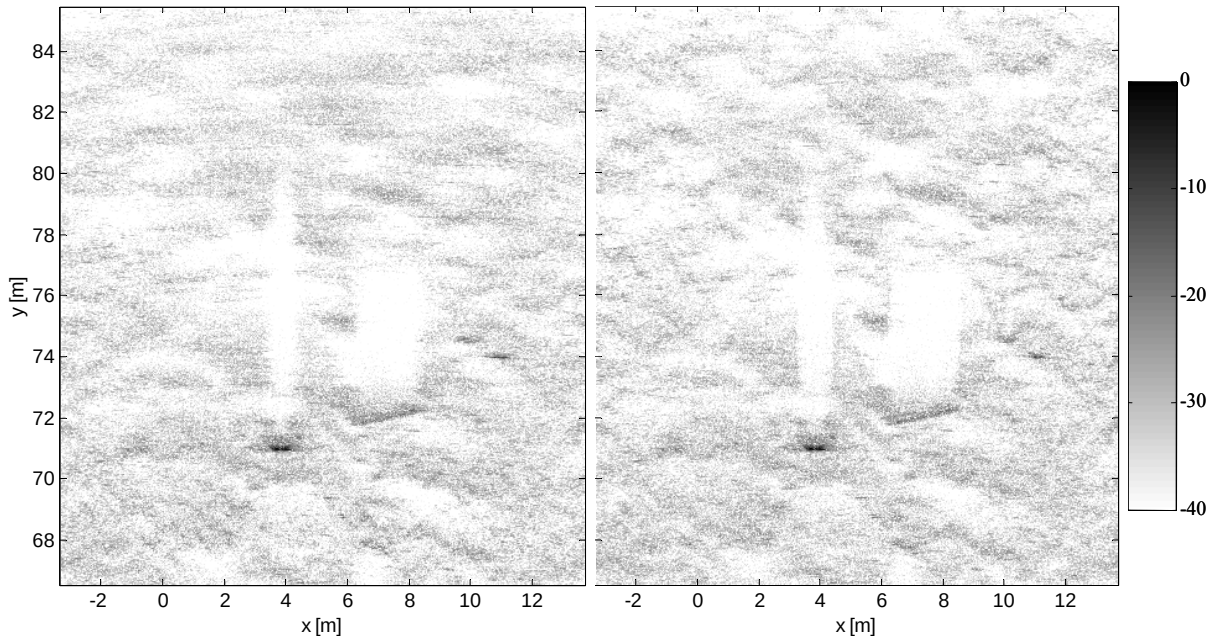


Figure 6-27 *Two resulting SAS images of experiment B. In the left image single-focus-range processing is applied, e.g. convolution imaging or SFI. In the right image correct-focus-range processing is applied, e.g. STI or Stolt migration.*

In Figure 6-27 the resulting SAS images of experiment B are shown. The images are more similar than in Figure 6-26 due to the smaller integration angle β, which yields a larger focus depth Δr. The difference is somewhat visible at the far end of the image between 82 and 84 m, where the left image is blurred and the image still shows bottom features. This is good news for the application of single-focus-range methods, although smearing is still visible in the upper half of the fixed-focus image.

6.6.2. Application to data from a UUV

In this section the application of the SAS imaging methods on experimental data from a UUV mounted sonar is demonstrated. The NATO research centre SACLANTCEN supplied this acoustic data set, which was recorded at a sea trial, referred to as the MASAI trial. The data set concerned insonification of a number of targets along a line at about 50 meters range. The total synthetic aperture length is about 33 m, but only a part of this is used for these SAS images, because the source beamwidth is limited. The resulting aperture is centered on a geometrically interesting object, a tripod.

The estimation of the surge, yaw and sway of the sonar by means of image correlation resulted in the reconstructed path shown in Figure 6-28.

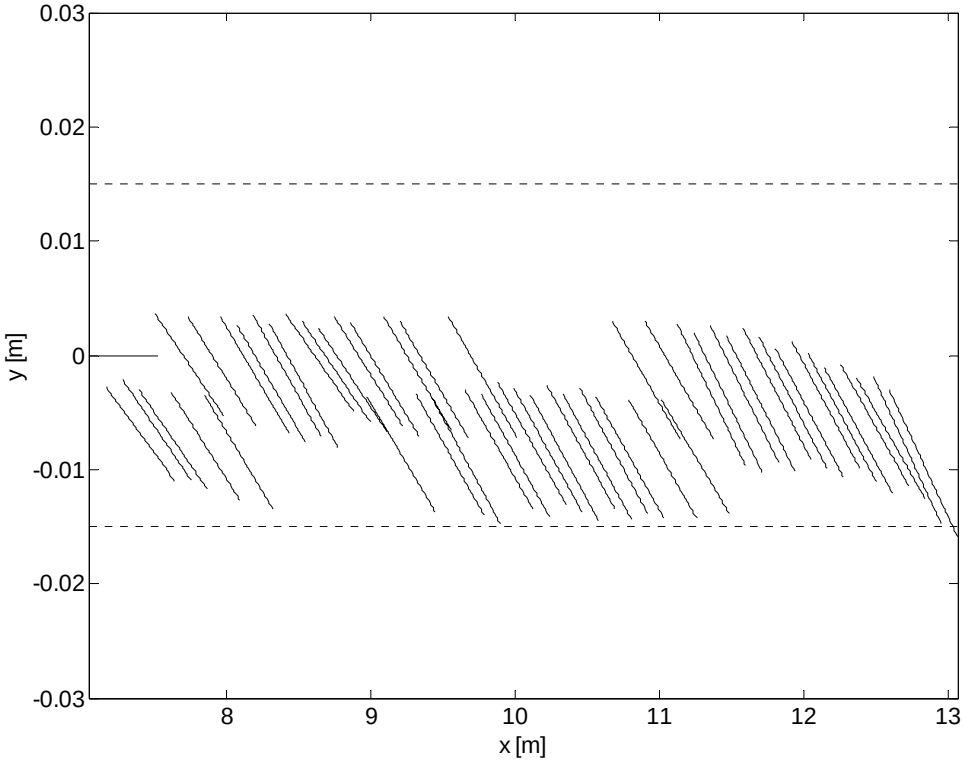


Figure 6-28 *Estimated track of the sonar during experiment C. The lines represent the sonar itself, i.e. the positions of the 32 phase centers. The dashed lines represent the wavelength at the center frequency of the transmitted waveforms.*

In Figure 6-28 the estimated path of the sonar, which is used for integration, is plotted. It should be noted that the scaling of *x*- and *y*-axis is not the same. The first ping only is initialized with a yaw of 0° and not used further for the imaging. The sonar appears to move very smoothly through the water. The deviation from the straight line is less than a wavelength, which already suggests that the application of the motion compensation algorithm should be successful. A final point that should be remarked is the large overlap between the different pings, which is clearly visible.

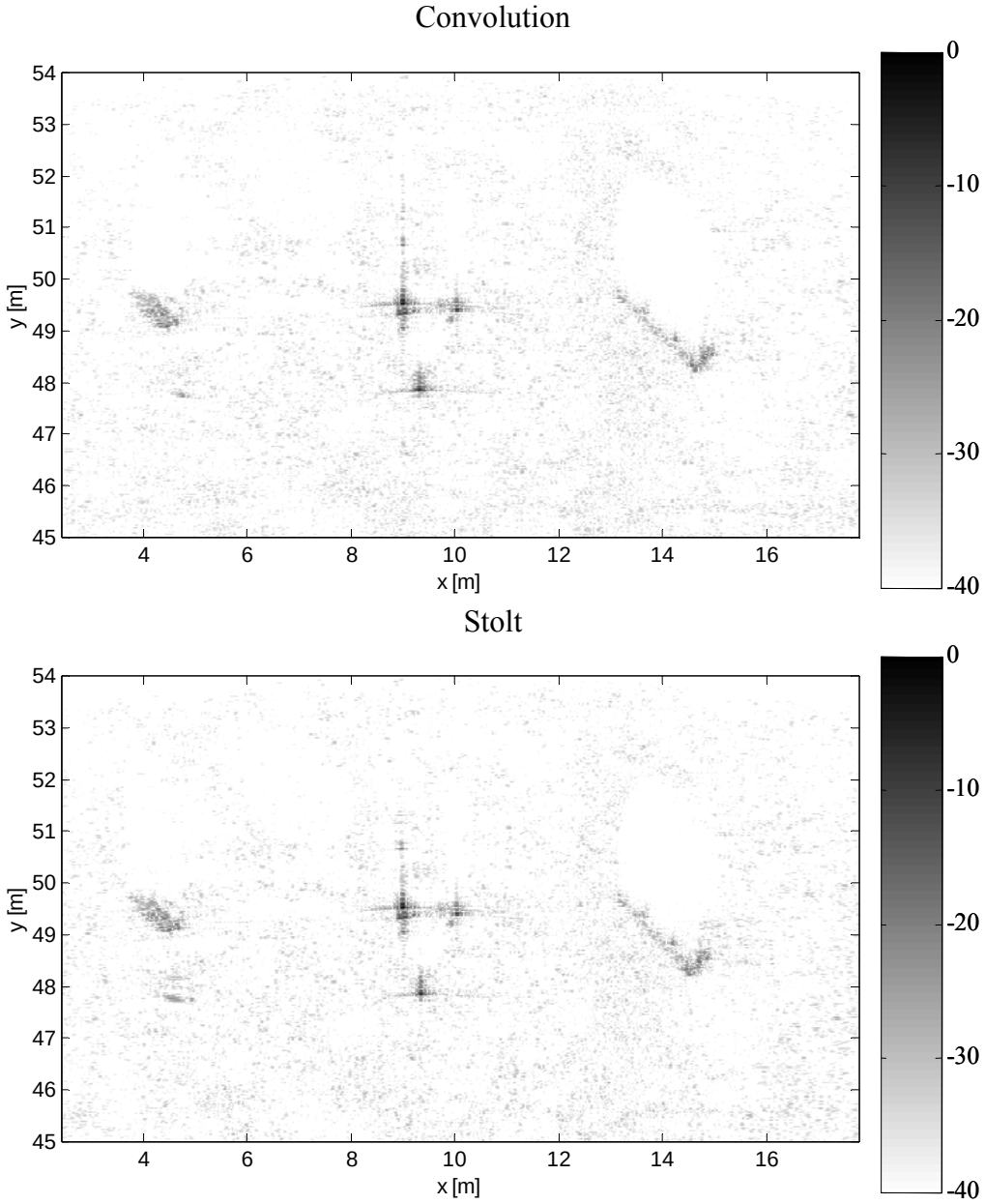


Figure 6-29 *Two SAS images of experiment C. In the upper image single-focus-range processing is applied, e.g. convolution imaging or SFI. In the lower image correct-focus-range processing is applied, e.g. STI or Stolt migration.*

In Figure 6-29 three objects are visible, i.e. from left to right: a rock, the tripod and a mine. The difference between the upper and lower image is small. It should be noted that all the objects are very close to the focus range of 49 m. If this parameter is shifted (~1 m) a defocusing effect becomes visible rather soon for single-focus-range methods. This shows that wavenumber frequency processing in combination with motion compensation has indeed potential for application to UUV mounted sonars.

6.6.3. Shadow enhancement

This section shows the results of application of the shadow enhancement algorithm described in Section 6.5. The most appropriate measured data set was the rail experiment in Section 6.6.1 with the sphere at about 25 meters range, because of its geometrical properties and stable sonar track. The integration angle is about 24 ^{o}, and the grazing angle about 20 ^{o}.

To get a feel for the significance of the shadow blurring for this specific scenario a few quality indices can be calculated assuming a plate of one by one meter instead of the sphere. According to Eq. (6.18), and with the use of Eq. (6.19) and the second formula of Eq. (6.20), the blurring area can be quantified. The original area A_0 is 2.92 m^2, the blurred area A_{blur} is 1.75 m^2 and the blurring ratio ξ is about 0.6. The blurring is indeed significant. Evaluating Eq. (6.23) at a frequency of 150 kHz, gives a maximum allowed integration angle of about 10 ^{o} for which the shadow is not blurred at all. This can also be verified in Figure 6-20.

The significance can also be seen in the images of Figure 6-30 comparing the result with Stolt migration and with convolution imaging. The steps to enhance the shadow are identical as for the simulated data, i.e.:

1. Construct a SAS image with Stolt migration
2. Detect the target
3. Construct a SAS image with convolution imaging focused at the target
4. Extract the shadow from the convolution imaging result
5. Replace the shadow in the Stolt image

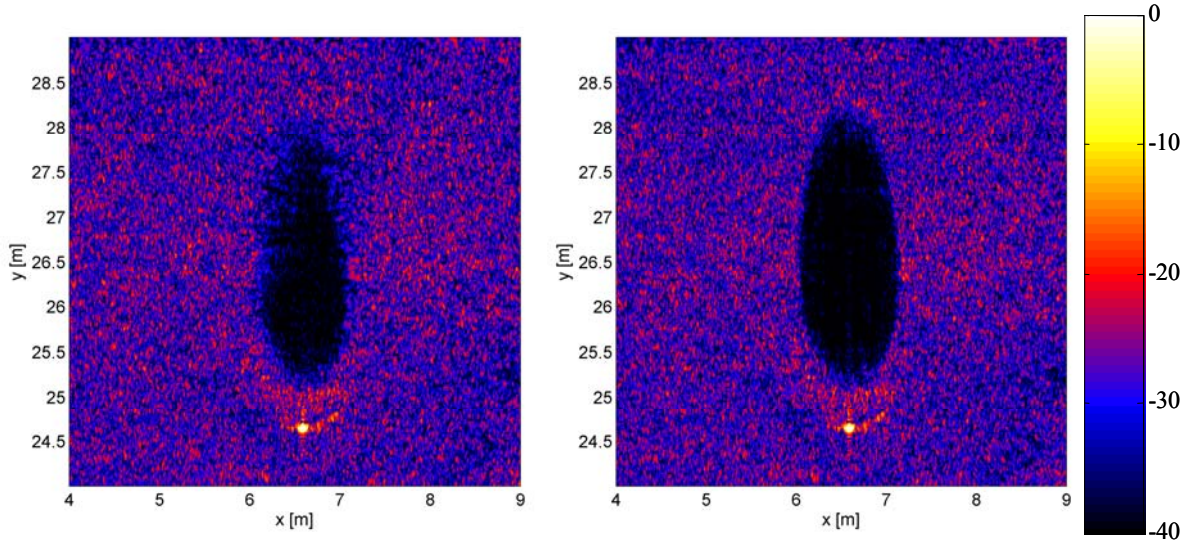


Figure 6-30 *On the left hand side a zoom on the target is shown as processed with Stolt migration. On the right hand side the same data are shown processed with convolution imaging focused on the target.*

The zoomed images of Figure 6-30 are similar except for the shadow. The reverberation grid around the target and the shadow are visually the same. The idea now is to extract the shadow from the right hand image and to use it as a replacement in the Stolt image. This is realized with the contour finding method as described in Section 6.5.3. The contour extraction is shown in Figure 6-31 and is obtained in the same way as for the simulated data shown in Figure 6-25.

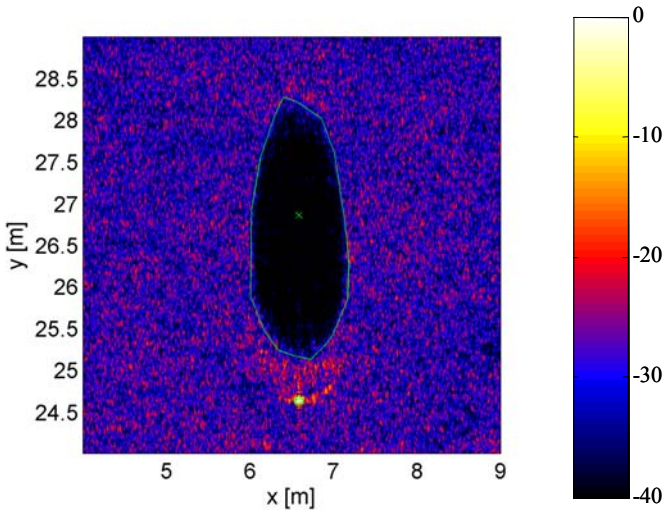


Figure 6-31 *The contour finding method applied to convolution imaging output.*

The contour finding method is successfully applied to the data. The result of the part of the image to be replaced is indeed the shape of the shadow. This ellipse-shaped data window is spliced into the overall Figure 6-32.

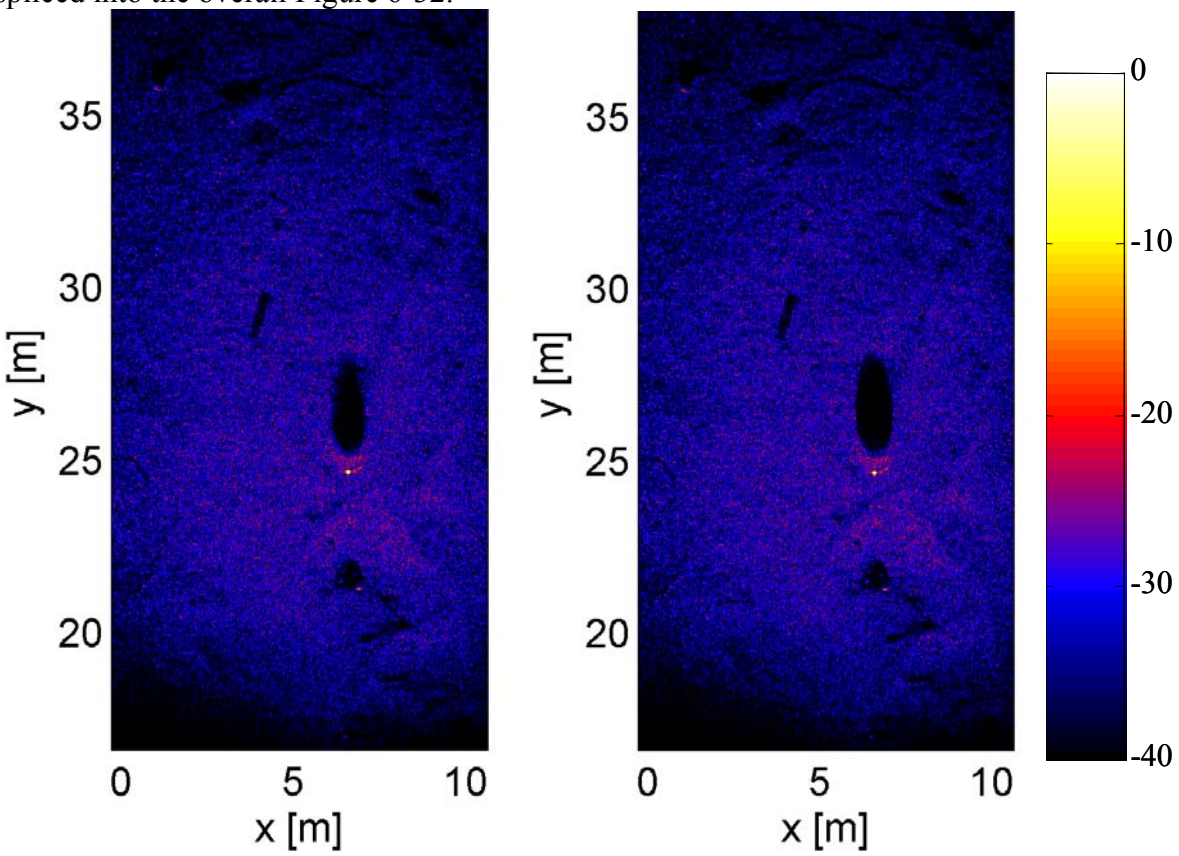


Figure 6-32 *Comparison between Stolt migration (left) and Stolt migration with the additional shadow enhancement (right).*

The complete image on the right hand side is still focused for every range and the shadow is much sharper. It can be concluded that the shadow theory and the application of the enhanced shadow algorithm is well in agreement with the derived results in Section 6.4.

6.6.4. Performance comparison

The performance of the methods is compared in this section. Of course not only the relative performance is important, but also the absolute performance. Several performance indicators have been suggested for measurement of the quality of the image. For the simulated data the choice was made to use the along-track resolution as the important indicator. However, on experimental data, this parameter does not suit the idea of quality, as shown in the previous two sections. After all, objects in the image are not necessarily point scatterers. It has been verified by Fortune (2001) that a suitable performance indicator to analyze the experimental data is the contrast in the image. The contrast σ_g^2 is calculated as the variance of the logarithmic image:

$$\begin{aligned} \sigma_g^2 &= \left\langle \hat{g}^2 \right\rangle - \left\langle \hat{g} \right\rangle^2 \\ \hat{g} &= 20 \log_{10}\left(|g|\right) \end{aligned}, \tag{6.31}$$

where $\langle \cdot \rangle$ refers to the expectation value. The contrast values of the three data sets are presented in Table 6.2.

Table 6.2 *Contrast σ_g^2 in decibels for the SAS images.*

Experiment	A	B	C
Convolution imaging	5.5	5.5	5.1
Stolt migration	5.6	5.7	5.1

It shows that the contrast is better in all three experimental data sets. The fact that this increase in contrast is very small is explained by the fact that the contrast value according to Eq. (6.31) implies small variations by definition.

6.7. Conclusion

The general conclusion of this chapter is that wavenumber frequency processing is an attractive way of SAS processing. It has computational advantages owing to the use of the 2D FFT. In the analyzed simulations and experiments, the Stolt migration technique shows to be well suited for SAS. However, due to the wide variety in SAS scenarios, it cannot be stated that wavenumber frequency processing is superior in general. Nevertheless, several cons of this method, like the ULA assumption, complexity, wrap-around effects, are solved in this chapter. It is concluded that a linear interpolation scheme with a factor two zeropadding is optimal. For each SAS application a multivariate decision should be made, which is based on inherent differences between signal processing methods, viz. need for computational gain and flexibility.

The new aspects of this chapter are first of all a derivation of a general formula of focus depth and maximum allowed deviation from a straight line for synthetic aperture sonar in general. The similar behavior of the two is investigated analytically and with plots. The other new as-

pect was the enhanced shadow processing by means of a Stolt migration and convolution imaging merge. The processing applies a two-step approach: target detection in a normal SAS image in step one, followed by shadow sharpening with the shadow improvement method in step two. The performance of a contour finding method on the sharpened shadow is much better than on the blurred shadow from standard SAS processing. The method has been tested on simulated data and on experimental data from a controlled set-up, using a rail. More advanced image classification methods are expected to benefit from the method.

7. CONCLUSIONS

The research in this thesis is aimed at finding solutions for limitations of sonar, a well-accepted technique for underwater observation. Sonar is often used in operations that require fast and robust results. For instance in naval operations a clear view of the underwater world is sometimes a matter of life and death. The application of sonar for two primary tasks of the navy was the main theme of this thesis. These tasks are anti-submarine warfare and mine warfare with the main difference of the two for sonar, and therefore this research, being the dimensions of the application.

It could be argued that, because sonar has been in use since the beginning of the previous century, it is rather extraordinary that the systems and their performance still need to and can be improved. However, the background to this further development can be found in three recent changes. The most important reason has been the progress in computational power of present day computers. It is this power, in combination with the relatively low cost and data storage and acquisition improvement, which has created openings for better sonar systems. The second change is the change and broadening in applications. During the previous century the mission of navies has been redirected continuously. An example of this is the shift in interest from deep water to shallow water areas. The design of a sonar system is very much dependent on the application. The underwater environment and the performance requirement for the applications have been changing continuously, and therefore, research has been ongoing. The third reason is the simple fact that the transducer and receiver technology, i.e. the wet-end hardware has improved significantly, even in recent years. For example the high source level and large bandwidth of present-day transducers has opened new possibilities to detect submarines at long ranges.

This thesis has focused on the signal processing for sonars. The signal processing is, nowadays, performed in a ‘box’ that converts the received acoustic data, the sonar data, to the data that is offered to the sonar operator on a console. The sonar signal processing has many aspects and an optimal design for the ‘box’ is not straightforward, because real-time or close to real-time requirements are always an issue. Optimization of the sonar performance by means of well-considered choices and advanced algorithms in the single processing chain has been an important issue in erstwhile and recent research as for instance described by Haykin (1985). It is a fact that when the physical process of the acoustic signals underwater is well-understood and well-modeled as explained by Widrow (1985), the performance of the sonar is, for an important part controllable. A physical process can be the signal behavior influenced by sonar motion, but also, for instance, signal behavior as a result of sound speed fluctuations in the water mass. Physical knowledge of the behavior of acoustic signals underwater can be inserted into the signal processing chain. In this thesis, the knowledge of sonar motion has been inserted into the signal processing chain in an optimal way. This may sound simple, but the opposite is true and the thesis has shown that it consists of scientifically interesting challenges.

A crucial tool for research and development of new sonar signal processing methods is a simulator that is capable of generating realistic sonar data. Experiments at sea are not always possible and when they are possible, always a limited variety in the experiments is at hand. This may for example be due to the weather or operational restrictions. Another advantage of a simulator is the control over the different physical effects. If one is not sure whether a certain unexplained effect is caused by sonar characteristics or by multi-path, in a simulation one can easily switch off the multi-path. The model developed for the signal processing methods in this thesis carries the name SIMONA. It has reached a high stage of fidelity and has proved useful for sonar performance prediction, signal processing development and generation of a high resolution sonar image database. It is clear that underlying models for acoustic shadow, reverberation statistics, Doppler and multi-path are essential. The model is verified with many test cases, which showed the importance of the different underlying modules.

The other 'crucial tool' for research and development of new sonar signal processing methods is experimental data. This may even be stressed more by the argument that experimental data are crucial for developing a good simulator. Identification of the difficulties and knowledge of the actual content of a sonar image contribution is needed to decide what the assumptions in the model should be. In the research described in each of the Chapters 3-6, experimental data analysis has played a major role. It implicated that all the signal processing methods presented have been actually validated on experimental data.

7.1. Anti-Submarine Warfare

The Anti-Submarine Warfare (ASW) platform aims to detect, localize and classify a submarine at a long range in order to be able to act in time. The new approach that is expected to have superior performance over the existing approaches is the use of a Low Frequency Active Sonar (LFAS) that is towed behind the ASW platform. Such an LFAS consists of an omnidirectional source and a receiving array. Chapter 3 and chapter 4 were dedicated to this application of sonar.

The receiving array that is towed behind the vessel is a linear array, i.e. the hydrophones are placed in a flexible tube or hose. A characteristic problem for such an array is the cone shaped ambiguity. This implies that when sailing straight, the sonar cannot tell whether a submarine is on the port side or on the starboard side of the sonar. Another problem that comes along with this is the fact that reverberation, e.g. from the coast, also shows up in the ambiguous beams. The best solution to this problem appeared a perpendicular extension of the receiving array. This can for instance be achieved by using triplets instead of hydrophones, which was investigated in Chapter 3. Steering these triplets in the port or starboard direction is called triplet beamforming, which is difficult, because the thickness of the tube in which the triplets are placed, is limited. The hydrophones are separated at only a small fraction of the wave length and the signals have small phase differences. Additionally, the array was found to have motion in the form of roll, which has a significant effect on the beamformed result and needs to be compensated for.

However, introducing models for the spatial correlation and adaptive beamforming showed that it is well possible to obtain enough port starboard discrimination without losing the signal. Three beamformers have been studied both theoretically and experimentally and their performance was shown to be primarily a function of noise spatial correlation. The roll motion estimation of the hydrophones was demonstrated to be possible with the two available roll sensors placed at the beginning and the end of the array. For this topic, the motion itself, therefore, appeared to be a minor problem. The two roll sensors are, nevertheless, a minimum requirement, because the tube may have a linear roll evolution along the array due to torsion. Behavior of the three beamformers under different tow speeds, for targets at different bearing and for transmit signals at different frequencies was investigated in both noise-and reverberation limited environments. The final result of this study is that triplet arrays with two roll sensors, processed with an adaptive triplet beamformer, combine high PS discrimination performance with additional array gain in both environments. The PS discrimination reached 25 dB and is sufficient to reject even the most severe coastal reverberation. The additional array gain during the trials varied from 0-5 dB depending on the tow speed and promises better detection performance than equal aperture single arrays. The analysis on the PS discrimination had a huge impact on the operations. Based on the results of Chapter 3, it can be concluded that it is indeed possible to operate a triplet array in a shallow water environment. The detection performance in the seaward bearings increases significantly, because the coastal upslope reverberation is suppressed by 25 dB. The signal processing chain equipped with appropriate triplet beamforming even gives sufficient results for the upslope bearings, i.e. a small increase in performance with respect tot a linear array.

Another issue for LFAS that was part of this research was optimal array processing during maneuvering of the tow vessel. With the shift from deep water to shallow water, regular maneuvering during the ASW operations is common. Besides the problem of increasing noise, the linear receiving array appears to deviate from the straight line during a maneuver. This is not taken into account in the existing signal processing chain.

It was found that the problem is even greater, because Doppler effects in the turn are non-stationary and also vary over the hydrophones. Whether or not this decreases the performance depends on the frequency used, the length of the array and the maneuver itself. The theory given in Chapter 4 shows that without countermeasures both Doppler effects and position errors may give rise to serious performance loss in operational scenarios. Formulae are provided that quantitatively address the performance loss for arbitrary types of towed array sonars. Three compensation methods were successfully examined with simulated and experimental data. It was shown that Shape and Doppler corrected beamforming (SDCB) fully compensates for the motion effects during maneuvers. Moreover, it was shown that the sensitivity of the non-acoustic input parameters of the method, i.e. the measured or estimated track of the sonar was low. It is so low that measuring the track with a heading sensor and a Global Positioning System (GPS) mounted on the tow vessel suffices. In 2003, in late summer, an experimental data set was gathered in the Mediterranean, both in active and in passive mode with a locator. Moreover, the environment was monitored carefully and taken into account in the experiments. Here, SDCB was successful on both the passive and active data set. In the end, all described data sets, both in a passive and active sonar setting, proved the benefit of shape and Doppler correction algorithms during sharp high speed tow ship maneuvers. The summarizing conclusion is that Doppler effects may induce significant maneuvering loss, but that with sophisticated processing this can be compensated for. This signal processing is relatively easy to implement. The gain is several decibels in practical conditions. Furthermore,

the performance was measured with several performance indicators, viz. gain, signal gain, range resolution and bearing resolution. Thus, the operational gain is high. It is expected that application of the signal processing methods avoids severe losses during maneuvers. On the one hand, this allows for more flexibility of the ASW vessel and on the other hand it increases overall detection probabilities.

7.2. Mine Hunting

The mine hunting platform aims to detect, localize and classify sea mines. In this research, the primary performance criterion for the mine hunting sonar concepts was resolution in the sonar image. Contrary to ASW, the target is not moving during the operation. This makes it relatively easy to combine the recorded data from different transmissions (pings). When the mine hunting platform moves and the recorded data is combined in a coherent way, this method is referred to a Synthetic Aperture Sonar (SAS). As its name suggests, an aperture is built up synthetically and since aperture is inversely proportional to resolution, SAS is regarded as an elegant and cheap way to achieve high resolution. SAS was the main theme in the Chapters 5 and 6.

For the sonar itself, synthetic aperture sonar is a technique that mainly has impact on the signal processing chain. The first steps of this research were the implementation of such a signal processing chain and the development of a simulation suite for the case of mine hunting. In the process from raw sonar data to an acoustic image, several processing modules can be identified. The modules are downsampling, matched filtering, signal conditioning, motion estimation, motion compensation and imaging. Downsampling, matched filtering and signal conditioning are relatively straightforward, and therefore, implemented as described in Chapter 2 and Chapter 5. The other three modules are not straightforward.

For proper coherent integration along the synthetic aperture, the motion of the sonar has to be known and incorporated down to a small fraction of the wavelength. Chapter 5 describes the SAS signal processing chain with the different approaches possible for motion estimation, motion compensation and imaging. The primary conclusion in Chapter 5 is that when applying synthetic aperture sonar techniques, it is indeed possible to improve the resolution by an order of magnitude. The concept was tested on a wide variety of geometries via simulation, but also on data sets from four sonars with different characteristics. For the estimation of motion, the techniques examined can be divided into three groups. These are the estimation via external sensors, motion estimation on a hydrophone level or motion estimation from the image. It was found that none of the techniques is superior for all applications. Chapter 5 gives a detailed conclusion on the drawbacks and complementary advantage of the techniques, which are very much case dependent. Motion compensation is a technique that is used to transform the sonar data to suitable data for the wavenumber frequency imaging methods. This means that the data needs to be propagated from the estimated track to a straight and equidistant array. It was concluded that, for the experimental data sets and for the interesting operational cases simulated, motion was small enough for valid wavenumber frequency imaging. Several imaging techniques were investigated and compared and it was concluded that the best imaging technique is Stolt migration.

When sources and receivers can be assumed to coincide after motion compensation, Stolt migration is a rather fast wavenumber frequency imaging method. Near real-time aspects play an important role in sonar signal processing, and therefore, this promising technique was examined in detail in Chapter 6.

The aforementioned deviation from the straight line causes a breakdown of the assumptions at some point. A theoretical analysis resulted in analytic formulae for the validity of motion compensation when applying wavenumber frequency processing. In parallel, multiple simulations demonstrated the effect of motion in the actual sonar image. The disadvantages of the method, like the uniform linear array assumption, complexity, wrap-around effects, have been solved. It is concluded that a linear interpolation scheme with a factor two oversampling is optimal. Another method applied in the wavenumber frequency domain, is the convolution imaging method. This method was found to be identical to Stolt migration apart from the interpolation step, which is absent for convolution imaging and results in correct focusing for only one range. A general formula for the area where convolution is still valid is derived and compared with the straight line deviation criterion. A new invention, merging Stolt migration and convolution imaging, was presented in Chapter 6. It appears that focusing on the target with convolution imaging also focuses the shadow. Thus one can detect a target in a normal SAS image in step one, followed by shadow sharpening with the shadow improvement method in step two. The performance of a contour finding method on the sharpened shadow is much better than on the blurred shadow from standard SAS processing. The method has been tested on simulated data and on experimental data from a controlled set-up, using a rail. More advanced image classification methods are expected to benefit from the method.

7.3. Recommendations

The models that resulted in the simulator SIMONA have shown a valuable tool in the development of new signal processing schemes. Additionally, as previously concluded, the simulated data can be used for model based classification. For instance a sonar image data base can be built from the simulated data. However, application of simulated data in this way needs validation with experimental data to a higher degree. The target model described in this thesis is expected to be limiting factor when comparing with experimental data. There are nevertheless different suggestions for improvement of the model. A first improvement would be to take into account the material properties of the target such as the reflection coefficient. Additionally, multiple reflections for irregularly shaped or partly transparent targets are recommended as an improvement. Furthermore, it should be relatively easy to equip the model to generate the waves that propagate within or around the object, such as Lamb-type waves. As a more rigorous option, it should also be possible to replace the target model with a finite element model.

The LFAS system with transducer and towed array is currently developed further in order to fit on the ASW frigates of the RNLN. Chapter 3 and 4 discussed two parts of the signal processing chain of the LFAS. In both chapters different signal processing techniques were compared by means of performance indicators. In Chapter 3 these were triplet gain and port star-

board discrimination and in Chapter 4 these were gain, signal gain, range resolution and bearing resolution. A better performance measure is achieved with a rigorous statistical analysis in terms of probability of detection and probability of false alarm. The data sets used in this thesis were not suitable for such an analysis, but with the feedback from naval operations, this should be possible.

In line with what is currently accomplished, it is recommended that the low frequency active sonar technology is developed as an operational system. The effects of the signal processing steps of the chain presented are well-understood and are ready for implementation. The LFAS at its current level of development, is expected to significantly outperform the systems currently in use with the RNLN (hull mounted sonar and passive towed array). Yet, it is not concluded that there should be no more research in the field of ASW signal processing. It is still expected that other techniques that fall outside of the scope of this thesis may contribute to the performance of the LFAS. Examples of these are model based processing, automatic classification, special transmit signals and multi-static sonar.

In the field of synthetic aperture sonar, a large research effort has been dedicated to motion estimation. This is still the case. The analysis in this thesis was limited, because of the focus towards the actual imaging and motion compensation. The research on motion estimation is scattered around the world and it would be a great step forward if a common open data set with its performance results would serve as a benchmark. Such a data set should cover the range of operational parameters and have enough ground truth data.

In mine hunting the data flow from the sonar to the sonar operator has increased significantly. Since the resolution of the sonars, mostly still in a research phase, have improved an order of magnitude in recent years, the data flow has at least increased in proportion. This overload calls for automatic treatment or post processing. It is foreseen that the research in mine hunting is shifting towards the end of the processing chain. Terms like automatic target recognition, computer aided detection and computer aided classification will become common in the coming years.

The imaging for synthetic aperture sonar has been presented in Chapter 6. As already discussed, it is recommended to use Stolt migration as the default processing techniques. However, for the application to an Autonomous Underwater Vehicle (AUV) that collects a huge amount of data during its mission, a less black and white conclusion should be drawn. It is suggested to process the data in different stages starting with low resolution and ending with the best possible image. The stages for this may consist of a sidescan image, a Stolt migration image and an image formed with all the available tools with for instance a sharp shadow. It is not clear at this point how these stages will be defined exactly, but they will be based on computational (time, memory) and operational requirements.

Appendix A. DETECTION THEORY

The derivation starts from elementary detection theory (see e.g. Van Trees (1968)). In detection theory it is common to solve the detection problem in Chapter 2 using hypotheses-tests, in which two hypotheses are postulated:

$$\begin{aligned} H_0 &: \quad \mathbf{x}_0 = \mathbf{n} \\ H_1 &: \quad \mathbf{x}_1 = \mathbf{s} + \mathbf{n} \end{aligned}, \tag{A.1}$$

in which **x** is the received data, **n** is isotropic zero-mean Gaussian noise and **s** is the signal. So H_0 states the detection of noise only and H_1 states that a signal is present in the noise. The aim is now to make a signal processor that decides which of the two hypotheses is chosen. There are 4 possibilities:

1. The choice H_0 is correctly adopted. Only noise is detected.
2. The choice H_0 is wrongly adopted, because H_1 is true. The target present is not detected.
3. The choice H_1 is wrongly adopted. A target is detected, which is not present: false alarm.
4. The choice H_1 is correctly adopted. The target present is detected.

In case 1) and 4) the decisions are correct. In case 2) and 3) the decisions are incorrect, the former being far more serious than the latter. For a proper consideration of the risks, cost-functions should be formulated (Van Trees (1968)). However, in most physical problems the formulation of cost-functions is cumbersome. In sonar detection problems a relatively simple criterion, viz. the *Neyman-Pearson criterion* is applied by Nielsen (1991). This criterion maximizes the detection probability if one accepts a certain probability of "false alarm". The Neyman-Pearson test involves the so-called *likelihood ratio* defined as:

$$\Lambda \equiv \frac{P(\mathbf{x}_1 \mid H_1)}{P(\mathbf{x}_0 \mid H_0)}. \tag{A.2}$$

This Λ is a detector in the sense that if Λ passes a threshold the choice is H_1 otherwise the choice is H_0. The probability density functions $P_0 = P(\mathbf{x}_0 \mid H_0)$ and $P_1 = P(\mathbf{x}_1 \mid H_1)$ are fixed for given distributions. The probability density function P_0 for a 3D Gaussian variable **x** is given by van Trees (1968):

$$P_0(\mathbf{x}) = \left(\frac{1}{2\pi}\right)^{3/2} (\det \mathbf{R}_0) \exp\left[-\frac{1}{2}\mathbf{x}^\dagger \mathbf{R}_0 \mathbf{x}\right], \tag{A.3}$$

in which $\mathbf{R}_0$ is the correlation matrix:

$$\mathbf{R}_0 = \mathbf{R}(\mathbf{x} \mid H_0) = \left\langle \mathbf{x}_0 \mathbf{x}_0^\dagger \right\rangle. \tag{A.4}$$

where the bracket $\langle . \rangle$ denotes the *expectation value*.

A similar expression for P_1 arises by replacing the subscript 1 by 0.

Under noise only hypothesis, $\mathbf{x} = \mathbf{n}$ is a complex, zero-mean Gaussian vector, with correlation matrix $\mathbf{R}_0 = \langle \mathbf{x}\mathbf{x}^\dagger \rangle = \langle \mathbf{n}\mathbf{n}^\dagger \rangle = \mathbf{R}_n$.

Assuming that the sonar receives a signal, which is radiated or reflected from a single point target: $\mathbf{x} = \mathbf{s} + \mathbf{n}$ is a complex vector, with correlation matrix $\mathbf{R}_1 = \frac{\sigma_n^2 \mathbf{R}_n + \sigma_s^2 \mathbf{d}\mathbf{d}^\dagger}{\sigma_n^2 + \sigma_s^2}$, where $\sigma_s{}^2$ is the signal variance (energy).

There are several beamformers that optimize the detector Λ for a fixed probability of false alarm. Such optimal processing schemes have been investigated extensively for many decades. The reader is referred to the books of van Trees (1968), Nielsen (1991), Haykin (1985) and Stergiopoulos (2001). The issue here is that different optimization criteria or constraints are required for the diverse sonar applications.

A.1. Minimum variance distortionless response beamforming

One of the beamformers that meets requirement for an optimum detector is the so-called minimum variance distortionless response beamforming (MVDR). In this section the general formulation of MVDR beamformer is derived and explained.

In all beamforming algorithms, the data is taken from an array of sensors, multiplied by a complex weight and summed. The weights are designed according to an optimality criterion which will be described below. The data received by the triplet array is a complex vector **b**. The idea now is to apply a weighting function to the input data. Such a weighting can be a vector **w** of the same size of **b**, which can, for example, affect the side lobes of the beamformed output. For the MVDR derivation, the most general operation is regarded, i.e. a weighting matrix **W** with complex elements. This results in the construction of a new input data vector by means of linear combinations of the old input data vector elements:

$$\mathbf{x} = \mathbf{d}^\dagger \mathbf{W} \mathbf{b} \,. \tag{A.5}$$

As the name MVDR implies, the weight matrix is calculated using the criterion of achieving minimum noise plus interference power and at the same time passing the signal of interest without distortion. When the noise correlation satisfies the abovementioned assumptions, the MVDR weight matrix is given by:

$$\mathbf{W} = \frac{\mathbf{R}_n^{-1}}{\mathbf{d}^\dagger \mathbf{R}_n^{-1} \mathbf{d}} \,. \tag{A.6}$$

In this equation the noise correlation matrix is assumed to be known. In practice, this correlation matrix is estimated from a model or from the sonar data. It is easy to verify that $\left|\mathbf{d}^\dagger \mathbf{W} \mathbf{s}\right| = 3\sigma_s^2$ is the same as $\left|\mathbf{d}^\dagger \mathbf{s}\right| = 3\sigma_s^2$, because $\mathbf{R}_n$ is a real-valued matrix for isotropic noise. The background noise, on the other hand, is optimally suppressed with

$\left|\mathbf{d}^{\dagger}\mathbf{W}\mathbf{n}\right| = \left|\mathbf{d}^{\dagger}\frac{\mathbf{R}_n^{-1}}{\mathbf{d}^{\dagger}\mathbf{R}_n^{-1}\mathbf{d}}\mathbf{R}_n\right|\sigma_n^2 = \sqrt{3}\sigma_n^2$ instead of $\left|\mathbf{d}^{\dagger}\mathbf{n}\right| = \left|\mathbf{d}^{\dagger}\mathbf{R}_n\right|\sigma_n^2 = \sqrt{3}(1+2\rho_n)\sigma_n^2$, with ρ_n the spatial correlation coefficient of the noise. In other words, the matrix $\mathbf{R}_n^{-1}$ decorrelates the noise such that is adds incoherently. Thus, in this case **Wn** is an uncorrelated zero-mean Gaussian vector.

The danger in the use of MVDR beamforming is the uncertainty in the estimation of $\mathbf{R}_n$ or in other situations than the noise-limited case more generally **R**. Combining Eq. (A.5) and Eq. (A.6) leads to the general expression that is used as a basis in Chapter 3.

$$\mathbf{h}^{\dagger} = \frac{\mathbf{d}^{\dagger}\mathbf{R}_n^{-1}}{\mathbf{d}^{\dagger}\mathbf{R}_n^{-1}\mathbf{d}}. \tag{A.7}$$

Notice that without a fixed choice for $\mathbf{R}_n$ this formula only defines the triplet beamforming as a linear combination of the input data. It is no more than a formulation, which is still not unique. The three beamformers discussed in Chapter 3 each have their own approach to fill in $\mathbf{R}_n$, because the false alarms for active sonar in shallow waters often are not caused by stationary Gaussian noise. It is useful to stick to this formulation, since it allows a direct comparison of each of those beamformers via the used (noise) correlation matrix.

Appendix B. SIGNAL DEFORMATION DURING A MANEUVER

In this Appendix is the physical change in the received (HFM) signal in a turn due to Doppler spreading is analyzed. The varying Doppler in time transforms the HFM signal into something that is not an HFM anymore. When the sonar is moving towards the target at the beginning of signal reception and moving away from the target at the end of reception the effect is strongest. The originally low frequencies at the beginning of the signal get higher in this case. For the high frequencies this occurs vice versa. This causes a distorted signal. In the remainder of this Appendix it is studied what the distortion does to the HFM response in terms of Doppler sensitivity and energy loss.

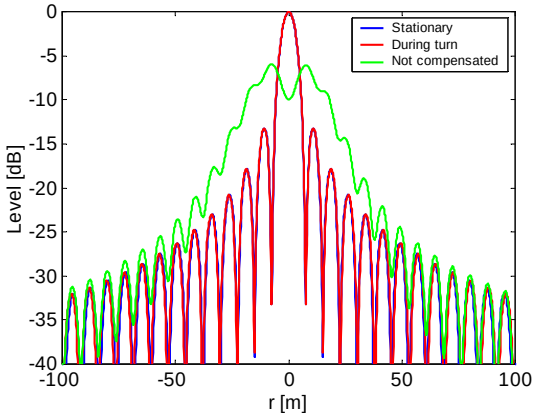


Figure B-1 *Point target response after matched filtering.*

When a matched filter is applied to an HFM signal approximately a sinc-like function is expected from a point target. Together with the expected response from the distorted HFM during a (the standard) turn this is plotted in Figure B-1. The bandwidth of the HFM signal is in this case 100 Hz and the speed is 5 m/s to be able to see clearly what happens to the response. To investigate whether the Doppler sensitivity of the distorted HFM is different, additionally a Doppler bank (from –10 to 10 m/s) is convolved with the original and distorted HFM. The result showed that the difference between the two waveforms was well within a tenth of a dB. It can be concluded that the HFM does not lose its properties when received on a sonar in a turn.

It can be verified from the green curve that the loss due to Doppler spreading in the turn is about 6 dB. This corresponds to the theoretical formula in Eq. (3.9) and the right image of Figure 3-6. This formula was nevertheless derived for one frequency. The formula can only be utilized when the maneuvering loss does not significantly depend on the HFM bandwidth. The maximum of the green plot from Figure B-1 can be determined for any bandwidth and the results are plotted in Figure B-2 together with the theoretical value in red. It can be seen that the difference between the two increases with bandwidth, but also that the difference is well within a decibel. Partly, the difference can be explained with the fact that an HFM signal

has more energy in the lower frequencies. The wobbly behavior is explained with the of the HFM correlation output itself, which is also visible in Figure B-1.

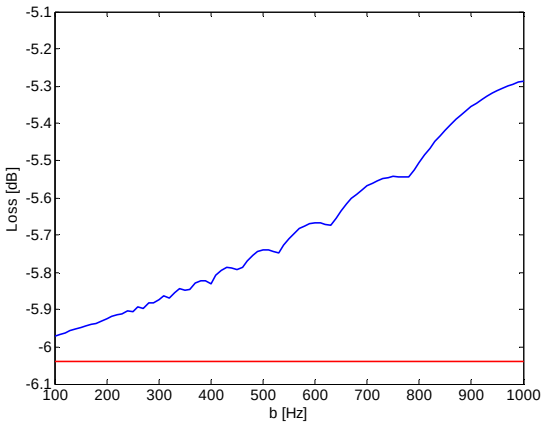


Figure B-2 *Maneuvering loss versus bandwidth of an HFM signal caused by the interaction of the different frequencies in the band.*

Appendix C. IMAGING FOR A HOMOGENEOUS MEDIUM: 2D CASE

C.1. General expression for 2D imaging

This Appendix derives the formulae that are needed for the justification of the imaging methods in Chapter 5 and Chapter 6.

Imaging is a calculation that results in the acoustic reflectivity in the image domain as a function of two spatial coordinates. Without loss of generality, it is assumed that these two coordinates are along track position x and across track position y. The received data equal the pressure generated by a source at x_s and received at x_r at the line $y = 0$ and can be written as $p(x_s,0;x_r,0;t)$. In the frequency domain, this is $P(x_s,0;x_r,0;\omega)$. The field in the image domain (x,y), generated by a source at $(x_s,0)$ can be calculated from the recordings at $(x_r,0)$ with help of the far field 2D Rayleigh integral as explained by Berkhout (1982):

$$P(x_s,0;x,y;\omega) = -\mathrm{i}y\sqrt{\frac{\mathrm{i}\omega}{2\pi c}}\int_{-\infty}^{\infty} P(x_s,0;x_r,0;\omega)\frac{e^{\mathrm{i}\frac{\omega}{c}\Delta r_r}}{\Delta r_r\sqrt{\Delta r_r}}\mathrm{d}x_r\,, \tag{C.1}$$

where $\Delta r_r = \sqrt{(x-x_r)^2 + y^2}$, ω is the angular frequency. Eq. (C.1) can be interpreted as a reconstruction of a recording by a receiver at (x,y) at the field generated by a source at $(x_s,0)$.

If many source records are available with sources at location $(x_s,0)$, well sampled along the line $y = 0$, the virtual recording of a wavefield in (x,y), generated by a source in (x,y) is calculated by:

$$\begin{aligned} P(x,y;x,y;\omega) &= -\mathrm{i}y\sqrt{\frac{\mathrm{i}\omega}{2\pi c}}\int_{-\infty}^{\infty} P(x_s,0;x,y;\omega)\frac{e^{\mathrm{i}\frac{\omega}{c}\Delta r_s}}{\Delta r_s\sqrt{\Delta r_s}}\mathrm{d}x_s \\ &= \frac{\mathrm{i}\omega y^2}{2\pi c}\int_{-\infty}^{\infty}\int_{-\infty}^{\infty} P(x_s,0;x_r,0;\omega)\frac{e^{\mathrm{i}\frac{\omega}{c}(\Delta r_r+\Delta r_s)}}{\Delta r_r^{\frac{3}{2}}\Delta r_s^{\frac{3}{2}}}\mathrm{d}x_r\mathrm{d}x_s \end{aligned}\,, \tag{C.2}$$

where $\Delta r_s = \sqrt{(x-x_s)^2 + y^2}$. Transformation back to the time domain yields:

$$p(x,y;x,y;t)=\frac{y^2}{2\pi c}\int_{-\infty}^{\infty}\int_{-\infty}^{\infty}\frac{\left[\dfrac{\partial p(x_s,0;x_r,0;t)}{\partial t}\right]_{t+\frac{1}{c}(\Delta r_r+\Delta r_s)}}{\Delta r_r^{\frac{3}{2}}\Delta r_s^{\frac{3}{2}}}\mathrm{d}x_r\mathrm{d}x_s\,. \tag{C.3}$$

The acoustic reflectivity for a pixel in the image $g(x,y)$ is now defined by the imaging condition:

$$g(x,y)\equiv p(x,y;x,y;t=0)\,. \tag{C.4}$$

The expression $g(x,y)$ is easily obtained by inserting Eq. (C.3) into Eq. (C.4):

$$g(x,y)=\frac{y^2}{2\pi c}\int_{-\infty}^{\infty}\int_{-\infty}^{\infty}\frac{\left[\dfrac{\partial p(x_s,0;x_r,0;t)}{\partial t}\right]_{t=\frac{1}{c}(\Delta r_r+\Delta r_s)}}{\Delta r_r^{\frac{3}{2}}\Delta r_s^{\frac{3}{2}}}\mathrm{d}x_r\mathrm{d}x_s\,. \tag{C.5}$$

This is the general expression for space time imaging including correct amplitudes. If one assumes that the amplitudes are constant over the sonar aperture, i.e. for both the sources and the receivers, yields a simplification. Ignoring the $\pi/2$ phase shift due to differentiation this expression simplifies to:

$$g(x,y)\approx\int_{-\infty}^{\infty}\int_{-\infty}^{\infty}p\left[x_s,0;x_r,0;\frac{1}{c}(\Delta r_r+\Delta r_s)\right]\mathrm{d}x_r\mathrm{d}x_s\,. \tag{C.6}$$

C.2. General expression for 2D Stolt migration

As in the previous section, the measurement is a pressure generated by sources at certain positions $(x_s,0)$ and received at positions $(x_r,0)$. This measurement is denoted by $p(x_s,0;x_r,0;t)$. Its Fourier transform is denoted by $P(x_s,0;x_r,0;\omega)$. Stolt migration is applied in the wavenumber frequency domain, which makes it necessary to add two definitions to this. The spatial Fourier transform of P over the receivers is denoted by:

$$\tilde{P}(x_s,0;k_r,0;\omega)\equiv\int_{-\infty}^{\infty}e^{\mathrm{i}k_r x_r}P(x_s,0;x_r,0;\omega)\mathrm{d}x_r\,. \tag{C.7}$$

Finally, a Fourier transform over the sources is defined:

$$\tilde{\tilde{P}}(k_s,0;k_r,0;\omega)=\int_{-\infty}^{\infty}e^{\mathrm{i}k_s x_s}\tilde{P}(x_s,0;k_r,0;\omega)\mathrm{d}x_s\,. \tag{C.8}$$

Inverse wavefield extrapolation in the k_s,k_r,y-domain is a simple phase shift operation:

$$\tilde{\tilde{P}}\left(k_s,0;k_r,y;\omega\right)=\tilde{\tilde{P}}\left(k_s,0;k_r,0;\omega\right)e^{\mathrm{i}y\,\mathrm{sgn}(\omega)\sqrt{\frac{\omega^2}{c^2}-k_r^2}}, \tag{C.9}$$

and:

$$\tilde{\tilde{P}}\left(k_s,y;k_r,y;\omega\right)=\tilde{\tilde{P}}\left(k_s,0;k_r,y;\omega\right)e^{\mathrm{i}y\,\mathrm{sgn}(\omega)\sqrt{\frac{\omega^2}{c^2}-k_s^2}}, \tag{C.10}$$

or:

$$\tilde{\tilde{P}}\left(k_s,y;k_r,y;\omega\right)=\tilde{\tilde{P}}\left(k_s,0;k_r,0;\omega\right)e^{\mathrm{i}yk_y}, \tag{C.11}$$

where

$$k_y=\left(\sqrt{\frac{\omega^2}{c^2}-k_s^2}+\sqrt{\frac{\omega^2}{c^2}-k_r^2}\right)\mathrm{sgn}\left(\omega\right) \tag{C.12}$$

and $\mathrm{sgn}(\omega) = \omega/|\omega|$. Transformation back to the time domain with the three inverse Fourier transforms results in:

$$\begin{aligned}p\left(x,y;x,y;t\right)&=\int_{-\infty}^{\infty}e^{-\mathrm{i}\omega t}\int_{-\infty}^{\infty}e^{-\mathrm{i}xk_r}\int_{-\infty}^{\infty}e^{-\mathrm{i}xk_s}\tilde{\tilde{P}}\left(k_s,y;k_r,y;\omega\right)\mathrm{d}k_s\mathrm{d}k_r\mathrm{d}\omega\\&=\int_{-\infty}^{\infty}\int_{-\infty}^{\infty}\int_{-\infty}^{\infty}e^{-\mathrm{i}\left[x\left(k_s+k_r\right)+\omega t\right]}e^{\mathrm{i}yk_y}\tilde{\tilde{P}}\left(k_s,0;k_r,0;\omega\right)\mathrm{d}k_s\mathrm{d}k_r\mathrm{d}\omega\end{aligned}. \tag{C.13}$$

Since ω and k_y are related according to Eq. (C.12), the integral over ω can be written as an inverse Fourier transform from k_y to y. Solving Eq. (C.12) for ω:

$$\omega=\frac{c}{2k_y}\sqrt{\left(k_y^2-k_s^2+k_r^2\right)^2+4k_y^2k_s^2} \tag{C.14}$$

and its derivative:

$$\frac{\mathrm{d}\omega}{\mathrm{d}k_y}=\frac{c}{2k_y^2}\frac{k_y^4-\left(k_s^2-k_r^2\right)^2}{\sqrt{\left(k_y^2-k_s^2+k_r^2\right)^2+4k_y^2k_s^2}}. \tag{C.15}$$

The integral in becomes:

$$p\left(x,y;x,y;t\right)=\int_{-\infty}^{\infty}\int_{-\infty}^{\infty}\int_{-\infty}^{\infty}e^{-\mathrm{i}\left[x\left(k_s+k_r\right)-yk_y+\omega t\right]}\frac{\mathrm{d}\omega}{\mathrm{d}k_y}\tilde{\tilde{P}}\left[k_s,0;k_r,0;\omega\left(k_y\right)\right]\mathrm{d}k_s\mathrm{d}k_r\mathrm{d}k_y, \tag{C.16}$$

where it is explicitly assumed that $\tilde{\tilde{P}}\left[k_s,0;k_r,0;\omega\left(k_y\right)\right]=0$ for $\left|\frac{\omega}{c}\right|<\max\left(\left|k_s\right|,\left|k_r\right|\right)$. Using the imaging condition of Eq. (C.4), the image contrast can be calculated as follows:

$$g\left(x,y\right)=\int_{-\infty}^{\infty}\int_{-\infty}^{\infty}\int_{-\infty}^{\infty}e^{-\mathrm{i}\left[x\left(k_s+k_r\right)-yk_y\right]}\frac{\mathrm{d}\omega}{\mathrm{d}k_y}\tilde{\tilde{P}}\left[k_s,0;k_r,0;\omega\left(k_y\right)\right]\mathrm{d}k_s\mathrm{d}k_r\mathrm{d}k_y. \tag{C.17}$$

For computational reasons, for synthetic aperture sonar, the assumption is made that each source-receiver combination can be replaced by a midpoint, which is called the phase center. This reduces the dimensions of the problem from three to two and replaces the integrals over k_s and k_r by an integral over k_x:

$$g\left(x,y\right)=\frac{c}{2}\int_{-\infty}^{\infty}\int_{-\infty}^{\infty}\frac{k_y}{\sqrt{k_y^2+4k_x^2}}e^{-\mathrm{i}\left(2xk_x-yk_y\right)}\tilde{P}\left[k_x,0;\frac{c}{2}\mathrm{sgn}\left(k_y\right)\sqrt{k_y^2+4k_x^2}\right]\mathrm{d}k_x\mathrm{d}k_y. \tag{C.18}$$

The terms in this formula show that the imaging method consists of a 2D Fourier transform, a mapping defined by $\left(k_x,k_y\right)=\left(k_x,\sqrt{\frac{\omega^2}{c^2}-4k_x^2}\right)$, a multiplication by $\frac{ck_y}{2\sqrt{k_y^2+4k_x^2}}$ and an inverse 2D Fourier transform. When the amplitudes are not taken into account this formula simplifies to:

$$g\left(x,y\right)=\int_{-\infty}^{\infty}\int_{-\infty}^{\infty}e^{-\mathrm{i}\left(2xk_x-yk_y\right)}\tilde{P}\left[k_x,0;\frac{c}{2}\mathrm{sgn}\left(k_y\right)\sqrt{k_y+4k_x^2}\right]\mathrm{d}k_x\mathrm{d}k_y. \tag{C.19}$$

References

Abraham D.A. & A.P. Lyons, 2002, *Novel physical interpretations of K-distributed reverberation.* IEEE Journal of Oceanic Engineering, Vol. 27, No. 4, October, pp. 800-813.

Abraham D.A. & A.P. Lyons, 2004, *Simulation of non-Rayleigh reverberation and clutter.* IEEE Journal of Oceanic Engineering, Vol. 29, No. 2, April, pp. 347-362.

Ainslie, M.A., C.H. Harrison, P.W. Burns, 1996, *Signal and reverberation prediction for active sonar by adding acoustic components*, IEE Proceedings of Radar, Sonar and Navigation, Vol. 143, No. 3, pp. 190-195.

Allensworth W.S., C.W. Kennedy, B.K. Newhall & I.W. Schurman, 1995, *Twin-line array development and performance in a shallow water littoral environment.* Johns Hopkins APL Technical Digest, vol. 16, no. 3, pp. 222-232.

Ballegooijen E.C. van, G.W.M. van Mierlo C. van Schooneveld, P.P.M van der Zalm, A.T. Parsons & H. Field, 1989, *Measurement of towed array position, shape and attitude*, IEEE Journal of Oceanic Engineering, Vol. 14, No. 4, October, pp. 375-383.

Banks S.M. & H.D. Griffiths, 2002, *Imaging and motion estimation for synthetic aperture sonar based on fast factorised back-projection*, Proceedings of the Sixth ECUA, Gdansk, Poland, June, pp. 529-534.

Banks S.M., Sutton, T. & Griffiths, H., 2000, *Noise susceptibility of phase unwrapping algorithms for interferometric synthetic aperture sonar.* Proceedings of the Fifth ECUA, Lyon, France, July, pp. 451-456.

Been R., 1996, *Application of a ML type Estimator to the Towed Array Shape Estimation Problem*, Proceedings of the International Conference on arrays and Beamforming in Sonar, Institute of Acoustics, pp. 1-14.

Beerens S.P., S.P. van IJsselmuide, C. Volwerk, E. Trouvé & Y. Doisy, 1999, *Flow Noise analysis of towed arrays.* Proceedings of UDT Europe, pp. 392-396.

Beerens S.P., R. Been, J. Groen, Y. Doisy & E. Noutary, 2000, *Port-Starboard discrimination on hydrophone triplets in active and passive towed arrays*, Proceedings of the UDT Pacific, pp. 63-68.

Berg, R., Schneider, H.G., Gilroy, L., Karasalo, I., MacGillivray, I., Ter Morshuizen, M. & Volker, A., 2003, *Acoustic target strength modelling: results from a workshop on a benchmark submarine*, Proceedings of the UDT Europe, CD-ROM.

Berkhout A. J., 1982, *Seismic migration, imaging of acoustic energy by wave field extrapolation.* Elsevier, Amsterdam, The Netherlands.

Bellettini A. & M.A. Pinto, 2000, *Experimental investigation of synthetic aperture sonar micronavigation.* Proceedings of the Fifth ECUA 2000, Lyon, France, July, pp. 445 - 450.

Bellettini A. & M.A. Pinto, 2002, *Theoretical accuracy of synthetic aperture sonar micronavigation using a displaced phase-center antenna*, IEEE Journal of Oceanic Engineering, Vol. 27, No. 4, October, pp. 780-789.

Berliner M.J. & J.F. Lindberg, 1995, *Acoustic particle velocity sensors; design, performance and applications.* American Institute of Pysics Conference Proceedings Vol. 368, pp. 1-464, Naval Undersea Warfare Center.

Bonifant W.W., 1999, *Interferometric synthetic aperture sonar processing*, MSc. Thesis, Georgia Institute of Technology.

Bouvet M., 1987, *Beamforming of a Distorted Line Array in the Presence of Uncertainties on the Sensor Positions*, Journal of the Acoustical Society of America, 81, 6, 1833-1840.

Bucker H.P., 1978, *Beamforming a Towed Linear Array of Unknown Shape*, Journal of the Acoustical Society of America, 63, 5, 1451-1454.

Bucknam, J.W., A.M. Chwastyk, H.D. Black & F. C. Paddison, 1974, *Synthetic aperture sonar*, Applied Physics Lab., the Johns Hopkins Univ., Technical Memorandum, pp. 1-46.

Callow H. J., M. P. Hayes & P. T. Gough, 2001, *Advanced wavenumber domain processing for reconstruction of broad-beam multiple-receiver synthetic aperture imagery*, Image and Vision Computing New Zealand IVCNZ, pp. 51–56.

Callow H.J., M.P. Hayes & P.T. Gough, 2001, *Noncoherent autofocus of single-receiver broad-band synthetic aperture sonar imagery*, Proceedings of IEEE Oceans, pp. 157-162.

Chapman, D.M.F. & D.D. Ellis, 1998, *The elusive decibel: thoughts on sonars and marine mammals*, Canadian Acoustics / Acoustique Canadienne, 26(2), pp. 29-31.

Chatillon, J., 2000, *Absence of Nyquist criterion for spatial sampling of a strip-map synthetic aperture sonar*, Proceedings of the Fifth ECUA 2000, Lyon, France, July, pp. 401 - 406.

Clay, C. & H. Medwin, 1977, *Acoustical oceanography: Principles and applications*, John Wiley & Sons Inc.

Ciany C. & W. Zurawski, 2001, *Performance of computer-aided detection/ classification and data fusion algorithms for automated detection and classification of underwater mines*, Proceedings of CAD/CAC, Halifax, Canada, November.

Cox H., R.M. Zeskind & M.M. Owen, 1991, *Robust adaptive beamforming.* IEEE Trans. Acoust. Speech, Signal Processing, vol. ASSP-35, no. 9 (September), pp. 1365-1376.

Curlander J.C. & R.N. McDonough, *Synthetic Aperture Radar: Systems and Signal Processing*, John Wiley and Sons, 1991.

Doisy Y., 1995, *Port-starboard discrimination performances on active towed array systems.* Proceedings of the UDT Europe, pp. 125-129.

Doisy Y., L. Deruaz, S.P. Beerens & R. Been, 2000, *Target Doppler estimation using wide-band Doppler sensitive pulses.* IEEE transactions on Signal Processing, Vol. 48, No. 5, May, pp. 1213-1224.

Doisy Y., L. Deruaz, S.P. van IJsselmuide, S.P. Beerens & R. Been, 2006, *Reverberation suppression using wideband Doppler sensitive pulses,* Accepted for IEEE Journal of Oceanic Engineering.

Dragonette, L.R., D.M. Drumheller, C.F. Gaumond, D.H. Hughes, B.T. o' Connor, N.-C. Yen & T.J. Yoder, 1996, *The application of two-dimensional signal transformations to the analysis and synthesis of structural excitations observed in acoustical scattering,* Proceedings of the IEEE, Vol. 84, No. 9, September, pp. 1249-1263.

Edelson, G.S. & Tufts, D.W., 1992, *On the ability to estimate narrow-band signal parameters using towed arrays*, IEEE Journal of Oceanic Engineering, Vol. 17, No. 1, January, pp. 48-61.

Eichel P.H., D.C. Ghiglia & C.V. Jakowatz, 1989, *Speckle processing method for synthetic-aperture-radar phase correction,* Optics Letters, Vol. 14, No. 1, pp. 1-3.

Ekhaus I., 1997, *Reduced wavenumber synthetic aperture for MCM applications*, Proceedings of the Fifth Annual Adaptive Sensor Array Processing Workshop, pp. 241-251.

Ellis D.D. & Franklin, J.B., 1994, *The importance of hybrid ray paths, bottom loss, and facet reflection on ocean bottom reverberation,* Progress in Underwater Acoustics, New York: Amer. Inst. Physics, pp. 75-84.

Felisberto P. & S.M. Jesus, 1996, *Towed Array Beamforming during ship's manoeuvring*, IEE Proc. Radar, Sonar, Navig., 143, 3, 210-215.

Fernandez J.E. & J.T. Christoff, 2000, *Multi-Aspect Synthetic Aperture Sonar*, Proceedings of IEEE Oceans, pp. 177-180.

Feuillet J.P., W.S. Allensworth & B.K. Newhall, 1995, *Nonambiguous beamforming for a high resolution twin-line array.* J. Acoust. Soc. Am., 97, 5, May, pp. 3292.

Fortune S.A., M. P. Hayes & P.T. Gough, 2001, Statistical autofocus of synthetic aperture sonar images using image contrast optimisation, Proceedings of IEEE Oceans, CD-ROM.

Francois, R.E. & G.R. Garrison, 1982, *Sound absorption based on ocean measurements: part I: pure water and magnesium sulfate contributions,* Journal of the Acoustical Society of America, Vol. 72, Issue 3, pp. 896-907.

Francois, R.E. & G.R. Garrison, 1982, *Sound absorption based on ocean measurements: part II: boric acid contribution and equation for total absorption*, Journal of the Acoustical Society of America, Vol. 72, Issue 6, pp. 1879-1890.

Fritsch, F.N. & R.E. Carlson, 1980, *Monotone Piecewise Cubic Interpolation*, SIAM Journal of Numerical Analysis, Vol. 17, pp.238-246.

Gaunaurd, G.C., 1985, *Sonar cross sections of bodies partially insonified by finite sound beams*, IEEE Journal of Oceanic Engineering, Vol. 10, No. 3, July, pp. 213-230.

Gerstoft P., W.S. Hodgkiss, W.A. Kuperman, H. Song, M. Siderius and P.L. Nielsen, 2003, *Adaptive beamforming of a towed array during a turn*, IEEE Journal of Oceanic Engineering, Vol. 28, No. 1, January, pp. 44-54.

Gough P.T. & D.W. Hawkins, 1997, *Imaging algorithms for a strip-map synthetic aperture sonar: minimizing the effects of aperture errors and aperture undersampling*, IEEE Journal of Oceanic Engineering, Vol. 22, No. 1, January, pp. 27-39.

Gough P.T., M. P. Hayes & H. J. Callow, 2000, *Strip-map path correction using phase matching autofocus*, Proceedings of the Fifth ECUA, Lyon, France, July, pp. 412-418.

Gray D.A., B.D.O. Anderson & R.R. Bitmead, 1993, *Towed Array Shape Estimation Using Kalman Filters - Theoretical Models*, IEEE Journal of Oceanic Engineering, Vol. 18, No. 4, October, pp. 543-556.

Griffiths H.D., T.A. Rafik, Z. Meng, C.F.N. Cowan, H. Shafeeu & D.K. Anthony, 1997, *Interferometric synthetic aperture sonar for high-resolution 3-D mapping of the seabed*, IEE Proceedings - Radar, Sonar and Navigation Vol. 144, No. 2, pp. 96-103.

Groen J., S.P. Beerens, R. Been, Y. Doisy & E. Noutary, 2005, *Adaptive Port-Starboard beamforming of Triplet Sonar Arrays*, IEEE Journal of Oceanic Engineering, Vol. 30, No. 2, April, pp. 348-359.

Groen J., J.C. Sabel & A. Hétet, 2001, *Synthetic aperture processing techniques applied to rail experiments with a mine hunting sonar*, Proceedings of the UDT Europe, CD-ROM.

Groen J., S.P. Beerens & Y. Doisy, 2004, *Shape and Doppler corrected beamforming for low frequency active sonars*, Proceedings of the UDT Europe, CD-ROM.

Groen J., S.P. Beerens & Y. Doisy, 2004, *Shape and Doppler correction for a towed sonar array*, Proceedings of IEEE/MTS Oceans, pp. 613-620.

Groen J. & J.C. Sabel, 2002, *Interaction Between Autofocusing and Synthetic Aperture Processing: A Study Based on Simulations and Experimental Rail Data*, Proceedings of the Sixth ECUA, Gdansk, Poland, June, pp. 235-240.

Groen J. & J.C. Sabel, 2002, *The choice for the signal-processing kernel in synthetic aperture sonar: considerations and implications*, Acta Acustica. Vol. 88, No. 5, pp. 658-662.

Groen J., R.E. Hansen & J.C. Sabel, 2003, *Sonar path correction in synthetic aperture processing*, Proceedings of the UDT Europe, CD-ROM.

Groen, J., B.A.J. Quesson, J.C. Sabel, R.E. Hansen, H.J. Callow & T.O. Sæbø, 2005, *Simulation of high resolution mine hunting sonar measurements*, Proceedings of the Underwater Acoustic Measurements conference, June 2005, Heraklion, Greece.

Hagen P.E., R.E. Hansen, K. Gade & E. Hammerstad, 2001, *Interferometric synthetic aperture sonar for AUV based mine hunting: the SENSOTEK project*, Proceedings of Unmanned Systems, CD-ROM.

Hagen P.E., N. Stoerkersen, K. Vestgaard, P. Kartvedt & G. Sten, 2002, *AUV Based Mine Hunting Demonstrated from MCMV*, Proceedings of the UDT Europe, CD-ROM.

Hawkins D.W., 1996, *Synthetic Aperture Imaging Algorithms with application to wideband sonar*, Ph.D. thesis, University of Canterbury, Christchurch, New Zealand.

Hayes M.P. & P.T. Gough, 1992, *Broadband synthetic aperture sonar*, IEEE Journal of Oceanic engineering, Vol. 17, No. 1, January, pp. 80-94.

Hayes M.P. & P.T. Gough, 2004, *Synthetic aperture sonar: a maturing discipline*, Proceedings of the Seventh ECUA, Delft, The Netherlands, June, pp. 1101-1106.

Haykin S., J.H. Justice, N.L. Owsley, J.L. Yen & A.C. Kak, 1985, *Array signal processing.* Prentice-Hall.

Hétet A.P., 2000, *Evaluation of specific effects of synthetic aperture sonar, by conducting at sea experiments with a rail, in the frame of mine hunting systems design.* Proceedings of the Fifth ECUA, Lyon, France, July, pp. 439 - 444.

Hétet, A.P., M. Amate, B. Zerr, M. Legris, R. Bellec, J.C. Sabel & J. Groen, 2004, *SAS processing results for the detection of buried objects with a ship-mounted sonar***,** Proc. of the Seventh ECUA, Delft, The Netherlands, July, pp. 1127 - 1132**.**

Horton, J.W., 1959, *Fundamentals of Sonar*, 2nd edition, United States Naval Institute, Annapolis.

Hunt, F.V., 1992, *Origins in acoustics***,** Acoustical Society of America**.**

Hunter, A. J., M. P. Hayes & P. T. Gough, 2003**,** *A comparison of fast factorised back-projection and wavenumber algorithms for SAS reconstruction.* Proceedings of the World Congress on Ultrasonics, Paris, France.

Hunter, A. J. & M. P. Hayes, 2005**,** *Towards more accurate shadow modelling for simulated SAS imagery.* Proceedings of IEEE Oceans, Brest, France.

Huygens, C., 1690, *Treatise on light*, The Hague, The Netherlands.

IJsselmuide, S.P. van, S.P. Beerens, Y. Doisy & L. Deruaz, 2003, *New sonar waveforms for active torpedo detection*, Proceedings of UDT Europe, CD-ROM.

Jakowatz Jr. C.V., D.E. Wahl, P.H. Eichel, D.C. Ghiglia & P.A. Thompson, 1996, *Spotlight-mode synthetic aperture radar: a signal processing approach*, ISBN 0-7923-9677-4.

Johnson K.A., M. P. Hayes & P.T. Gough, 1995, *Estimating sub-wavelength sway of sonar towfish*, IEEE Journal of Oceanic engineering, Vol. 20, No. 4, October, pp. 258-267.

Karasalo, I. & P. Skogqvist, 2005, *Identification of object parameters from transient bistatic scattering data*, Boundary influences in high frequency shallow water acoustics conference, Bath, United Kingdom, pp. 357-365.

Kirsteins, I.P., A. Tesei & R. Lim, 2004, Methodologies for extracting the spatially semi-coherent components of the scattering response from buried symmetric targets, Proceedings of the Seventh ECUA, Delft, The Netherlands, July, pp. 489-496.

Kramer S.A., 1967, *Doppler and acceleration tolerances of high-gain, wideband linear FM correlation sonars*, Proceedings of the IEEE, Vol. 55, 627-636.

Kramer S.A., 1969, *Statistical analysis of wide-band pseudorandom matched filter sonars*, IEEE Transactions on Aerospace and Electronic Systems, Vol. AES-5, no. 2, March, pp. 152-155.

Lambert, J.H., 1760, *Photometria*, Augsburg.

Lurton, X., 2004, *An introduction to underwater acoustics*, Springer-Verlag.

Maksym J.N. & M.S. Sandys-Wunsch, 1997, *Adaptive beamforming against reverberation for a three-sensor array*. J. Acoust. Soc. Am. 102, 6, December, pp. 3433-3438.

Marx D., M. Nelson, E. Chang, W. Gillespie, A. Putney & K. Warman, 2000, *An Introduction to Synthetic Aperture Sonar,* IEEE Signal Processing Workshop on Statistical Signal and Array Processing, pp. 717-721.

Mchugh R., S. Shaw, S. & N. Taylor, 1998, *Spatial sampling ambiguities in synthetic aperture sonar for broadside and squint look operations*, Proceedings of IEEE Oceans, Nice, France, Oct 1998, pp. 960-964.

Mchugh R., S. Shaw, S. & N. Taylor, 1995, *The application of pixel based imaging to synthetic aperture sonar*, Proceedings IOA, Volume 17, part 8, December 1995, pp. 21-30.

Mchugh R., 1997, *Synthetic aperture sonar: a focused beamforming approach*, IEE Eurel Meeting on Radar and Signal Processing, Peebles, 5-8 July, paper no. 30, pp. 1-2.

Mierlo G.W.M. van, S.P. Beerens, R. Been, Y. Doisy & E. Trouvé, 1997, *Port/Starboard discrimination on hydrophone triplets in active and passive towed arrays.* Proceedings of the UDT Europe, pp. 176-181.

Monzingo R.A. & T.W. Miller, 1980, *Introduction to adaptive arrays.* John Wiley & Sons.

Neubauer, W.G, 1958, *Acoustic reflection from surfaces and shapes*, Naval Research Laboratory.

Nielsen R.O., 1991, *Sonar Signal Processing.* Artech house.

Owsley N.L. et al., 1985, *Array signal processing.* Prentice-Hall.

Pouliquen, E., O. Bergem & N. Pace, 1999, *Time-evolution modeling of seafloor scatter. I. Concept*, Journal of the Acoustical Society of America, Vol. 105, Issue 6, pp. 3136-3141.

Quesson, B.A.J., Schippers, P., Groen, J., Sabel, J.C. & Driessen, F.P.G., 2005, *Validation of high frequency acoustic target modelling***,** Proceedings of IEEE Oceans, CD-ROM.

Raney R.K. & P.W. Vachon, 1988, *P.W. Synthetic aperture radar imaging of ocean waves from an airborne platform: focus and tracking issues*, Journal of Geophysical research, Vol. 93, October, pp. 12475-12483.

Raney, R.K., H. Runge, R. Balmer, I.G. Cumming & F.H. Wong, 1994, *Precision SAR processing using chirp scaling*, IEEE Transactions on Geoscience and remote sensing, vol. 32 (4), July, pp. 786-799.

Reed S., J. Bell, J. & Y. Petillot, 2001, *Unsupervised mine detection and analysis in side-scan sonar: A comparison of Markov Random Fields and Statistical Snakes*, Proceedings of CAD/CAC, Halifax, Canada, November, CD-ROM.

Sabel J.C., J. Groen, & B.A.J. Quesson, 2005, *Shadow enhancement in synthetic aperture sonar imagery for improved target classification.* International conference on Underwater Acoustic Measurements: technologies and results, Crete, F.O.R.T.H., Heraklion, CD-ROM.

Sabel J.C., J. Groen, & B.A.J. Quesson, 2004, *Experiments with a ship-mounted low frequency SAS for the detection of buried objects*, Proceedings of the Seventh ECUA, Delft, The Netherlands, June, pp. 1133-1138.

Schippers, P., 2004, *Validation of the propagation, target echo and sonar performance model ALMOST with near field target echo measurements*, Crete, F.O.R.T.H., Heraklion, CD-ROM.

Shippey G., P. Ulriksen & Q. Liu, 1998, *Wideband swath bathymetry, SAS autofocus and underwater navigation fixes: three related problems in echo/image correlation.* Proc. Int. Conf. On Sonar Signal Processing, pp. 1-10.

Shippey G., J. Pihl & M. Jönsson, 2001, *Autopositioning for Synthetic Aperture Sonar using Fast Factorised Back Projection*, Proceedings of CAD/CAC, Halifax, Canada, November.

Stansfield, D, 1991, *Underwater electroacoustic transducers*, Bath University Press, Bath.

Stergiopoulos S. & H. Urban, 1992, *A new passive synthetic aperture technique for towed arrays*, IEEE Journal of Oceanic engineering, January. Vol. 17, No. 1, January, pp. 16-25.

Stergiopoulos S., 2001, *Advanced signal processing handbook: theory and implementation for radar, sonar, and medical imaging real-time systems*. Boca Raton: CRC Press.

Stolt R.H., 1978, *Migration by Fourier Transform*, *Geophysics*, Vol. 23, No. 1.

Sutton T.J., S.A. Chapman & H.D. Griffiths, 2000, *Robustness and effectiveness of autofocus algorithms applied to diverse seabed environments*, Proceedings of the Fifth ECUA, Lyon, France, July, pp. 407-412.

Tesei, A., A. Maguer, W.L.J. Fox, R. Lim & H. Schmidt, 2002, *Measurements and modeling of acoustic scattering from partially and completely buried spherical shells*, Journal of the Acoustical Society of America, Vol. 112, Issue 5, pp. 1817-1830.

THOMSON-CSF, 1989, *Antenne hydrophonique linéaire et dispositif électronique de levée d'ambiguïté droite gauche associé à cette antenne.* Patent Number 89-11749, Septembre 8.

Thorp, W.H., 1967, *Analytic description of the low-frequency attenuation coefficient*, Journal of the Acoustical Society of America, Vol. 42, Issue 1, pp. 270-271.

Trees H.L. van, 1968, *Detection, Estimation, and Modulation Theory*. John Wiley & Sons.

Ulander L.M.H., Hellsten, H. & Stenstrom, G., 2000, *Synthetic-aperture radar processing using fast factorised backprojection*, Proceedings of EUSAR, Munich, Germany, pp. 753-756.

Upadhyay S.K., 2004, *Seismic Reflection Processing*, Springer-Verlag, New York.

Urick R.J., 1975, *Principles of Underwater Sound*, McGraw Hill.

Veen B.D. van, 1991, *Minimum variance beamforming with soft response constraints.* IEEE Trans. Signal Processing, Vol. 39, No.9, September, pp. 1964-1972.

Vlieger J.H. de & E.C. van Ballegooijen, 1995, *ALF an experimental low frequency active sonar system.* Proceedings of the UDT Europe, pp. 131-136.

Warhonowicz T., H. Schmidt-Schierhorn & H. Höstermann, 1999, *Port/Starboard discrimination performance by a twin line array for a LFAS sonar system.* Proceedings of the UDT Europe, pp. 398.

Widrow B. & S.D. Stearns, 1985, *Adaptive Signal Processing.* Prentice-Hall.

Woodward, P.M., 1964**,** *Probability and information theory, with applications to radar*, 2nd edition, Pergamon Press, New York.

List of symbols and abbreviations

Matrices and vectors are represented by **bold** face characters. Scalars are written in single *italic* face characters except the terms of the sonar equation, which are not written in italic face and may consist of more than one character. Vectors are assumed to be column vectors unless stated otherwise. The Euclidean norm of a vector $\mathbf{x}$ is written as $|\mathbf{x}|$. Convolution is denoted with * and the Hermitian operation is denoted with †.

Roman upper case:

A	amplitude
A_0	shadow area for a point source
A_{blur}	blurred area of the acoustic shadow
A_m	representative reverberation scatter area of scatterer m
AL	Attenuation Loss
ASG_∞	Array Signal Gain of an ideal array
B	beamformer output
$\mathbf{C}$	ping-to-ping correlation matrix for Displaced Phase Center (DPC) method
DI	Directivity Index
G	triplet gain (Chapter 3), Fourier transform of sonar image (Chapter 5 & Chapter 6)
G_n	noise gain
G_s	Green's function (Chapter 2), signal gain (Chapter 3)
H	hypothesis of detection (noise or signal plus noise)
I_i	incident intensity
IL	Loss at the Interface from water to sediment
I_s	scattered intensity
L	array length
ML	Maneuvering Loss
ML_1	Maneuvering Loss due to position errors
ML_2	Maneuvering Loss due to Doppler shift
ML_2	Maneuvering Loss due to Doppler spreading
N	number of samples
N_h	number of hydrophones
N_p	number of pings
NL	Noise Level
P	Fourier transform of acoustic pressure p
P_i	pressure of incident field
P_s	pressure of scattered field
PL	Propagation Loss
PL_1	Propagation Loss from the acoustic source to target
PL_2	Propagation Loss from the target to the receiver
$\mathbf{R}$	correlation matrix
R	turn radius
$\mathbf{R}_n$	noise correlation matrix

RL	Reverberation Level
R_r	reflection coefficient
R_i	reflection coefficient at the interface between water and sediment
S	Signal level
S	target surface
S_p	passive target spectral signature
SRR	Signal to Reverberation Ratio
SNR	Signal to Noise Ratio
SSL	Spherical Spreading Loss from the acoustic source to target
SSL_1	Spherical Spreading Loss from the acoustic source to target
SSL_2	Spherical Spreading Loss from the target to the receiver
T	signal duration
T_p	ping repetition time
TPL	Total Path Loss
TS	Target Strength
V	tow speed
$\mathbf{W}$	matrix with weighting coefficients
Y	Fourier transform of beamformed output

Roman lower case:

b	frequency bandwidth
$\mathbf{b}$	single array beamformed output
c	sound speed in water
c_s	sound speed in sediment
c_t	sound speed in target
d, d_r	receiver spacing
d_d	distance between two discretization points
d_F	maximum separation between source and receiver
f	frequency
f_c	centre frequency
f_p	probability density function
f_s	sample frequency
$\mathbf{h}$	beamform coefficients
h	height
k	acoustic wavenumber
k_r	acoustic wavenumber corresponding to the range axis
k_x	acoustic wavenumber corresponding to the x-axis
k_y	acoustic wavenumber corresponding to the y-axis
l	position along the array
i	time sample index
$\mathbf{n}$	outward normal vector on the target surface
n_h	hydrophone index
$\mathbf{n_k}$	outward normal vector for discretization point k
n_p	ping index
$\mathbf{n_{r,k}}$	unit vector pointing from discretization point k to receiver
$\mathbf{n_{s,k}}$	unit vector pointing from discretization point k to source
$\mathbf{n}_x$	vector containing x-coordinates of outward normal vectors on the target surface

$\mathbf{n}_y$	vector containing y-coordinates of outward normal vectors on the target surface
$\mathbf{n}_z$	vector containing z-coordinates of outward normal vectors on the target surface
p	acoustic pressure
p_{MF}	matched filter output
p_{RMS}	root mean square pressure
r	range
r_{focus}, y_{focus}	focus range
r_{PS}	port starboard rejection
r_s	radius of spherical object
r_t	triplet radius
s	signal
s_r	replica signal
t	time
t_i	time sample
u_s	velocity coordinate in x direction of the sonar
v_{st}	relative speed of the target relative to the source
v_{rt}	relative speed of the target relative to the receiver
$\mathbf{v}$	velocity vector
w	width
$\mathbf{x}$	Cartesian coordinate vector (x,y,z)
x	spatial coordinate
x_m	x-coordinate of midpoint or phase center
$\mathbf{x_p}$	sediment penetration point for acoustic ray from source to target (x_p,y_p,z_p)
$\mathbf{x_q}$	sediment penetration point for acoustic ray from target to receiver (x_q,y_q,z_q)
$\mathbf{x_r}$	receiver position (x_r,y_r,z_r)
$\mathbf{x}_{\mathrm{reverberation}}$	vector containing x-coordinates of reverberation point scatterers
x_s	x-coordinate of acoustic source position
$\mathbf{x_s}$	acoustic source position (x_s,y_s,z_s)
$\mathbf{x}_{\mathrm{shadow}}$	projected shadow position $(x_{\mathrm{shadow}},y_{\mathrm{shadow}},z_{\mathrm{shadow}})$
$\mathbf{x}_{\mathrm{sonar}}$	vector containing x-coordinates of sonar sources and receivers
x_t, x_T	x-coordinate of target
$\mathbf{x_t}$	acoustic target position (x_t,y_t,z_t)
$\mathbf{x}_{\mathrm{target}}$	vector containing x-coordinates of targets
y	spatial coordinate
y_m	y-coordinate of midpoint or phase center
$\mathbf{y}_{\mathrm{reverberation}}$	vector containing y-coordinates of reverberation point scatterers
y_s	y-coordinate of acoustic source position
$\mathbf{y}_{\mathrm{sonar}}$	vector containing y-coordinates of sonar sources and receivers
y_t, y_T	y-coordinate of target
$\mathbf{y}_{\mathrm{target}}$	vector containing y-coordinates of targets
z	spatial coordinate
$\mathbf{z}_{\mathrm{reverberation}}$	vector containing z-coordinates of reverberation point scatterers
z_s	z-coordinate of acoustic source position
$\mathbf{z}_{\mathrm{sonar}}$	vector containing z-coordinates of sonar sources and receivers
z_t	z-coordinate of target
$\mathbf{z}_{\mathrm{target}}$	vector containing z-coordinates of targets

Greek:

α	Doppler compression factor
α_w	attenuation in water
α_s	attenuation in sediment
β	integration angle for synthetic aperture sonar
γ	ping-to-ping correlation coefficient (Chapter 5), grazing angle (Chapter 6)
δ	dirac Delta function
ε	diagonal loading for correlation matrix
ε_R	inaccuracy in radius of curvature
ε_V	inaccuracy in velocity
η	phase
θ	angle relative to the sonar
$\theta_{3\text{dB}}$	3-dB beamwidth
θ_s	refracted angle in sediment
ϑ	angle between middle of the image and broadside
λ	acoustic wavelength
Λ	likelihood ratio
μ	Lambert's parameter
ν	triplet roll
ν_j	roll of hydrophone j inside the triplet
ξ	blur ratio: blurred area in the image divided by the expected affected shadow area
ρ	density of water (Chapter 2), correlation coefficient (Chapter 3)
ρ_s	density of sediment
ρ_t	density of target
σ	standard deviation
σ_g	square root of image contrast
τ	time delay
υ, υ_1, υ_2	stochastic variable
φ	angle relative to the sonar
χ	target roughness factor
ψ	array heading
ω	angular frequency

Abbreviations:

ALMOST	Sonar model Acoustic Loss Model for Operational Studies and Tasks
ASDIC	Anti Submarine Detection Investigation Committee (ASDIC)
ASW	Anti-Submarine Warfare
AUV	Autonomous Underwater Vehicle
CAPTAS	Combined Active Passive Towed Array Sonar
CO	Contrast Optimization
CPA	Closest Point of Approach
CW	Transmit signal (Continuous Wave signal)
DERA	British research institute (Defence Evaluation and Research Agency)
DMC	Directional Motion Compensation
DPC	Displace Phase Center
DPCA	Displace Phase Center Antenna
EdgeTech	Synthetic Aperture Sonar system built by EdgeTech

FEL	Physics and Electronics Laboratory
FFI	Norwegian Defense Research Establishment
FFT	Fast Fourier Transform
GESMA	French Defense Agency (Groupe des Etudes Sous-Marines de l'Atlantique)
GPS	Global Position System
HFM	Transmit signal (Hyperbolic Frequency Modulated signal)
HNLMS	Her Netherlands Majesty's Ship
HUGIN	AUV built by Kongsberg
IC	Image Correlation
LFAS	Low Frequency Active Sonar
LFM	Transmit signal (Linear Frequency Modulated signal)
MH	Mine Hunting
MVDR	Minimum Variance Distortionless Response
NDMC	Non-Directional Motion Compensation
PAP	Remotely operated vehicle for inspection with a camera (Poison Auto Propulsé)
PGA	Phase Gradient Autofocus
PS	Port/Starboard
PTR	Point Target Response
RNLN	Royal Netherlands Navy
SAR	Synthetic Aperture Radar
SAS	Synthetic Aperture Sonar
SCB	Shape Corrected Beamforming
SDCB	Shape and Doppler Corrected Beamforming
SENSOTEK	Synthetic aperture sonar system built by FFI and Kongsberg
SEWACO	Division of the RNLN (Sensor Weapon and Command systems)
SFI	Space-Frequency Imaging
SIMONA	TNO sonar simulator (SIMulation Of Non-acoustics and Acoustics)
SOCRATES	TNO Low Frequency Sonar Source (SOund CalibRAtion and TESting)
SSP	Sound Speed Profile
STI	Space-Time Imaging
TNO	Netherlands Organization for Applied Scientific Research
TUS	Thales Underwater Systems
ULA	Uniform Linear Array
UUV	Unmanned Underwater Vehicle

Adaptive motion compensation in sonar array processing

Summary

In recent years, sonar performance has mainly improved via a significant increase in array aperture, signal bandwidth and computational power. The research in this thesis is aimed at improving sonar array processing techniques based on these three steps forward. In many cases motion of the sonar needs to be accounted for, to allow further performance enhancement. Motion problems appear in applications for anti-submarine warfare and mine hunting.

For towed anti-submarine warfare sonar, beamforming methods are developed for the port/starboard (PS) discrimination problem and for compensation of Doppler effects. The sonar system considered consists of a towed source and receiving array containing hydrophone triplets in one bendable hose. In mine hunting, synthetic aperture sonar (SAS) is a promising technique to improve sonar performance by combination of multiple pings. Data flow for real-time SAS processing is problematic, and thus faster imaging techniques are examined. Sonar performance of fast techniques decreases when the sonar deviates from the required straight track. Motion compensation prior to imaging is possible and is examined in addition.

Investigation of each of the processing methods resulted in implementation, application to different test datasets and performance assessment. For the PS discrimination problem three beamformers are investigated. These beamformers and the Doppler compensation methods are investigated theoretically, with simulations and with datasets recorded at sea. The Doppler compensation analysis also resulted in analytic expressions for performance degradation and sensor requirements. A complete SAS processing chain is developed with as primary modules motion estimation, motion compensation and imaging. For the imaging methods, the trade-off between computational load and sonar performance is analyzed. Requirements and applicability of fast imaging, achieved in the wavenumber-frequency domain, are analyzed with regard to focusing, motion and interpolation. The SAS processing is tested on simulations and on five independent experimental datasets with different frequencies, targets and geometries.

The array processing techniques proposed in this thesis substantially improve the performance of the sonars considered. Triplet technology is a successful solution for the PS discrimination problem. The ambiguous direction can be sufficiently suppressed with the proposed beamforming methods. The requirements for Doppler compensation are derived analytically and compensation is achieved with minor adaptations to the signal processing chain using the available sensor suite. The SAS research showed that for the considered cases, wavenumber frequency imaging is preferred and proper motion compensation is feasible. An important finding while comparing the proposed imaging algorithms was the way to enhance an important classification clue in the sonar image, the acoustic shadow.

Johannes Groen

Adaptieve bewegingscompensatie

in sonar array processing

Samenvatting

Sonar prestatie is de afgelopen jaren vooral verbeterd door een significante toename in array apertuur, signaal bandbreedte en rekenkracht. Dit onderzoek heeft ten doel om sonar array processing technieken te verbeteren op basis van deze drie redenen. Voor verdere verbetering van sonars, moet in veel gevallen beweging van de sonar opgenomen worden in de signaalverwerking. Dit probleem is actueel voor onderzeebootbestrijding en mijnenjacht.

De bundelvormingsmethoden voor onderzeebootbestrijding zijn ontwikkeld om het probleem van links/rechts onderscheid en de problemen met Doppler effecten op te lossen. Het sonar systeem dat in dit onderzoek is gebruikt bestaat uit een gesleepte bron en ontvangst array, een slang met hydrofoon triplets. Synthetische Apertuur Sonar (SAS), gebaseerd op combineren van meerdere pings, is een veelbelovende techniek om de prestaties van mijnenjacht sonar te verbeteren. De datastroom voor SAS processing is problematisch en maakt het noodzakelijk om snellere afbeeldingstechnieken te onderzoeken. Een sonar met deze snelle technieken presteert echter slechter als de sonar zich niet langs de vereiste rechte lijn beweegt. De oplossing hiervoor, bewegingscompensatie, is onderzocht en blijkt mogelijk te zijn.

Het onderzoek naar deze processing methoden heeft geresulteerd in implementatie, toepassing op verschillende datasets en sonarprestatie evaluaties. Het links/rechts probleem is opgelost met drie bundelvormingstechnieken en het Doppler probleem is opgelost met drie technieken. In het kader van het SAS onderzoek is een volledige signaalverwerkingsketen ontwikkeld met als primaire modules bewegingsschatting, bewegingscompensatie en afbeelding. De toepasbaarheid van snelle golfgetal-frequentie domein afbeeldingstechnieken blijken sterk afhankelijk van focuseringseisen, beweging en interpolatie. De SAS signaalverwerking is getest op simulaties en vijf onafhankelijke experimentele datasets.

De voorgestelde array processing technieken blijken de prestaties van sonars substantieel te verbeteren. De triplet technologie biedt een oplossing voor het links/rechts probleem. De ambigue richting kan voldoende onderdrukt worden met de voorgestelde bundelvormers. De eisen voor Doppler compensatie kunnen expliciet en analytisch berekend worden en bewegingscompensatie kan verwezenlijkt worden met de huidige sensor capaciteit en minimale aanpassingen in de processing. De golfgetal-frequentie afbeeldingstechnieken in combinatie met passende bewegingscompensatie blijken voor de bekeken scenario’s de beste manier om SAS beelden te maken. Een belangrijke ontdekking tijdens het vergelijken van de afbeeldingstechnieken is de methode om de akoestische schaduw scherper af te beelden.

Johannes Groen

Acknowledgements

Na een afstudeerstage van tien maanden bij de afdeling Onderwater Akoestiek, begon ik op 1 februari 1998 als wetenschappelijk medewerker bij diezelfde afdeling van TNO. Na ongeveer drie jaar ervaring in het onderzoek naar laagfrequente actieve sonarsystemen samen met collega's Peter Beerens, Sander van IJsselmuide, Rob Been en Wilco Volwerk, kwam naar voren dat wetenschappelijk onderzoek toch meer bij me paste dan andere aspecten van het werk. Aangemoedigd door Peter, ben ik toen op zoek gegaan naar een manier om mijn carrière in die richting te sturen. Gerrit Blacquière, toen werkzaam bij TNO en verbonden aan de vakgroep Seismiek en Akoestiek als deeltijdhoogleraar vond het een goed idee om een promotieonderzoek te starten in het kader van verbeterde sonar signaalverwerkingstechnieken. Nadat Gerrit en ik ook nog Eric Verschuur enthousiast gemaakt hadden kon het onderzoek in gang gezet worden. Vanaf 2001 ben ik op regelmatige basis, één dag per week, in de vakgroep Seismiek en Akoestiek mee gaan draaien om te zien of de kennis aldaar van toepassing was voor mijn onderzoek. Gerrit en Eric hebben mij laten zien dat het inderdaad mogelijk was om seismische methoden toe te passen in synthetische apertuur sonar (zie Hoofdstuk 5 en Hoofdstuk 6). In Delft, kwam ik op de kamer bij Karin, John en Ewoud, die later afgelost werden door Maurice, Sandra en Gert-Jan. Bedankt voor de gezellige tijd. Ook de vakgroepgenoten Henry, Paul, Edo, Margaret, Arno, Paul, Barbara, Kees, Ayon, Edith en nog vele anderen hebben bijgedragen aan het feit dat ik me er thuis voelde als 'part-timer'. Dan rest er nog één persoon uit de vakgroep, Professor Gisolf, die intensief betrokken is geweest bij de eindfase van mijn promotieonderzoek. Ik ervaar onze samenwerking als prettig. Professor Gisolf heeft de rol van promotor professioneel opgepakt en heeft, ondanks de lastig te begrijpen 'sonar-taal', een grote bijdrage geleverd aan de totstandkoming van het proefschrift. Ook Professor Simons, mijn andere promotor en ook betrokken geraakt in de eindfase van het onderzoek, heeft een belangrijke bijdrage geleverd aan de kwaliteit van het proefschrift. Vooral zijn didaktische tips, hebben het werk leesbaar gemaakt voor een breder publiek.

Dan is het tijd om terug te gaan naar TNO waar ik tenslotte tachtig procent van mijn promotietijd doorbracht. Het onderzoek bij TNO wordt gedaan in projecten, die voornamelijk uitgevoerd worden voor en in samenwerking met de Koninkijke Marine (KM). De goede samenwerking tussen TNO en de KM was essentieel vooral voor het uitvoeren van experimenten en gebruik van metingen voor het onderzoek in dit proefschrift. Ik wil de gehele afdeling onderwater akoestiek, tegenwoordig under water technology, bedanken. Bij velen van hen is in de loop der jaren, naast collegaliteit, ook vriendschap gegroeid. De afdelingshoofden, Coenraad Ort en Frank Driessen, hebben mij altijd positief ondersteund met betrekking tot dit onderzoek. Ik wil graag mijn gezellige collega's Benoit (Beeno-iet), Paul (de Wal), Martin (de Adder) en Sander (HWD) bedanken en kan hen aanbevelen als kamergenoot. Dan is er nog Jan Cees, vaak optredend als de projectleider van mijnenjacht projecten waarin ik een groot deel van het onderzoek kon doen. Hij heeft mij veelvuldig geholpen om te publiceren en zich sterk gemaakt voor voldoende fundamenteel onderzoek. Ook de samenwerkingen in de verschillende projecten met Frans-Peter, Pascal, Tilly, Mathieu, Myriam, Nurit, Jeroen en Ton hebben, soms indirekt, bijgedragen aan dit boekje. Michael verdient dan als laatste nog een schouderklopje voor de onwaarschijnlijke prestatie om in één weekend het volledige proefschrift te lezen en te corrigeren.

Sonar research in the Netherlands takes place in an international scene. As an employee of TNO, I have been part of many international collaborations in which data and knowledge were distributed over the borders of the countries involved. In this respect, I would like to acknowledge a number of agencies and people in particular. First, Roy Hansen of the Norwegian Defense Resesarch Agency, FFI is acknowledged. He contributed by arranging distribution of several data sets that are used in Chapter 2 and Chapter 5. It was also a pleasure to publish with him and his colleagues Torstein Sæbø and Hayden Callow. Yves Doisy and Edmond Noutary of Thales Underwater Systems (France) are thanked for their contribution to the research on Anti Submarine Warfare. Furthermore, Marc Pinto and Andrea Bellettini of the NATO Undersea Research Centre (Italy), Sean Chapman of the Defense Research Agency in the United Kingdom and Alain Hétet of GESMA (France) are thanked for their efforts to supply data within our international collaboration framework. The experimental data results in Chapter 5 and Chapter 6 would not have been achieved without these efforts.

Ik wil eindigen met het bedanken van familie en vrienden voor hun belangstelling gedurende promotieperiode. Ik hoop dat jullie erbij zijn als ik de inhoud van dit boekje moet verdedigen. Bijzondere dank gaat uit naar mijn partner Nadja voor het artistiek beoordelen van de plaatjes in het boek en bovenal voor haar nooit verminderde steun.

Hans Groen
Den Haag, 28 December 2005

Curriculum Vitae

Johannes Groen was born in The Hague, The Netherlands, on September 5, 1974. He attended secondary school at the 'VWO' of the 'Christelijke scholengemeenschap Zandvliet' in The Hague. He graduated with the M.Sc. degree in mathematics in 1998, from the Delft University of Technology. His master's thesis on modeling of hydrodynamic behavior of a towed sonar system was supervised by Prof. dr. ir. A.J. Hermans and was conducted at TNO.

Since 1998 he has been working as a scientist at the Netherlands Organization for Applied Scientific Research (TNO), Defense, Security and Safety. In parallel he has started a Ph.D. research with the Seismics and Acoustics group of the Delft University of Technology in 2001. At TNO he has led several research projects and was engaged in a number of international collaboration projects.

Research projects he worked and still works in at TNO are related to active and passive Anti Submarine Warfare (ASW) sonar signal processing, synthetic aperture sonar and sonar simulator development for civil applications, mine hunting and ASW.